UNIVERSITY OF SOUTHAMPTON

FACULTY OF PHYSICAL SCIENCES AND ENGINEERING

School of Physics and Astronomy

Coherent atomic manipulation and cooling using composite optical pulse sequences

by

Alexander J. Dunning

Thesis for the degree of Doctor of Philosophy

March 2014

UNIVERSITY OF SOUTHAMPTON

ABSTRACT

FACULTY OF PHYSICAL SCIENCES AND ENGINEERING

School of Physics and Astronomy

Doctor of Philosophy

COHERENT ATOMIC MANIPULATION AND COOLING USING COMPOSITE OPTICAL PULSE SEQUENCES

by Alexander J. Dunning

The laser cooling of atoms to ultracold temperatures has propelled many groundbreaking advances in fundamental research and precision measurement, through such applications as quantum simulators and interferometric sensors. Laser cooling remains, however, highly species-selective, and techniques for its application to molecules are still in their infancy.

This thesis broadly concerns the development of laser cooling schemes, based on sequences of coherent optical pulses, which can in principle be applied to a wide range of species. We describe a cooling scheme, in which a velocity-selective impulse analogous to that in Doppler cooling is generated by a light-pulse Ramsey interferometer, and present a proof-of-concept demonstration of the scheme using ultracold rubidium-85 atoms as a test-bed. We realise an interferometer for the atoms, as they are in free-fall after release from a magneto-optical trap, by inducing stimulated Raman transitions between their ground hyperfine states. We provide a comprehensive characterisation of these Raman light-pulse interferometer optics, where particular attention is paid to light shift effects.

Raman pulses, and indeed coherent operations in *any* quantum control system, unavoidably suffer from systematic errors in the control field intensity and frequency, and these lead to reductions in pulse fidelity and readout contrast. In parallel to the work on interferometric cooling in this thesis, we report our preliminary investigations into composite pulses, whereby 'naive' single pulses are replaced by sequences of rotations with tailored durations and phases, for improving pulse fidelity in the presence of inhomogeneities. We find that composite pulses can indeed be highly effective in our cold atom system, and propose that their application in such devices as interferometric sensors is a promising prospect.

Contents

Declaration of Authorship

I, Alexander J. Dunning , declare that the thesis entitled ***Coherent atomic manipulation and cooling using composite optical pulse sequences*** and the work presented in the thesis are both my own, and have been generated by me as the result of my own original research. I confirm that:

- this work was done wholly or mainly while in candidature for a research degree at this University;
- where any part of this thesis has previously been submitted for a degree or any other qualification at this University or any other institution, this has been clearly stated;
- where I have consulted the published work of others, this is always clearly attributed;
- where I have quoted from the work of others, the source is always given. With the exception of such quotations, this thesis is entirely my own work;
- I have acknowledged all main sources of help;
- where the thesis is based on work done by myself jointly with others, I have made clear exactly what was done by others and what I have contributed myself;
- none of this work has been published before submission

Signed:.....

Date:.....

Acknowledgements

I'm greatly indebted to many people for their help and advice during my PhD at Southampton. First, I'll thank my supervisor, Tim Freegarde, for soliciting the funding for my PhD, and for providing an invaluable wealth of wisdom and support throughout it. There would appear to be two classes of PhD student in experimental atomic physics: those who put blood, sweat and tears into building an experiment from the ground up; and those who inherit an experiment from the former, and with some luck and minor changes, get some results. I am the latter, and this interjection provides a springboard for an expression of gratitude towards two of the former, namely James Bateman and Matt Himsworth. James and Matt did most of the hard work in the early stages of the experiment, during their respective PhDs (they survived), and they were immensely helpful and generous throughout the course of mine. I'd like to thank Rachel Gregory, for adding a sense of theoretical expertise to the project and for taking the reigns of the experiment upon my departure, and also Jo Rushton, for his advanced super-knowledge and programming skills, which on many occasions made my life easier. Two other (now former) group members I'd like to thank are Hamid Ohadi, who passed on many skills to me in the beginning, and Nathan Cooper, whose hard work led (via publications) to big improvements in the experiment. I'd also like to thank everyone else in the Quantum control group past and present who made my PhD a quasi-enjoyable experience at times. In particular, Woody, Jeff and Steve, for coming to the rescue when problems were difficult to articulate. Outside of the group, I'd like to thank Jonathan Jones of the University of Oxford for his guidance regarding composite pulses, and Damon Grimsey of the mechanical workshop at Southampton for his masterful tweaks to the apparatus.

Finally, I'd like to thank Ashlee, my wife, for making sure I occasionally ate something during my PhD, for keeping a diary when I forgot stuff, and for her endless support and encouragement.

"That drink," said the machine sweetly, "was individually tailored to meet your personal requirements for nutrition and pleasure."

"Ah," said Arthur, "so I'm a masochist on a diet am I?"

"Share and enjoy."

"Oh, shut up."

"Will that be all?"

Arthur decided to give up.

"Yes," he said.

Then he decided he'd be damned if he'd give up.

"No," he said, "look, it's very, very simple ... all I want ... is a cup of tea. You are going to make one for me. Keep quiet and listen."

And he sat. He told the Nutri-Matic about India, he told it about China, he told it about Ceylon. He told it about broad leaves drying in the sun. He told it about silver teapots. He told it about summer afternoons on the lawn. He told it about putting the milk in before the tea so it wouldn't get scalded. He even told it (briefly) about the history of the East India Company.

"So that's it, is it?" said the Nutri-Matic when he had finished.

"Yes, " said Arthur, "that is what I want."

"You want the taste of dried leaves boiled in water?"

"Er, yes. With milk."

"Squirted out of a cow?"

"Well, in a manner of speaking, I suppose ..."

– *The Restaurant at the End of the Universe* (1980), Douglas Adams

Chapter 1

Introduction

The ability to cool atomic gases to ultracold temperatures and quantum degeneracy has revolutionized experimental atomic physics [1]. Previously, spectroscopists working with room temperature or buffer-gas-cooled atomic vapours or beams, or indeed supersonic jets, had to contend with significant Doppler and transit-time broadening when measuring atomic spectra, and quantum coherence effects were largely undetectable.

The production of ultracold atomic gases was made possible by the invention and developent of *laser cooling* [2–4], whereby atoms preferentially absorb red-detuned laser photons which act to reduce the atomic speed, via the Doppler effect. In a magneto-optical trap (MOT) [5], atoms are simultaneously laser cooled and *confined*, via position dependent absorption, and further technical extensions to this, such as magnetic confinement and evaporative cooling, allow for the production of Bose-Einstein condensates (BECs) [6, 7]. The many applications of laser cooled atoms include quantum simulations of many-body interactions in optical lattices [8, 9], quantum information processing (QIP) with cold trapped ions [10], ultra-precice frequency standards with atomic clocks [11], and atom intereferometric inertial sensors [12].

Just as ultracold atoms have revolutionised the field of atomic physics, the study of cold and ultracold *molecules* opens up many new and exciting avenues of research [13], of which ultracold chemistry [14] and tests for variations of the fundamental constants [15, 16] are two prominent examples. Until recently, their complex internal structure has precluded the laser cooling of molecules. Traditional laser cooling requires a closed optical transition, such that many thousands of photon momenta can be imparted. In

molecules, the myriad ro-vibrational decay routes make this very difficult to achieve (indeed, even the simplest of *atomic* structures requires a repumping laser). Schemes involving multiple repumping frequencies have, however, recently been applied to succesfully laser cool diatomic molecules [17–19], although the applicable species are few.

Aside from laser cooling, the photo-association [20] of (laser cooled) atoms, has already been used to create ultracold bi-alkali molecules in the ground vibrational state [21, 22], however such schemes are restricted to those few elements which are accessible to traditional laser cooling. Other means of cooling molecular samples have been tested, including buffer-gas cooling [23], evaporative [24] and sympathetic [25] cooling, and the *slowing* of molecular beams has been demonstrated using Stark [26] and Zeeman [27] decelerators.

In [28] Weitz and Hänsch propose a scheme, based on a series of coherent femtosecond laser pulses which form the optics of a matter-wave interferometer, for the laser cooling of atoms and molecules. The advantage of this '*interferometric cooling*' scheme is that photon absorption can be made independent of the laser detuning from an optical resonance, hence cooling can be applied on several transitions within a ro-vibrational structure simultaneously. Furthermore, the short pulse durations (and their spectrally broad profiles) allow for broad simultaneous excitation of multiple ro-vibrational transitions.

One of the two main lines of investigation of this thesis concerns an experimental proof-of-concept of interferometric cooling in already-ultracold atoms. A proof-of-concept in atoms would represent the first experimental step towards the application of the scheme to molecules. More broadly speaking, the overarching research goal of the project is to develop pulse-based laser cooling schemes which can be applied to a wider range of species' than traditional laser cooling permits.

Interferometric cooling, and atom interferometry in general, requires coherent optical control over a quantum system of two metastable atomic levels. As in many other atom interferometry experiments (see, for example [12]), we realise such control with *stimulated Raman transitions* between ground hyperfine states in ultracold atoms, and our choice of element is rubidium-85. With our experimental system we are able to apply timed pulses with controlled intensity, frequency and phase to a cloud of atoms, whose

Zeeman sublevels are degenerate, after release from a magneto-optical trap (MOT) at a temperature of $20 - 100$ microkelvin. The description and characterisation of this cold atom control system forms a large proportion of the work presented in this thesis.

To achieve high interferometric contrast, coherent operations must exhibit high *fidelity*. This is compromised in our Raman system by systematic errors in the pulse area and detuning, due respectively to the range of transition dipole matrix elements (and, to a lesser extent, intensity inhomogeneities), and to Doppler-broadening. Similar systematic errors are in fact commonplace in *all* experiments involving the coherent control of quantum systems, and accordingly there exist techniques for actively reducing their detrimental effects.

The second line of investigation of this thesis concerns the use of *composite pulses* [29] for improving the fidelity of coherent operations in quantum control systems. Composite pulses, whereby single rectangular pulses are replaced by series' of pulses with tailored durations and phases, are yet to be fully exploited by the atomic physics community. We expect that along with other fidelity-enhancing techniques such as adiabatic transfer [30, 31], composite pulses have the potential to significantly improve the performance of cold-atom-based devices in the presence of systematic errors, and indeed that they have potential for use in interferometric cooling experiments.

Thesis Layout

In chapter 2 we present the theory of stimulated Raman transitions, upon which our manipulation schemes are based. We derive the effective two-level Hamiltonian and associated equations of motion for the Raman system, and describe the Bloch sphere picture for visualisation of coherent pulses. Rubidium-85, which is our test species throughout this thesis, is discussed, along with the dipole selection rules for Raman transitions.

Chapters 3 and 4 then describe the experimental apparatus and procedures involved, respectively, in the construction of a magneto-optical trap (MOT) for rubidium, and the generation of Raman pulses.

In chapter 5 we characterise the behaviour of the Raman pulses. We present measurements of Zeeman splitting and light-shifts before characterising spectral Raman profiles and Rabi flopping, where the dephasing effects of systematic errors are highlighted. By comparing numerical simulations to the experimental data, we provide useful insight into the behaviour of the pulses.

In light of the dephasing observed in chapter 5, chapter 6 details our exploration of composite pulses for improving pulse fidelity in the presence of systematic errors. We describe a model for visualision of systematic errors and fidelity in coherent operations, and present novel results demonstrating rotary spin echoes, before characterising a range of composite inversion pulses and discussing their relative performance in the context of atom interferometry.

With a good understanding of the systen in place, we then present results of our preliminary tests of interferometric cooling in chapter 7. This chapter begins with a discussion of the proposed cooling scheme, followed by an experimental characterisation of its constituent components. We then show modulation of the velocity distribution at a range of system parameters, before presenting a first demonstration of interferometric atomic cooling. We finish this chapter with a discussion of the enhancements required should interferometric cooling be applied to molecules.

Appendix A provides some general theory of atom-laser interactions, including more detailed explanations of principles which are briefly referred to in the main text. In appendix B we describe (and present sample code for) the numerical simulations performed throughout the thesis. Appendix C provides an introduction to the principles and techniques of atom interferometry, and matter-wave interferometry in general, for the interested reader. Finally, in appenix D we list the publications (existing and potential), talks and poster presentations arising from the work performed in this thesis.

Note that detailed discussions of composite pulses and interferometric cooling are left largely to chapters 6 and 7, respectively. In the preceding chapters (2–5) we present the theory behind, and experimental characterisations *of*, the cold atom system which we use for their implementation.

Part I

Theory

Chapter 2

Coherent Manipulation & Interferometry

The interferometric laser cooling and composite pulse schemes explored in this thesis are based on coherent transitions in a two-level atomic system, and we realise this experimentally by inducing stimulated Raman transitions between the ground hyperfine states of rubidium-85. Broadly speaking, a stimulated Raman transition is a two-photon process, whereby two counter-propagating laser beams, far-detuned from resonance with a radiative upper level and with a frequency difference equal typically to the ground hyperfine interval, induce coherent population transfer between (meta)stable states.

This chapter details the theory governing velocity-sensitive stimulated Raman transitions. Firstly, we introduce the stimulated Raman system, and derive the equations of motion of the state amplitudes. We then describe the Bloch sphere picture for visualisation of coherent pulses, and discuss the velocity-sensitive Ramsey interferometer which forms the basis of the cooling schemes of chapter 7. We then give a brief summary of the atomic structure of rubidium-85, and finish by presenting a vector formalism for stimulated Raman transitions.

2.1 Raman Transitions

In this section we derive the general equations of motion for the hyperfine state amplitudes during interaction with two counter-propagating laser beams, which are far-detuned from atomic resonance. We begin with a three-level system, then apply a series of transormations and approximations to derive an effective two-level Hamiltonian for the system, from which the equations of motion are obtained. A particularly detailed treatment of velocity-selective stimulated Raman theory in the context of cold atoms can be found in [32]. For the interested reader, and in order to explain particular aspects of the theory not discussed in the main text, we give a summary of the theory governing two-level atom-laser interactions in appendix A.1.

2.1.1 3-level system & the Rabi frequency

We start by considering a three-level atomic system, as shown in figure 2.1, in which there are two lower levels, labelled (ignoring their momenta, for now) $|1\rangle$ and $|2\rangle$ separated by the difference between their atomic frequencies $\omega_{12} \equiv \omega_2 - \omega_1$, and an upper level with atomic frequency ω_3, labelled $|3\rangle$. The lower levels represent ground atomic hyperfine states, from which population cannot spontaneously decay. The upper level represents an *intermediate* state, from which spontaneous decay *is* possible, at an optical interval from the lower levels. Our atom is irradiated by two laser beams of frequencies ω_{L1} and ω_{L2}, which are counter-propagating along the z-axis. The electric field of the laser beams is described by

$$\mathbf{E} = \frac{1}{2}\mathbf{E}_1 e^{i(\mathbf{k}_{L1}\cdot\mathbf{z}-\omega_{L1}t+\phi_{L1})} + \frac{1}{2}\mathbf{E}_2 e^{-i(\mathbf{k}_{L2}\cdot\mathbf{z}-\omega_{L2}t-\phi_{L2})} + c.c. \tag{2.1}$$

where $\mathbf{k}_{L1} \simeq -\mathbf{k}_{L2}$. By the dipole interaction, the laser ω_{La}, where $a = 1, 2$, couples the state $|n\rangle$, where $n = 1, 2$, to $|3\rangle$. The two beams are detuned by a large amount Δ_{na} from single photon resonance with $|3\rangle$, thus making transfer of population to the upper level negligible, and allowing for the pair of components with a common detuning $\Delta_{nn} = \Delta$ to induce coherent transitions between $|1\rangle$ and $|2\rangle$. This type of two-photon transition is known as a stimulated *Raman* transition. A photon carries momentum $\hbar\mathbf{k}$, and we expect the transitions to occur within a closed basis, which we therefore

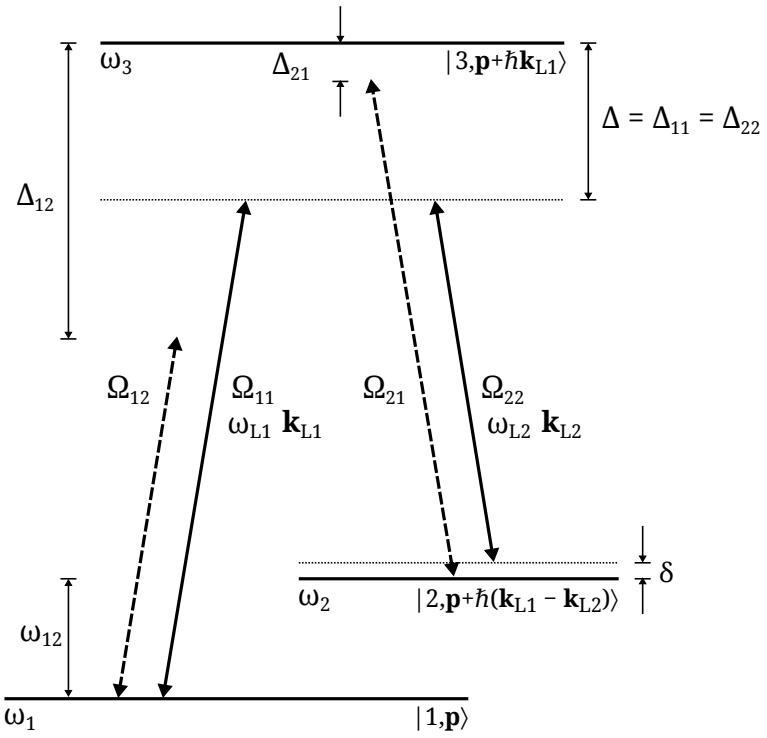

Figure 2.1: The 3-level Raman system. The arrows indicate the two Raman field components, each with its associated frequency ω_{La} and wavevector $\mathbf{k}_{La}$. The solid (dashed) arrows indicate interaction of level n with laser a, where $n = a$ ($n \neq a$). The Rabi frequencies are denoted Ω_{na}, and the single-photon detunings are Δ_{na}.

preemptively define as $|1, \mathbf{p}\rangle$, $|3, \mathbf{p} + \hbar\mathbf{k}_{L1}\rangle$ and $|2, \mathbf{p} + \hbar(\mathbf{k}_{L1} - \mathbf{k}_{L2})\rangle$ (this choice of basis will become clear in subsection 2.1.2), where $\mathbf{p}$ is the initial atomic momentum. The atomic wavefunction can be written in terms of the amplitudes associated with these basis states:

$$|\Psi(t)\rangle = a_1(t)|1, \mathbf{p}\rangle + a_3(t)|3, \mathbf{p} + \hbar\mathbf{k}_{L1}\rangle + a_2(t)|2, \mathbf{p} + \hbar(\mathbf{k}_{L1} - \mathbf{k}_{L2})\rangle = \begin{pmatrix} a_1(t) \\ a_2(t) \\ a_3(t) \end{pmatrix}, \quad (2.2)$$

and this will evolve according to the time dependent Schrödinger equation (TDSE)

$$i\hbar\frac{\partial}{\partial t}|\Psi(t)\rangle = \hat{H}|\Psi(t)\rangle, \quad (2.3)$$

where the Hamiltonian $\hat{H} = \hat{H}_A + V$ is the sum of the *atomic* Hamiltonian $\hat{H}_A = \sum_n \omega_n |n\rangle\langle n| + \hat{\mathbf{p}}^2/2M$ (where M is the atom's mass) and the *interaction* Hamiltonian

$V = -\hat{\mathbf{d}} \cdot \mathbf{E}$. The Hamiltonian can be written explicitly as [33]

$$\hat{H} = \frac{\hat{\mathbf{p}}^2}{2M} + \hbar\omega_1|1\rangle\langle 1| + \hbar\omega_3|3\rangle\langle 3| + \hbar\omega_2|2\rangle\langle 2| - \hat{\mathbf{d}} \cdot \mathbf{E}, \tag{2.4}$$

where the $\hat{\mathbf{p}}$ term acts on the momentum portion of the basis states. The interaction term $V = -\hat{\mathbf{d}} \cdot \mathbf{E} = -e\hat{\mathbf{r}} \cdot \mathbf{E}$ represents the atom-field *dipole* interaction, where $\mathbf{r}$ is the vector defining the position of the electron relative to the atomic nucleus. The matrix elements of V are defined as

$$V_{n3} = \langle n|V|3\rangle = \sum_{a=1,2} \frac{\hbar\Omega_{na}}{2} \left(e^{i(\mathbf{k}_{La}\cdot\mathbf{z} + (-1)^a \omega_{La} t + \phi_{La})} + c.c. \right) |3\rangle\langle n|, \ n = 1, 2 \tag{2.5}$$

where we introduce the *Rabi frequency* Ω_{na} for coupling of level $|n\rangle$ to level $|3\rangle$ by laser a:

$$\Omega_{na} = -\frac{\langle n|\hat{\mathbf{d}} \cdot \mathbf{E}_a|3\rangle}{\hbar}, \ n = 1, 2. \tag{2.6}$$

The Rabi frequency is the angular frequency at which population will 'Rabi flop' between two states due to interaction with a resonant laser.

2.1.2 The momentum operator

We now explain the reasoning behind the choice of momentum-inclusive basis. The matrix elements V_{n3} contain the terms $e^{\pm i\mathbf{k}_{La}\cdot\mathbf{z}}$ which, when we align $\mathbf{k}_{La}$ parallel to $\mathbf{z}$, become $e^{\pm ik_{La}z}$. We can re-write this with the closure relation $\int dp\,|p\rangle\langle p| = 1$ as

$$1 \times e^{\pm ik_{La}z} = \int dp\, e^{\pm ik_{La}z} |p\rangle\langle p|, \tag{2.7}$$

where the momentum-state wavefunction $|p\rangle$ can be expressed as

$$|p\rangle = \int_{-\infty}^{\infty} dz\, |z\rangle\langle z|p\rangle = \frac{1}{\sqrt{2\pi\hbar}} \int_{-\infty}^{\infty} dz\, e^{ipz/\hbar} |z\rangle. \tag{2.8}$$

Substituting equation 2.8 into equation 2.7 gives

$$e^{ik_{La}z} = \frac{1}{\sqrt{2\pi\hbar}} \int_{-\infty}^{\infty} dp \int_{-\infty}^{\infty} dz\, e^{i(p\pm\hbar k_{La})z/\hbar} |z\rangle\langle p| \ = \int dp\, |p \pm \hbar k_{La}\rangle\langle p|. \tag{2.9}$$

This shows that the $e^{\pm i\mathbf{k}_{La}\cdot\mathbf{z}}$ part of the interaction term V_{n3} acting on the momentum portion $|\mathbf{p}\rangle$ of the atomic state gives rise to a change in the atomic momentum by $\pm\hbar\mathbf{k}_{La}$. Therefore for an atom initially in the state $|1,\mathbf{p}\rangle$, coupling to $|3,\mathbf{p}+\hbar\mathbf{k}_{L1}\rangle$ can occur by absorption of a photon at ω_{L1} (where $\omega_{La} = c/k_{La}$), and subsequently[1] coupling from $|3,\mathbf{p}+\hbar\mathbf{k}_{L1}\rangle$ to $|2,\mathbf{p}+\hbar(\mathbf{k}_{L1}-\mathbf{k}_{L2})\rangle$ can occur by the *stimulated* emission of a photon at ω_{L2}. This justifies the choice of momentum-inclusive basis made in the previous subsection.

2.1.3 The 3-level Hamiltonian

If we apply the rotating wave approximation (which removes the off-resonant terms in the interaction Hamiltonian, as described in appendix A.1.1), we can write out the full Hamiltonian for the three-level system in the absence of spontaneous emission from $|3\rangle$ [33]

$$\hat{H} = \begin{pmatrix} \frac{\mathbf{p}^2}{2M} + \hbar\omega_1 & 0 & \frac{\hbar\Omega_{11}}{2}e^{i(\omega_{L1}t-\phi_{L1})} \\ 0 & \frac{(\mathbf{p}+\hbar(\mathbf{k}_{L1}-\mathbf{k}_{L2}))^2}{2M} + \hbar\omega_2 & \frac{\hbar\Omega_{22}}{2}e^{i(\omega_{L2}t+\phi_{L2})} \\ \frac{\hbar\Omega_{11}^*}{2}e^{-i(\omega_{L1}t-\phi_{L1})} & \frac{\hbar\Omega_{22}^*}{2}e^{-i(\omega_{L2}t+\phi_{L2})} & \frac{(\mathbf{p}+\hbar\mathbf{k}_{L1})^2}{2M} + \hbar\omega_3 \end{pmatrix}. \tag{2.10}$$

It is important to be aware of the absent terms here: we have considered only $a = n$ couplings, that is, where the field at frequency ω_{La} only interacts with the 'correct' level $|a\rangle$. In reality, both lasers will couple to *both* levels, as illustrated in figure 2.1 and described by equation 2.5. A treatment considering all combinations of a and n is given in appendix A.2, and as we discuss there, the result is simply an additional term in the light shift of each level, which we re-insert later on in this section.

With the Hamiltonian given in equation 2.10, the TDSE exhibits fast oscillations of $a_1(t)$, $a_2(t)$ and $a_3(t)$ at frequencies specified by their respective atomic frequencies and momenta, alongside relatively slow oscillations due to interaction with the laser. In the following we take steps to transform this Hamiltonian into a more manageable form.

We have the freedom to make the transformation $|\Psi'\rangle = \hat{O}|\Psi\rangle$, where $\hat{O}$ is some operator ($\hat{O}^\dagger\hat{O} = \mathbb{I}$) and $|\psi'\rangle$ is a transformed state vector. With such a substitution, the TDSE

[1] It is important to note that the Raman transition is not a sequential absorption *then* stimulated emission process (as is, for example, the case for STIRAP [34]), but is closer to a simultaneous absorption *and* stimulated emission process.

becomes

$$i\hbar\frac{\partial}{\partial t}(\hat{O}^\dagger|\Psi'\rangle) = \hat{H}(\hat{O}^\dagger|\Psi'\rangle), \tag{2.11}$$

and if we apply the product rule to the left hand side, operate with $\hat{O}$ from the left, and re-arrange, we find

$$i\hbar\frac{\partial}{\partial t}|\Psi'\rangle = \left(\hat{O}\hat{H}\hat{O}^\dagger - i\hbar\hat{O}\frac{\partial}{\partial t}\hat{O}^\dagger\right)|\Psi'\rangle, \tag{2.12}$$

where the term inside the brackets is the transformed Hamiltonian. Using the above, we can factor out the fast oscillations in the TDSE by making the substitutions

$$\begin{aligned} a_1(t) &= b_1(t)e^{-i\left(\frac{\mathbf{p}^2}{2M}+\hbar\omega_1\right)t} \\ a_2(t) &= b_2(t)e^{-i\left(\frac{(\mathbf{p}+\hbar(\mathbf{k}_{L1}-\mathbf{k}_{L2})^2}{2M}+\hbar\omega_2\right)t} \\ a_3(t) &= b_3(t)e^{-i\left(\frac{(\mathbf{p}+\hbar\mathbf{k}_{L1})^2}{2M}+\hbar\omega_3\right)t}, \end{aligned} \tag{2.13}$$

which is equivalent to the transformation $|\Psi'\rangle = \hat{T}_1|\Psi\rangle$ with the diagonal matrix

$$\hat{T}_1 = \begin{pmatrix} e^{i\left[\frac{\mathbf{p}^2}{2M}+\hbar\omega_1\right]t} & 0 & 0 \\ 0 & e^{i\left[\frac{(\mathbf{p}+\hbar(\mathbf{k}_{L1}-\mathbf{k}_{L2}))^2}{2M}+\hbar\omega_2\right]t} & 0 \\ 0 & 0 & e^{i\left[\frac{(\mathbf{p}+\hbar\mathbf{k}_{L1})^2}{2M}+\hbar\omega_3\right]t} \end{pmatrix}, \tag{2.14}$$

where $|\Psi'\rangle$ is the wavefunction described by the new amplitudes $b_n(t)$. By equation 2.12, the transformed Hamiltonian then takes the more convenient form

$$\hat{H} = \begin{pmatrix} 0 & 0 & \frac{\hbar\Omega_{11}}{2}e^{-i[\Delta t+\phi_{L1}]} \\ 0 & 0 & \frac{\hbar\Omega_{22}}{2}e^{-i[(\Delta+\delta)t-\phi_{L2}]} \\ \frac{\hbar\Omega_{11}^*}{2}e^{i[\Delta t+\phi_{L1}]} & \frac{\hbar\Omega_{22}^*}{2}e^{i[(\Delta+\delta)t-\phi_{L2}]} & 0 \end{pmatrix} \tag{2.15}$$

where Δ and δ are defined overleaf, and if we write out the transformed TDSE for each level we obtain three coupled differential equations describing the time-evolution of the

amplitudes of each state:

$$i\hbar\frac{\partial}{\partial t}b_1(t) = \frac{\hbar\Omega_{11}}{2}e^{-i[\Delta t+\phi_{L1}]}b_3(t) \tag{2.16a}$$

$$i\hbar\frac{\partial}{\partial t}b_2(t) = \frac{\hbar\Omega_{22}}{2}e^{-i[(\Delta+\delta)t-\phi_{L2}]}b_3(t) \tag{2.16b}$$

$$i\hbar\frac{\partial}{\partial t}b_3(t) = \frac{\hbar\Omega_{11}^*}{2}e^{i[\Delta t+\phi_{L1}]}b_1(t) + \frac{\hbar\Omega_{22}^*}{2}e^{i[(\Delta+\delta)t-\phi_{L2}]}b_2(t). \tag{2.16c}$$

In the above equations, we have defined the detuning Δ of the lasers ω_{Ln} from *single-photon* resonance with the transition $|n\rangle$ to $|3\rangle$ as

$$\Delta = \left(\frac{(\mathbf{p}+\hbar\mathbf{k}_{L1})^2}{2M\hbar}+\omega_3\right) - \left(\frac{\mathbf{p}^2}{2M\hbar}+\omega_1\right) - \omega_{L1}, \tag{2.17}$$

and the detuning δ from the *two-photon* Raman resonance, which is applied to laser ω_{L2}, as

$$\delta = \left(\frac{(\mathbf{p}+\hbar(\mathbf{k}_{L1}-\mathbf{k}_{L2}))^2}{2M\hbar}+\omega_2\right) - \left(\frac{\mathbf{p}^2}{2M\hbar}+\omega_1\right) - (\omega_{L2}-\omega_{L1}). \tag{2.18}$$

Whilst Δ is large and therefore relatively insensitive to the momentum terms, δ is much smaller, and is highly sensitive to the atomic momentum. At this point we define the *laser detuning* from the rest-frame resonance as

$$\delta_L = (\omega_1-\omega_2) - (\omega_{L1}-\omega_{L2}). \tag{2.19}$$

The above transformation represents a move to the *interaction picture* (we began in the Schrödinger picture), in which some of the time evolution of the state amplitudes is 'shunted' into the transformation operators.

2.1.4 Effective two-level system

In the Raman arrangement the detuning Δ is large, such that $\Delta \gg |\Omega_{11}|, |\Omega_{22}|, |\delta|$, and therefore the population of $|3\rangle$, and the associated spontaneous emission *from* $|3\rangle$, is negligible. In order to simplify our equations further, we make the assumption that the populations $b_1(t)$ and $b_2(t)$ oscillate (via the Raman transition) at a frequency much smaller than the detuning Δ. In this case, the exponential terms in equation 2.16c oscillate much faster than $b_1(t)$ and $b_2(t)$ (and $\Delta \gg \delta$), and we can therefore integrate

2.16c, assuming $b_1(t)$ and $b_2(t)$ to be effectively constant:

$$\begin{aligned} i\hbar \int_{t_0}^{t_0+t} \frac{\partial}{\partial t'} b_3(t')dt' &= i\hbar \left[-b_3(t_0) + b_3(t_0+t)\right] \\ &= i\hbar \left[-b_3(t_0) - \frac{\Omega_{11}^*}{2\Delta} e^{i[\Delta t+\phi_{L1}]} b_1(t) - \frac{\Omega_{22}^*}{2\Delta} e^{i[(\Delta+\delta)t+\phi_{L2}]} b_2(t)\right]. \end{aligned} \tag{2.20}$$

We then substitute this into equations 2.16 which respectively become

$$i\hbar \frac{\partial}{\partial t} b_1(t) = -\frac{\hbar|\Omega_{11}|^2}{4\Delta} b_1(t) - \frac{\hbar\Omega_{11}\Omega_{22}^*}{4\Delta} e^{i(\delta t-\phi_L)} b_2(t) \tag{2.21a}$$

$$i\hbar \frac{\partial}{\partial t} b_2(t) = -\frac{\hbar\Omega_{11}^*\Omega_{22}}{4\Delta} e^{-i(\delta t-\phi_L)} b_1(t) - \frac{\hbar|\Omega_{22}|^2}{4\Delta} b_2(t), \tag{2.21b}$$

$$i\hbar \frac{\partial}{\partial t} b_3(t) = \frac{\hbar\Omega_{11}^*}{2} e^{i[\Delta t+\phi_{L1}]} b_1(t) + \frac{\hbar\Omega_{22}^*}{2} e^{i[(\Delta+\delta)t-\phi_{L2}]} b_2(t), \tag{2.21c}$$

where we have defined the *effective* laser phase $\phi_L = \phi_{L1} + \phi_{L2}$, which is the two-photon analog to the individual laser phase. Equation 2.21c exhibits only fast oscillations $e^{\pm i\Delta t}$ (where $\Delta \gg \delta$) of the intermediate state amplitude $b_3(t)$. These oscillations quickly average out to zero, and can be omitted [33] from the TDSE, leaving an effective two-level system.

We can now write down the simplified, *two-level* Hamiltonian [35]

$$\hat{H} = -\hbar \begin{pmatrix} \Omega_1^{AC} & \frac{\Omega_R}{2} e^{i(\delta t-\phi_L)} \\ \frac{\Omega_R^*}{2} e^{-i(\delta t-\phi_L)} & \Omega_2^{AC} \end{pmatrix}, \tag{2.22}$$

which acts to couple the states $|1, \mathbf{p}\rangle$ and $|2, \mathbf{p} + \hbar(\mathbf{k}_{L1} - \mathbf{k}_{L2})\rangle$, whilst the population in $|3, \mathbf{p} + \hbar\mathbf{k}_{L1}\rangle$ remains zero. In equation 2.22, the diagonal terms represent the light shift of the associated level. As stated previously, this treatment has omitted couplings where $a \neq n$, since they act only to alter the light shifts. The full two-level Hamiltonian *including* these terms is given in appendix A.2, and at this point we re-introduce them in the definition of the light shift of level n:

$$\Omega_n^{AC} = \sum_{a=1,2} \frac{|\Omega_{na}|^2}{4\Delta_{na}}, \quad n = 1, 2. \tag{2.23}$$

These are consistent with the far-detuned light shifts obtained with single-photon couplings in the dressed state picture, as described in appendix section A.1.3. The *two-photon* Rabi frequency, the rate at which population 'Rabi flops' between $|1\rangle$ and $|2\rangle$ on resonance, is defined as

$$\Omega_R = \frac{\Omega_{11}^* \Omega_{22}}{2\Delta}. \tag{2.24}$$

2.1.5 The dressed state approach

The time-dependent Schrödinger equation for this effective two-level system can be solved if we shunt the remaining time-dependent terms into transformation operators, and convert to what is known as the *dressed state* picture, as follows. We first apply a uniform shift of $-(\Omega_1^{AC} + \Omega_2^{AC})\hbar/2$ to the energy scale. This is equivalent to a transformation ($|\Psi''\rangle = \hat{T}_2|\Psi'\rangle$, as in equations 2.11 and 2.12) using the diagonal matrix $\hat{T}_2 = e^{-i(\Omega_1^{AC}+\Omega_2^{AC})t/2}\mathbb{I}$. The transformed Hamiltonian has diagonal elements $\pm\hbar\delta^{AC}/2$, where

$$\delta^{AC} = (\Omega_1^{AC} - \Omega_2^{AC}) \tag{2.25}$$

is the relative light-shift between the two levels. As in appendix A.1.1, we can remove the time-dependent off-diagonal terms in H if we make a transformation $|\Psi\rangle_R = \hat{R}|\Psi\rangle = |1\rangle_R + |2\rangle_R$ with the *rotation* operator

$$\hat{R} = e^{i\boldsymbol{\sigma}_z \delta t/2} = \begin{pmatrix} e^{-i\delta t/2} & 0 \\ 0 & e^{i\delta t/2} \end{pmatrix}, \tag{2.26}$$

where $\boldsymbol{\sigma}_z$ is a Pauli spin matrix. For reference, the exponent of a Pauli matrix $\boldsymbol{\sigma}$ is given by $e^{ia\boldsymbol{\sigma}} = \mathbb{I}\cos a + i\boldsymbol{\sigma}\sin a$. This acts to rotate the frame of reference at a rate δ about the z-axis. Substituting $\hat{R}$ into equation 2.12 gives a transformed time-independent Hamiltonian (with known solutions) in the *rotating frame*:

$$\hat{H}_R = -\hbar \begin{pmatrix} \frac{(\delta^{AC}-\delta)}{2} & \frac{\Omega_R}{2} e^{-i\phi_L} \\ \frac{\Omega_R^*}{2} e^{i\phi_L} & -\frac{(\delta^{AC}-\delta)}{2} \end{pmatrix}. \tag{2.27}$$

The eigenvalues of this matrix are $\lambda_\pm = \pm\frac{\hbar}{2}\tilde{\Omega}_R$, where we define the *generalised*, off-resonant two-photon Rabi frequency as

$$\tilde{\Omega}_R = \sqrt{|\Omega_R|^2 + (\delta^{AC} - \delta)^2}\,. \tag{2.28}$$

This gives the angular frequency at which the atom will oscillate between $|1\rangle$ and $|2\rangle$. The procedure for finding the eigenvectors of a matrix of the form $\hat{H}_R$ are given in appendix A.1.2. Here, we simply write them down as

$$|\lambda_+\rangle = \cos\frac{\Theta}{2}|1\rangle_R\, e^{-i\phi_L/2} - \sin\frac{\Theta}{2}|2\rangle_R\, e^{i\phi_L/2} \tag{2.29}$$

$$|\lambda_-\rangle = \sin\frac{\Theta}{2}|1\rangle_R\, e^{-i\phi_L/2} + \cos\frac{\Theta}{2}|2\rangle_R\, e^{i\phi_L/2}. \tag{2.30}$$

These are known as the dressed-state eigenvectors, where we have defined

$$\tan\Theta = \frac{-\Omega_r}{(\delta^{AC} - \delta)} \tag{2.31a}$$

$$\cos\Theta = \frac{-(\delta^{AC} - \delta)}{\tilde{\Omega}_R} \tag{2.31b}$$

$$\sin\Theta = \frac{\Omega_R}{\tilde{\Omega}_R}. \tag{2.31c}$$

2.1.6 Solutions to the two-level TDSE

Now that we have a time-independent Hamiltonian, for which we have defined energy eigenvalues and eigenvectors, we are able to derive the solutions to the time-dependent Schrödinger equation in the interaction picture. The following describes the procedure from starting-state to solutions, as adapted from [35].

We begin at time t_0 with our effective two-level atom in the state $|\Psi'(t_0)\rangle = c_1(t_0)|1\rangle + c_2(t_0)|2\rangle$, where we have already made the transformation with a two-level version of $\hat{T}_1$. We first make the transformation $|\Psi''(t_0)\rangle = \hat{T}_2|\Psi'(t_0)\rangle$ to antisymmetrise the Hamiltonian as in section 2.1.5. Next we transform $|\Psi''(t_0)\rangle$ to the rotating frame, in which we have defined the eigenvectors $|\lambda_\pm\rangle$, by acting on it with the operator $\hat{R}(t_0)$ from equation 2.26. The wavefunction in the rotating frame becomes

$$|\Psi(t_0)\rangle_R = c_1(t_0)e^{-i(\Omega_1^{AC}+\Omega_2^{AC})t/2}e^{-i\delta t_0/2}|1\rangle + c_2(t_0)e^{-i(\Omega_1^{AC}+\Omega_2^{AC})t/2}e^{i\delta t_0/2}|2\rangle. \tag{2.32}$$

During an interaction with the laser of duration t, the atom will evolve according to the TDSE with the Hamiltonian $\hat{H}_R$, which can be solved in terms of the time-evolution operator $U(t_0, t)$:

$$|\Psi(t_0 + t)\rangle_R = U(t_0, t)|\Psi(t_0)\rangle_R, \text{ where } U(t_0, t) = e^{-i\hat{H}_R(t-t_0)/\hbar}. \tag{2.33}$$

Given that we have a set of eigenvalues $\lambda_\pm$ and eigenvectors $|\lambda_\pm\rangle$, which are represented in the eigenvalue equations $\hat{H}_R|\lambda_\pm\rangle = \lambda_\pm|\lambda_\pm\rangle$, a function $f(\hat{H}_R)$ of the Hamiltonian (an operator) will obey the equation $f(\hat{H}_R)|\lambda_\pm\rangle = f(\lambda_\pm)|\lambda_\pm\rangle$. This can be applied to the exponential function $U(t_0, t)$ in equation 2.33 along with the closure relation $|\lambda_+\rangle\langle\lambda_+| + |\lambda_-\rangle\langle\lambda_-| = \mathbb{1}$ in our two-eigenvector basis to give

$$\begin{aligned} U(t_0, t) &= e^{-i\hat{H}_R(t-t_0)/\hbar}\left(|\lambda_+\rangle\langle\lambda_+| + |\lambda_-\rangle\langle\lambda_-|\right) \\ &= e^{i\lambda_+(t-t_0)/\hbar}|\lambda_+\rangle\langle\lambda_+| + e^{i\lambda_-(t-t_0)/\hbar}|\lambda_-\rangle\langle\lambda_-|. \end{aligned} \tag{2.34}$$

We can then use $\hat{R}^\dagger(t_0 + t)$ and $\hat{T}_2^\dagger(t_0 + t)$ to convert back to the initial basis:

$$|\Psi^\dagger(t_0 + t)\rangle = \hat{T}_2^\dagger(t_0 + t)\hat{R}^\dagger(t_0 + t)|\Psi(t_0 + t)\rangle_R \tag{2.35}$$

From this we obtain the amplitudes $c_1(t_0 + t)$ and $c_2(t_0 + t)$ after an interaction of duration t with the laser field (see, for example [33, 35], or earlier work by Ramsey [36]):

$$\begin{aligned} c_1(t_0 + t) = e^{i(\Omega_1^{AC} + \Omega_2^{AC})t/2} e^{i\delta t/2}\Bigg(& c_2(t_0) e^{i(\delta t_0 - \phi_L)}\left[i \sin\Theta \sin\left(\frac{\tilde{\Omega}_R t}{2}\right)\right] \\ & + c_1(t_0)\left[\cos\left(\frac{\tilde{\Omega}_R t}{2}\right) - i\cos\Theta\sin\left(\frac{\tilde{\Omega}_R t}{2}\right)\right]\Bigg) \end{aligned} \tag{2.36a}$$

$$\begin{aligned} c_2(t_0 + t) = e^{i(\Omega_1^{AC} + \Omega_2^{AC})t/2} e^{-i\delta t/2}\Bigg(& c_2(t_0)\left[\cos\left(\frac{\tilde{\Omega}_R t}{2}\right) + i\cos\Theta\sin\left(\frac{\tilde{\Omega}_R t}{2}\right)\right] \\ & + c_1(t_0) e^{-i(\delta t_0 - \phi_L)}\left[i \sin\Theta \sin\left(\frac{\tilde{\Omega}_R t}{2}\right)\right]\Bigg). \end{aligned} \tag{2.36b}$$

These equations are the work horses of all numerical simulations in this thesis. The amplitudes $c_1(t)$ and $c_2(t)$ can be numerically calculated and squared to give the resultant

populations (or probabilities) $|c_1(t)|^2$ and $|c_2(t)|^2$ for any pulse or pulse sequence with a given laser intensity, laser detuning (both Δ and δ), laser phase, atomic dipole coupling strength and atomic momentum. Whilst useful for simulations, equations 2.36 offer little intuitive insight into the population dynamics of coherent Raman pulses. The next section presents a more visually-intuitive approach to coherent transitions, and provides a toolkit for understanding the key coherent pulses in atom interferometry.

2.2 The Bloch sphere picture

A useful method for visualisation of coherent pulses, and the topic of this section, is the Bloch sphere picture. It allows us to visually map out pulses as rotations of a state vector around the surface of the unit sphere, and gives us a more intuitive understanding of what occurs during a Raman pulse when, for example, the laser interaction time, phase or detuning is changed. This treatment was adapted by Feynman [37] from early nuclear magnetic resonance work by Rabi, Ramsey and Schwinger [38], and (earlier still) Bloch [39]. A particularly good description of the Bloch sphere picture is given by Shor in [40].

2.2.1 Time evolution of the density matrix

We begin our introduction to the Bloch sphere picture by defining the density matrix $\hat{\rho}$, which describes a many-level quantum system as a statistical ensemble in a mixed state:

$$\hat{\rho} = \sum_{n,m} c_n c_m^* |n\rangle\langle m|, \tag{2.37}$$

where c_n is the amplitude of the pure state $|n\rangle$. In an effective two-level system, the density matrix can be written as

$$\hat{\rho} = |\Psi'\rangle\langle\Psi'| = \begin{pmatrix} |c_1|^2 & c_1 c_2^* \\ c_2 c_1^* & |c_2|^2 \end{pmatrix} = \begin{pmatrix} \rho_{11} & \rho_{12} \\ \rho_{21} & \rho_{22} \end{pmatrix}, \tag{2.38}$$

where we have dropped the time-dependence notation for simplicity. In the density matrix, the off-diagonal terms ρ_{12} and ρ_{21} are known as *coherences*, and describe coupling between the two levels due to interaction with a driving field. The diagonal terms ρ_{11} and ρ_{22} are the *populations*, which are simply the probabilities of the atom being found

in the associated pure state. We can write the TDSE in its *Liouville variant* form:

$$i\hbar\frac{\partial\hat{\rho}}{\partial t} = [\hat{H}, \hat{\rho}], \tag{2.39}$$

which for the Hamiltonian in equation 2.22 gives the equations of motion for the elements of the density matrix as

$$i\hbar\frac{\partial\rho_{11}}{\partial t} = -\frac{\hbar\Omega_R}{2}e^{i(\delta t-\phi_L)}\rho_{21} + \frac{\hbar\Omega_R^*}{2}e^{-i(\delta t-\phi_L)}\rho_{12} \tag{2.40a}$$

$$i\hbar\frac{\partial\rho_{12}}{\partial t} = -\hbar(\Omega_1^{AC} - \Omega_2^{AC})\rho_{12} + \frac{\hbar\Omega_R}{2}e^{i(\delta t-\phi_L)}(\rho_{11} - \rho_{22}) \tag{2.40b}$$

$$i\hbar\frac{\partial\rho_{21}}{\partial t} = \hbar(\Omega_1^{AC} - \Omega_2^{AC})\rho_{21} - \frac{\hbar\Omega_R^*}{2}e^{-i(\delta t-\phi_L)}(\rho_{11} - \rho_{22}) \tag{2.40c}$$

$$i\hbar\frac{\partial\rho_{22}}{\partial t} = -\frac{\hbar\Omega_R^*}{2}e^{-i(\delta t-\phi_L)}\rho_{12} + \frac{\hbar\Omega_R}{2}e^{i(\delta t-\phi_L)}\rho_{21}. \tag{2.40d}$$

To simplify these equations, we transform to the rotating frame by making the substitutions

$$\tilde{c}_1 = c_1 e^{-i\delta t/2} \tag{2.41a}$$

$$\tilde{c}_2 = c_2 e^{i\delta t/2}, \tag{2.41b}$$

which transform the coherences of the density matrix to

$$\tilde{\rho}_{12} = \rho_{12}e^{-i\delta t} \tag{2.42a}$$

$$\tilde{\rho}_{21} = \rho_{21}e^{i\delta t}, \tag{2.42b}$$

and leave the populations unchanged ($\tilde{\rho}_{11} = \rho_{11}$ and $\tilde{\rho}_{22} = \rho_{22}$). We can then re-write equations 2.40 as

$$i\hbar\frac{\partial\tilde{\rho}_{11}}{\partial t} = -\frac{\hbar\Omega_R}{2}e^{-i\phi_L}\tilde{\rho}_{21} + \frac{\hbar\Omega_R^*}{2}e^{i\phi_L}\tilde{\rho}_{12} \tag{2.43a}$$

$$i\hbar\frac{\partial\tilde{\rho}_{12}}{\partial t} = \hbar\left(\delta - \delta^{AC}\right)\tilde{\rho}_{12} + \frac{\hbar\Omega_R}{2}e^{-i\phi_L}(\tilde{\rho}_{11} - \tilde{\rho}_{22}) \tag{2.43b}$$

$$i\hbar\frac{\partial\tilde{\rho}_{21}}{\partial t} = -\hbar\left(\delta - \delta^{AC}\right)\tilde{\rho}_{21} - \frac{\hbar\Omega_R^*}{2}e^{i\phi_L}(\tilde{\rho}_{11} - \tilde{\rho}_{22}) \tag{2.43c}$$

$$i\hbar\frac{\partial\tilde{\rho}_{22}}{\partial t} = -\frac{\hbar\Omega_R^*}{2}e^{i\phi_L}\tilde{\rho}_{12} + \frac{\hbar\Omega_R}{2}e^{-i\phi_L}\tilde{\rho}_{21}, \tag{2.43d}$$

where we have made the substitution $\delta^{AC} = \Omega_1^{AC} - \Omega_2^{AC}$.

2.2.2 The optical Bloch equations

The expectation value of an operator $\hat{A}$ can be written in terms of the density matrix as $\langle\hat{A}\rangle = \mathrm{Tr}(A\rho)$ [41]. Considering the expectation values of the Pauli spin matrices, which are projections of the state vector on to each of the three Cartesian axes x, y and z, we define the variables

$$u = \mathrm{Tr}(\sigma_x\rho) = \tilde{\rho}_{12} + \tilde{\rho}_{21} \tag{2.44a}$$

$$v = \mathrm{Tr}(\sigma_y\rho) = -i(\tilde{\rho}_{21} - \tilde{\rho}_{12}) \tag{2.44b}$$

$$w = \mathrm{Tr}(\sigma_z\rho) = \tilde{\rho}_{11} - \tilde{\rho}_{22}. \tag{2.44c}$$

Equations 2.44 are then substituted into equations 2.43 to give three coupled differential equations:

$$\frac{\partial u}{\partial t} = -\left(\delta - \delta^{AC}\right) v - \frac{i}{2}\left(\Omega_R e^{-i\phi_L} - \Omega_R^* e^{i\phi_L}\right) w \tag{2.45a}$$

$$\frac{\partial v}{\partial t} = \left(\delta - \delta^{AC}\right) u + \frac{1}{2}\left(\Omega_R e^{-i\phi_L} + \Omega_R^* e^{i\phi_L}\right) w \tag{2.45b}$$

$$\frac{\partial w}{\partial t} = -i(\Omega_R^* e^{i\phi_L}\tilde{\rho}_{12} - \Omega_R e^{-i\phi_L}\tilde{\rho}_{21}). \tag{2.45c}$$

These are a simplified form of the *optical Bloch equations* (OBEs). The full, general form incorporates loss due to spontaneous emission, however we choose to neglect such effects here. In the case where Ω_R is real ($\Omega_R = \Omega_R^*$), the OBEs become

$$\frac{\partial u}{\partial t} = -\left(\delta - \delta^{AC}\right) v - \Omega_R \sin(\phi_L) w \tag{2.46a}$$

$$\frac{\partial v}{\partial t} = \left(\delta - \delta^{AC}\right) u + \Omega_R \cos(\phi_L) w \tag{2.46b}$$

$$\frac{\partial w}{\partial t} = -\Omega_R \cos(\phi_L) v + \Omega_R \sin(\phi_L) u. \tag{2.46c}$$

2.2.3 The Bloch vector

We can now define the *Bloch vector* $\mathbf{R}$, of which u, v and w are the amplitudes along x, y and z respectively:

$$\mathbf{R} = u\hat{\mathbf{x}} + v\hat{\mathbf{y}} + w\hat{\mathbf{z}}. \tag{2.47}$$

Differentiating $\mathbf{R}$ gives the time-evolution of the Bloch vector, which can be represented as a *torque* on $\mathbf{R}$ caused by the *field vector* $\mathbf{\Omega}$:

$$\frac{d\mathbf{R}}{dt} = \mathbf{R} \times \mathbf{\Omega}, , \tag{2.48}$$

where by inspection we find

$$\mathbf{\Omega} = \Omega_R \cos\phi_L \hat{\mathbf{x}} + \Omega_R \sin\phi_L \hat{\mathbf{y}} - \left(\delta - \delta^{AC}\right) \hat{\mathbf{z}}. \tag{2.49}$$

Given that $d\mathbf{R}/dt$ and $\mathbf{\Omega}$ are orthogonal, we can see that $\mathbf{R}$ rotates *around* the axis defined by $\mathbf{\Omega}$, and that (in the absence of any loss processes, such as spontaneous emission) $\mathbf{R}$ maintains a constant length. $\mathbf{\Omega}$ has horizontal components Ω_R and a vertical component $\delta - \delta^{AC}$, hence it is inclined out of the x-y plane by an angle $\arctan\left((\delta - \delta^{AC})/\Omega_R\right)$. Furthermore, we note here that the field vector lies along the eigenvectors given in equations 2.29 and 2.30. The sphere on whose surface the Bloch vector $\mathbf{R}$ exists is known as the *Bloch sphere*. We can also see from equation 2.48 that the angular frequency at which $\mathbf{R}$ rotates around $\mathbf{\Omega}$ is given by

$$|\mathbf{\Omega}| = \sqrt{\Omega_R^2 + (\delta - \delta^{AC})^2}, \tag{2.50}$$

which is identical to the generalised, two-photon Rabi frequency $\tilde{\Omega}_R$ given in equation 2.28. We can gain some insight into the behaviour of our coherent Raman pulses by plotting the evolution of the Bloch vector as a function of pulse time for a range of pulse parameters. The detuning of the laser with respect to the atomic transition, which we characterise by the term $\delta - \delta^{AC}$, affects the trajectory of the Bloch vector as depicted in figure 2.2. A *resonant* pulse ($\delta - \delta^{AC} = 0$), as shown in figure 2.2 (a), exhibits (for $\phi_L = 0$) a field vector along the x axis. The Bloch vector therefore traces out a great circle in the y-z plane at an angular frequency $\tilde{\Omega}_R = \Omega_R$. An *off-resonant* pulse ($|\delta - \delta^{AC}| > 0$) is characterised by a field vector which does not lie in the x-y plane. In this case the Bloch vector traces out a tilted, *small* circle on the Bloch sphere as shown in figure 2.2 (b) and (c), at an increased angular frequency $\tilde{\Omega}_R = \sqrt{\Omega_R^2 + (\delta - \delta^{AC})^2}$. It is useful to note that the *linear speed* along the sphere's surface remains the same, as defined by Ω_R, regardless of the detuning. The lower plot in the figure shows the normalised temporal evolution of $(1 - w)/2$, which is equal to the population in state

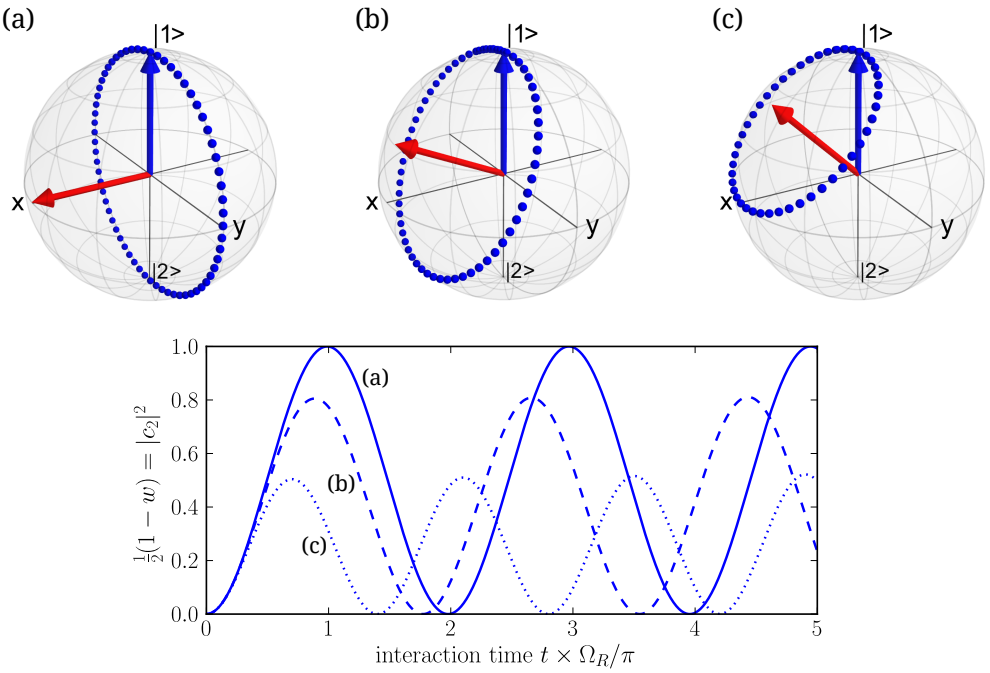

Figure 2.2: **Top:** Bloch sphere plots showing the initial Bloch vector (blue arrow), the field vector (red arrow), and the rotation trajectory of the Bloch vector (blue dots), for (a) a *resonant* pulse with $\delta - \delta^{AC} = 0$, (b) an *off-resonant* pulse with $(\delta - \delta^{AC})/\Omega_R = 0.5$, and (c) an off-resonant pulse with $(\delta - \delta^{AC})/\Omega_R = 1.0$. In all cases $\phi_L = 0$. **Bottom:** The excited state population as a function of the normalised atom-laser interaction time for the parameters given in the upper plots. (a) – solid line, (b) – dashed line, and (c) – dotted line.

$|2\rangle$, corresponding to the upper plots. We can see that only in the on-resonance case can we achieve complete population inversion.

Bloch vector trajectories for different values of the Raman beam phase ϕ_L on resonance are shown in figure 2.3. Altering ϕ_L simply acts to rotate the field vector around the z-axis by the angle ϕ_L. We can make the Bloch vector rotate in the x-z plane by setting $\phi_L = \pi/2$, for example, and we can reverse its direction of rotation by shifting ϕ_L by π. This freedom to control the axis of rotation is essential in composite pulses (chapter 6) and atom interferometry (chapter 7) experiments.

2.2.4 The coherent pulse toolkit

To end this section, we introduce the key operations in atom interferometry. By tailoring the duration t of our coherent pulses we are able to achieve rotations by well-defined angles around the Bloch sphere. The two most useful rotations in atom interferometry are the *resonant* $\pi/2$ and π, which are shown in figure 2.4 (a) and (b) respectively. To

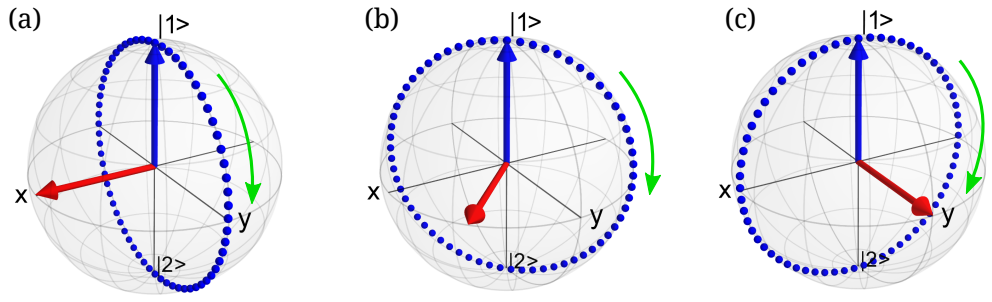

Figure 2.3: Bloch sphere plots showing the initial Bloch vector (blue arrow), the field vector (red arrow), and the rotation trajectory of the Bloch vector (blue dots), for resonant ($\delta - \delta^{AC} = 0$) pulses with (a) laser phase $\phi_L = 0$, (b) $\phi_L = \pi/4$, and (c) $\phi_L = \pi/2$. The green arrow in each case shows the direction of rotation.

achieve a $\pi/2$ pulse, we set $\Omega_R t = \pi/2$. This gives rise to a rotation by an angle $\pi/2$ around the field vector, and (for a state initially at the pole) induces an equal superposition of the two atomic states. Since the two states constituting this superposition have different momenta and therefore follow different paths in space, the $\pi/2$ pulse is analogous to a *beamsplitter* in an optical interferometer. To achieve a π pulse, we set $\Omega_R t = \pi$. This induces population inversion, which is represented by a π rotation around the field vector. The π pulse is analogous to a *mirror* in an optical interferometer, since it physically deflects the atomic wavepacket, and does so in opposite directions for the two states, as if approaching a mirror that bisects the angle between them. The third and final operation in the toolkit is *free evolution*, which is simply the evolution of the Bloch vector in the absence of any driving field, as shown in figure 2.4 (c). If the detuning $\delta - \delta^{AC}$ is non-zero, the Bloch vector will precess around the z-axis at a rate equal to this detuning.

The lower plot in the figure shows the population in state $|2\rangle$ as a function of the *normalised* detuning parameter $(\delta - \delta^{AC})/\Omega_R$, which may be non-zero due to a non-zero velocity or laser detuning, for pulse durations corresponding to a resonant $\pi/2$ and a resonant π pulse. At zero detuning, we find their excited state populations $|c_2|^2$ to be 0.5 and 1.0, respectively. The curves exhibit a 'sinc-squared' line-shape, whose spectral width (FWHM $= \pi/2$) is linearly dependent on the two-photon Rabi frequency Ω_R. The increase in spectral width with increasing Ω_R is known as *power-broadening*. These key operations will be combined in the next section, which discusses velocity-selective atom interferometry.

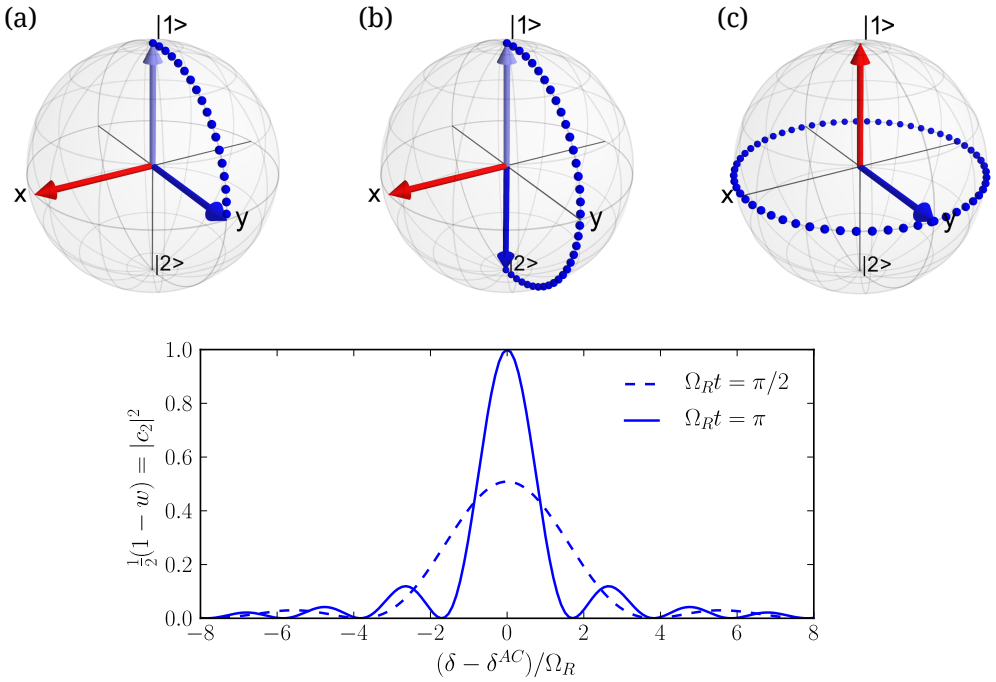

Figure 2.4: **Top:** Bloch sphere plots showing the three main operations in atom interferometry. Plots (a) and (b) show a $\pi/2$ and π pulse, respectively, with the field vector (red arrow), the initial/final Bloch vectors (light/dark blue arrows), and the Bloch vector trajectory (blue dots). Plot (c) shows *Free evolution* where $\Omega_R = 0$ and the Bloch vector precesses about the z-axis. **Bottom:** Resultant excited state population as a function of the normalised detuning parameter for a $\pi/2$ pulse (dashed line) and a π pulse (solid line).

2.3 Velocity-selective atom interferometry

This toolkit of coherent pulses allows the construction of a light-pulse atom interferometer. The interferometer schemes of interest in this work are those which are velocity-sensitive, that is, where the phase accrued between the two paths in the interferometer depends on the initial velocity of the atom. One example of this is the most basic interferometer sequence: $\frac{\pi}{2} - \frac{\pi}{2}$. This is commonly referred to as the *Ramsey* sequence, since it is inspired by Ramsey's early work on his method of separated oscillatory fields [36]. In the following we give a short treatment of the phase accrued within this interferometer, and discuss its dependence on the atomic velocity.

2.3.1 The Ramsey interferometer

This sequence is summarised in figure 2.5. We begin with an atom in the state $|1, \mathbf{p}\rangle$, such that $c_1(t_0) = 1$ and $c_2(t_0) = 0$. A Raman $\frac{\pi}{2}$ pulse of length $\tau = \frac{\pi}{2\tilde{\Omega}_R}$ at $t_0 = 0$ puts

the atom into an equal superposition of the states $|1, \mathbf{p}\rangle$ and $|2, \mathbf{p} + \hbar(\mathbf{k}_{L1} - \mathbf{k}_{L2})\rangle$. This pulse has an effective phase $\phi_L^{(1)}$. Application of equations 2.36 to find the state at the end of the $\frac{\pi}{2}$ yeilds

$$\begin{aligned} c_1(\tau) &= e^{i(\Omega_1^{AC}+\Omega_2^{AC})\tau/2} e^{i\delta\tau/2} \frac{1}{\sqrt{2}} (1 - i\cos\Theta) \\ c_2(\tau) &= e^{i(\Omega_1^{AC}+\Omega_2^{AC})\tau/2} e^{-i\delta\tau/2} \frac{1}{\sqrt{2}} \left(e^{i\phi_L^{(1)}} i\sin\Theta \right). \end{aligned} \tag{2.51}$$

The two coherent components of this superposition subsequently diverge in space, since they have different momenta. After the initial pulse, the atom is left to evolve for a time T with the Raman interaction switched off. During this period of free evolution $\Omega_1 = \Omega_2 = \Omega_R = 0$, hence $\tilde{\Omega}_R = -\delta$, $\cos\Theta = -1$ and $\sin\Theta = 0$ (the light-shift terms also disappear), and the Bloch vector precesses around the z-axis at the angular frequency δ. The state amplitudes become

$$\begin{aligned} c_1(\tau + T) &= e^{i\delta\tau/2} c_1(\tau) \left[\cos\left(\frac{-\delta T}{2}\right) + i\sin\left(\frac{-\delta T}{2}\right) \right] = c_1(\tau) \\ c_2(\tau + T) &= e^{-i\delta\tau/2} c_2(\tau) \left[\cos\left(\frac{-\delta T}{2}\right) - i\sin\left(\frac{-\delta T}{2}\right) \right] = c_2(\tau), \end{aligned} \tag{2.52}$$

and we find, as expected since the state eigenenergies have been factored out in the interaction picture, that the amplitudes are unchanged during free evolution. Finally, another $\frac{\pi}{2}$ pulse is applied, with a laser phase $\phi_L^{(2)}$, after which the amplitude of the upper state $|2, \mathbf{p} + \hbar(\mathbf{k}_{L1} - \mathbf{k}_{L2})\rangle$ is

$$\begin{aligned} c_2(2\tau + T) = e^{i(\Omega_1^{AC}+\Omega_2^{AC})\tau} e^{-i\delta\tau} \times \\ \frac{1}{2}\sin\Theta \left[e^{i\phi_L^{(1)}} (i - \cos\Theta) + e^{i\phi_L^{(2)}} e^{-i\delta T} (i + \cos\Theta) \right]. \end{aligned} \tag{2.53}$$

We can simplify this by defining a *relative* phase $\phi_L^{(\mathrm{rel})} = \phi_L^{(2)} - \phi_L^{(1)}$ between the two $\frac{\pi}{2}$ pulses, and taking $e^{i\phi_L^{(1)}}$ outside the square brackets:

$$\begin{aligned} c_2(2\tau + T) = e^{i(\Omega_1^{AC}+\Omega_2^{AC})\tau} e^{-i\delta\tau} e^{-i\delta T/2} e^{i\phi_L^{(1)}} \times \\ \frac{1}{2}\sin\Theta \left[(i - \cos\Theta) + e^{-i(\delta T - \phi_L^{(\mathrm{rel})})} (i + \cos\Theta) \right]. \end{aligned} \tag{2.54}$$

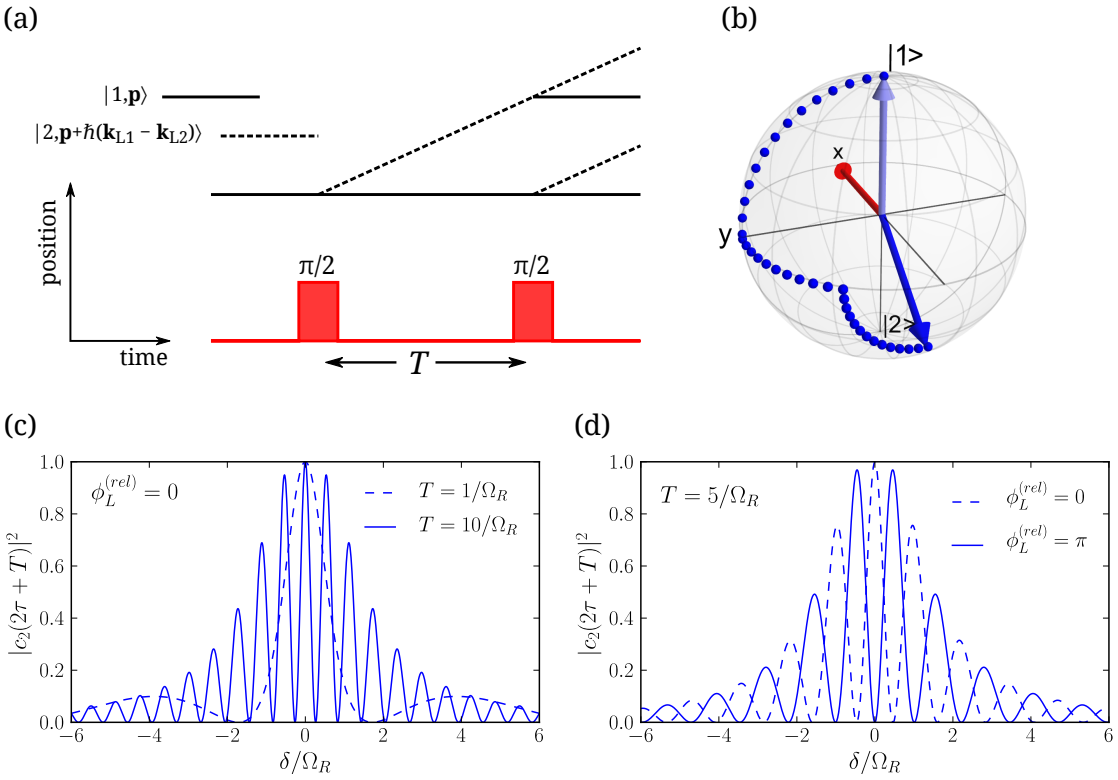

Figure 2.5: The $\frac{\pi}{2} - \frac{\pi}{2}$ (Ramsey) interferometer. (a) Wavepacket position-time diagrams for the interferometer, in the absence of external potentials. (b) An example Bloch sphere representation of the $\frac{\pi}{2} - \frac{\pi}{2}$ sequence, in which the phase of both pulses is $\phi_L = 0$. The light (dark) blue arrow is the initial (final) state vector, and the red arrow is the field vector. (c) Resultant upper state populations (equation 2.55) as a function of detuning δ for fixed relative pulse phase and different pulse spacings T, given in the legend. (d) As (c), with fixed T and different relative phases.

To clarify, this relative phase is distinct from the effective phase introduced in section 2.1.4. The amplitude $c_2(2\tau + T)$ is squared to give the population of the state

$$|c_2(2\tau + T)|^2 = \sin^2\Theta \left[\cos\left(\frac{\delta\, T - \phi_L^{(\mathrm{rel})}}{2}\right) - \cos\Theta \sin\left(\frac{\delta\, T - \phi_L^{(\mathrm{rel})}}{2}\right)\right]^2, \tag{2.55}$$

which in the case where the laser is close to resonance ($\delta^{AC} - \delta \ll \Omega_R$, and therefore $\cos\Theta \simeq 0$ and $\sin\Theta \simeq 1$) becomes

$$|c_2(2\tau + T)|^2 \simeq \frac{1}{2}\left[1 + \cos(\delta\, T - \phi_L^{(\mathrm{rel})})\right]. \tag{2.56}$$

The resultant upper state population follows an oscillation whose period is dependent on the time T between the $\frac{\pi}{2}$ pulses, as illustrated in figure 2.5 c where we plot equation 2.55 as a function of the detuning δ for a fixed relative laser phase. We find an increased

period at smaller values of T. Figure 2.5 d shows the effects of the relative phases of the two $\frac{\pi}{2}$ pulses. Shifting $\phi_L^{(\mathrm{rel})}$ by π simply shifts the maxima of the Ramsey pattern along by half of one oscillation period. In both 2.5 c and 2.5 d the light-shift $\delta^{AC} = 0$. The curves are enclosed within a Gaussian envelope, which we can shift left or right by making δ^{AC} non-zero. It is important to note that an interference pattern is only observed if the two wavepackets are still spatially overlapping as the second pulse is applied. The spatial extent of a wavepacket, otherwise known as its *coherence length*, is limited by the position-momentum uncertainty principle $l_{\mathrm{coh}} = \hbar/2\Delta p \geq \Delta z$, and therefore fringes are observed if the momentum-spread Δp of the wavepacket is sufficiently small.

2.3.2 Velocity-dependent phase

As we have seen in figure 2.5, the output state of the interferometer, as determined by the interferometer *phase*, depends on the value δ attributed to the atom. Returning to the definition of δ given in equation 2.18, we can write the momentum-inclusive detuning as

$$\delta = -\delta_L + \frac{\mathbf{p}\cdot(\mathbf{k}_{L1} - \mathbf{k}_{L2})}{M} + \frac{\hbar(\mathbf{k}_{L1} - \mathbf{k}_{L2})^2}{2M}. \tag{2.57}$$

The first term on the right hand side is, as described, the laser detuning. The second is the velocity-dependent, or *Doppler shift* term which can be written as $\mathbf{v}\cdot(\mathbf{k}_{L1} - \mathbf{k}_{L2})$ where $\mathbf{v}$ is the atomic velocity. For a cold atom moving at 50 mm/s and interacting with counter-propagating ($\mathbf{k}_{L1} = -\mathbf{k}_{L2}$) 780 nm beams, this term is equal to around $2\pi \times 128$ kHz. It is useful to define at this stage the *Raman recoil velocity*,[2] *i.e.* the change in atomic velocity upon undergoing the Raman transition, as

$$\mathbf{v}_R = \frac{\hbar(\mathbf{k}_{L1} - \mathbf{k}_{L2})}{M}. \tag{2.58}$$

We can therefore label the third term in equation 2.57 as the Raman *recoil shift* $M\mathbf{v}_R^2/2\hbar$, which for a rubidium-85 atom (mass number 85) interacting again with 780 nm light is approximately $2\pi \times 15.4$ kHz. The corresponding Raman recoil velocity is $v_R = 12$ mm/s.

We can see from the above that the output state of the $\frac{\pi}{2} - \frac{\pi}{2}$ interferometer is dependent on the initial velocity of the atom. Since the output state determines whether or not the

[2] As opposed to the single-photon recoil velocity, which is half of this value.

atom has absorbed a photon (or two in the case of Raman transitions), this represents a velocity-dependent *impulse*. Chapter 7 explores this principle, and its use in engineering atomic *cooling* forces.

2.4 Rubidium-85

In the previous sections we have discussed Raman transitions and interferometry based on a system of three atomic levels, namely $|1, \mathbf{p}\rangle$, $|3, \mathbf{p} + \hbar\mathbf{k}_{L1}\rangle$ and $|2, \mathbf{p} + \hbar(\mathbf{k}_{L1} - \mathbf{k}_{L2})\rangle$. This section describes an atomic system of such form in rubidium-85, which we use in experiments in the lab.

We begin this section with a brief summary of atomic structure. Note that detailed explanations can be found in many textbooks, including Foot [42] and Atkins [43].

2.4.1 Atomic structure

We describe the state of an atom by its corresponding set of *quantum numbers*. It is important to note that here we consider only the (hydrogen-like) alkali metals, which exhibit a single outer electron. Ignoring the electron spin for now, the necessary quantum numbers are n, l and m_l, and the electron wavefunction, described by these quantum numbers, can be written as the product of a radial and an angular part:

$$\psi_{n,l,m_l}(r, \theta, \phi) = R_{n,l}(r) Y_{l,m_l}(\theta, \phi). \tag{2.59}$$

The radial part of the wavefunction is represented by the Laguerre polynomials $R_{n,l}(r)$. The *principal* quantum number $n = 1, 2, 3, \ldots$, which originates from the Bohr model of the atom, specifies the orbital 'shell' in which the outermost electron is situated, and describes the electronic energy according to $E_n \propto 1/n^2$.

The angular part of the wavefunction is described by the spherical harmonics $Y_{l,m_l}(\theta, \phi)$, which satisfy the simultaneous eigenvalue equations $\hat{\mathbf{L}}^2 Y_{l,m_l} = l(l+1)\hbar^2 Y_{l,m_l}$ and $\hat{L}_z Y_{l,m_l} = \hbar m_l Y_{l,m_l}$, where $\hat{\mathbf{L}}$ is the angular momentum operator, whose z-component is $\hat{L}_z = -i\hbar\frac{\partial}{\partial\phi}$. The *orbital angular momentum* quantum number l takes the values $l = 0, 1, 2, \ldots, n-1$, and specifies the angular momentum eigenvalue of the electron according to $\sqrt{l(l+1)}\hbar$.

The *magnetic* quantum number m_l, which describes the projection of l along the z-axis, takes the values $m_l = -l, -l+1, \ldots, l$, and specifies the z-component of angular momentum as $m_l\hbar$.

The electronic *spin* angular momentum $\mathbf{S}$, described by the quantum numbers $s = \frac{1}{2}$ and $m_s = \pm\frac{1}{2}$ (since electrons are spin-$\frac{1}{2}$ particles), gives rise to an intrinsic electron magnetic moment $\boldsymbol{\mu}_s = -\mu_B g_s \mathbf{S}/\hbar$, where μ_B is the Bohr magneton and $g_S \approx 2$ is the electron g-factor. The interaction between $\boldsymbol{\mu}_s$ and the magnetic field created by the orbiting electron is known as the *spin-orbit interaction*. This leads to the definition of the *total* electronic angular momentum $\mathbf{J} = \mathbf{L} + \mathbf{S}$, where the quantum numbers j and m_j, which respectively describe the total electronic angular momentum and its projection along the z axis, take the values $j = |l-s|, |l-s+1|, \ldots, l+s$, and $m_j = -j, -j+1 \ldots, j$. The spin-orbit interaction acts to split the levels into states separated typically by many THz, giving the atom so-called *fine structure*.

The atomic nucleus also exhibits spin angular momentum $\mathbf{I}$, specified by the quantum number I. This gives rise to an intrinsic nuclear magnetic moment, which in turn interacts with the magnetic fields generated by the electron. In light of this we define the total angular momentum $\mathbf{F} = \mathbf{J} + \mathbf{I}$, which we specify by the total atomic angular momentum quantum number $F = |j-I|, |j-I+1|, \ldots, j+I$ and its magnetic counterpart $m_F = -F, -F+1 \ldots, F$. These interactions with the nuclear spin give rise to energy level structure typically on the scale of GHz, known as *hyperfine structure*. In our experiments, we induce coherent transitions between levels within this hyperfine structure.

Each hyperfine state F is split into $2F+1$ magnetic-sensitive substates labelled m_F. We refer to these sublevels as *Zeeman* sublevels, since the magnetic fields considered in our experiments induce Zeeman-like (weak field) splitting. The energy shift of a Zeeman sublevel m_F due to an external magnetic field of magnitude B is given by

$$\Delta E_{\text{Zeeman}} = \mu_B g_F m_F B, \tag{2.60}$$

where μ_B is the Bohr magneton and g_F is the Landé g-factor, which can be measured experimentally for a given transition.

The set of quantum numbers given in the above allows us to write the full spectroscopic notation, or term symbol, for an atomic state as

$$n^{2S+1}L_J(F, m_F), \tag{2.61}$$

in which for hydrogenic atoms, $S = s$, $L = l$ and $J = j$. Conventionally we replace the numbers $L = l = 0, 1, 2, \ldots$ with the letters $L = S, P, D, \ldots$, giving rise to the notion of 's-orbitals', etc.

2.4.1.1 Rubidium-85 structure

The structure of rubidium-85 (^{85}Rb, atomic number $Z = 37$), relevant to the experiments in this work, is shown in figure 2.6. This particular sub-section of the structure is known as the rubidium D_2 line, which is represented by fine structure transitions within the manifold defined by the levels $|5^2S_{1/2}\rangle$ and $|5^2P_{3/2}\rangle$, and can be addressed by tuning our laser to around 780 nm. Within these two levels, the nuclear ($I = 5/2$) and electronic (lower, upper $J = 1/2, 3/2$ respectively) angular momenta interact to give a hyperfine level splitting defined by the quantum numbers F and m_F as described previously. As shown in the figure, the lower level is split into two hyperfine states $|5^2S_{1/2}, F = 2, 3\rangle$, separated by 3.036 GHz, and the upper level is split into four $|5^2P_{3/2}, F = 1, 2, 3, 4\rangle$, separated by smaller intervals. In our experiments, we drive Raman transitions between the levels $|5^2S_{1/2}, F = 2\rangle$ and $|5^2S_{1/2}, F = 3\rangle$ which are respectively split into 5 and 7 magnetic-sensitive Zeeman sublevels. The Landé g-factors for each hyperfine level are given in figure 2.6, along with the coefficient $\mu_B g_F$, which is quoted in MHz/G.

2.4.2 Dipole transitions

Broadly speaking, dipole transitions between atomic levels occur when the frequency of an applied alternating electric field coincides with an inter-level frequency interval, or atomic *resonance*. They obey selection rules governed by the conservation of angular momentum, which to some extent we are able to visualise in terms of an *overlap* between the atom and photon wavefunctions. For a dipole transition from state $|\alpha, F, m_F\rangle$ to $|\alpha', F', m'_F\rangle$, where α describes all quantum numbers other than F and m_F, the coupling

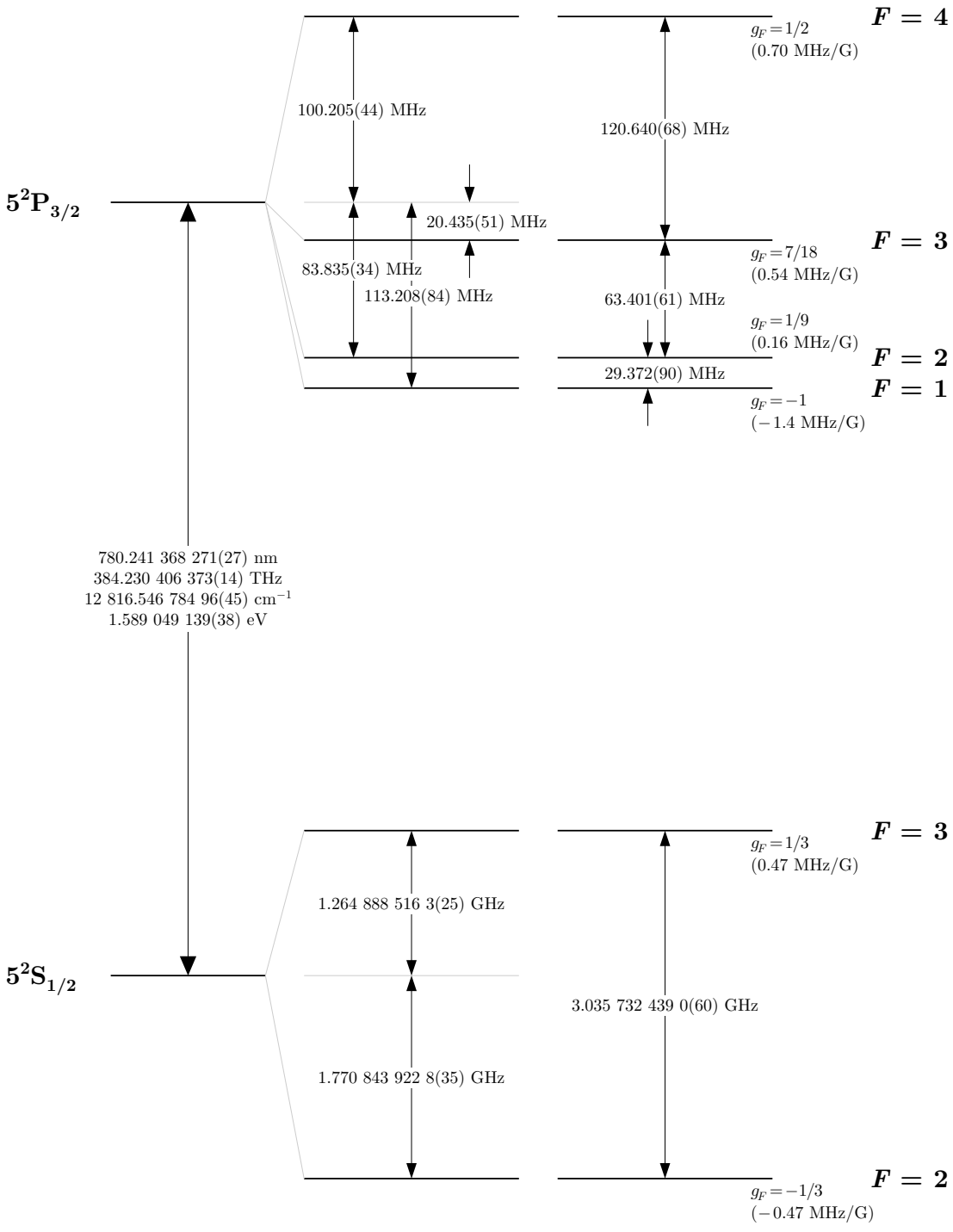

Figure 2.6: (Taken from [44]) Rubidium 85 energy level diagram.

strength, or Rabi frequency, is given by the overlap integral

$$\Omega^{(a)}_{|F,m_F\rangle,|F',m'_F\rangle} = -\frac{1}{\hbar}\langle \alpha', F', m'_F|\mathbf{d}\cdot\mathbf{E}_a|\alpha, F, m_F\rangle, \tag{2.62}$$

where $\mathbf{E}_a$ ($a = 1, 2$ in the Raman system indicates the particular beam) is the electric field vector, and $\mathbf{d} = e\mathbf{r}$ is the atomic *dipole moment*, as determined by the electron's charge e and position $\mathbf{r}$ relative to the nucleus. We can decompose both $\mathbf{r}$ and $\mathbf{E}_a$ into irreducible components within the spherical basis defined by the unit vectors

$$\hat{\mathbf{e}}_{+1} = -(\hat{\mathbf{x}} + i\hat{\mathbf{y}})/\sqrt{2}, \tag{2.63a}$$

$$\hat{\mathbf{e}}_0 = \hat{\mathbf{z}}, \tag{2.63b}$$

$$\hat{\mathbf{e}}_{-1} = (\hat{\mathbf{x}} - i\hat{\mathbf{y}})/\sqrt{2}, \tag{2.63c}$$

in which the scalar product is given by (Appendix F in [45])

$$\mathbf{d}\cdot\mathbf{E}_a = eE_a\sum_q (-1)^q r_q \epsilon_{-q}, \tag{2.64}$$

where $q = -1, 0, 1$ and ϵ_q describe the polarisation of the electric field, in order to re-write equation 2.62 as

$$\Omega^{(a)}_{|F,m_F\rangle,|F',m'_F\rangle} = -\frac{eE_a}{\hbar}\sum_q (-1)^q \epsilon_{-q}\langle J', F', m'_F|r_q|J, F, m_F\rangle. \tag{2.65}$$

We are able to simplify this by application of the Wigner-Eckart theorem, which states that for an irreducible tensor operator T^k_q, the overlap integral $\langle \alpha', F', m'_F|T^k_q|\alpha, F, m_F\rangle$, where α describes all quantum numbers other than F and m_F, is proportional to the Clebsch-Gordan coefficient

$$\langle F', m'_F|F, k, m_F, q\rangle = (-1)^{F'-k+m_F}\sqrt{2F+1}\begin{pmatrix} F' & k & F \\ m'_F & q & -m_F \end{pmatrix} \tag{2.66}$$

in which k and q depend on the properties of the operator and the term in parentheses is a Wigner 3–j symbol [46], with a constant of proportionality $\langle \alpha', F'\|T^k\|\alpha, F\rangle$, known as the *reduced* matrix element. The reduced matrix element is independent of m_F and q, and we are able to factor out its dependence on F, leaving a reduced matrix element

that depends only on the initial and final n, L, and J quantum numbers by writing

$$\begin{aligned}\langle \alpha', F' \| T^k \| \alpha, F \rangle =& \langle \alpha', J' \| T^k \| \alpha, J \rangle (-1)^{F'+J+k+I} \times \\ & \sqrt{(2F'+1)(2J+1)} \begin{Bmatrix} J & J' & k \\ F' & F & I \end{Bmatrix},\end{aligned} \tag{2.67}$$

in which the term in braces is a Wigner 6–j symbol. Since it is a vector, the position operator $\hat{\mathbf{r}}$ has rank $k = 1$, hence by applying the Wigner-Eckart theorem to equation 2.65 we arrive at the final form for the Rabi frequency

$$\Omega^{(a)}_{|F,m_F\rangle,|F',m'_F\rangle} = -\frac{eE_a}{\hbar} \langle J' \| \mathbf{d} \| J \rangle \sum_q (-1)^q \epsilon_{-q}\, G(F', F, J', J, I, m'_F, m_F, q). \tag{2.68}$$

where we have separated the experimental, empirically soluble parameters from the purely geometrical term

$$\begin{aligned}G(F', F, J', J, I, m'_F, m_F, q) =& (-1)^{2F'+J+I+m_F} \sqrt{(2F+1)(2F'+1)(2J+1)} \times \\ & \begin{pmatrix} F' & 1 & F \\ m'_F & q & -m_F \end{pmatrix} \begin{Bmatrix} J & J' & 1 \\ F' & F & I \end{Bmatrix}.\end{aligned} \tag{2.69}$$

The Wigner 3–j and 6–j symbols can be calculated using the `ThreeJSymbol` and `SixJSymbol` functions in Mathematica [47], and the reduced dipole matrix element for the $5S_{1/2} \rightarrow 5P_{3/2}$ transition as found in Steck's alkali D line data [44] (along with tabulated values of G) is $3.58425(74) \times 10^{-29}\,\mathrm{C\,m}$.

The 3–j and 6–j symbols in the above equations impose a neat statement of the selection rules based on the associated transition quantum numbers: the product of the symbols

Polarisation	Transition	Δm_F
Left circular (LCP) $\mathbf{k} \parallel \hat{\mathbf{e}}_0$	σ^+	$+1$
Right circular (RCP) $\mathbf{k} \parallel \hat{\mathbf{e}}_0$	σ^-	-1
Linear $\boldsymbol{\epsilon} \parallel \hat{\mathbf{e}}_0$ ($\boldsymbol{\epsilon} \parallel \hat{\mathbf{z}}$)	π^0	0
Linear $\boldsymbol{\epsilon} \parallel \hat{\mathbf{y}}$	$\pi^+ = (\sigma^+ + \sigma^-)/\sqrt{2}$	± 1
Linear $\boldsymbol{\epsilon} \parallel \hat{\mathbf{x}}$	$\pi^- = (\sigma^+ - \sigma^-)/\sqrt{2}$	± 1

Table 2.1: Table showing the possible polarisation states of the driving field photon, and their associated dipole transitions, where $\hat{\mathbf{e}}_0 = \hat{\mathbf{z}}$ is the quantisation axis of the transition, and $\boldsymbol{\epsilon}$ is the polarisation vector of the photon. For the circularly polarised cases, the photon is considered to be moving in the positive $\hat{\mathbf{e}}_0$ direction.

is equal to zero unless:

1. $\Delta J = J' - J = 0, \pm 1$ except for $J = 0 \rightarrow J' = 0$.
2. $\Delta F = F' - F = 0, \pm 1$ except for $F = 0 \rightarrow F' = 0$.
3. $\Delta m_F = m'_F - m_F = -q$.

These selection rules reflect angular momentum conservation. The angular momentum of the photon is added to (subtracted from) the atom in any absorption (emission) event, and this imposes restrictions on the types of transitions allowed, dependent on the photon polarisation and the intitial and final m_F states. A *linearly* polarised photon whose wavevector is perpendicular to the quantisation axis ($\mathbf{k} \perp \hat{\mathbf{e}}_0$) and whose polarisation vector is parallel to it ($\boldsymbol{\epsilon} \parallel \hat{\mathbf{e}}_0$) drives a π^0 transition, whereby $\Delta m_F = 0$. A *circularly* polarised photon whose wavevector is *parallel* to the quantisation axis ($\mathbf{k} \parallel \hat{\mathbf{e}}_0$, moving in the positive $\hat{\mathbf{e}}_0$ direction) and whose polarisation vector rotates counter-clockwise as observed from the reciever is denoted LCP (left-circularly-polarised, helicity $+1$), and drives σ^+ transitions, whereby $\Delta m_F = +1$. This is represented by the $q = -1$ component of equation 2.68. Similarly, an RCP (right-circularly-polarised, helicity -1) photon, *ceteris paribus*, drives σ^- transitions, whereby $\Delta m_F = -1$, as represented by the $q = 1$ component of equation 2.68. A good description of the circular polarisation and corresponding helicity states is given in [**?**].

Furthermore, a linearly polarised photon whose electric field vector is *perpendicular* to $\hat{\mathbf{e}}_0$ (*i.e.* along $\hat{\mathbf{x}} = -(\hat{\mathbf{e}}_{+1} - \hat{\mathbf{e}}_{-1})/\sqrt{2}$ or $\hat{\mathbf{y}} = i(\hat{\mathbf{e}}_{+1} + \hat{\mathbf{e}}_{-1})/\sqrt{2}$) drives an equal superposition of σ^+ and σ^- transitions. These are labelled $\pi^+ = (\sigma^+ + \sigma^-)/\sqrt{2}$ for polarisation parallel to $\hat{\mathbf{y}}$ and $\pi^- = (\sigma^+ - \sigma^-)/\sqrt{2}$ for polarisation parallel to $\hat{\mathbf{x}}$. All of the above polarisation states and their associated labels and m_F selection rules are summarised in table 2.1.

2.4.3 Raman transitions

In order to create a Raman system in ^{85}Rb we require two laser beams at $780.243 + \frac{2\pi c}{\Delta}$ nm, separated in frequency by the lower hyperfine splitting $\omega_{\mathrm{HFS}} = 2\pi \times 3.036\,\mathrm{GHz}$. With this we can drive Raman transitions between $|5S_{1/2}, F = 2\rangle = |1, \mathbf{p}\rangle$ and $|5S_{1/2}, F = 3\rangle = |2, \mathbf{p} + \hbar(\mathbf{k}_{L1} - \mathbf{k}_{L2})\rangle$ via the upper states $|5P_{3/2}, F'\rangle = |3, \mathbf{p} + \hbar\mathbf{k}_{L1}\rangle$, provided that the detuning Δ from single-photon resonance is large. The coupling strength for the

Raman transition (equation 2.24) is determined by the product of the two single-photon transition coupling strengths, and by inspection of the dipole selection rules given in the previous section, we find that Raman transitions may occur via more than one upper F' hyperfine level. This makes the problem of describing the system rather more complex, however a useful formalism for describing Raman transitions via multiple atomic levels, which we adopt here, is given by Bateman *et al* in [48]. We discuss the general concepts of this formalism in the following.

2.4.3.1 Vector formalism for multiple Raman routes

In the regime where the hyperfine splitting of the upper state levels is much smaller than the single-photon detuning Δ we can make the approximation $\Delta_{|F,m_F\rangle,|1,m'_F\rangle} \approx \Delta_{|F,m_F\rangle,|2,m'_F\rangle} \approx \cdots \approx \Delta$, and treat all transitions as having the same Δ.

Considering the system consisting of two lower and four upper hyperfine levels ($F = 2, 3$ and $F' = 1, 2, 3, 4$), we can write the single-photon couplings (equation 2.62) associated with the two Raman beams as components of two vectors:

$$\mathbf{\Omega}_{1a} = \left(\Omega^{(a)}_{|2,m_F\rangle,|1,m'_F\rangle},\ \Omega^{(a)}_{|2,m_F\rangle,|2,m'_F\rangle},\ \Omega^{(a)}_{|2,m_F\rangle,|3,m'_F\rangle},\ \Omega^{(a)}_{|2,m_F\rangle,|4,m'_F\rangle}\right) \tag{2.70a}$$

$$\mathbf{\Omega}_{2a} = \left(\Omega^{(a)}_{|3,m_F\rangle,|1,m'_F\rangle},\ \Omega^{(a)}_{|3,m_F\rangle,|2,m'_F\rangle},\ \Omega^{(a)}_{|3,m_F\rangle,|3,m'_F\rangle},\ \Omega^{(a)}_{|3,m_F\rangle,|4,m'_F\rangle}\right). \tag{2.70b}$$

Next, the two-photon Rabi frequency is re-written for the system of multiple upper levels as the scalar product[3] of these two vectors where $a = n$

$$\Omega_R = \frac{|\mathbf{\Omega}_{11} \cdot \mathbf{\Omega}_{22}|}{2\Delta}, \tag{2.71}$$

(we omitted the terms Ω_{an} with $a \neq n$ earlier due to their fast oscillatory nature) and this can be expressed in terms of the reduced matrix element, the electric field strengths, and the detuning Δ as

$$\Omega_R = \frac{|\langle J'\|\mathbf{d}\|J\rangle|^2}{2\Delta\hbar^2} E_1^* E_2 |\mathbf{G}_{11} \cdot \mathbf{G}_{22}|, \tag{2.72}$$

[3]Note that this vector formalism is a subset of a more general *tensor* notation for transitions between multiple levels, and for systems with larger numbers of levels, tensor products must be considered when calculating the coupling strengths.

where the vectors $\mathbf{G}_{na}$ constitute the corresponding single-photon G coefficients (see equation 2.69) for coupling of level n by laser a. In this formalism, we have separated the experimental parameters from the purely geometrical term $|\mathbf{G}_{11} \cdot \mathbf{G}_{22}|$, which describes the dipole matrix elements of the Raman transition.

By inspecting equations 2.70 and considering the selection rule $\Delta F = 0, \pm 1$, we can see that both the fourth component of $\mathbf{\Omega}_{11}$ and the first component of $\mathbf{\Omega}_{22}$ (and their corresponding components in $\mathbf{G}_{11,22}$) are equal to zero. This makes the term $|\mathbf{G}_{11} \cdot \mathbf{G}_{22}|$ only dependent on the middle two components, *i.e.* our Raman transitions occur via $F' = 2, 3$.

This vector formalism is also useful for expressing light-shifts in the Raman system. In order to incorporate the effect due to all upper levels we can re-write the light shift term as

$$\delta^{AC} = \sum_{a=1,2} \left(\frac{\|\mathbf{\Omega}_{1a}\|^2}{4\Delta_{1a}} - \frac{\|\mathbf{\Omega}_{2a}\|^2}{4\Delta_{2a}} \right), \tag{2.73}$$

where we have used double-bars to denote the vector norm.

Finally, for completeness we express the generalised, off-resonant two-photon Rabi frequency in the vector formalism as

$$\tilde{\Omega}_R = \sqrt{\left(\frac{|\mathbf{\Omega}_{11} \cdot \mathbf{\Omega}_{22}|}{2\Delta} \right)^2 + \left[\sum_{a=1,2} \left(\frac{\|\mathbf{\Omega}_{1a}\|^2}{4\Delta_{1a}} - \frac{\|\mathbf{\Omega}_{2a}\|^2}{4\Delta_{2a}} \right) - \delta \right]^2}. \tag{2.74}$$

2.4.3.2 Raman polarisation arrangements

The polarisations of the two Raman beams determine the allowed transitions between the various m_F states. For example, with two counter-propagating opposite-circularly polarised photons, one with LCP (helicity -1) propagating in the positive $\hat{\mathbf{e}}_0$ direction and the other with RCP (helicity $+1$) propagating along $-\hat{\mathbf{e}}_0$, we can drive Raman transitions between the lower levels $|2, m_F\rangle$ and $|3, m_F\rangle$ via the two upper levels $|F', m_F + 1\rangle$, where $F' = 2, 3$. This is the relatively simple arrangement which we label, for obvious reasons, $\sigma^+ - \sigma^+$. As another example, if we have two orthogonal linearly polarised photons whose electric field vectors are both perpendicular to the quantisation axis $\hat{\mathbf{e}}_0 = \hat{\mathbf{z}}$, *i.e.* $\boldsymbol{\epsilon}_1 \parallel \hat{\mathbf{y}}$ and $\boldsymbol{\epsilon}_2 \parallel \hat{\mathbf{x}}$, then we drive Raman transitions along four distinct routes, namely: $|2, m_F\rangle \leftrightarrow |3, m_F\rangle$ via $|F', m_F \pm 1\rangle$, where $F' = 2, 3$. This arrangement

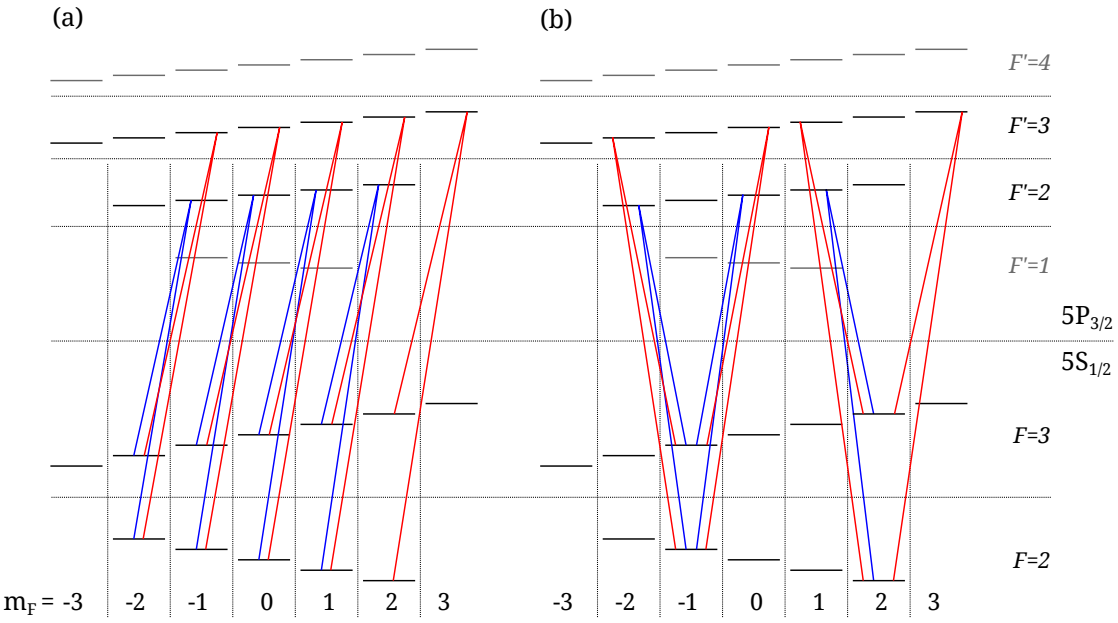

Figure 2.7: Allowed Raman routes on the ^{85}Rb D_2 line in: (a) the $\sigma^+ - \sigma^+$ polarisation arrangement; and (b) the $\pi^+ - \pi^-$ polarisation arrangement. The blue (red) lines indicate Raman routes via $F' = 2$ (3). In (b), only Raman routes from two starting m_F states are shown in order to avoid overcrowding. The splittings of the levels are not shown to scale.

is labelled $\pi^+ - \pi^-$, and is commonly referred to as 'lin-perp-lin'. The Raman routes associated with the two aforementioned polarisation arrangements are depicted in figure 2.7, and we give a summary of these and other polarisation combinations and their allowed Raman routes in table 2.2.

It is interesting to note that the $\pi^+ - \pi^+$, $\pi^- - \pi^-$, $\pi^0 - \pi^0$ and $\sigma^\pm - \sigma^\mp$ arrangements

Transitions	**Raman Routes**	**(via)**
$\sigma^+ - \sigma^+$	$\|2, m_F\rangle \leftrightarrow \|3, m_F\rangle$	$\|F', m_F + 1\rangle$
$\sigma^- - \sigma^-$	$\|2, m_F\rangle \leftrightarrow \|3, m_F\rangle$	$\|F', m_F - 1\rangle$
$\pi^0 - \sigma^+$	$\|2, m_F\rangle \leftrightarrow \|3, m_F - 1\rangle$	$\|F', m_F\rangle$
$\pi^0 - \sigma^-$	$\|2, m_F\rangle \leftrightarrow \|3, m_F + 1\rangle$	$\|F', m_F\rangle$
$\pi^0 - \pi^+$	$\|2, m_F\rangle \leftrightarrow \|3, m_F + 1\rangle$ $\|2, m_F\rangle \leftrightarrow \|3, m_F - 1\rangle$	$\|F', m_F\rangle$ $\|F', m_F\rangle$
$\pi^+ - \pi^-$	$\|2, m_F\rangle \leftrightarrow \|3, m_F\rangle$ $\|2, m_F\rangle \leftrightarrow \|3, m_F\rangle$	$\|F', m_F + 1\rangle$ $\|F', m_F - 1\rangle$

Table 2.2: Table summarising the polarisation states of the two Raman driving field photons and their associated dipole-allowed Raman routes. The two polarisation vectors are $\boldsymbol{\epsilon}_{1,2}$, and the quantisation axis is $\hat{\mathbf{e}}_0 = \hat{\mathbf{z}}$. In all cases, $F' = 2, 3$.

(*i.e.* parallel linear and orthogonal circular) do not drive Raman transitions, because the dipole matrix elements for their allowed Raman routes via $F' = 2$ and $F' = 3$ cancel each other out. As an example of this, we look at the $m_F = 1$ sublevel in the $\pi^0 - \pi^0$ arrangement. In this case $\epsilon_1 = \epsilon_2 = 0$, and the scalar product of the G-coefficient vectors is

$$|\mathbf{G}_1 \cdot \mathbf{G}_2| = (\sqrt{3/20},\ \sqrt{7/108},\ -\sqrt{16/135},\ 0) \cdot (0,\ \sqrt{8/189},\ \sqrt{5/216},\ -\sqrt{15/56}), \tag{2.75}$$

which is equal to zero. This is the same for all m_F levels in all of the above-mentioned arrangements, and provides the reasoning for the absence of $|2, m_F\rangle \leftrightarrow |3, m_F \pm 2\rangle$ (via $|F', m_F + 1\rangle$, where $F' = 2, 3$) transitions in the lin-perp-lin arrangement. This is only valid if we treat all the upper levels as having the same single-photon detuning Δ – the approximation we set out with.

Part II

Experimental setup and procedures

Chapter 3

Rubidium MOT & experimental procedures

In order to realise the Raman system described in the previous chapter, we require an ultracold sample of rubidium atoms isolated from their environment, and a means to prepare and measure their internal state before and after the Raman pulses are applied. As in most cold atom labs, the starting point is the magneto-optical trap (MOT) [5]. The MOT, a three-dimensional arrangement of counter-propagating laser beams converging on the zero-point of a quadrupole magnetic field, achieves confinement and cooling of atoms via position- and velocity-dependent absorption of photons. With the MOT in place, atomic state preparation and detection is performed by optical pumping.

This chapter describes the experimental setup and procedures regarding the rubidium MOT. We begin with a brief introduction to the key theoretical principles behind the MOT, before describing and characterising key aspects of the setup. Here we do not offer a detailed treatment of magneto-optical trapping theory. For this we refer the reader to previous PhD theses in this work [49, 50], and to the extensive literature, for example Metcalf & Van der Straten [51], Weiner & Ho [52] or Foot [42]. Furthermore, many *experimental* aspects of our MOT are extensively documented in previous PhD theses [49, 50, 53, 54]. We choose here only to discuss the experimental aspects which are of greatest relevance to the Raman experiments of the following chapters, and refer the reader to these theses for insight into the more technical aspects of the setup, such as specific details of the lasers, spectroscopy, and vacuum chamber.

3.1 Principles of magneto-optical trapping

The *scattering* force imparted on a two-level atom by a near-resonant laser beam is given by the photon momentum $\hbar\mathbf{k}$, where $\mathbf{k}$ is the wavevector, multiplied by the rate of photon scattering $R_{\text{scat}} = \Gamma\rho_{22}$, in which Γ is the spontaneous decay rate, or linewidth, and ρ_{22} is the population of the upper level, as introduced in section 2.2. By solving the optical Bloch equations, which are identical to equations 2.43 except for the inclusion of the decay term Γ, we can find the form of ρ_{22} in the steady-state. The force then becomes

$$\mathbf{F}_{\text{scat}} = \hbar\mathbf{k}\frac{\Gamma\Omega^2/4}{\delta^2 + \Gamma^2/4 + \Omega^2/2}, \tag{3.1}$$

where Ω is the transition Rabi frequency and δ is the detuning from resonance, as seen by the moving atom. As we have seen in chapter 2, the detuning δ of the laser from the atomic transition is dependent on the velocity of the atom, via the Doppler shift. There is also an implicit dependence of δ on the magnetic field B via the Zeeman shift for an atom with internal magnetic-sensitive sub-structure. These effects conspire to give an atomic detuning

$$\delta = \delta_L - \mathbf{k}\cdot\mathbf{v} - \mu_B g m B, \tag{3.2}$$

where $\delta_L = \omega - \omega_L$ is the detuning of the laser from the unperturbed resonance, $\mathbf{k}\cdot\mathbf{v}$ is the Doppler shift (where $\mathbf{v}$ is the velocity of the atom), and $\mu_B g m B$ is the Zeeman shift (where g is the Landé g-factor and m is the magnetic quantum number). Since the likelihood of the atom to absorb photons, and therefore the impulse, depends on $|\delta|$, we can engineer forces based on the velocity and the magnetic field. More specifically, the Doppler term allows for a velocity-dependent force, and the Zeeman term allows, if we have some position-dependence in the magnetic field, for a position-dependent force.

We can generate a one-dimensional *cooling* force, known as *optical molasses*, by illuminating our atom with two *counter-propagating* laser beams, whose frequencies are red-detuned ($\delta_L > 0$) from the atomic resonance. In this case $|\delta|$ becomes smaller when $\mathbf{k}$ and $\mathbf{v}$ are opposing, and therefore absorption (and the associated recoil) becomes more likely when the atom is moving *towards* the beam. The resulting effect is a 1–D velocity-dependent damping force, which acts to cool atoms within a small range of velocities.

This can be extended to three dimensions by simply employing *three orthogonal pairs* of these beams.

Furthermore, if we situate our atom at the centre of a quadrupole magnetic field, whose magnitude B increases with increasing distance from the centre, we can engineer a position-dependent restoring, or *trapping* force on the atom, whereby absorption becomes more likely as the atom moves away from the trap centre. This is only possible when the counter-propagating pairs of cooling beams are *orthogonally polarised*, that is either perpendicular-linear or left-right circular.

With these methods in place we can cool the atom whilst confining it to a small region of space, however cooling cannot occur indefinitely. The rate at which the atom is cooled by the optical molasses is at some point balanced by the rate of *heating* due to spontaneous emission events and their associated directionally-random recoils. Equating these two rates, and now considering the one-dimensional *temperature* T where $m\mathbf{v}^2/2 = k_B T/2$, we find the *Doppler cooling limit* to be

$$T_D = \frac{\hbar\Gamma}{2k_B}, \tag{3.3}$$

which occurs for $\delta_L = \Gamma/2$. For ^{85}Rb, the Doppler cooling limit is $T_D = 146\,\mu$K. In practice, temperatures much lower than T_D are achievable with optical molasses, due to the somewhat fortuitous presence of *sub-Doppler* cooling mechanisms. Sub-Doppler cooling arises due to dissipative redistribution of population between, and differential light shifts *of*, the atomic Zeeman sublevels in the presence of polarisation gradients and changing quantisation axes. Whilst we exploit the effects of sub-Doppler cooling in our experiments, we choose to refer the reader to the literature (for example [51, 52]) for a more involved discussion of the theory behind it.

3.2 MOT lasers

In order to make a MOT for ^{85}Rb we require our lasers to address a two-level *closed*, or cycling, optical transition within the atomic structure. The transition must be closed because we require many thousands of scattering events for efficient cooling and trapping. A suitable candidate in ^{85}Rb is the $|5S_{1/2}, F = 3\rangle \rightarrow |5P_{3/2}, F' = 4\rangle$ transition, since

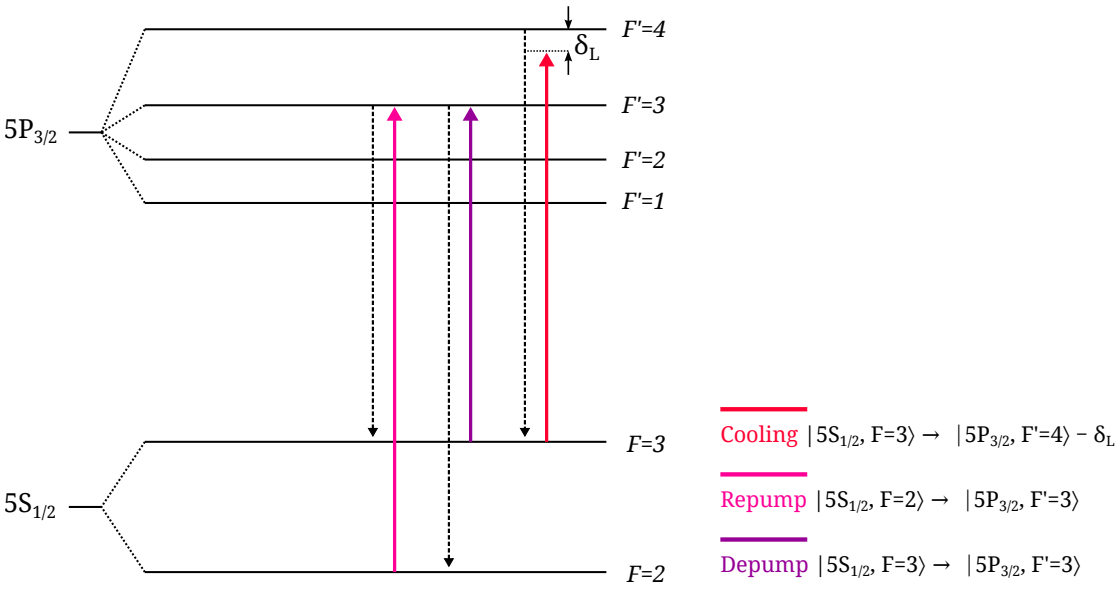

Figure 3.1: Optical transitions in ^{85}Rb used in the experiments. The cooling and repump transitons are used for magneto optical trapping, the depump transition is used for optical depumping into $F = 2$. The solid arrows indicate absorption routes, whilst the dashed arrows indicate the associated spontaneous emission routes. The colour-associations in this diagram are applied consistently in the remainder of this chapter.

the only decay route from the upper level allowed by the dipole selection rules takes the atom back to $|5S_{1/2}, F = 3\rangle$, and the cycle can continue. This is known as the cooling transition, and to this we tune our *cooling laser*. We detune from resonance by δ_L (typically $1 - 3\,\Gamma$) in order to allow for Doppler cooling.

Operating at this frequency, the cooling laser will occasionally, with some small yet non-negligible probability, excite atoms into the $|5P_{3/2}, F' = 3\rangle$ level, from which spontaneous decay into the *dark* (*i.e.* not coupled by the cooling laser) lower level $|5S_{1/2}, F = 2\rangle$ is possible. In order to pump population out of this dark state and back onto the cooling transition we employ a *repump* laser, tuned to the $|5S_{1/2}, F = 2\rangle \rightarrow |5P_{3/2}, F' = 3\rangle$ transition[1]. This quickly re-populates $|5S_{1/2}, F' = 3\rangle$ via spontaneous emission from the upper level.

The levels discussed above are depicted in figure 3.1. We also include in figure 3.1 the *depump* laser which, whilst not at all necessary for magneto-optical trapping, is an important component in chapter 7 of this thesis. The depump laser is resonant with the transition $|5S_{1/2}, F = 3\rangle \rightarrow |5P_{3/2}, F' = 3\rangle$, and therefore allows for rapid optical

[1] A repump laser resonant with the $|5P_{3/2}, F' = 2\rangle$ upper state would also be suitable.

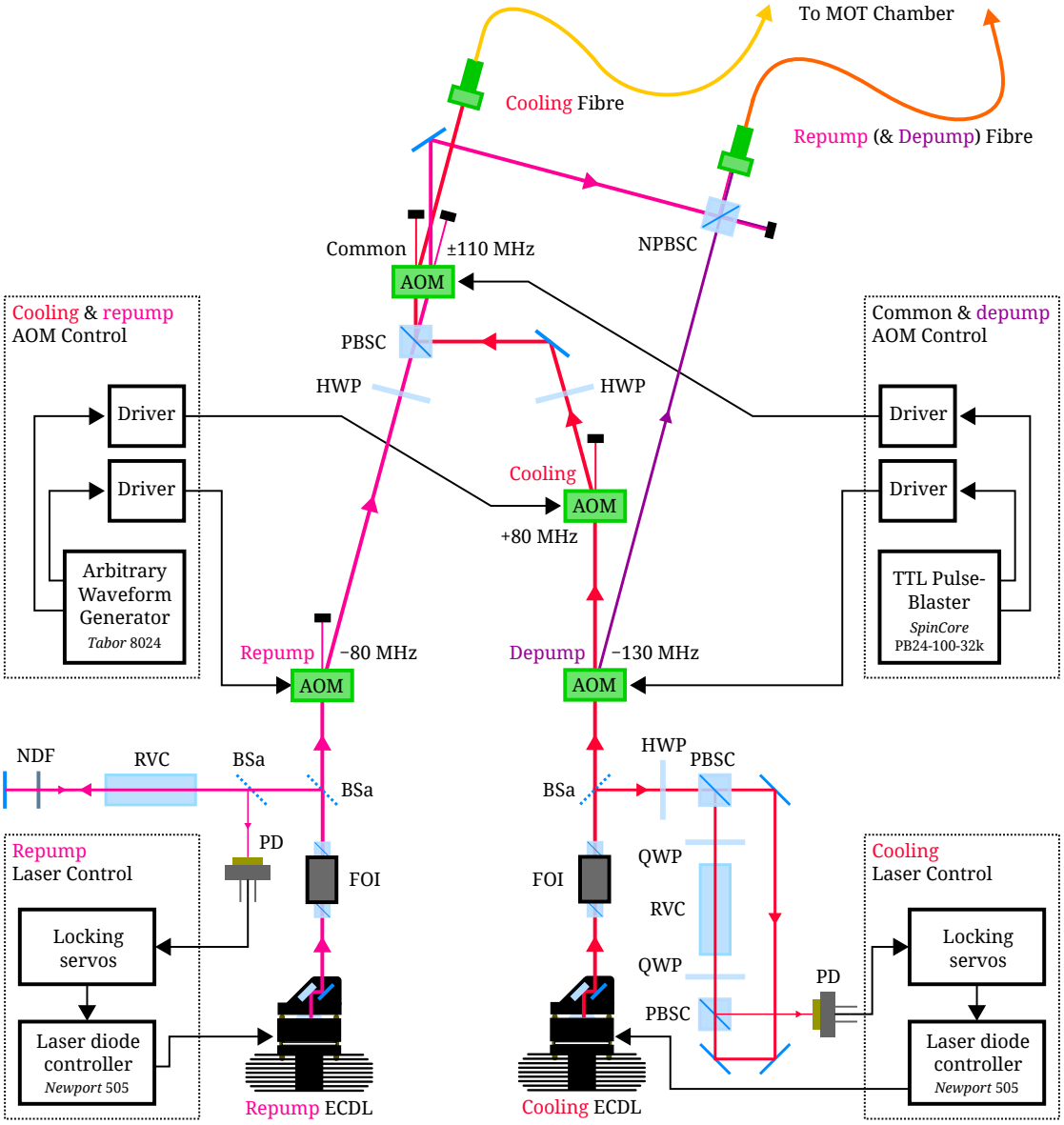

Figure 3.2: Schematic of the lasers, spectroscopy and switching apparatus for the MOT. HWP – half waveplate; QWP – quarter waveplate; (N)PBSC – (non-)polarising beam-splitter cube; FOI – Faraday optical isolator; RVC – rubidium vapour cell; BSa – beam sampler; NDF – neutral density filter; PD – photodiode.

pumping of all population into the $|5S_{1/2}, F = 2\rangle$ level. A schematic of the MOT laser apparatus is shown in figure 3.2, and described in the following.

3.2.1 Cooling & Repump lasers

The MOT laser beams (cooling – red, repump – pink) are derived from in-house-built external cavity diode lasers (ECDLs), which output around 45 mW. Each ECDL consists of a *Sharp* GH07895A6C laser diode (nominally 785 nm but can be tuned to 780 nm) and

an 1800 lines/mm *Edmund Optics* holographic grating in the Littrow configuration. The current to the laser diode is controlled by a *Newport* 505 LD controller, and the tuning angle of the grating is controlled by application of voltage to a *Thorlabs* AE0203D04F piezo stack. The temperature of the laser diode is regulated by a *Newport* 300 temperature controller connected to a *Laird* SH10,95,06 Peltier thermoelectric cooler and AD590 temperature sensor. Each laser is frequency-stabilised via pump-probe frequency modulation spectroscopy (FMS) in a rubidium vapour cell. All modulation and locking circuitry was designed and constructed by Matt Himsworth, and particularly good descriptions of the spectroscopy and PID, along with details and characterisation of the ECDLs, can be found in his PhD thesis [50].

3.2.2 Beam Switching

We require the ability to switch the MOT beams on and off quickly, and to control their individual intensities during experiments. This is achieved by a series of acousto-optical modulators (AOMs). An AOM consists of a transparent crystal through which, upon application of an oscillating voltage to a piezo stack, an acoustic wave is passed. An optical beam passing through is diffracted (*i.e.* spatially deflected) and shifted in frequency according to $\mathbf{k}_{\text{beam out}} = \mathbf{k}_{\text{beam in}} + n\mathbf{k}_{\text{acoustic wave}}$ where n is the diffraction order, $\mathbf{k}_{...}$ is the associated wavevector, and the amount of light diffracted is dependent on the amplitude of the acoustic wave. We employ a combination of *Gooch & Housego* and *AA Optoelectronic* AOMs, each driven by an *AA Optoelectronic* VCO-amplifier driver. The beams are switched by separate primary AOMs (labelled 'cooling' and 'repump' in figure 3.2), before being passed through a common secondary AOM (labelled 'Common'), which directs the two beams into separate optical fibres. We achieve $80-85\,\%$ diffraction efficiency into the 1st order of the AOMs. One benefit of switching the beams with two AOMs in series rather than just one is the extra extinction (60 dB rather than 30 dB), which is necessary in our experiment where small residual intensities can cause state-altering optical pumping. Another advantage is that if the two AOMs in series apply equal-and-opposite frequency shifts to the diffracted laser beam there is a net shift of zero after switching, and therefore no offset is required in the laser locking.[2]

[2] This can be difficult in pump-probe spectroscopy, however an offset-lock or phase-lock [55] would provide one possible solution.

This is the case for the repump beam in our setup: the primary repump AOM shifts the frequency by $-110\,\text{MHz}$, and the common by $+110\,\text{MHz}$. On the cooling beam path, the primary AOM shifts the frequency by $+80\,\text{MHz}$, and the common by $-110\,\text{MHz}$, giving a combined frequency shift post-locking of $-30\,\text{MHz}$. This represents, if we are to lock to the centre of the $|5S_{1/2}, F = 3\rangle \rightarrow |5P_{3/2}, F' = 4\rangle$ transition, a detuning $\delta_L \approx 5\Gamma$ (where $\Gamma = 2\pi \times 6.06\,\text{MHz}$), which larger than desired for efficient cooling and trapping. To reduce δ_L, we shift our FMS locking signal zero-point by $\sim 10\,\text{MHz}$ using an electronically-generated offset in the PID loop, and we typlically work at a detuning $\delta_L \approx 3\Gamma$. The two primary AOMs are separately controlled using the two outputs of a *Tabor* 8024 arbitrary waveform generator, connected to the modulation pins of the respective AOM amplifiers. This allows for arbitrary time-dependent control over the beam intensities. To control the common AOM, since we do not require arbitrary control over its diffracted intensity, we use a TTL signal ($0, 5\,\text{V}$ only) generated from one of the 8 outputs of a computer-controlled *SpinCore* PB24-100-32k Pulse-Blaster.

3.2.3 Depump beam

The depump beam (purple) is generated by picking off and down-shifting a portion of the cooling beam before its primary switching AOM with another AOM. The depump AOM's central resonant frequency is $110\,\text{MHz}$, but we drive it at $130\,\text{MHz}$ using an independent variable *Mini-Circuits* POS-150+ voltage-controlled oscillator and ZHL-1-2W amplifier. We are able to achieve diffraction efficiency of $\sim 35\,\%$ into the depump beam with this setup. This beam, as previously mentioned, is not required for magneto-optical trapping and is used only in the interferometric cooling experiments of chapter 7. When switched on, it is combined at a non-polarising beamsplitter cube with the repump beam. The cooling and repump/depump beams are sent to the MOT chamber through separate optical fibres.

3.3 MOT chamber

The vacuum chamber in which we form our magneto-optical trap is an octagonal stainless-steel construction which was machined in the departmental mechanical workshop. The chamber has ample optical access via anti-reflection-coated viewports, and is mounted

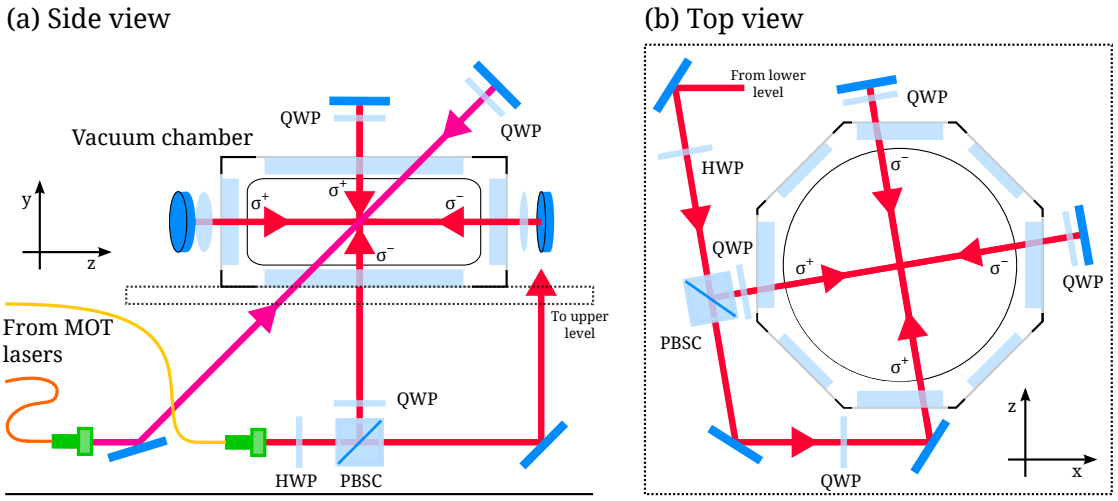

Figure 3.3: Diagram of the optical setup surrounding the MOT chamber, which is situated on an elevated breadboard. (a) View from the side of the chamber, showing the repump and cooling beam paths, where only one horizontal cooling beam is included to avoid overcrowding. (b) View from the top, showing only the horizontal cooling beams. $\sigma^{\pm}$ indicates the polarisation of the beam, and the origin of the coordinate system is the crossing point of the cooling beams. HWP – half waveplate; QWP – quarter waveplate; PBSC – polarising beamsplitter cube.

on an optical breadboard and elevated above the optical bench to allow access from below. It is held at a pressure of less than 10^{-9} mbar by an ion pump, and rubidium gas is dispensed upon the passing of current through getters housed inside. We once again choose to refer the reader elsewhere for technical details. A particularly detailed description of the MOT chamber and its assembly and preparation can be found in Sunil Patel's thesis [54].

3.3.1 Optical fields

The optical apparatus surrounding the MOT chamber is illustrated in figure 3.3. At the output of the fibre, the cooling beam is collimated to a $1/e^2$ diameter of 7.5 mm by a *Thorlabs* F810APC-780 doublet lens system. The beam, which has an optial power typically around 8 mW, is split 1:2 by a half waveplate and polarising beamsplitter cube, and one third of the light is sent upwards through the centre of the chamber via a quarter waveplate. The ingoing beam is right-circularly polarised, such that σ^- transitions are dipole-allowed. Upon exit through the top viewport the beam is retro-reflected, and double-passed through another quarter waveplate such that upon re-entry through the top viewport the beam is left-circularly polarised, and the retro-reflected beam drives

σ^+ transitions. The remaining two thirds of the cooling light are diverted up towards the optics situated on the elevated breadboard, and then split 1:1 by another polarising beamsplitter cube. The resulting two beams are sent, again via quarter waveplates and again retro-reflected, along the two orthogonal horizontal directions depicted in the figure. Whereas the vertical beam enters the chamber with σ^- polarisation, the horizontal beams enter with σ^+. This polarisation arrangement is necessary for trapping in three dimensions due to the orientation of the field lines within the quadrupole field. Note that the horizontal MOT beams are rotated about the centre of the chamber. This is to allow access for the Raman beams (chapter 4), which we align along the z-axis.

The repump (and depump) beam enters the chamber separately from below, with circular polarisation (preparation optics not shown in the figure) and at an angle of approximately 45° to the optical table. It intersects the crossing point of the cooling beams, and upon exit from the chamber it is retroreflected via a quarter waveplate such that the polarisation on the retro-reflected path is orthogonal to the input.

3.3.2 Magnetic fields

The magneto-optical trap requires a quadrupole magnetic field, which we generate with a pair of current-carrying coils in the anti-Helmholtz configuration, that is, where the axial distance between the two identical coils is equal to their radii and the current flows in opposite directions, as shown in figure 3.4 a. These coils comprise 432 turns of 22 gauge insulated copper wire, wound on aluminium former rings, and mounted on the top and bottom of the MOT chamber. Passing 2 A through the quadrupole coils gives a field gradient of around 5 G/cm along the coil axis. The quadrupole coils are water-cooled to avoid overheating.

In order to compensate for stray magnetic fields, which arise primarily due to the Earth's core and the ion pump, and act to offset the quadrupole field zero, we employ three orthogonal pairs of current-carrying shim coils, as depicted in figure 3.4 b. These each consist of 330 turns of copper wire wound on aluminium former rings, and mounted on opposite sides of the MOT chamber along all three Cartesian axes. We apply current to the shim coils using voltage-to-current converter circuits capable of 0.1mA resolution in order to allow fine adjustment of the fields. The two coils in each pair are connected in

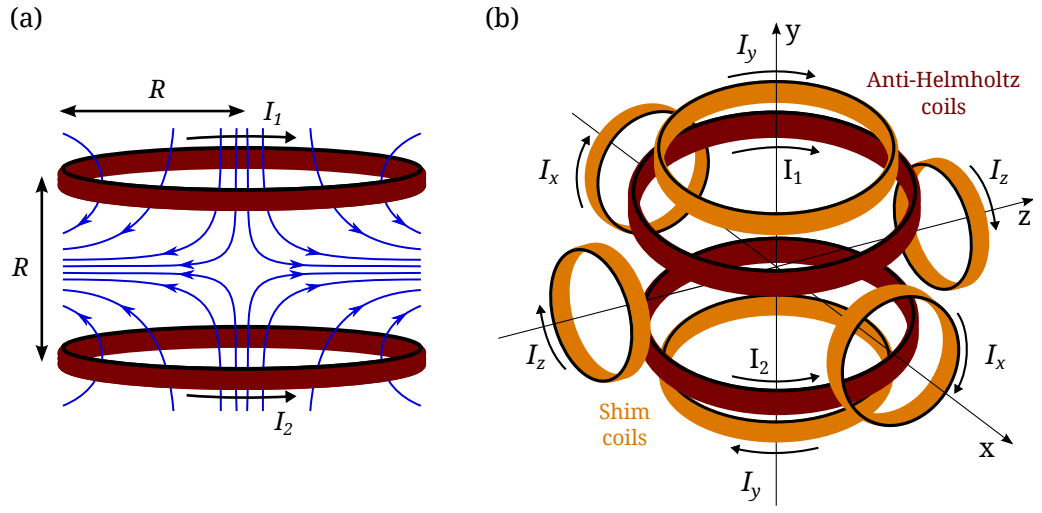

Figure 3.4: Diagram of the magnetic field setup around the MOT chamber. (a) Sketch of the magnetic quadrupole field (blue lines) due to an anti-Helmholtz coil pair. (b) Current-carrying coil arrangement: orange – shim coils; red – anti-Helmholtz MOT coils. The direction of applied current is given in all cases, and $I_1 = -I_2$. The origin of the axis set is the position of the MOT cloud.

series to give equal (and equi-directional) currents, and give a magnetic field along their common axial direction which varies by less than 0.5% across the width of the cooling beams at the centre of the chamber. We also use the z-axis shim coil pair to provide a quantisation field for Raman transitions, where the Raman beams lie along the z-axis (see chapter 4).

3.3.2.1 Switching

For the Raman experiments of interest in this work, and in order to allow sub-Doppler cooling mechanisms to occur effectively, we require the ability to switch off the quadrupole field quickly and efficiently. To this end, the quadrupole coils are linked to a simple field-effect transistor (FET) switch [56], as shown in figure 3.5 a, where a suppression diode is placed in parallel with each coil to limit the inductive voltage spike. We also place a Zener diode with Zener voltage $V_Z = 39\,\mathrm{V}$ in series with the suppression diode to allow some voltage overshoot, which leads to a faster current switch-off according to the formula $V = -L\frac{dI}{dt}$ where V is the voltage, I is the current, and L is the coil inductance. The larger the Zener voltage, the larger the inductive voltage spike and the faster the field switch-off.

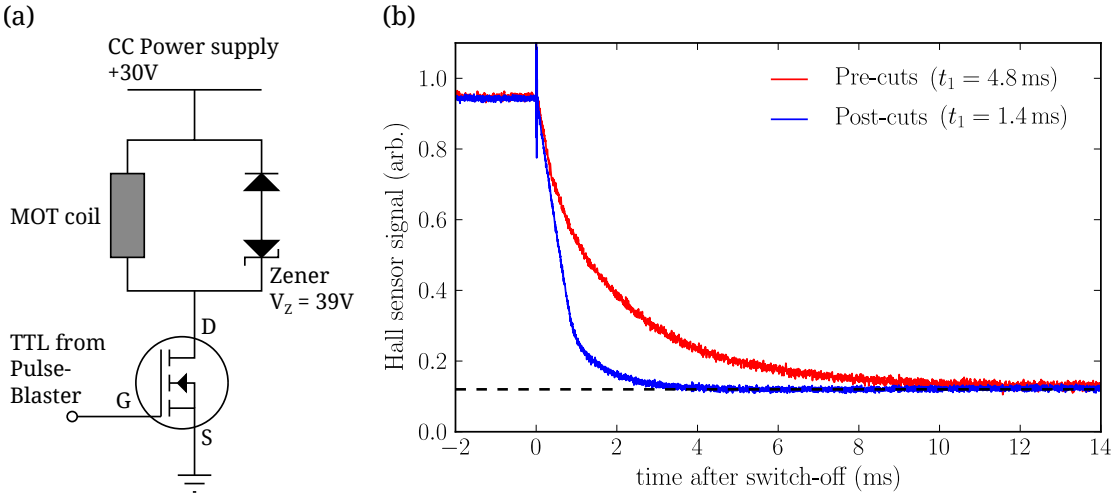

Figure 3.5: (a) Circuit diagram for MOT coil switching. (b) Measurement of the magnetic field decay after the quadrupole coils are switched off. The red curve was taken before the aluminium rings on which the copper coils are wound were cut, and the blue curve was taken after. These curves were measured using a Hall effect sensor placed close to one of the quadrupole coils.

3.3.2.2 Eddy currents

Fast switch-off of the quadrupole field is inhibited by eddy currents flowing in large conductive loops around the MOT chamber. These eddy currents, which are caused by the changing magnetic field at the time of switch-off, in turn create magnetic fields at the centre of the chamber which take several milliseconds to decay. The primary conductors of eddy currents are the aluminium rings around which all the coils are wound.[3] In order to preclude eddy currents in the aluminium rings, we simply made a cut in each to break the conducting loop. This was of course anything *but* simple, since the copper coils were already wound on them, however Damon Grimsey of the mechanical workshop carried out the job skilfully. The effects of cutting the aluminium former rings is shown in figure 3.5 b. These data were taken by measuring the signal from a *Honeywell* SS94AF Hall effect sensor placed close to the quadrupole coils. The time taken for the field to decay to 10% of its *on* state, which we label t_1, was reduced from 4.8 ms to 1.4 ms as a result of the cuts – a significant reduction. It is assumed that t_1 is approximately the same at all points inside the chamber.

[3]The resistivity of aluminium is only a factor of 1.7 greater than that of copper. As a further note, whilst we cannot preclude eddy currents in the vacuum chamber itself, the resistivity of stainless steel (from which it is formed) is large: ~ 41 times that of copper.

An important consideration regarding eddy currents is the *symmetry* of the experimental arrangement. If there is a large conducting loop on one side of the chamber but not the other, for example, then the switch-off of the fields will be asymmetric about the centre of the chamber, and in the presence of the MOT beams the atoms will be pushed out of the trapping region. After cutting the aluminium coil rings there remained, unfortunately, some significantly-sized conducting loops which could not be cut, such as the optics mounts and, to a lesser extent, the chamber itself. Although eddy currents cannot be stopped in these components, care was taken to ensure that they were arranged around the chamber in a symmetric manner in order to avoid an asymmetric switch-off. One particularly notable contributor to asymmetric eddy currents was the aluminium optical breadboard on which the MOT chamber itself was mounted. We relieved ourselves of this problem by taking a hacksaw to the breadboard, ensuring of course that the structure would remain sound.

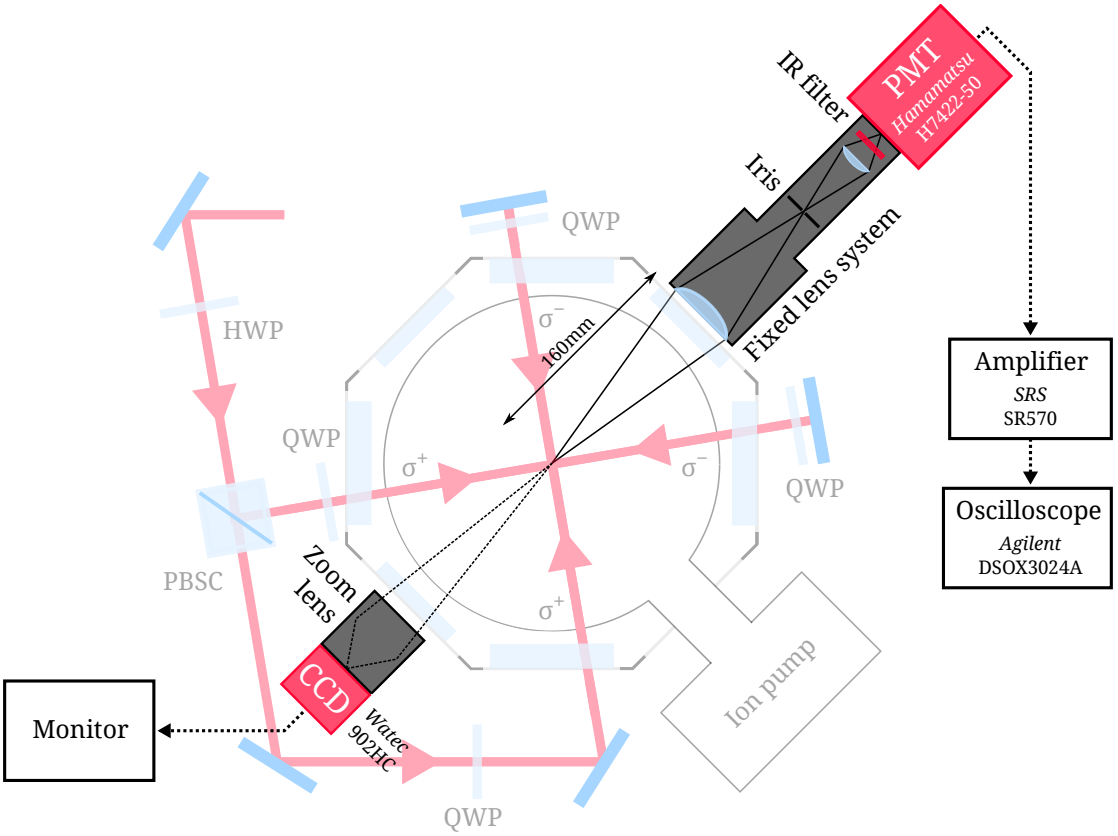

Figure 3.6: Optical arrangement for imaging and detection of the MOT cloud. The PMT system is used for fluorescence detection, and the CCD system is used for video monitoring.

3.4 Imaging and detection

The MOT imaging and detection setup is illustrated in figure 3.6. When in the presence of the MOT lasers, the atom cloud fluoresces at 780 nm, making it relatively simple to image. Basic video imaging is performed with a *Watec* 902HC Ultimate CCD camera and zoom lens system, which is connected to a monitor. This is used primarily to check for the presence of the MOT, and as a diagnostic tool when locking the MOT lasers.

More precise detection is performed using a *Hamamatsu* H7422-50 photo-multiplier tube (PMT) and fixed custom telescopic lens system, which collects fluorescence from the atom cloud. The current signal from the PMT is amplified by a *Stanford Research Systems* SR570 amplifier before being sent to an *Agilent* DSOX3024A oscilloscope. This detection method can be used to measure the relative population in the two hyperfine ground states as discussed in section 3.5.3.

3.5 Preparation and readout sequence

The experimental sequence applied for preparing the atoms for Raman manipulation, and then measuring their internal state afterwards, is represented in figure 3.7. The steps are as follows:

1. **MOT:** Atoms are initially trapped and cooled to $80 < T < 230$ μK in the magneto-optical trap.

2. **Molasses cooling:** (See section 3.5.1.) The quadrupole field is switched off and the intensities of the cooling and repump beams are ramped down linearly over 1 ms to 20 % of their normal MOT values. The atom cloud is then allowed to cool in the molasses beams for a few ms (t_M, typically 6 ms), after which the velocity distribution resembles that in figure 5.10, and the temperature is typically $20 < T < 80$ μK.

3. **State preparation:** (See section 3.5.2.) The repump beam is switched off and the atoms are optically pumped in $t_{SP} = 1$ ms into the $|5S_{1/2}, F = 2\rangle$ state by the cooling laser.

4. **Raman pulse window:** (see chapter 4) Raman pulses are applied to the atoms.

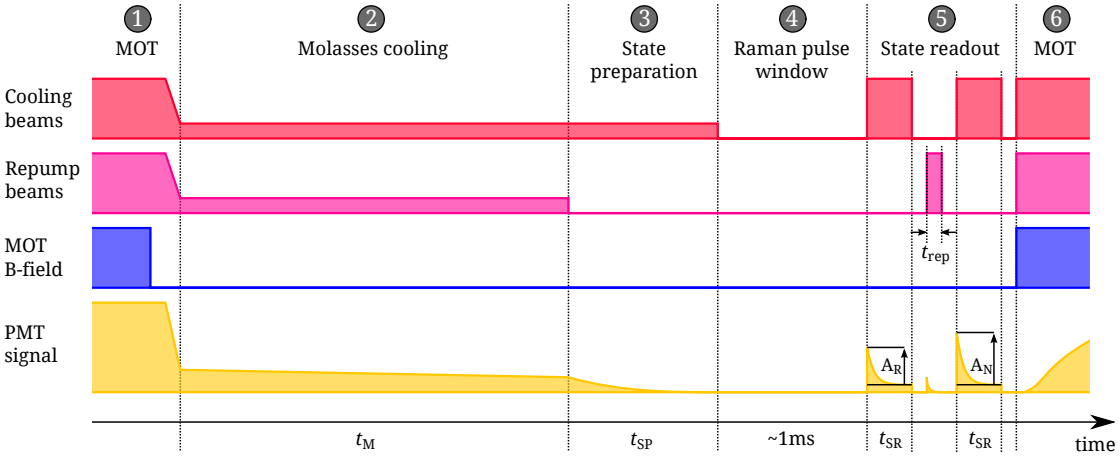

Figure 3.7: Diagram of the experiment sequence timings (not to scale). The individual stages are described in the text.

5. **State readout:** (See section 3.5.3.) The cooling laser is switched on for $t_{SR} = 300\,\mu$s, causing atoms in $|5S_{1/2}, F = 3\rangle$ to fluoresce, and to be gradually pumped into $|5S_{1/2}, F = 2\rangle$ (as in step 2). Immediately after this, *all* atoms are pumped to $|5S_{1/2}, F = 3\rangle$ by the repump laser ($t_{\text{rep}} = 5\,\mu$s pulse), and the cooling laser is switched on once again for t_{SR} to pump atoms back to $|5S_{1/2}, F = 2\rangle$. The ratio of amplitudes of the decay curves during the two cooling laser pulses (A_R/A_N), as measured with the PMT, is a normalised measure of the upper hyperfine state population $|c_2|^2$.

6. **MOT:** Both MOT lasers and the quadrupole field are switched on, and atoms are trapped and cooled in the MOT for $\sim 500\,$ms before the sequence is repeated.

3.5.1 Molasses cooling

As mentioned previously, we do not offer a theoretical discussion of sub-Doppler cooling mechanisms here. We do exploit them, however, in order to bring the temperature of the atom cloud down further before the Raman pulses are applied. We do this to minimise the Doppler-broadening-induced dephasing effects apparent in Raman manipulation with limited Rabi frequencies (see chapter 6). For sub-Doppler cooling to occur effectively accross the entire cloud, the quadrupole field must be switched off, and any stray magnetic fields nulled. Furthermore, sub-Doppler mechanisms occur more readily at lower laser intensities than those of the near-saturation-intensity cooling beams. This is because atoms require time to move across significant lengths of a periodic potential

landscape created by relative AC Stark shifts in polarisation gradients, before they are optically pumped by the beams. Lower intensity beams lead to a lower scattering rate, and in general more efficient sub-Doppler cooling. In fact, the resultant temperature is found to be approximately linearly proportional to the intensity in [57]. It is possible also to reduce the scattering rate by increasing the cooling beam detuning, however in our setup reducing the intensity is much easier. In a similar sense, the magnetic fields must be nulled such that light shifts within the potential landscape are not dwarfed by Zeeman shifts.

After the quadrupole coils are switched off, the intensities of the cooling and repump beams are linearly ramped down to 20% of their normal MOT values over a period of 1 ms. We ramp the intensity, as opposed to stepping it, because the velocity capture-range of the molasses decreases with decreasing intensity, and we wish for this to happen gradually so as to minimise the loss of atoms. The cloud is then left to undergo sub-Doppler cooling in the molasses beams for a time t_M (typically 6 ms) after which the temperature of the atoms is sufficiently reduced. The velocity distribution of the atoms at this stage is given in figure 5.10 b of section 5.2.1. It is important to note that some experiments in this work are performed in the velocity-insensitive arrangement, whereby the Raman beams co-propagate. In this case the molasses cooling stage is not necessary, since Doppler-broadening does affect the Raman transition.

3.5.2 State preparation

Before Raman pulses are applied, the atoms are prepared by optical pumping into state $|1\rangle$, the lower hyperfine level $|5S_{1/2}, F = 2\rangle$. This is done by irradiating the atoms with only the cooling beams. Since the cooling laser occasionally couples to $|5P_{3/2}, F = 3\rangle$, atoms are gradually lost from the $|5S_{1/2}, F = 3\rangle \leftrightarrow |5P_{3/2}, F = 4\rangle$ cooling cycle to $|5S_{1/2}, F = 2\rangle$, which is a dark state in the absence of the repump laser. At the reduced cooling beam intensity (the same as that applied in the molasses stage), the state preparation process is complete within $t_{SP} = 1$ ms, and the atoms end up approximately evenly distributed across the 5 Zeeman sublevels of the $|5S_{1/2}, F = 2\rangle$ state.[4] Preparation into $|5S_{1/2}, F = 2\rangle$ could be achieved using the depump laser (see figure 3.1) in a much shorter time (a few μs since the depump transition is not closed), but we choose

[4] This is verified in section 5.1.2.

instead to use the cooling laser since it continues to provide an optical molasses for the atoms during the preparation stage.

The depump laser *is* used when we apply multiple sequences of Raman pulses and require *fast* optical pumping into the $|5S_{1/2}, F = 2\rangle$ level *between* sequences (see chapter 7). This is the depump laser's only purpose in this work, however it could also be applied in conjunction with the repump laser to achieve *spin-polarisation* [58] of the atoms, described as follows. If both the repump and depump lasers are applied linearly polarised along the quantisation axis, which we can define with a magnetic field, such that both beams induce π^0 transitions, then $|5S_{1/2}, F = 3, m_F = 0\rangle$ is a dark state (the dipole matrix elements for transitions from this state are zero). After a number of spontaneous emission cycles, all atoms accumulate in this dark state, which is insensitive to magnetic fields. Our current experimental setup allows for application of this technique without requiring any experimental alterations. Although not tested in this work, spin-polarisation is commonly used when preparing atoms for interferometry experiments, since atoms in a single, magnetically-insensitive state exhibit a more homogeneous Rabi frequency than atoms distributed across all Zeeman sublevels.

3.5.3 State readout

After the Raman pulses have been applied, we measure the resultant internal state of the atoms. The initial *readout pulse* is a $t_{SR} = 300\,\mu$s application of the cooling beams. As described in the previous sub-section, in the presence of the cooling laser (no repump), population in $|5S_{1/2}, F = 3\rangle$ is gradually pumped into $|5S_{1/2}, F = 2\rangle$. The PMT fluorescence signal during the readout pulse exhibits an exponential decay as a function of time, and the amplitude A_R of this decay signal is proportional to the number of atoms in $|5S_{1/2}, F = 3\rangle$. In order to measure the population (*i.e.* the *total* fraction of the cloud) in $|5S_{1/2}, F = 3\rangle$, which we label $|c_2|^2$, we must normalise A_R according to the amplitude observed when *all* atoms begin in $|5S_{1/2}, F = 3\rangle$. To this end, after the initial readout pulse, we pump all atoms into $|5S_{1/2}, F = 3\rangle$ with a $t_{\text{rep}} = 5\,\mu$s pulse of the repump laser, before applying the *normalisation pulse*, which is simply another $t_{SR} = 300\,\mu$s application of the cooling beams. We label the amplitude of the decaying exponential as measured by the PMT during the normalisation pulse

A_N. Decaying exponetials are fitted to the data pulled from the oscilloscope, and the ratio $A_R/A_N = |c_2|^2$.

3.6 MOT characterisation

The following contains a characterisation of the aspects of the MOT which are important for the Raman experiments of later chapters. For a full characterisation, including details of the loading rate and steady state atom number, we refer the reader to previous theses on this work [49, 50, 53, 54]. The most important characteristics of the MOT are its size and temperature, and we discuss these in the following.

The temperature of our MOT cloud in normal MOT operation, *i.e* without pure molasses cooling, has been measured previously using the release and recapture method [59], giving results which vary between $80 < T < 230$ μK. These temperatures are normal for a MOT, and the wide range is due to varying experimental conditions between measurements. A particularly thorough treatment of this can be found in James Bateman's PhD thesis [49]. The release and recapture method can tell us the temperature, but does not offer a detailed picture of the *velocity distribution*, which is an important factor in determining the behaviour of Raman transitions.

In this thesis, we measure the velocity distribution of the atoms using a technique known as *Raman velocimetry*. Understanding the application of this method requires some appreciation of how our Raman beams are applied, and this can be gained from the following chapters. We therefore choose to include the results, and the necessary brief digression into the theory, in section 5.2.1.

3.6.1 Size and shape

Figure 3.8 shows an image of the MOT cloud taken with the *Watec* CCD camera. We deduced the length scales by photographing a standard rule with the same imaging system. The cloud has an approximately Gaussian shape, as illustrated in subplots (b) and (c), where deviations from the perfect Gaussian are due to slight misalignments of, and imperfections *in*, the MOT beams and/or magnetic fields. It is important to note that the size and shape of the MOT varies from day-to-day due to changing temperature

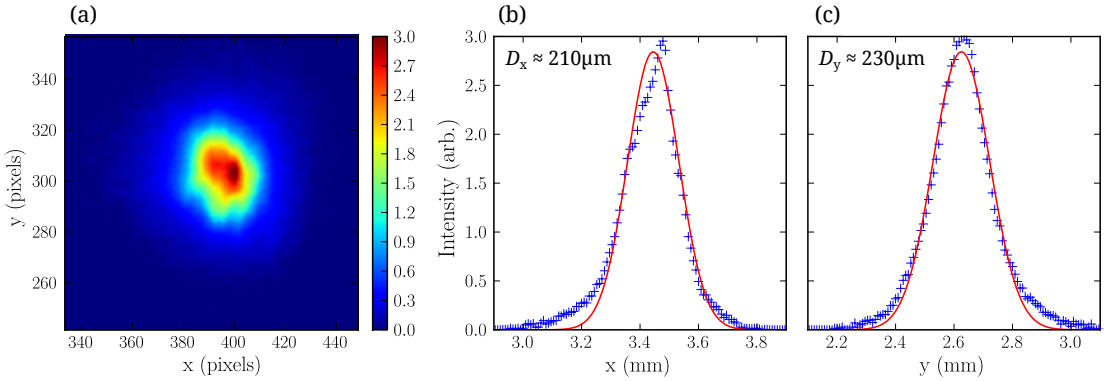

Figure 3.8: Imaging the magneto-optical trap. (a) is a false-color image of the MOT cloud, taken with a CCD camera. (b) and (c) are 1D slices through the centre of the MOT cloud along the x and y directions, respectively, where the blue crosses are data, and the red curves are least-squares fits of Gaussian functions to the data. $D_{x,y}$ is the full-width half-maximum of the respective fit.

and magnetic fields (certain components of the apparatus can become magnetised, for example), and to small drifts in the alignment and tuning of the MOT beams. Figure 3.8 represents one of the more visually appealing manifestations of the cloud.

We find the full-width at half-maximum diameter of the cloud to be $\sim 210\,\mu$m in the horizontal direction and $\sim 230\,\mu$m in the vertical direction. This difference is partly accounted for by the fact that the gradient of the quadrupole field is different along the vertical and horizontal directions. Furthermore, differences in intensity between the three cooling beam pairs can lead to a 'squeezing' of the cloud along one particular direction. Such small effects, however, are not critical to the behaviour of the experiments. A more important result is that the entire MOT cloud fits well within a square of side 1mm. We shall use this when considering suitable Raman beam profiles, as discussed in chapter 4.

3.6.2 Expansion in free-fall

When the quadrupole coils are switched off, leaving the cooling and repump beams *on*, the trapping force on the atoms is removed. However, some non-trapping, position-dependent forces may remain, due for example to stray magnetic fields, as described in section 3.3.2.2. One good diagnostic method for detecting stray fields is to image the expansion of the atom cloud in the presence of the MOT beams after the quadrupole field has been switched off. If stray fields are present, the atoms will be 'thrown' out of

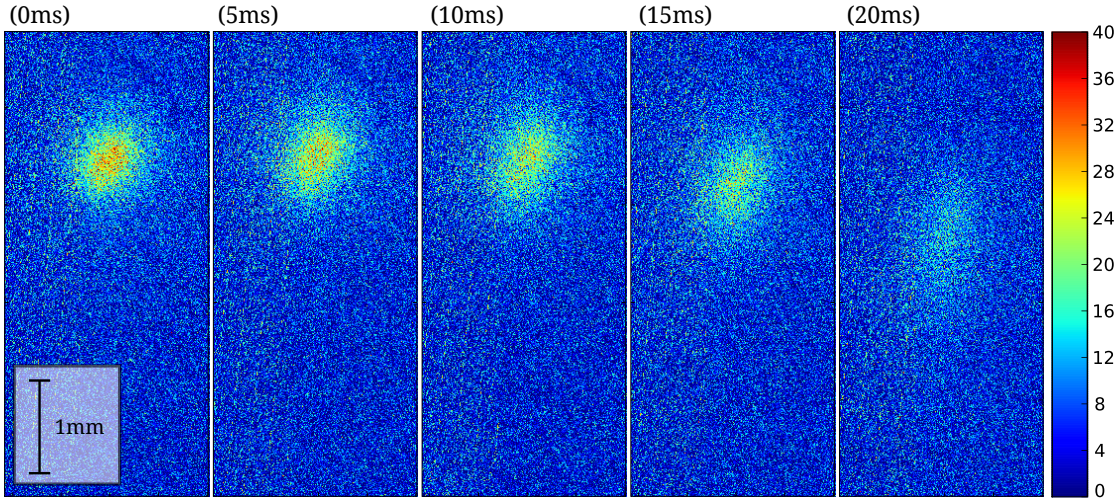

Figure 3.9: Monitoring the magneto-optical trap with a fast camera as the quadrupole field is switched off. The time above each plot is the approximate time after switch-off.

the trapping region upon switch-off. Since the MOT beams cause the atoms to fluoresce, imaging is easily done with a fast camera. We use a *ProSilica* GigE680 500 frame-per-second CCD camera, mounted on the imaging system in place of the PMT, and record the falling atoms in real time. We monitor the free-fall motion, and tweak the shim coil currents until it resembles a vertical drop (as opposed to a throw) under gravity. The results of this are shown in figure 3.9. The time after switch-off of the quadrupole coils is given above each sub-plot. No advanced triggering was employed in this case, so these times are only rough approximations based on the respective time-stamps of the video frames. We observe an accelerating downward displacement over time, indicating that stray fields have been mostly nulled, however the displacement appears less than expected under gravity (after 10 ms we expect a displacement of 500 μm, and after 20 ms, 2 mm). This can be attributed to either a systematic offset in the given timings, or the non-instantaneous switch-off of the trapping potential. Since the quadrupole field takes around 3 ms to null completely, there will remain a residual trapping potential for this time, acting to inhibit the free fall of the cloud. Importantly, what the free-fall data also tell us is that 10 ms after the quadrupole field is switched off, the atom cloud fills a cross-section of space not much larger than 1mm across. This means that we can allow the atoms to cool in the molasses beams (after the quadrupole coils are switched off) for an ample period of time (10 ms is more than enough) without significant ballistic expansion and the associated loss of signal.

Chapter 4

Raman pulse generation

To induce coherent stimulated Raman transitions (see chapter 2) in our atom cloud we require two mutually phase-coherent 'Raman beams' which are spatially separable. The two Raman beams are required to have a frequency difference equal to the ground hyperfine splitting in rubidium-85 $\omega_{\mathrm{HFS}} = 2\pi \times 3.035732440\,\mathrm{GHz}$ plus a precisely controllable detuning δ_L, and control of the beams' relative phase ϕ_L is also required. It is possible to build such a system with two independent, narrow-linewidth lasers as the Raman beams, mutually phase-locked [55] via a frequency reference, as in [60]. We choose in this work, however, to derive the two Raman beams from a single laser source, and generate the required spatial and spectral splitting using acousto- and electro-optical modulators, as in [12, 61]. With this well-established technique, phase coherence is built-in and the linewidth of the Raman transitions is limited only by the stability of the synthesised microwave frequency.

This chapter describes the experimental setup used to generate Raman pulses. We begin with an overview of the experimental setup, and go on to describe each of its key aspects in detail.

4.1 Overview

A schematic of the experimental setup for generation of Raman pulses is shown in figure 4.1. The setup is summarised in the following paragraph, and a more detailed description of the constituent apparati and procedures is provided in the remaining sections of this chapter.

The continuous-wave laser beam from a high power external cavity diode laser is spatially split into two beams using an acousto-optical modulator (AOM) at 310 MHz. The first-order deflected (and therefore frequency-shifted) output from the AOM is chosen as one of the Raman beams, and is at this stage ready for amplification. The undeflected beam at the output of the AOM is passed through an electro-optical modulator (EOM) operating at $2.725732440 + \delta_L/2\pi$ GHz. This generates two first-order sidebands on the beam, one of which is separated in frequency from the AOM-deflected beam by an amount equal to the ground hyperfine splitting ω_{HFS} plus the detuning δ_L. The carrier wave and unwanted sideband are removed from the optical spectrum of the beam using polarisation optics and frequency-domain interferometry respectively. The frequency and phase difference of the beams are controlled by a microwave frequency synthesiser linked to an I&Q modulator with inputs generated by an arbitrary waveform generator. After spectral preparation, the Raman beams are individually amplified by tapered amplifiers in order to increase the achievable Rabi frequency. They are then combined at a polarising beamsplitter cube with orthogonal polarisations and passed through an AOM, which acts as a fast switch to shape the Raman pulses. The beams are sent to the MOT chamber independently via two optical fibres, and the particular fibre through which each beam is passed can be inverted using a Pockels cell and polarising beamsplitter cube. At the output of the respective fibre, each beam is passed through a refractive beam shaper and focussing lens to produce a 'top-hat' beam profile which is imaged onto the cold atoms. The beams are aligned counter-propagating along the z-axis, and we apply a current I_z to the z-axis shim coils to provide a quantisation field for the transitions.

In the following sections, the respective stages of Raman pulse generation are described in more detail.

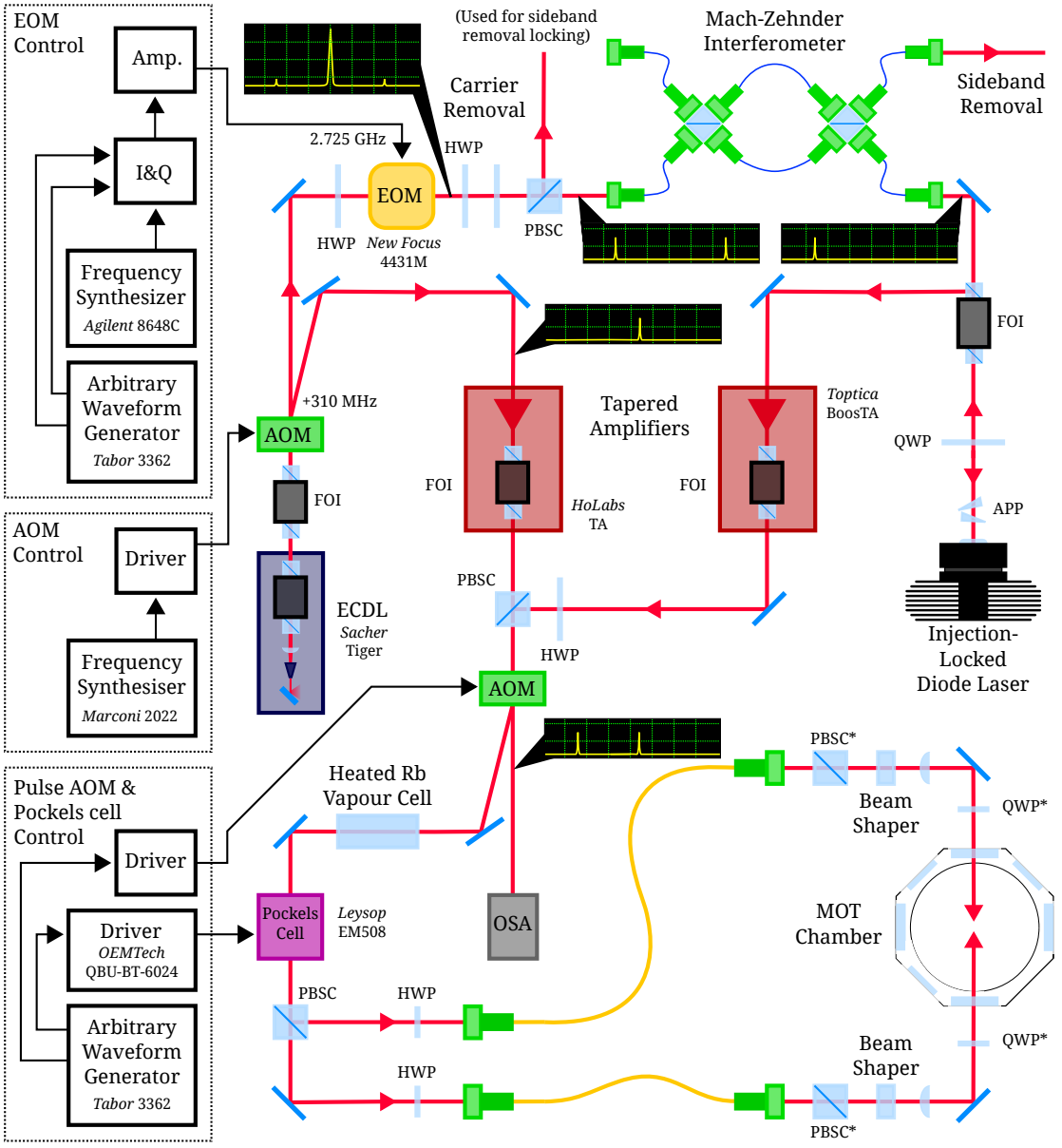

Figure 4.1: Experimental schematic for Raman pulse generation. The annotation bubbles indicate the beam spectrum at the corresponding point. *Present only in the $\sigma - \sigma$ arrangement. QWP – quarter waveplate; HWP – half waveplate; PBSC – polarising beamsplitter cube; APP – anamorphic prism pair; FOI – Faraday optical isolator; BSa – beam sampler; OSA – optical spectrum analyser.

4.2 Laser Beam Source

The initial continuous wave laser beam is derived from a *Sacher* Tiger high power external cavity diode laser. This incorporates an anti-reflection-coated tapered diode chip which emits from its narrow back facet onto an optical grating in the Littrow configuration. The grating disperses unwanted frequency components and reflects the required component back into the tapered chip, which in a single pass amplifies the signal to an optical power of $\sim 200\,\mathrm{mW}$[1] and outputs a beam at $\lambda_0 = 2\pi c/\omega_0 \approx 780.27\,\mathrm{nm}$ at its enlarged output facet. We can adjust this wavelength, which we monitor with an *Advantest* Q8326 wavemeter (accuracy 0.001 nm), by tuning the coarse and fine grating angles (adjustment screws and piezo actuator respectively), and the laser diode current, which is typically around 2.6 A. The laser diode output is collimated and passed through two Faraday optical isolators, both of which are necessary for stability of the diode. Although the Tiger laser offers a higher power than standard diodes in a simple configuration, its mechanical construction does not lend itself to its usability. For example, the vertical and horizontal tuning actuators for the grating are coupled, making tuning the wavelength whilst maintaining constant optical power difficult. However once aligned and tuned we find the device sufficient for our experiments. The Tiger laser is not actively stabilised to a frequency reference, because fluctuations in its output frequency, which translate into variations in the detuning Δ, are on the order of MHz and are therefore not detrimental to the fidelity of stimulated Raman transitions where Δ is typically many GHz.

4.3 Microwave Frequency Shift

The microwave frequency shift is generated by modulation of the optical spectrum, using stable electronically synthesised signals with a common frequency reference, as described in the following.

[1] The manufacturer specifies a maximum output power of 1W, however the highest achieved with this particular device is $\sim 350\,\mathrm{mW}$.

4.3.1 Acousto-Optical Modulator

In order to induce velocity-sensitive transitions in the atom cloud, we require that the two Raman beams are counter-propagating when interrogating the atoms, and a prerequisite for this is that the two beams are spatially separate. To create two separate beams (and to provide a proportion of the frequency shift) we split the output beam from the Tiger laser into two using a *Gooch and Housego* FS310-2F-SU4 acousto-optical modulator (AOM), which is driven continuously at $\Omega_{\mathrm{AOM}} = 2\pi \times 310\,\mathrm{MHz}$. The AOM is driven by a *Marconi* 2022 signal generator in series with a *RFPA* 05 2616 amplifier, which supplies a sine wave at 1.5 W, 310 MHz to the AOM's transducer terminal. Approximately 15% of the optical power is diverted into the AOM's first order and undergoes a frequency shift of +310 MHz. The deflected beam at the output of the AOM is chosen as one of the final Raman field components. It has an angular frequency $\omega_A = \omega_0 + \Omega_{\mathrm{AOM}}$, and is at this stage ready for amplification (see section 4.6).

4.3.2 Electro-Optical Modulator

The majority of the frequency shift is generated by passing the undeflected beam at the output of the AOM through a *New Focus* 4431M electro-optical modulator (EOM) operating at $\Omega_E = \omega_{\mathrm{HFS}} - \Omega_{\mathrm{AOM}} + \delta_L = 2\pi \times (2.725732440 + \delta_L\ \mathrm{GHz})$. The EOM generates a series of spectral sidebands on the beam with angular frequency $\omega_n = \omega_0 + n\Omega_E$, where n ($\neq 0$) is an integer and the amplitude of the respective components becomes negligibly small where $|n| > 1$. At the output of the EOM, the beam spectrum consists of the carrier (ω_0) and two spectral sidebands with angular frequency $\omega_{\pm 1} = \omega_0 \pm \Omega_E$. Taking the difference in angular frequency between the lower sideband at the output of the EOM and the single component comprising the AOM-deflected beam gives

$$\omega_A - \omega_{-1} = \omega_0 + \Omega_{\mathrm{AOM}} - (\omega_0 - \Omega_E) = \Omega_{\mathrm{AOM}} + \omega_{\mathrm{HFS}} - \Omega_{\mathrm{AOM}} + \delta_L = \omega_{\mathrm{HFS}} + \delta_L. \quad (4.1)$$

It follows that we have two spatially separated optical fields with a controllable frequency difference approximately equal to the hyperfine splitting in rubidium, as required for stimulated Raman transitions. The procedures for removing the remaining unwanted frequency components from the EOM output spectrum are described in sections 4.4 and 4.5.

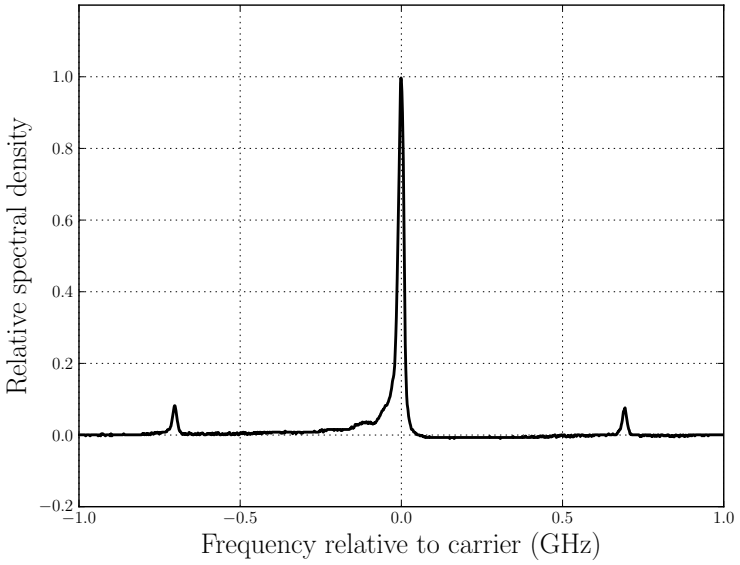

Figure 4.2: Spectral density plot taken from an optical spectrum analyser (OSA) at the output of the EOM. The free spectral range of the OSA is 2 GHz, hence the two peaks at ± 2.725 GHz appear at ± 0.725 GHz.

The electro-optic modulator device consists of a Mangesium Oxide doped Lithium Niobate MgO:$LiNbO_3$ electro-optic crystal positioned inside a microwave cavity. The crystal exhibits a birefringence which is dependent on the electric field inside the cavity, and modulates the phase of one polarisation component of the incoming laser beam at a frequency equal to the applied microwave signal. The EOM is driven by an *Agilent* 8648C frequency synthesiser in series with a *Miteq* AMF-6B-027029-40-37P amplifier, which applies a sine wave at 5W to the input terminal of the microwave cavity. A characterisation of our EOM, from which we state key findings here, can be found in James Bateman's PhD thesis [49].

The relative sideband power available is much lower than expected given the manufacturer-specified ratings. We observe a reduced performance, as if only 44% of the beam is being modulated by the EOM. If this can be attributed to under-performing circuitry, this is equivalent to a microwave cavity quality factor $Q \simeq 124$ (specified in the ratings as 273). It follows that the EOM is probably partially damaged (part of the crystal may have degraded due to excessive power dissipation, for example) however despite this the relative sideband power available is just sufficient for our requirements. Another important characteristic of the EOM is the full-width half-maximum of its cavity resonance.

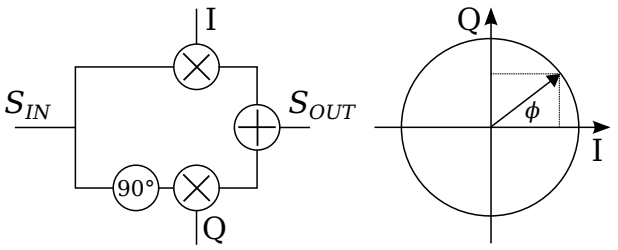

Figure 4.3: The I&Q modulator. Left – block diagram of the device; Right – I vs Q, where the phase shift applied to the signal is $\phi = \arctan(Q/I)$.

This was found to be 22 MHz, which is sufficient for broad detuning around Raman resonances.

4.3.3 Phase & Frequency Control

The frequency generated by the *Agilent* 8648C is computer-controllable with 1 Hz resolution by serial commands via GPIB, however the relatively slow ($\sim$ 40 ms) GPIB interface does not suffice for altering the EOM frequency *during* a (typically $>$ 1 ms) pulse sequence, and the *Agilent* is not capable of varying the *phase* of the two Raman beams without additional apparatus.

We require control of the relative phase ϕ_L (we drop the 'L' subscript for the remainder of this chapter, for simplicity) between the two Raman beams in order to manipulate the trajectory of the atomic state around the Bloch sphere during transitions. To do this we use a *Miteq* in-phase & quadrature-phase (I&Q) modulator in the signal path between the Agilent frequency synthesiser and the Miteq amplifier. A schematic diagram of the I&Q modulator is shown in figure 4.3. The signal $S_{\mathrm{IN}} = \cos(\Omega_E t)$ at the input of the I&Q modulator is split into two paths, one of which is phase-shifted by 90°. The non-shifted ($S_{\mathrm{I}} = \cos(\Omega_E t)$) and shifted ($S_{\mathrm{Q}} = \cos(\Omega_E t + \pi/2) = \sin(\Omega_E t)$) signals are independently mixed with signals generated by a *Tabor* 3362 arbitrary waveform generator, and then summed together at the output of the device. With application of voltages $I = \cos\phi$ & $Q = \sin\phi$ to the respective I&Q mixer inputs, the output signal becomes

$$S_{\mathrm{OUT}} = \cos(\Omega_E t) \times \cos(\phi) + \sin(\Omega_E t) \times \sin(\phi) = \sin(\Omega_E t - \phi) \tag{4.2}$$

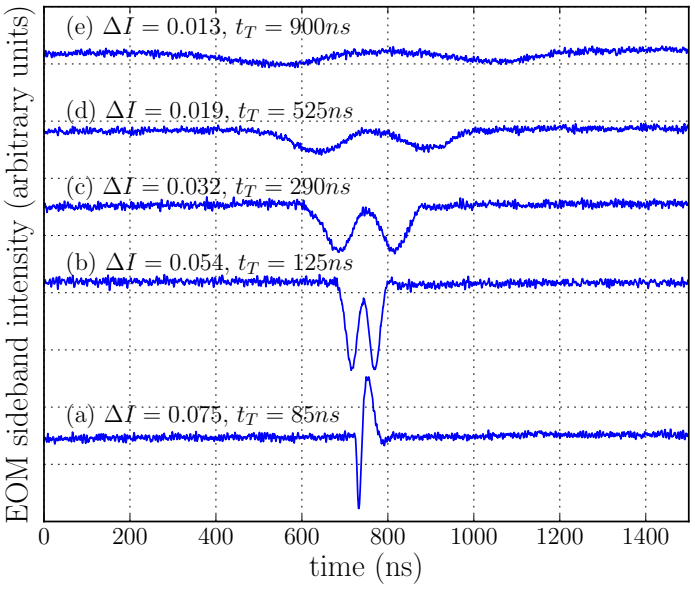

Figure 4.4: Intensity fluctuations of the EOM output sideband measured during a π phase shift by the I&Q modulator. In (a) the phase change $0 \rightarrow \pi$ is applied instantaneously. In the upper traces, the phase is swept from $0 \rightarrow \pi$ over a short time t, where in (b) $t = 20\,ns$, (c) $t = 50\,ns$, (d) $t = 100\,ns$, and (e) $t = 200\,ns$. In each case, ΔI is the intensity contrast $(I_{\max} - I_{\min})/(I_{\max} + I_{\min})$, which quantifies the intensity excursion, and t_T is the duration of the transient.

and the phase of the signal at the output is shifted by $\phi = \arctan(Q/I)$ relative to the input.

From equation 4.2 we see that it is possible to alter the *frequency* of the EOM signal by applying sinusoidal functions to the mixer inputs of the I&Q Modulator. The output signal can be detuned from the input signal in frequency by setting $\phi = \delta_L t$ and applying the required time-varying voltages to the I&Q mixer inputs. This is particularly useful in applications where the frequency must be changed quickly during a pulse sequence, or where chirped pulses are required such as in adiabatic rapid passage (ARP) sequences. In the following paragraphs we investigate the performance of the I&Q modulator.

Due to the nature of the device, which operates by single-sideband modulation [62], there must be a non-zero signal on one of the I&Q ports for any signal to be output by the modulator. When performing a π phase shift from any starting phase, both I&Q voltages pass through zero simultaneously (easily visualised with figure 4.3), and as they do so the output is instantaneously switched off. This leads to transients in the intensity of the EOM sideband during π phase shifts, as shown in figure 4.4(a). We also show in figure

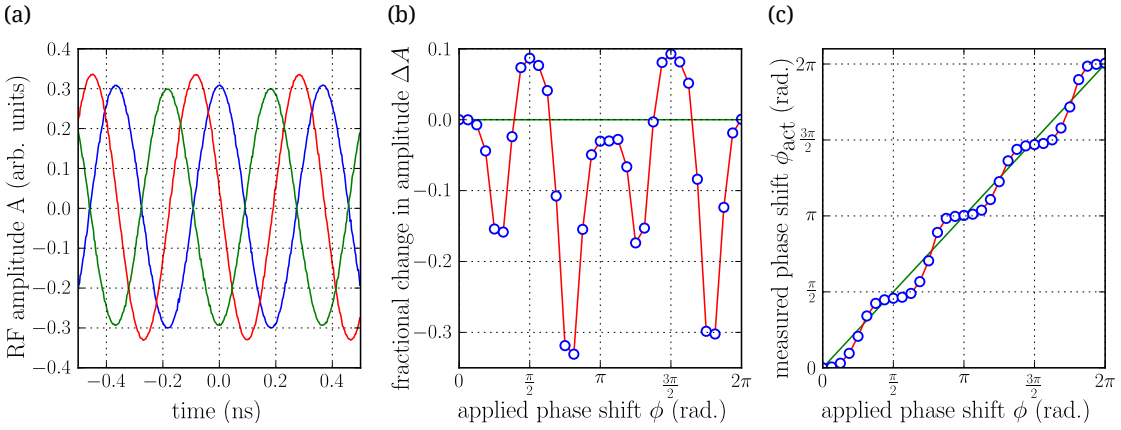

Figure 4.5: RF signals measured directly at the output of the I&Q modulator. (a): Raw data for phase shifts $\phi = 0$ (blue), $\phi = \frac{\pi}{2}$ (red), and $\phi = \pi$ (green). (b): Output RF amplitude as a function of the applied phase shift ϕ. (c): Output *measured* phase ϕ_{act} as a function of the applied phase shift ϕ. In the latter two the dashed line represents the ideal behaviour.

4.4 how these transients vary when the phase is swept from $0 \rightarrow \pi$ for a range of sweep-durations t. In the case where the phase is changed instantaneously, we observe the largest intensity excursion ($\Delta I = [I_{\text{max}} - I_{\text{min}}]/[I_{\text{max}} + I_{\text{min}}] = 0.075$), and the shortest-lived transient ($t_T = 85\,\text{ns}$). Since ΔI and t_T are small in this case, we expect there to be no significant unwanted effects on the Raman transition during instantaneous phase changes. Sweeping the phase over time reduces the intensity excursion ΔI (increasingly with increasing t), but extends the duration t_T of the transient, so we choose not to employ phase sweeps in the Raman experiments of the following chapters.

As a further diagnostic, we used an *Agilent* 86100C DCA fast oscilloscope to directly monitor the 2.726 GHz signal at the output of the I&Q modulator at a range of different applied phase shifts. Figure 4.5 a shows three RF waveforms at different values of the phase shift ϕ. With these data, we were able to measure the *actual* phase shift and amplitude of the modulated RF signal directly. Figure 4.5 b shows the fractional change in RF output amplitude ΔA as a function of the phase shift ϕ. This is calculated by $\Delta A(\phi) = [A(\phi_0 + \phi) - A(\phi_0)]/A(\phi_0)$. It is important to note that in these scans the *total* phase shift applied to the signal is $\phi_0 + \phi$, where we set the offset phase $\phi_0 = \arctan(Q_0/I_0) = \pi/4$, and therefore $I_0 = Q_0 = 1/\sqrt{2}$. We can see from the figure that the amplitude depends upon ϕ. The maximum fractional amplitude excursion is $\Delta A = -0.33$, which occurs at $\phi \approx 3\pi/4$, and there is a similar reduction at $\phi \approx 7\pi/4$. These points represent regions where $Q_0 + Q \approx 0$. We also observe amplitude changes

of around $\Delta A = 0.09$ at $\phi \approx \pi/4$ and $5\pi/4$, where $I_0 + I \approx 0$. Figure 4.5 c shows the measured phase shift ϕ_{act} as a function of the applied phase shift ϕ. We can see from the plot that the relationship is non-linear. The curve exhibits plateau regions around integer multiples of $\pi/2$, and at odd-integer multiples, $\phi_{\text{act}} \neq \phi$.

This behavior is likely to be due to non-linearities in the I&Q mixer stages within the device. We plan to calibrate the signals applied to the device to correct for these non-linearities in the future, however since these data were taken late on in the writing of this thesis, we simply use them to adjust numerical simulations, for example in chapter 6, where phase shifts are used in composite Raman pulse experiments.

4.4 EOM-Output Carrier Removal

As shown in figure 4.2, the beam contains unwanted spectral components after passing through the EOM. The carrier, at angular frequency ω_0, must be removed from the beam in order to avoid single photon coupling to the intermediate level during Raman transitions. Here we achieve carrier removal by using simple polarisation optics at the output of the EOM, along with feedback to a liquid crystal cell for stabilisation (see figure 4.6). A paper on this technique has been published (Cooper *et al* [63]), and the following is a brief digression into the theory behind it.

The electro-optic modulator acts on only one polarisation component of the linearly polarised input beam. We assume this to be the vertical component, and write the EOM output beam in Jones matrix notation as

$$\mathbf{E} = A \begin{pmatrix} e^{i(\omega_0 t + m\cos\Omega_E t)}\cos\theta \\ e^{i\omega_0 t}\sin\theta \end{pmatrix}, \tag{4.3}$$

which, when expanded using the Jacobi-Anger identity can be written as

$$\mathbf{E} = A \begin{pmatrix} J_0(m)\cos\theta \\ \sin\theta \end{pmatrix} e^{i\omega_0 t} + A \begin{pmatrix} \cos\theta \\ 0 \end{pmatrix} e^{i\omega_0 t} \sum_{n\neq 0} i^n J_n(m) e^{in\Omega_E t}. \tag{4.4}$$

The first term represents the carrier wave, and the second represents the series of side-bands each denoted by their index n. $J_n(m)$ is the nth order Bessel function of the

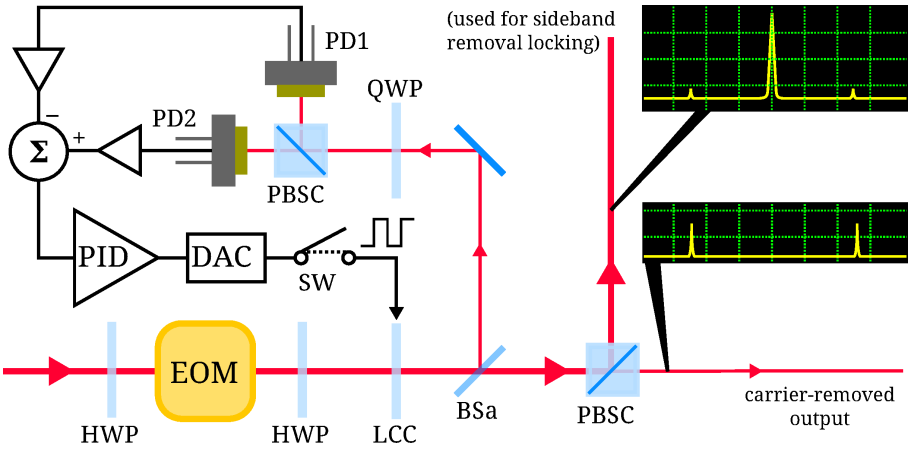

Figure 4.6: Optics and feedback electronics for removing the carrier from the EOM output spectrum. LCC – liquid crystal cell; QWP – quarter waveplate; HWP – half waveplate; PBSC – polarising beamsplitter cube; BSa – beam sampler; PD – photodiode; DAC – digital-to-analogue converter; SW – switch.

first kind as a function of the modulation depth m of the EOM which is $\sim \frac{\pi}{5}$. If a polarising beamsplitter is placed in the beam path with its transmission axis orthogonal to the polarisation of the carrier, the transmitted beam will comprise only a reduced proportion of the sidebands, given by

$$\mathbf{E}_{\mathbf{sidebands}} = A \begin{pmatrix} -\sin\varphi \\ \cos\varphi \end{pmatrix} \cos\theta \sin\varphi \sum_{n\neq 0} i^n J_n(m) e^{i(\omega_0 + n\Omega_E)t}, \tag{4.5}$$

where $\varphi = \arctan(J_n(m)/\tan\theta)$ is the angle between the polarising beamsplitter's transmission axis and the modulation axis (vertical). It follows that the power remaining in the first order sidebands is equal to

$$P_1 = A^2 \cos^2\theta \sin^2\varphi J_1(m)^2 = \frac{A^2 \cos^2\theta J_1(m)^2}{1 + (J_0(m)\cot\theta)^2} \tag{4.6}$$

which is maximised where $\cos^2\theta = 1/(1 + |J_0(m)|)$. From this we can see that there is a substantial loss of power ($\sim 75\%$) in the sidebands after carrier-removal, however the spectral purity of the beam is maintained, and power can be recovered by optical amplification of the low-power sidebands (see section 4.6).

In practice, unwanted birefringence in the EOM crystal causes the polarisation of the output to become elliptical, thus reducing the ability of the polarising beamsplitter to remove the carrier from the spectrum. This birefringence is temperature-dependent and varies over periods of minutes, therefore unless we maintain a constant temperature in

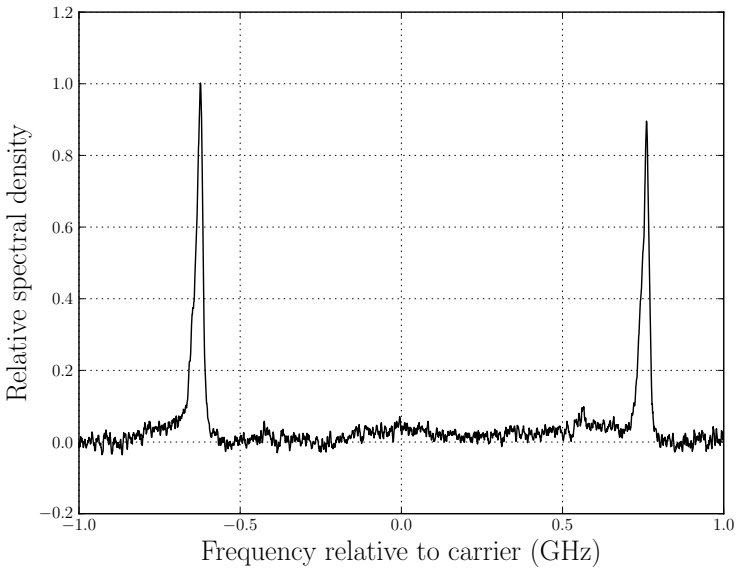

Figure 4.7: Spectral density plot taken from an optical spectrum analyser after removal of the carrier from the EOM output spectrum. The free spectral range of the OSA is 2 GHz, causing the sidebands (±2.725 GHz) to wrap.

the lab, active correction of the output polarisation is required to maintan low carrier power. This is achieved experimentally by using an E7 liquid crystal cell in the beam path as a variable phase retarder. The phase delay of one polarisation component passing through the cell is controlled by applying a variable-voltage AC signal at 1 kHz and 1-3 Volts, generated by an *Arduino* micro-controller and digital-to-analog converter chip, to the electrodes of the cell. The polarisation spectroscopy based Hänsch-Couillaud [64, 65] method is used to generate an error signal which has a finite gradient and crosses zero where the polarisation of the ouptut is linear, as described in previous work [65], and locking can be maintained for periods of hours. Carrier suppression of 30dB is achievable with this technique, thus effective removal of the carrier is achieved as shown in figure 4.7.

4.5 EOM-Output Sideband Removal

Once the carrier has been removed from the beam spectrum (Section 4.4), we are left with two sidebands at $\omega_0 \pm \Omega_E$. One sideband constitutes one of the Raman beams (this lower-frequency beam is known as the 'anti-Stokes' field), and the other is an off-resonant

field which, although it does not induce unwanted atomic transitions, induces a light-shift in the energy levels. For a pulse sequence consisting of equal-intensity pulses this light-shift is merely a constant, correctable frequency offset, however where the pulse intensity is varied, the level shift is more difficult to correct. The light shift affects Raman transitions within different Zeeman sublevels differently, such that a larger light shift accompanying the Zeeman splitting is observed for higher-intensity pulses (see section 5.1.2). It is possible to nullify this light-shift by adjusting the magnetic field, but its behaviour becomes more difficult to predict when multiple laser frequency components are present. With this in mind, and with a view to increasing the available power in the anti-Stokes frequency component (upon amplification, power must be shared between all present frequency components), we remove the off-resonant sideband from the beam spectrum. This is done using a Mach-Zehnder interferometer. A paper on this technique has been published (Cooper *et al* [66]), and we describe its implementation in our setup in the following. It is important to note that we here re-use algebraic variables (δ, Ω *etc*) which do not necessarily correspond to those defined previously.

Within a Mach-Zehnder interferometer, phase difference accrues between the two interferometer arms according to $\delta(\omega) = \omega\eta(\omega)\Delta l/c$, where $\eta(\omega)$ is the refractive index of the medium and Δl is the length difference between the arms. For two frequency components separated by an angular frequency $\Delta\Omega$ we have a difference in phase difference, assuming a constant dispersion, given by

$$\Delta\delta(\Delta\Omega) = \frac{d\delta(\omega)}{d\omega}\Delta\Omega = \frac{\Delta l}{c}\left[\eta(\omega) + \omega\frac{d\eta}{d\omega}\right]\Delta\Omega = \frac{\pi}{\omega_s}\Delta\Omega \tag{4.7}$$

where ω_s is the frequency difference between components separable by the interferometer, given by

$$\omega_s = \frac{\pi c}{\Delta l\left[\eta(\omega) + \omega\frac{d\eta}{d\omega}\right]}. \tag{4.8}$$

At the output port of the interferometer, the transmitted intensity of an input frequency component will vary as $|1 - e^{i\delta(\omega)}|^2$, and in our case $\Delta\Omega$ in equation 4.7 is equal to $2\Omega_E$, so if we choose the path length difference such that $\omega_s = 2\Omega_E$, we can separate the two EOM-output sidebands.

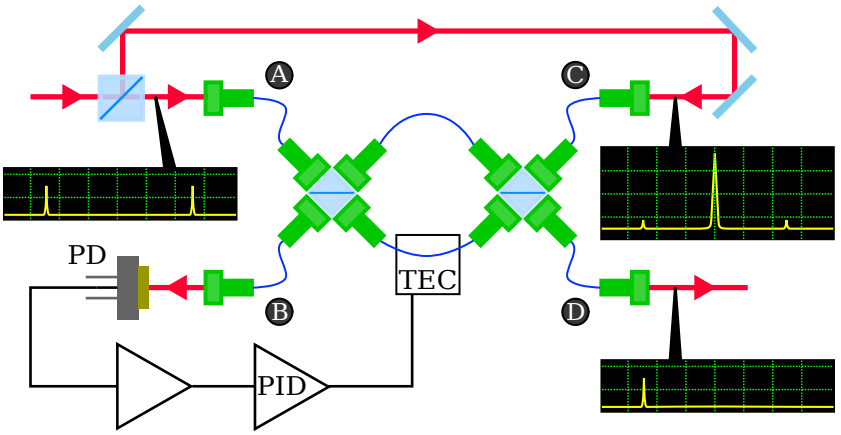

Figure 4.8: Optics for removing off-resonant sideband from the EOM output spectrum. TEC – thermo-electric cooler; PD – photodiode; PID – proportional-integral servo. The annotation bubbles indicate the beam spectrum at the corresponding point.

4.5.1 Mach-Zehnder Interferometer

We use a custom-made fibre optic Mach-Zehnder interferometer (figure 4.8) from *Oz Optics*, which is constructed with polarisation-maintaining fibres aligned to non-polarising beamsplitter cubes. The inner arms of the interferometer differ in length by ~ 19.5mm, equivalent to $\Delta l = \pi c/\omega_s \approx 27.5$mm in free space, with the longer arm length roughly 15cm. The interferometer is highly sensitive to changes in temperature in the lab, so it must be actively locked to the desired phase difference in order to achieve long-term stability. This could be achieved by feedback to a stress-inducing piezo-electric transducer on one arm of the interferometer, however we choose to stabilise the device by controlling the temperature. To generate a suitable error signal we take the carrier light removed from the main beam using the polarising beamsplitter cube as described in section 4.4, and pass it backwards through the secondary output port (C) of the interferometer. A photodiode is placed at the secondary input port (B) to monitor the backwards-transmitted carrier intensity, which is determined by $|1 - e^{i\delta(\omega_{-1}+\Omega_E)}|^2$, where $\delta(\omega_{-1}+\Omega_E) = \delta(\omega_{-1}) + \Delta\delta(\Omega_E)$. From equation 4.7, for a modulation frequency $\Omega_E = \omega_s/2$, we achieve an error signal equal to $|1 - e^{(\delta(\omega_{-1})+\frac{\pi}{2})}|^2$, which has a finite gradient and is equal to half of its maximum value where $\delta(\omega_{-1}) = 0$ and $\delta(\omega_{+1}) = \pi$, *i.e.* where the unwanted sideband is minimised at the output port. The photodiode current is amplified and passed into an *Arduino* micro-processor, where a proportional-integral (PI) feedback signal is generated in software. Feedback is applied in the form of

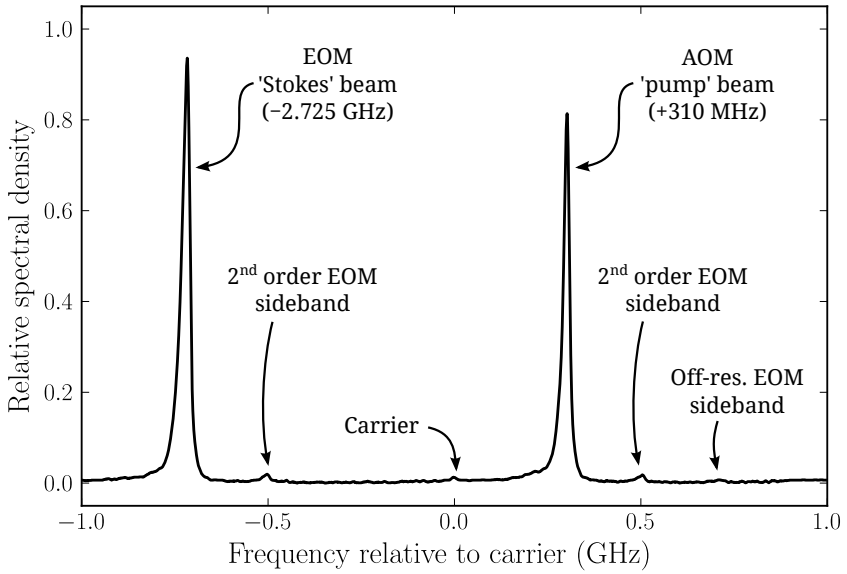

Figure 4.9: Complete spectrum of the combined Raman beams measured with an optical spectrum analyser (OSA) after spectral filtering of the carrier and off-resonant EOM sideband, and power amplification. The free spectral range of the OSA is 2 GHz, causing some components to wrap.

a square-wave with variable duty-cycle to the gate pin of a FET which switches current to a Peltier thermo-electric cooler (TEC).

The sideband suppression achieved with the stabilised Mach-Zehnder is illustrated in figure 4.9, where we plot the spectrum of the combined Raman beams after carrier and EOM sideband removal, and amplification (see section 4.6). We can achieve sideband extinction of ~ 30 dB, limited by the error in the fibre arm length difference and alignment of the attached beamsplitter cubes. The interferometer remains stabilised for periods of hours, and is subject to slight drift due to slow variations in carrier intensity. This could in principle be corrected by monitoring the signal intensity at port C with a beam sampler and photodiode, and adjusting the error signal accordingly.

4.6 Power Amplification

After spectral preparation, the AOM and EOM output beams have optical powers of less than 5mW, which is insufficient for high Rabi frequency Raman experiments. Pre-amplification and 'cleanup' of the EOM output beam is required between the carrier removal and sideband removal stages, due to insufficient optical power and poor spatial beam-quality. This is achieved by injection locking a laser diode (with no external

cavity), which is thermally regulated and controlled as described in section 3.2.1. An anamorphic prism pair (APP in figure 4.1) is placed at the input to the diode's aspheric collimating lens to aid mode-matching. The output beam is a spectrally pure copy of the input, with optical power around 12mW (diode DC current 110mA) and a cleaner spatial beam profile which is suitable for coupling into the fibre-optic Mach-Zehnder interferometer. At the output of the interferometer, with which we can achieve 40% throughput, the sideband power is approximately 3mW.

The two Raman components are individually amplified by tapered amplifiers. We employ a *Toptica* BoosTA amplifier, which outputs $\sim$ 300mW at maximum current with 3mW seed power for the EOM beam, and an in-house built *HOLabs* tapered amplifier, which outputs up to $500mW$ with 5mW seed power for the AOM beam. After amplification, the two beams are combined with orthogonal polarisations at a polarising beamsplitter cube. Figure 4.9 shows the spectrum of the combined Raman beams after spectral filtering (see sections 4.4 and 4.5) and amplification. Note that the second-order EOM sidebands are visible on the Raman beam spectrum. These extra off-resonant spectral components will lead to minor additional light shifts of the atomic levels, although these are found to be negligible in experiments.

Although it is not always strictly necessary, we employ a heated Rb vapour cell to absorb any resonant amplified spontaneous emission (ASE) from within the Raman beams. This ASE emerges from the Tiger laser itself, and also in part from the tapered amplifiers. The heated vapour cell is placed after the pulse-shaping AOM, which we describe below.

4.7 Pulse Generation

To generate the Raman pulses we pass the combined continuous-wave Raman beams through a *Gooch and Housego* M080-2B/F acousto-optical modulator, which is driven by an *AA opto-electronic* MDA80-B4 80 MHz VCO and amplifier. Pulses are applied to this AOM by a computer-programmed *Tabor* 8024 arbitrary function generator, and the 1st order diffracted beam at the output forms the Raman pulse. We achieve a coupling efficiency into the 1st order of 0.85 with a collimated beam, and the 90% rise/fall time of the pulse as measured with a *Thorlabs* DET10A photodiode is 365ns, as illustrated in figure 4.10. This rise/fall time means that our Raman pulses do not have the desired

'rectangular' temporal shape, but instead exhibit smoothed edges, which at short pulse times ($t < 5\,\mu s$) will form a significant portion of the pulse. Furthermore, there appear to remain long ($> 1\,\mu$s) 'tails' after switching. This is clear from the non-zero intensity apparent in figure 4.10 a after the 2nd dashed red line. Such effects will impact the behaviour of Raman transitions, and are to be considered when analysing performance. The rise/fall time of the AOM could be decreased by reducing the width of the Raman beam passing through the AOM crystal, thus making the acoustic wave traverse the beam in a shorter time. The intensity of the Raman pulse can be varied by changing the voltage applied by the function generator.

4.8 Direction Switching

For some of the atom interferometry experiments performed in this work, we require the ability to invert the relative directions of the two Raman beams impinging on the atom cloud. This allows us to move out of the closed momentum basis and impart a momentum greater than $\hbar(\mathbf{k}_{L1} - \mathbf{k}_{L2})$ to the atom during a pulse sequence. To invert the

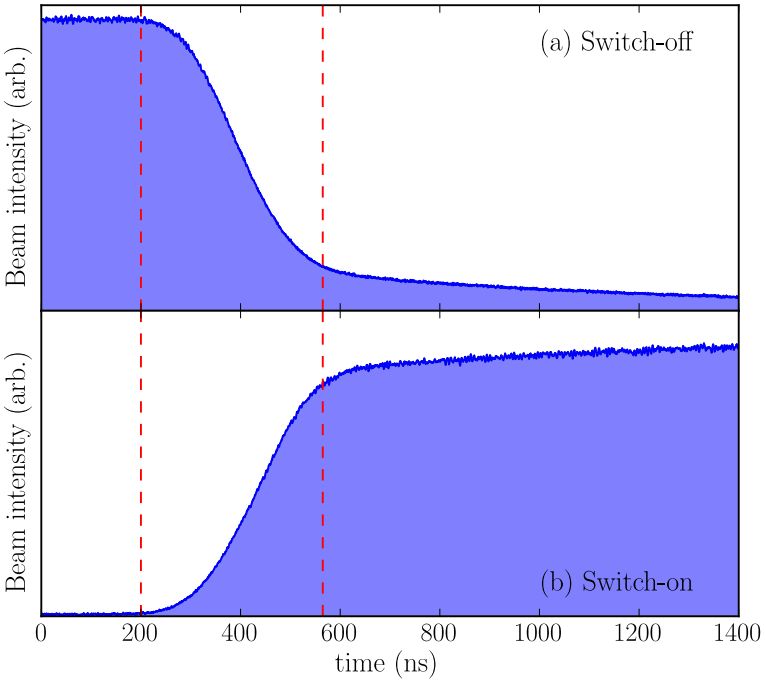

Figure 4.10: Intensity in the 1st-order diffracted beam of the Raman-pulse AOM as a function of time, as measured with a fast photodiode for (a) switch-off $5 \rightarrow 0V$ and (b) switch-on $0 \rightarrow 5V$. In both plots, the switch occurs (1st red line) at 200 ns and the 90% rise/fall mark (2nd red line) is at 565 ns, indicating a rise/fall-time of 365 ns.

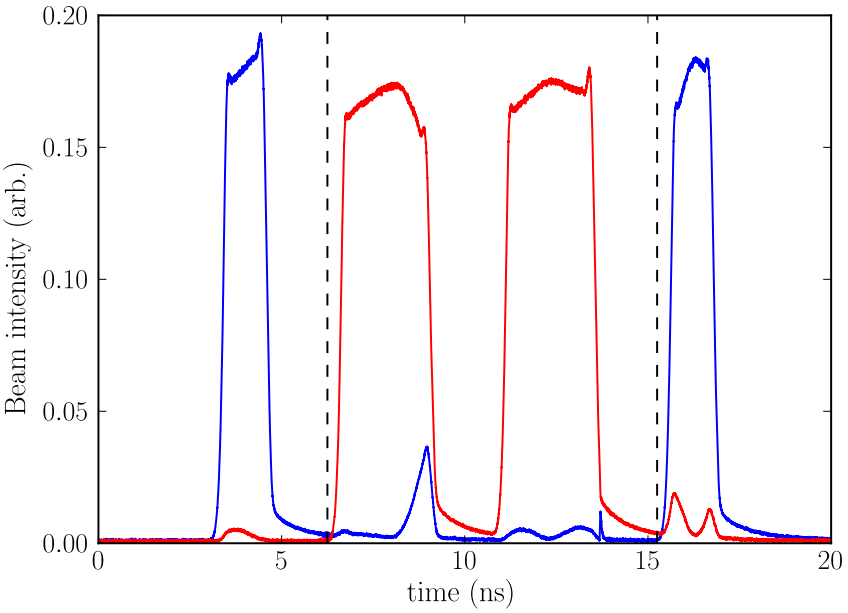

Figure 4.11: Measured intensity at the output of the polarising beamsplitter cube after the Pockels cell, during a sample AOM pulse sequence for a single linearly polarised beam. The Pockels cell is switched on between the two dashed vertical lines. The red curve corresponds to one output, and the blue to the (orthogonal) other.

relative beam orientation we pass the combined Raman beams with orthogonal linear polarisations (one vertical, the other horizontal), through a Pockels cell, which upon recieving a high-voltage pulse to its electrodes, rotates the polarisation of each beam by 90°. The two Raman beams are then separated according to their polarisation along each of the two orthogonal output ports of a polarising beamsplitter cube (PBSC). and passed along single-mode optical fibres toward the MOT chamber.

4.8.1 Pockels Cell

The Pockels cell we employ is a *Leysop* EM508 KD*P (Potassium Dideuterium Phosphate) cell, whose half-wave voltage at 780 nm is ~ 4.5 kV. It is driven by an *OEM Tech* QBU-BT-6024 Pockels cell driver, which can apply HV pulses up to 6 kV synchronously with an external 5 V signal, which we generate with a computer-programmed *Tabor* 8024. The rise time of the Pockels cell according to the manufacturer is typically < 0.5 ns.

We characterise the switching performance of the Pockels cell by measuring the intensity at the output of each port of the PBSC for a single input polarisation, as shown in figure 4.11. We apply a sequence of four Raman beam pulses, with polarisation aligned to one

axis of the PBSC, to the Pockels cell. A 4.5 kV signal is applied to the cell before the 2nd pulse, and is later switched off after the 3rd, as indicated by the dashed lines in the figure. We therefore expect the 2nd and 3rd pulses to exit from the opposite PBSC port to the 1st and 4th. The most important characteristic is the *extinction* provided by the cell between output ports, and figure 4.11 shows this to be close to 100%. Interestingly, however, there appear to be significant non-linearities in the switching extinction. Some of the light emerges with the incorrect polarisation for short periods during each pulse, including when the Pockels cell is switched off. Whilst the reasoning behind this behaviour is not understood, it constitutes another factor to be considered when analysing the behaviour of our Raman transitions.

4.9 Beam Shaping

The effective Rabi frequency Ω_{eff} in Raman transitions (see section 2.1.5) depends strongly on the local intensity of the laser beams. An atom cloud illuminated by a Gaussian beam, for example, will exhibit a higher Rabi frequency at the centre of the beam than at the edges, and, depending on the extent of this intensity gradient, dephasing of the atomic states will occur during a Raman pulse. Therefore, to avoid dephasing in Raman pulses we would like to work with a spatially homogeneous beam across the extent of the atom cloud, which after a typical period of ballistic expansion is ~ 1 mm across (see section 3.6.2). There are two routes to a homogeneous beam: first, we could employ large-radius (> 10 mm) Gaussian beams such that the atom cloud 'sees' only the central, relatively homogeneous region of the beam, and increase the total laser power to maintain a high intensity; or second, we could use beam-shaping optics to generate a homogeneous profile. The former allows for spatially homogeneous, *collimated* Gaussian beams which are essential for many large area atom interferometry (and in particular *gravimetry* [12]) experiments, however the required extra laser power, which scales as the radius squared, is not achievable in our system. The latter approach offers the possibility of generating a small, flat-top profile in which all the laser power is contained. The disadvantage of this technique for many interferometry experiments is that typically the beam profile is only spatially homogeneous along a small longitudinal focal region

of the beam[2], however this is not a problem in our experiments, so we proceed with this approach.

To shape the Raman beams, we use a refractive, graded-index *Topag Lasertechnik* GTH-4.2.2 Gauss-to-top-hat beam shaper, as shown in figure 4.12, in the path of each beam. The GTH-4.2.2 converts a spatially-filtered, collimated Gaussian beam of $1/e^2$ diameter 4mm to a square top-hat beam in the focal plane of a spherical lens, which is placed after the beam-shaper. The side-length l of the flat-top profile is dependent on the focal length f of the lens, by the relationship $l = f \times 2.2/1000$ where l and f are in mm. The spatial beam profiles of the spectally-filtered (un-collimated) and $f = 400\,\text{mm}$ flat-top beams are shown in figure 4.13. In the Raman experiments of the following chapters, we use lenses with $f = 750\,\text{mm}$, which according to the specifications should give approximately square ($l_x \simeq l_y = l$) top hat beams with side $l = 1.65\,\text{mm}$. In practice, we observe different sizes, namely $l_1 = 1.7\,\text{mm}$ and $l_2 = 1.4\,\text{mm}$, and this leads to different intensities $I_{1,2} = P_{1,2}/l_{1,2}^2$ where the beam powers $P_{1,2}$ are equal (by a factor of $I_2/I_1 \approx 1.5$).[3] Since the light shift due to beam a is dependent on its intensity I_a, we expect that the resultant effect will be a constant light shift. In experiments where the beam directions are swapped, this may be a problem, however in our particular arrangement, simulations suggest that an imbalance of intensities of this order has only a small effect on the overall light shift. The spatial quality of the top-hat profile is extremely sensitive to the quality and characteristics of the input beam. Careful pre-spatial-filtering is essential for a good top-hat profile, and interestingly it does not suffice to use the collimated output of a single-mode optical fibre.

[2] Generating a collimated flat-top beam using beam-shaping optics is difficult and not considered here.

[3] Note that here $l_{1,2}$ indicate the side lengths of the two different square-profile beams, and in figure 4.13 $l_{x,y}$ indicate the side lengths of a single beam in the x and y directions, where $l_x \simeq l_y$.

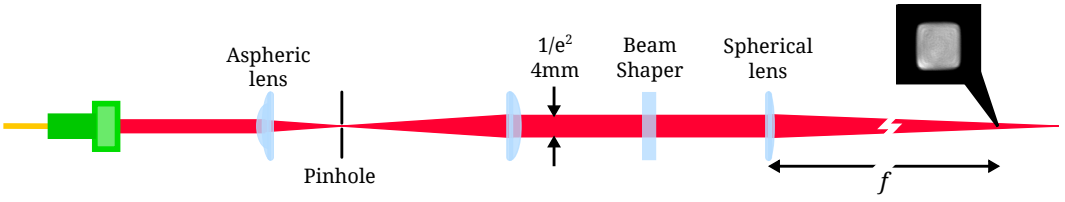

Figure 4.12: Optics for shaping each Gaussian Raman beam into a top-hat. The beam is collimated at the output of an optical fibre and then passed through a spatial filter. It is re-collimated with a $1/e^2$ diameter $d = 4\,\text{mm}$, then passed through a polarising filter (PBSC), before the GTH-4.2.2 beam shaper. The top-hat beam is then formed in the focal plane of the subsequent spherical lens.

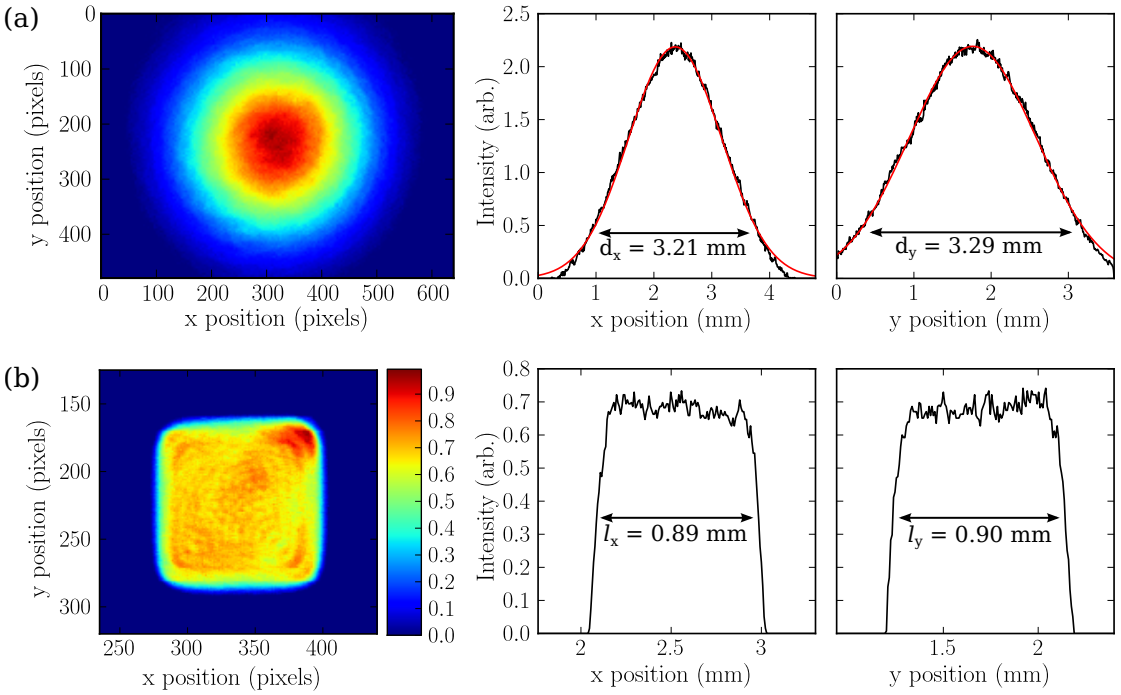

Figure 4.13: Spatial laser beam profiles measured with a CCD camera. (a) is the beam after the spatial filtering pinhole, and (b) is the top-hat beam in the focal plane of the lens with $f = 400\,\text{mm}$. The 1D plots on the right are slices taken through the centre of the beam perpendicular to the corresponding axis, and in (a) each red line is a least-squares fit to a Gaussian function. $d_{x,y}$ are the horizontal and vertical $1/e^2$ diameters as determined by the fits, and $l_{x,y}$ are the horizontal and vertical side-lengths of the top hat.

To align each Raman beam onto the atom cloud, we use a CCD camera and zoom lens system to image the MOT directly along the Raman beam path by looking into the heavily attenuated beam, and adjust steering mirrors to overlap the beam with the MOT cloud. The beams are aligned with their wavevectors $\mathbf{k}_{L1,L2}$ along the z-axis, that is, (anti-)parallel to the magnetic field created at the MOT location by the z-axis shim coils (see figure 3.4). The z-axis is therefore taken to be quantisation axis of the Raman transition, and we can control Zeeman splitting in the atomic sublevels by tuning the shim coil current I_z. This is characterised in the next chapter.

Part III

Results

Chapter 5

Raman pulse characterisation

With the MOT and Raman systems in place, we are able to realise two-level, velocity-sensitive manipulation of cold rubidium-85 atoms. Raman pulses, with their associated momentum recoils, form the beamsplitters and mirrors of our rubidium interferometer, used in chapter 7 to generate a velocity-selective excitation.

This chapter details the demonstration and characterisation of coherent Raman transitions in our system. We initially investigate *co-propagating*, velocity-insensitive Raman transitions, and in this arrangement characterise the Zeeman structure, light shifts, and Rabi frequency. We then explore the inherently more inhomogeneous *counter-propagating*, velocity-sensitive arrangement, in which we perform temperature measurements via Raman velocimetry. Particular attention is paid to *dephasing* in Raman pulses, which we attempt to actively repress in chapter 6 by way of composite pulses.

5.1 Velocity-insensitive Raman pulses

In the co-propagating arrangement, Raman transitions can be treated in the manner introduced in section 2.1, but with the momentum-dependent terms removed from the equations. This results in transitions which are not Doppler-broadened, and therefore suffer less dephasing at low Rabi frequencies, because the detuning δ is not sensitive to the atomic velocity. Without momentum-dependence, we simply write the ket states for the three level system as $|1\rangle = |5S_{1/2}, F = 2\rangle$, $|2\rangle = |5S_{1/2}, F = 3\rangle$, and $|3\rangle = |5P_{3/2}, F' = 2, 3\rangle$, where the corresponding state amplitudes are c_1, c_2, and c_3.

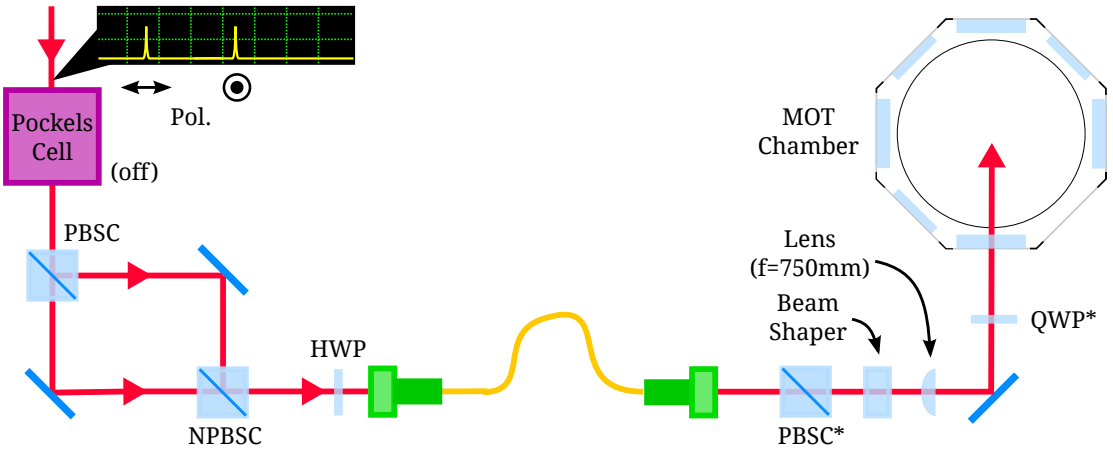

Figure 5.1: Optical setup (after spectral preparation – see figure 4.1) used to produce co-propagating Raman beams. *Present only in the $\sigma - \sigma$ arrangement. QWP – quarter waveplate; HWP – half waveplate; (N)PBSC – (non-)polarising beamsplitter cube.

Since the Zeeman splitting, light-shifts, and Rabi frequency of the Raman transition behave in the same way in both the co- and counter-propagating arrangements (except for the extra momentum-dependent detuning in the latter), we can gain a good understanding of the behaviour of both by characterising the system in the simpler case of co-propagating beams. Experimentally, we produce co-propagating beams by making a small adjustment to the optical setup described in the previous chapter, as illustrated in figure 5.1. Both beams are sent to the MOT chamber through the same optical fibre, and their relative polarisations are controlled by the half waveplate at the input, and the quarter waveplate and polarising beamsplitter cube at the output. We use the arm which provides a top-hat beam with side length $l_2 = 1.4\,\text{mm}$, and in this arrangement we can balance the intensities $I_{1,2}$ simply by equalising the beam powers $P_{1,2}$.

5.1.1 Zeeman structure

In this section we characterise the magnetic field dependent splitting of the Zeeman sublevels. By testing this, we can gain insight into how to adjust the magnetic fields in order to achieve Zeeman degeneracy, and calibrate the shim coil current dependence of the resultant field. Figure 5.2 shows co-propagating Raman transitions in the $\sigma^+ - \sigma^+$ arrangement at different values of the z-axis shim coil current I_z (see figure 3.4), which is proportional to the magnetic field strength B_z along the axis of the Raman beams. In each of the subplots in figure 5.2 a, the detuning δ_L is scanned whilst Δ, the laser power and the pulse length (all given in the figure caption) are held constant. The

relatively long pulse length was chosen so that the measurements reflected the *steady-state* (dephased – see section 5.1.4) hyperfine populations. Each point is an average over 8 shots, and each scan takes approximately 7 minutes. The red curve in each plot is a 4-point moving average of the data. Figure 5.2 b shows the detuning (shift in position of the peak) of each Zeeman sublevel as a function of I_z, where the points are measured values and the lines are weighted least-square fits to the data. The peak positions (and errors thereof) are judged by eye, taking into consideration their width, shape and visibility. We observe linearly increasing splitting of the 5 Zeeman sublevels with increasing shim coil current, where Zeeman degeneracy occurs at $\sim 74\,\mathrm{mA}$.

The peak $|c_2|^2$ values in each scan indicate the resonant steady-state populations of the levels. In the lower plots 5.2 a iii & iv we observe steady-state populations for each Zeeman sublevel of ~ 0.1, which is expected in the case where the atoms are evenly distributed across the 5 sublevels. The upper subplot 5.2 a i shows a Zeeman-degenerate steady state population of ~ 0.45. In the absence of inhomogeneities we would expect this to be 0.5, however since the Zeeman levels have different coupling strengths due to their different dipole matrix elements, there are multiple resonant Rabi frequencies Ω_R present during the transition. This limits the maximum transfer fraction (which is essentially the *average* transfer fraction over the 5 sublevels for an optimal pulse length) to around 0.96 and therefore sets the maximum steady-state population at half of this value. The remaining difference can be made up by other sources of dephasing, which are discussed along with the above in section 5.1.4.

Prior to performing this scan, the magnetic fields in the x and y directions were calibrated to allow Zeeman degeneracy by iteratively adjusting I_x and I_y (the x and y shim coil currents) and measuring the Zeeman splitting in the same way as figure 5.2. With a strong magnetic field perpendicular to the equal-circularly-polarised Raman beams, we observe suppression of the Zeeman peaks shown in figure 5.2. These peaks are replaced by peaks attributed to Raman transitions between $|2, m_F\rangle \leftrightarrow |3, m_F \pm 1\rangle$, as discussed in [67]. This is explained by the relative orientation of the magnetic (quantisation) field vector and rotational plane of the beams' polarisation vectors. If the magnetic field vector is orthogonal to the wavevector of the Raman beams, then for dipole transitions the light is effectively *linearly* polarised, with components both parallel *and* perpendicular to the quantisation axis. This is described by the two-beam polarisation state

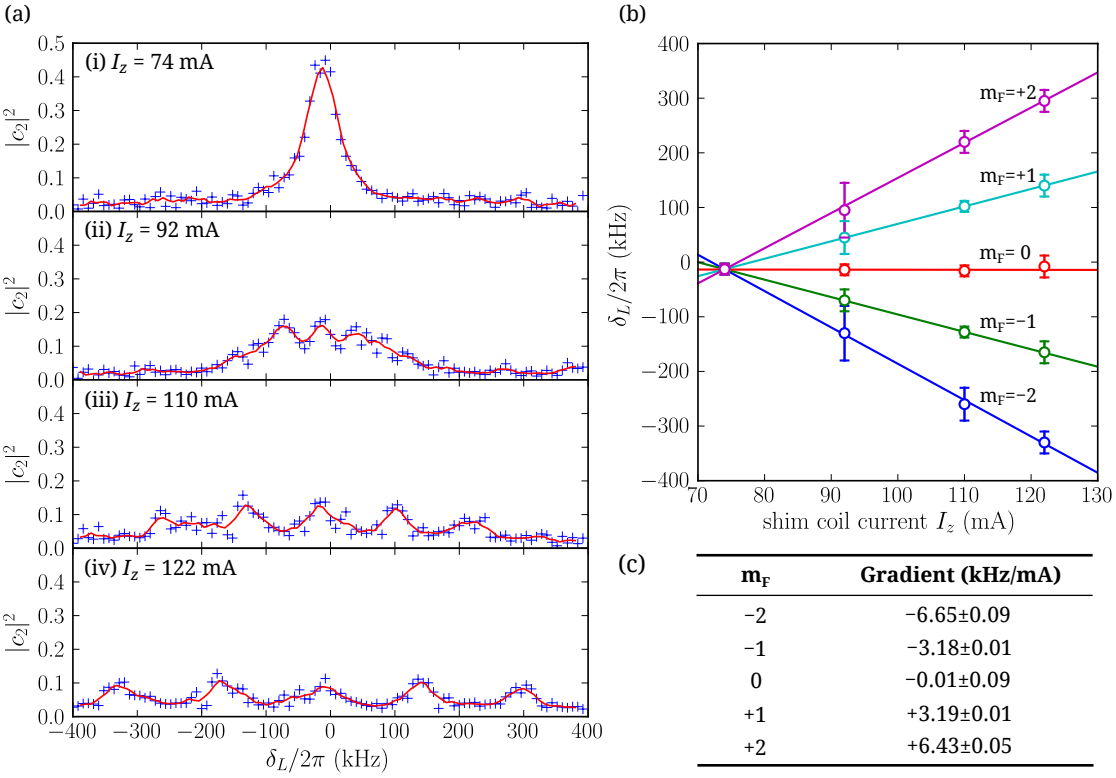

(c)

m_F	Gradient (kHz/mA)
−2	−6.65±0.09
−1	−3.18±0.01
0	−0.01±0.09
+1	+3.19±0.01
+2	+6.43±0.05

Figure 5.2: Zeeman sublevel splitting in the co-propagating $\sigma^+ - \sigma^+$ arrangement. (a) Zeeman spectra at different values of the z-axis shim coil current I_z. In each plot, the blue crosses are experimental data and the red curve is a 4 point moving average of the data. (b) Sublevel peak positions as a function of I_z. The circles are measured values, and the lines are least-square fits, whose gradients are tabulated in (c). The combined Raman beam power is $P = 13\,\mathrm{mW}$, the detuning $\Delta = 2\pi \times 10.5\,\mathrm{GHz}$, and the pulse length is $50\,\mu\mathrm{s}$.

$q = (0, \pm 1)$, which gives rise to the aforementioned transitions.

The Zeeman sublevels are shifted in energy by the magnetic field B_z according to equation 2.60, where the shift in frequency is given by $\Delta f_{\mathrm{Zeeman}} = \Delta E_{\mathrm{Zeeman}}/h\,\mathrm{Hz}$. For the sublevel m_F in rubidium-85 the Zeeman frequency shift is $\Delta f_{\mathrm{Zeeman}} = g_F m_F \times 1400$ kHz/G, where $g_F = 1/3$ for the $|5S_{1/2}, F = 3\rangle$ state and $g_F = -1/3$ for $|5S_{1/2}, F = 2\rangle$. Comparing this to the weighted average of the 4 magnetic-sensitive curve gradients (divided by m_F) in figure 5.2, which is $3.2(3 \pm 4)\,\mathrm{kHz/mA}$, we calculate the magnetic field strength as a function of current to be $3.4(3 \pm 4)$ mG/mA.

Another inference which we draw from these data is that the magnetic field at the interrogation region is, to a good approximation, uniform. A non-uniformity in B_z across the spatial extent of the atom cloud would be manifest in a broadening of the magnetic-sensitive sublevels $m_F \neq 0$, and this is not observed.

5.1.2 Light Shifts

As discussed in section 2.1 and appendix A.1.3, we expect to observe shifts in the energies of the atomic levels due to the presence of alternating electric fields. These *light shifts* [68], or *AC Stark shifts*, are given, for a single-photon transition, by $\Omega^{AC} = |\Omega|^2/4\Delta$, where Ω is the transition Rabi frequency and Δ is the detuning of the field from the transition resonance. These shifts emerge from the single-beam, two-level dressed state picture in the limit of large detuning ($\Delta \gg \Omega$). In Raman transitions the quantity of interest is the difference between the light shifts of the lower hyperfine levels $|5S_{1/2}, F = 2\rangle$, level $|1\rangle$, and $|5S_{1/2}, F = 3\rangle$, level $|2\rangle$, which we defined (in the vector formalism) in equation 2.73.

Due to variations in the Rabi frequency between the different m_F sublevels, dependent in part on the polarisation, we expect the light shift to vary between sublevels. This will potentially give rise to intensity-dependent *splitting* of the Zeeman levels which, when applying pulse sequences with varying intensity, is undesirable. In the following, we investigate the behaviour of the light shift in both the $\sigma^+ - \sigma^+$ and $\pi^+ - \pi^-$ polarisation arrangements (see table 2.2 and figure 5.3 b), and compare the results with estimated values based on equation 2.73.

Weiss *et al* in [69] state that in order to equalise the light-shifts of the two levels in the Raman system, one must adjust the intensities $I_{1,2}$ to satisfy the condition

$$\frac{I_1}{I_2} = 1 + \frac{2\Delta}{\omega_{HFS} - \Delta}, \tag{5.1}$$

which can be easily derived by setting equation 2.73 equal to zero and rearranging. This will only yield positive values of I_1/I_2 in the case where $|\Delta| < \omega_{HFS}$. Since in our experiment the detuning $|\Delta|$ always exceeds ω_{HFS}, no such condition is possible, and the light shifts cannot be balanced.

5.1.2.1 $\sigma^+ - \sigma^+$

The results for the $\sigma^+ - \sigma^+$ case are shown in figure 5.4. The plots in figure 5.4 a show the Zeeman spectra for 5 different combined Raman beam powers $P = P_1 + P_2$ (given in the plots) where $P_1 \approx P_2$, obtained in the same way as in figure 5.2, and figure 5.4 b shows

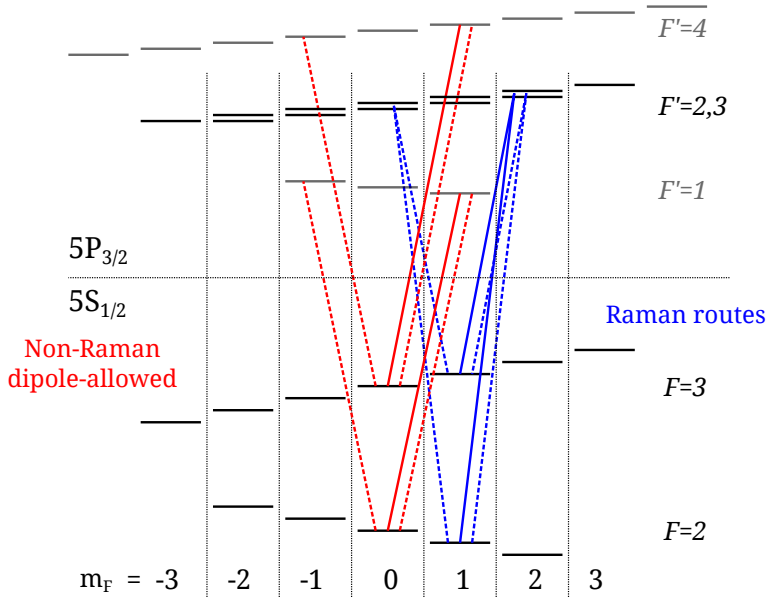

Figure 5.3: Sublevel couplings contributing to light shifts in the Raman system. The dashed lines are dipole-allowed routes in the $\pi^+ - \pi^-$ arrangement, and the solid lines are those in $\sigma^+ - \sigma^+$. The blue lines indicate transitions which form part of a Raman route, and the red lines indicate those which do not. We only show a select few lines to avoid overcrowding.

the peak positions of the individual Zeeman levels as functions of P. The degeneracy of the m_F levels was lifted by setting the z-axis shim coil current to $I_z = 122\,\mathrm{mA}$, thus providing a sufficiently strong magnetic field. In figure 5.4 b, the points are the measured values, (the horizontal error bars account for uncertainty on the beam power measurement) the dashed lines are least-square fits to the points, and the solid lines are numerical simulations based on equation 2.73. For a rough quantitative comparison between experiment and theory, we tabulate the line gradients in kHz/mW in figure 5.4 c. Broadly speaking, what we observe in the $\sigma^+ - \sigma^+$ arrangement is a linear *Zeeman-like* light shift induced *splitting* of the m_F levels, dependent on the Raman beam power. We observe an average splitting between adjacent sublevels of $3.2 \pm 0.3\,\mathrm{kHz/mW}$, where the combined top-hat Raman beam has side length $l_2 = 1.4\,\mathrm{mm}$. We find good qualitative agreement between experiment and theory for all of the sublevels. Quantitatively, not all of the simulated gradients lie within the stated experimental errors, but this can be attributed to further uncertainties, such as that in the detuning Δ, which are not considered in the simulations. The non-zero gradient of the $m_F = 0$ curve, and the overall asymmetry between $\pm m_F$ ($\neq 0$) sublevels about $\delta_L = 0$, arises due to the $a \neq n$ terms in the light shift. As mentioned previously, it is not experimentally possible where

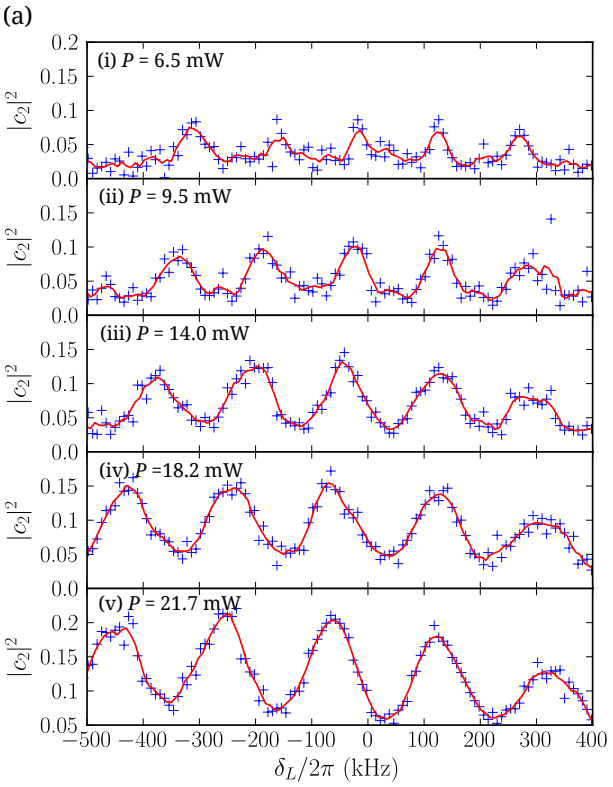

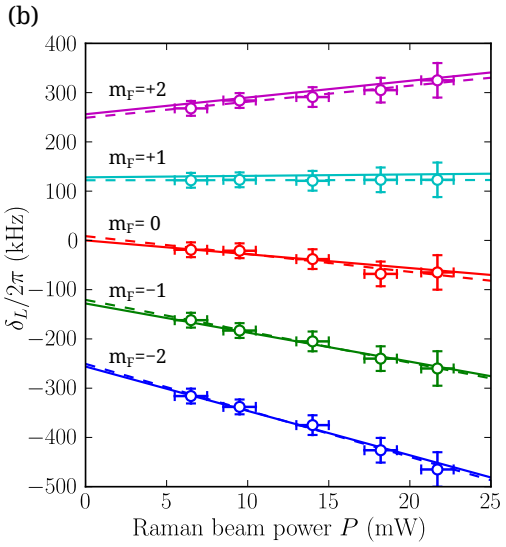

(c)

m_F	Theory	Experiment
−2	−9.00	−9.44±0.62
−1	−5.91	−6.38±0.32
0	−2.81	−3.62±0.69
+1	+0.29	+0.02±0.09
+2	+3.39	+3.25±0.43

Figure 5.4: Light shifts of the individual Zeeman sublevels in the co-propagating $\sigma^+ - \sigma^+$ arrangement. (a) Zeeman spectra at 5 different Raman combined Raman beam powers $P = P_1 + P_2$ where $P_1 \approx P_2$. (b) Peak positions as functions of P for each m_F sublevel (individually labelled) where the circles are measured values, the dashed lines are least-square fits to the circles, and the solid lines are theoretical values based on equation 2.73 assuming the experimentally-measured parameters $\Delta = 2\pi \times 10.5\,\text{GHz}$ and $I_z = 122\,\text{mA}$. (c) Tabulated gradients of the fits and simulations in b, given in kHz/mW.

$|\Delta| > \omega_{HFS}$ to remove this asymmetry by balancing the intensities.

By subtracting the light shifts at 13 mW as observed in figure 5.4 from the Zeeman shift curves in figure 5.2, we estimate that the true zero-point of magnetic field along the z-axis occurs at $I_z^{(0)} = 86 \pm 5\,\text{mA}$. We impose the error on $I_z^{(0)}$ empirically to reflect the fact that it will vary with changing MOT position (when the MOT beams are realigned, for example), and with drifting stray fields in the lab.

5.1.2.2 $\pi^+ - \pi^-$

The results for the $\pi^+ - \pi^-$ arrangement are shown in figure 5.5. We observe distinctly different behaviour to the $\sigma^+ - \sigma^+$ arrangement, in that all the Zeeman sublevels in the $\pi^+ - \pi^-$ arrangement are light-shifted in the same direction. Moreover, the gradients of the curves are all similar, and we do not observe a Zeeman-like *splitting* of the levels. We

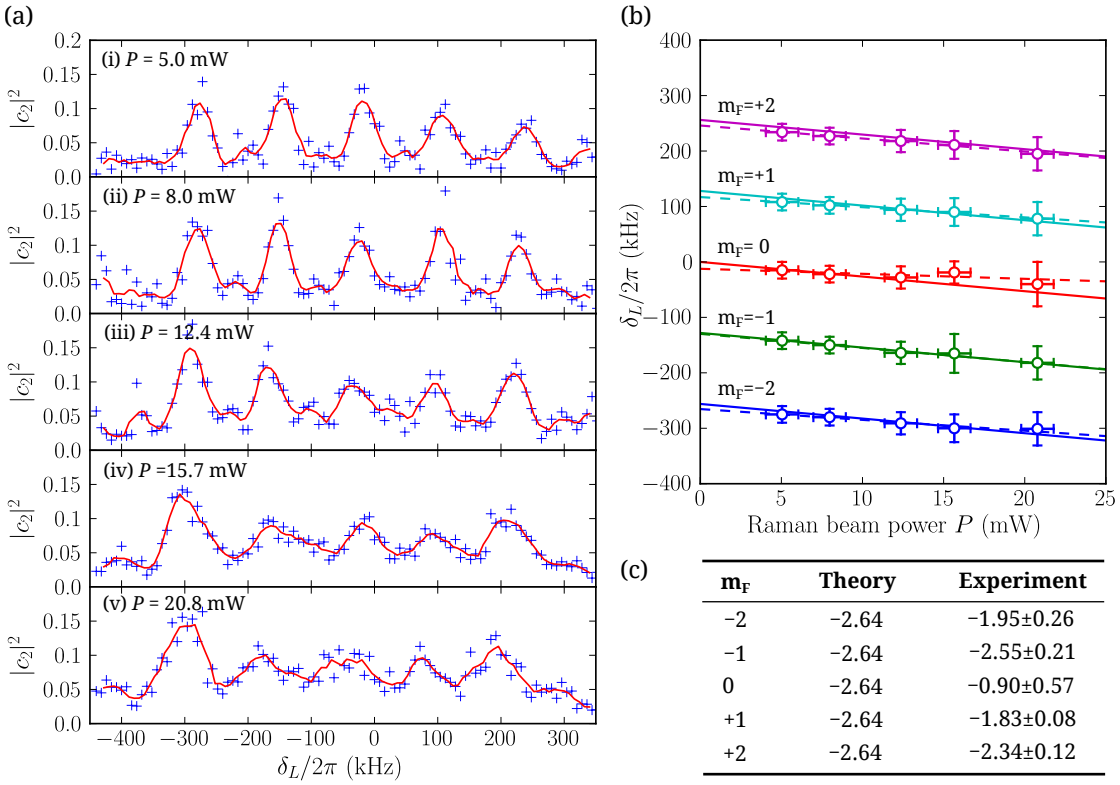

(c)

m_F	Theory	Experiment
−2	−2.64	−1.95±0.26
−1	−2.64	−2.55±0.21
0	−2.64	−0.90±0.57
+1	−2.64	−1.83±0.08
+2	−2.64	−2.34±0.12

Figure 5.5: Light shifts of the individual Zeeman levels in the co-propagating $\pi^+ - \pi^-$ arrangement. (a) Zeeman spectra at 5 different Raman combined Raman beam powers $P = P_1 + P_2$ where $P_1 \approx P_2$. (b) Peak positions as functions of P for each m_F sublevel (individually labelled) where the circles are measured values, the dashed lines are least-square fits to the circles, and the solid lines are theoretical values based on equation 2.73 assuming the experimentally-measured parameters $\Delta = 2\pi \times 10.8\,\text{GHz}$ and $I_z = 122\,\text{mA}$. (c) Tabulated gradients of the fits and simulations in b, given in kHz/mW.

once again observe an overall asymmetry about $\delta_L = 0$, and the apparent discrepancy between experiment and theory for the $m_F = 0$ sublevel arises due to the off-trend position of its peak in subplot 5.5 a iv, which is not observed for any of the other sublevels.

The detailed quantitative analysis of this data, and its level of agreement with the model, is rather less interesting than what the general trends tell us about the light shifts in different polarisation arrangements. In the $\sigma^+ - \sigma^+$ case we observe an intensity-dependent splitting of the levels. Therefore if the atoms are Zeeman-degenerate for a pulse at intensity I_A, they will not be Zeeman-degenerate at some different intensity I_B. Since the splitting is approximately linear, *i.e* $\Delta f_{LS} \propto m_F \times I$, we can correct for this, and regain Zeeman degeneracy by varying the magnetic field B_z along the axis of the Raman beams (where $\Delta f_{\text{Zeeman}} \propto m_F \times B_z$) via the Zeeman effect. However in

rapid pulse sequences where, say, an intense pulse is immediately followed by a weak one, fast-switching of the magnetic field is not possible on the necessary timescales. In the $\pi^+ - \pi^-$ arrangement we need not worry so much about such effects because all the sublevels are shifted by a roughly equal amount. We therefore conclude that the $\pi^+ - \pi^-$ polarisation arrangement is more robust in this respect. This is suggested briefly in the context of Raman cooling in [61] however no data, or indeed theory, regarding the light shifts is given in that particular article.

5.1.3 Spectral pulse profile

With some understanding of the Zeeman and light shift behaviour, we are able to adjust the parameters of the experiment to allow for Zeeman-degenerate Raman pulses. In this section, we demonstrate a Zeeman-degenerate π pulse in the co-propagating $\sigma^+ - \sigma^+$ Raman arrangement, and characterise it by comparison with a numerical simulation. The spectral profile of the π pulse is shown in figure 5.6. This was obtained after correcting for Zeeman and light-shift-induced splitting by adjusting the shim coil currents. The resultant population $|c_2|^2$ is measured at a range of laser detunings δ_L for a fixed pulse duration $\tau = 6\,\mu$s. We determine the required τ for the π pulse by measuring the position of the first peak in a Rabi flopping experiment (see section 5.1.4), after the light-shifted resonant frequency $\delta_L - \delta^{AC} = 0$ is determined empirically from a preliminary spectral scan with a fixed pulse length. In this experiment, the duration of the molasses phase was $t_M = 3\,$ms. It is important to stress that the temperature does not affect the spectral properties of a Raman transition in the co-propagating arrangement, so the additional cooling afforded by the molasses phase provides little benefit. Each data point (blue circles) is an average over 8 shots, and the complete experiment takes around 7 minutes. The combined Raman beam power was measured at $24 \pm 1\,$mW, giving a combined intensity of approximately $12\,\mathrm{kW/m^2}$. The single photon detuning Δ was measured to be $9.5 \pm 0.5\,$GHz, and the z-axis shim coil current was $I_z = 58.5\,$mA, which corresponds to a magnetic field of $B_z = -101\,$mG if we take the zero-point to be $I_z^{(0)} = 88.0\,$mA (a reasonable estimate – see section 5.1.2.1).

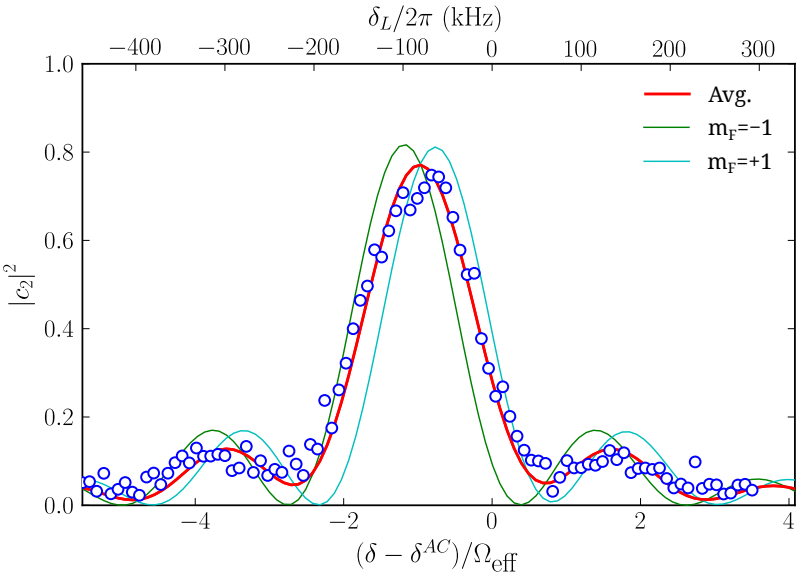

Param.	Value
I_1	5.5±0.5 kW/m^2
I_2	5.5±0.5 kW/m^2
Δ	$2\pi \times 9.5$ GHz
B_z	−101 mG
τ	6 µs
S	0.95

Figure 5.6: Spectral profile of a Zeeman-degenerate Raman transition in the co-propagating $\sigma^+ - \sigma^+$ arrangement. The blue circles are experimental data, and the thick red curve is a numerical simulation of the average $|c_2|^2$ over all $m_F = -2, \ldots, 2$, assuming the parameters given in the table to the right and an equal distribution across sublevels. The thin curves are simulations for the individual $m_F = -1, 1$ sublevels. Experimentally-measured parameters were $I_{1,2} = 6 \pm 0.5\,\text{kW/m}^2$, and $\Delta = 2\pi \times 9.5 \pm 0.5\,\text{GHz}$.

The data exhibit a sinc-squared-like shape as expected (see figure 2.4), which is somewhat washed out at the shoulders. We can gain some insight into the effects of certain experimental parameters, and test agreement between experiment and theory, by comparing the data to a numerical simulation. The thick red curve in figure 5.6 is a simulation of the average resultant $|c_2|^2$ across the five sublevels $m_F = -2, \ldots, 2$ (the observed quantity in the experiment) corresponding to the parameters given in the table to the right of the plot, calculated using equations 2.36. In the simulation we find a good fit to the data with $I_{1,2}$ slightly lower than the experimentally measured values, where Δ is as measured. The parameter S is discussed in section 5.1.3.1. We use the field intensities $I_{1,2}$ and detuning Δ along with equation 2.72 to calculate the Raman Rabi frequencies Ω_R, and the light shifts are calculated using equation 2.73. The magnetic field is included in the simulation by addition of the Zeeman shift term $\mu_B g_F m_F B_z$ to the detuning δ in equations 2.36. In these velocity-insensitive simulations, the momentum terms are removed from the equations. It is important to note that this simulation, along with all others in this thesis, considers an *even* initial distribution of atoms across the five Zeeman sublevels. That is, we assume each level constitutes 20% of the total number of atoms – an assumption reinforced by the data in figures 5.2 a, 5.4 a, and 5.5 a.

We find that the washing out at the shoulders is due to the fact that B_z does not fully compensate for the light shift induced splitting of the m_F sublevels (see section 5.1.2.1). This is illustrated in the plot by the thin lines depicting the individual sublevels $m_F = -1$ (green) and $m_F = +1$ (cyan), which are non-degenerate. Intensity *noise* is included in this simulation (indicated by the 'errors' on $I_{1,2}$) to account for the inhomogeneity of the Raman beam profile. The effect of this is illustrated more clearly in section 5.1.4, where we also explain its implementation.

The only 'free' parameter in the numerical simulation is S, a scaling factor which multiplies the simulated resultant value of $|c_2|^2$. This is required because, although their spectral *shape* agrees well with the data, the simulations give *amplitudes* slightly higher than what we observe. The inclusion of a scaling factor might be considered unsatisfying, however its origins are clear, as described below.

5.1.3.1 Loss of atoms

We expect some fraction of the atoms to leave the interrogation region (the $l_2 = 1.4\,\text{mm}$ cross-section of the Raman beams) under ballistic expansion during and immediately after the molasses phase, leading to a reduction in the maximum achievable $|c_2|^2$, as illustrated in figure 5.7 a. The readout and normalisation pulses (see section 3.5) cause atoms within the detection region (the $D \sim 7\,\text{mm}$ cross-section of the cooling beams) to fluoresce. Therefore atoms expanding out of the interrogation region but remaining inside the detection region, will be detected by the readout pulse but not excited by the Raman pulse, and a number of atoms contributing to the readout signal will not have 'seen' the Raman beams. This effect was partly characterised in section 3.6.2, where we concluded that the majority of the cloud remained within a 1 mm-side cross section over 10 ms after the quadrupole field was switched off. However, it would appear that there is a greater loss of atoms from the interrogation region than suggested in figure 3.9.

In order to investigate whether loss of atoms was the reason behind the lower-than-expected observed $|c_2|^2$, we measured $|c_2|^2$ on-resonance ($\delta - \delta^{AC} = 0$) for a π pulse applied at different times. The duration of the molasses phase was $t_M = 1.5\,\text{ms}$, and we applied a $500\,\mu\text{s}$ preparation pulse as normal. At a time t_S after the preparation pulse, the π pulse was applied ($7\,\mu\text{s}$ in this case). The state readout pulse was applied

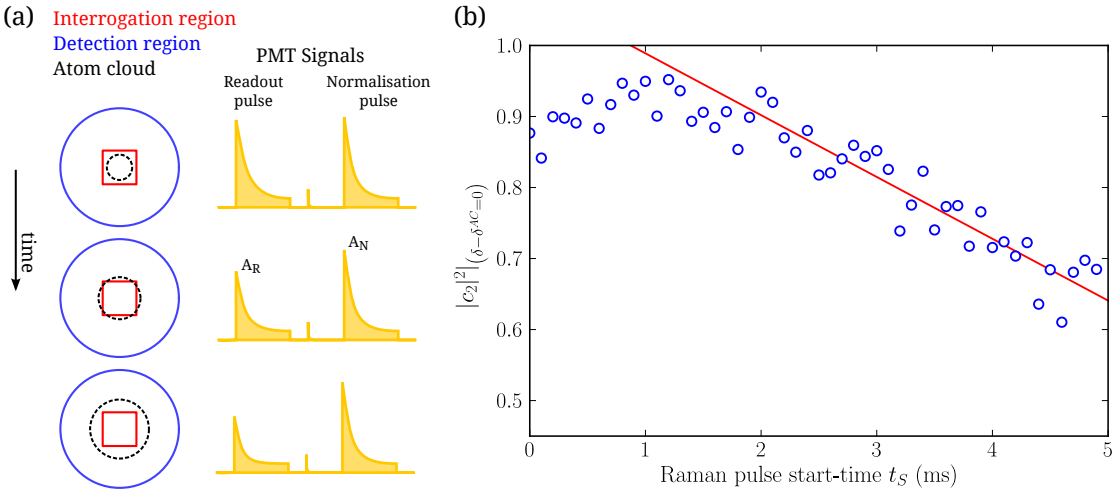

Figure 5.7: Demonstration of the loss of atoms from the interrogation region. (a) Sketch showing atoms ballistically expanding out of the interrogation region, and the associated PMT signals. The readout amplitude is smaller as atoms are lost, but the normalisation amplitude remains constant ($|c_2|^2 = A_R/A_N$). (b) Population in $|2\rangle$ after a resonant π pulse, as a function of the start-time t_S of the pulse.

at a fixed time (5 ms) after the preparation pulse. Figure 5.7 b shows the results of the experiment.

At low t_S we observe $|c_2|^2$ values of around 0.9, which is close to the maximum achievable (~ 0.96), and after $t_S = 1$ ms $|c_2|^2$ begins to decrease. The red line on the graph is a least-squares fit of a straight line to the data after $t_S = 2$ ms, and is intended merely as an aid to the eye. After 4 ms the resonant transfer fraction has decreased to ~ 0.7, representing a scaling factor at this point of $S = 0.7/0.96 = 0.73$. This behaviour represents evidence that atoms are indeed being lost from the interrogation region as the atom cloud ballistically expands. Whereas in the above experiment the atom cloud was left to expand in the absence of the cooling and repump beams, in all other experiments in this thesis the Raman pulses are applied immediately after the state preparation pulse, following a molasses duration t_M. Since the molasses will continue to provide a cooling and impeding effect, even in the absence of the quadrupole field, we can consider the values of S here as a *lower bound* on the parameter (the upper bound is 1) in our simulations, and we expect S to be larger in the other experiments.

5.1.4 Rabi Flopping

When the resonant ($\delta - \delta^{AC} = 0$) Raman beams are switched on, we expect the atoms, which we prepare in state $|1\rangle$, to oscillate, or 'Rabi flop', between the hyperfine levels $|1\rangle$ and $|2\rangle$ at a rate equal to the two-photon Rabi frequency Ω_R, given in equation 2.72. We can test this experimentally by measuring the evolution of the population in state $|2\rangle$ as a function of the duration of the Raman pulse. A characterisation of the two-photon Rabi frequency is given in section 5.1.4.1.

Since there are many atoms in the cloud, and many environmental and internal effects to which they are sensitive, we expect there to be inhomogeneities in the Rabi frequency, borne out in dephasing of the Rabi oscillations. This was observed to some extent in the previous section, however it is illustrated more effectively when considering Rabi flopping. We discuss the prominent sources of dephasing in section 5.1.4.2, and afterwards go on to demonstrate 'optimal' Rabi flopping, where dephasing has been minimised.

5.1.4.1 Two-photon Rabi frequency

The two-photon Raman Rabi frequency is proportional to the product of the two single-photon Rabi frequencies, as shown in equation 2.72. In order to test this experimentally, we measured the frequency of Rabi flopping at a range of Raman beam powers. The results are shown in figure 5.8. Part a of the figure shows the measured population in state $|2\rangle$ as a function of the Raman pulse length, for 5 different Raman beam powers (given in the plots) at a detuning $\Delta = 2\pi \times 12.5 \pm 0.5$ GHz. Each point is an average over 8 shots, and a complete scan takes approximately 7 minutes. The red curve in each plot is a 6-point moving average of the data. These scans are taken close to resonance, such that $\delta^{AC} - \delta \ll \Omega_R$, and we have attempted to minimise the light-shift splitting by compensation with a magnetic field, as discussed in the previous section. Since these data were taken in the $\sigma^+ - \sigma^+$ arrangement, we expect to see a change in the maximum value of $|c_2|^2$ with changing beam powers, due to the light-shift. This is indeed shown by the data, since the curves have different amplitudes. Figure 5.8 b shows the Rabi frequency as a function of the combined Raman beam power $P = P_1 + P_2$, where the beam powers are approximately equal ($P_1 \approx P_2$), as measured from the scans in 5.8 a. We expect Ω_R to be proportional to $\sqrt{P_1}\sqrt{P_2}$, since $\Omega_{na} \propto E_a \propto \sqrt{I_a} \propto \sqrt{P_a}$, and

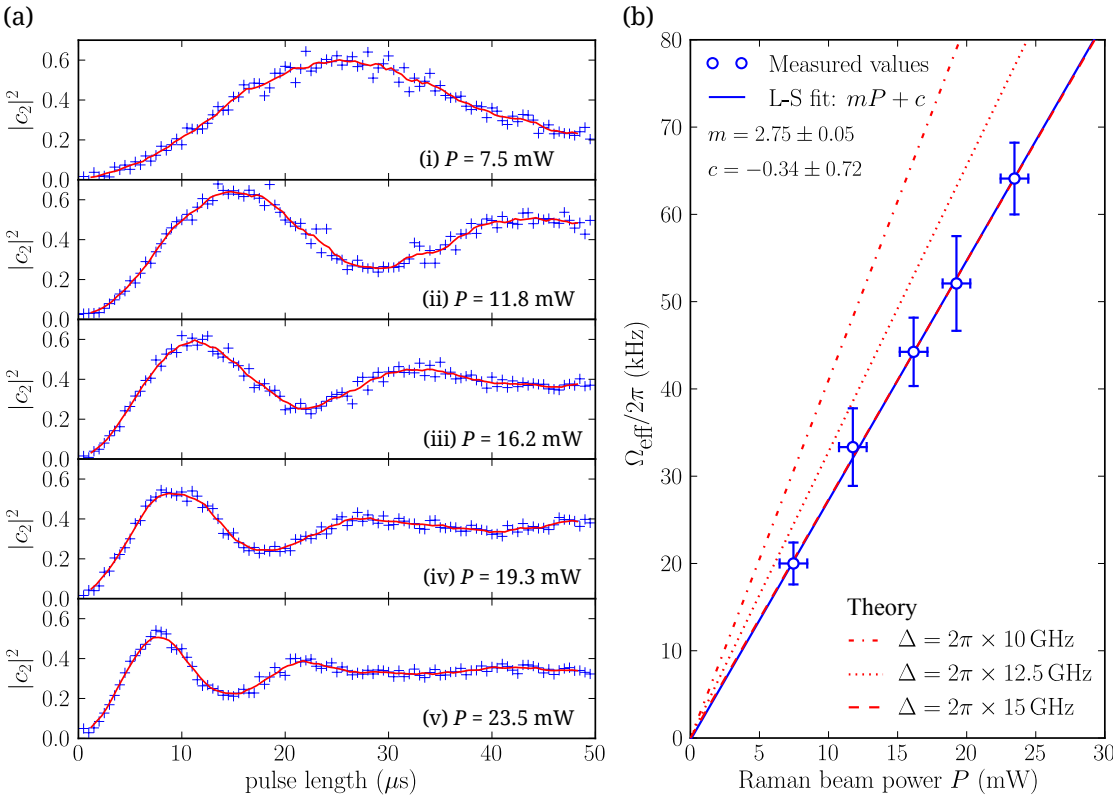

Figure 5.8: Rabi flopping in the co-propagating $\sigma^+ - \sigma^+$ arrangement. (a) Measured $F = 3$ state population as a function of Raman pulse length t at a measured detuning $\Delta = 2\pi \times 12.5$ GHz for five Raman beam powers $P = P_1 + P_2 \approx 2P_1$ (given in the plots). (b) Rabi frequency as a function of P: circles – measured values from (a); solid blue curve – least squares fit to the circles; red curves – theoretical values assuming detunings given in the legend.

therefore where the powers are equal $\Omega_R \propto P$. We calculate the *effective* Rabi frequency (so-called since we are observing the combined, or average, value of Ω_R across all m_F levels) by measuring the half-period of oscillation $\tau_{\text{eff}}/2$ and applying it in the formula $\Omega_{\text{eff}} = 1/\tau_{\text{eff}}$. The error on $\tau_{\text{eff}}/2$ is judged by eye according to the 'sharpness' of the initial Rabi flopping peak, and appears large in the plot due to the nature of the error propagation. The solid blue line on the graph is a least-squares fit to the data, which is linear as expected and exhibits a y-axis intersection of $c = -0.34 \pm 0.72$, which is consistent with the origin. The red curves on the plot are theoretical values, which we calculate using the formula

$$\begin{aligned}\Omega_{\text{eff}} &= \frac{1}{2\Delta N_{m_F}} \sum_{m_F} |\boldsymbol{\Omega}_{11} \cdot \boldsymbol{\Omega}_{22}| \\ &= \frac{1}{2\Delta N_{m_F}} \sum_{m_F} \sum_{F'} \left(\Omega^{(1)}_{|2,m_F\rangle,|F',m'_F\rangle} \Omega^{(2)}_{|3,m_F\rangle,|F',m'_F\rangle} \right),\end{aligned} \tag{5.2}$$

in which $N_{m_F} = 5$ is the number of Zeeman sublevels, and since we are using the $\sigma^+ - \sigma^+$ arrangement, $m'_F = m_F + 1$. Once again, we can evaluate this by calculating (or looking up in Steck [44]) the associated dipole matrix elements for each transition, and inputting the measured beam intensities $I_{1,2} = P_{1,2}/l_2^2$ (where $l_2 = 1.4\,\text{mm}$) and detuning Δ. In the figure we show curves for three different values of Δ (given in the legend). We find that the gradient of the experimental curve is smaller than that of the theory, assuming the measured parameters in the simulation, and the difference is equivalent to a 20% over(under)estimate of the measured value of P (Δ). Δ is measured using a wavemeter into which *both* Raman beams ($\sim 3\,\text{GHz}$ apart) are channelled, and since the resulting measurement is some combination of the two wavelengths, a systematic discrepancy in the measurement may arise. Further to this, a systematic offset in the measured intensity of the Raman beams may arise due to an asymmetric top-hat profile, or to regions of lower/higher than average intensity within the cross-section of the beams. These discrepancies are considered in the simulations of the remainder of this thesis.

5.1.4.2 Sources of dephasing

Figure 5.8 a shows that much dephasing occurs during Rabi flopping. The upper state population $|c_2|^2$ reaches its steady state in all cases after only two Rabi cycles, and its peak value, which occurs after half of one Rabi cycle, is much lower than what we desire for an efficient π pulse. The primary sources of dephasing during Raman pulses are:

1. **Differences in resonant two-photon coupling strengths between the Zeeman sublevels**

   This is unavoidable when working with Zeeman-degenerate transitions. Raman routes within all of the five Zeeman sublevels (see figure 2.7 a) contribute to the measured average $|c_2|^2$, and the two-photon Rabi frequency $\Omega_R = |\mathbf{\Omega}_{11} \cdot \mathbf{\Omega}_{22}|/2\Delta$ for each m_F level is different. Note that Ω_R for the sublevel m_F is equal to that of the sublevel $-m_F$, hence assuming complete Zeeman-degeneracy there are three distinct Rabi frequencies present. On-resonance, this source of dephasing puts an upper limit on $|c_2|^2$ for a π pulse of approximately 0.96.

2. **Intensity variations across the Raman beam profile**

   The top-hat Raman beam exhibits spatial intensity inhomogeneities, as shown in

figure 4.13 b. Since the Rabi frequency is dependent on the electric field strength, such inhomogeneities cause variations in the Rabi frequency across the extent of the atom cloud, giving rise to dephasing. Even the most spatially homogeneous top-hat achievable with the current setup exhibits an intensity noise of around ±5%.

3. **Zeeman non-degeneracy**

   This occurs when (a) there is a non-zero magnetic field perpendicular to the Raman beams, or (b) the magnetic field parallel to the Raman beams does not cancel the light-shift-induced splitting of the levels (see section 5.1.2 and figure 5.6). Zeeman non-degeneracy leads to a different value of the laser detuning δ_L, and therefore a different $\tilde{\Omega}_R$, for each of the Zeeman sublevels.

4. **Broadening of the detuning δ**

   Where δ varies from the expected value, there is an associated variation in the two-photon Rabi frequency $\tilde{\Omega}_R$. This can occur due to systematic changes in the laser detuning δ_L, or to the Doppler effect via the detuning term $(\mathbf{k}_{L1} - \mathbf{k}_{L2}) \cdot \mathbf{v}$ in the velocity-sensitive arrangement. For small splittings between the sublevels ($\Delta f_{\text{Zeeman}} + \Delta f_{\text{LS}} \ll \Omega_R$), source 3 can be considered as an effective broadening of δ.

Assuming optimal beam quality, the only significant handle available to us if we are trying to minimise dephasing in the co-propagating arrangement, is the magnetic field, which we control by changing the currents $I_{x,y,z}$ through the three independent, orthogonal pairs of shim coils (see figure 3.4). Painstaking tweaking of these currents can lead to a significant increase in performance, as shown in the following section. All of the above sources of dephasing can be considered as *systematic errors*, and we take a more active approach to suppressing them, by way of composite pulses, in chapter 6.

5.1.4.3 Near-optimal performance

Figure 5.9 shows Rabi flopping at $\Omega_{\text{eff}} \approx 2\pi \times 32\,\text{kHz}$ where the magnetic fields have been optimised to give maximal Zeeman-degeneracy. The experimental parameters for this scan were measured to be $\Delta = 2\pi \times 16.5 \pm 0.5\,\text{GHz}$, $I_z = 78\,\text{mA}$, $\delta_L = 2\pi \times -10\,\text{kHz}$, and the combined power $P = P_1 + P_2 = 16 \pm 1\,\text{mW}$. We can see from the plot that the peak $|c_2|^2$ value is significantly increased compared to the scans in figure 5.8, and that the experimental contrast of the Rabi oscillations is greater. The thick red curve in the

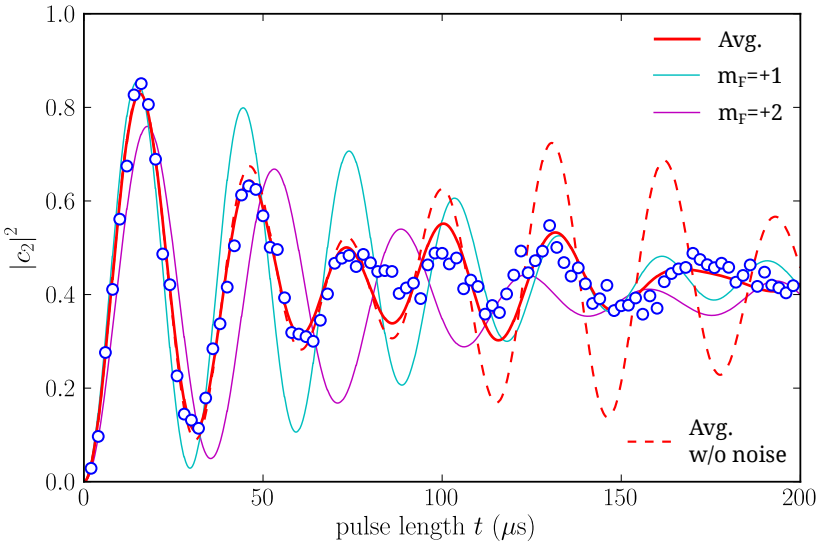

Param.	Value
I_1	4.0±0.5 kW/m^2
I_2	4.0±0.5 kW/m^2
Δ	$2\pi \times 16.7$ GHz
δ_L	$2\pi \times -10.0$ kHz
B_z	− 21 mG
S	0.9

Figure 5.9: Rabi flopping in the co-propagating $\sigma^+ - \sigma^+$ arrangement where the magnetic fields have been adjusted to give maximal Zeeman degeneracy. The blue circles are experimental data, and the thick red curve is a numerical simulation, assuming the parameters given in the table to the right. The dashed red curve is a simulation with identical parameters, except without noise on $I_{1,2}$. The thin solid lines show two of the five individual m_F sublevels, indicated in the legend.

figure is a numerical simulation of the average $|c_2|^2$ assuming the parameters given in the table to the right of the plot, where in this case we find good agreement with the data assuming the experimentally measured values of P and Δ.

The dephasing in this case is dominated by sources 1 and 2 in the above list, the effects of which we are able to simulate. We simulate the effects of source 2 by adding $\eta \times \Delta I$, where η is a uniformly pseudo-randomly generated number $-1 \leq \eta > 1$ and ΔI (denoted as the 'error' on I in the parameter table) is the maximum intensity excursion, to the intensity $I_{1,2}$. We simulate a Rabi flopping curve for 50 different pairs of intensities $I_1 + \eta_1 \Delta_1$, $I_2 + \eta_2 \Delta_2$ and take an average of these to get the resultant curve. Furthermore, each of the 50 curves are themselves averages of 5 sub-curves corresponding to the 5 $\sigma^+ - \sigma^+$ Raman routes (associated with the 5 Zeeman sublevels), which differ due to their different associated dipole matrix elements. We find that without intensity noise, as shown by the dashed curve in figure 5.9, some of the contrast is maintained at longer pulse times, but the effect is somewhat negligible for the first two Rabi cycles. It is important to note that the intensity noise is only *spatial* in these simulations, and we do not consider *intra-pulse* intensity variations – this would be very difficult to simulate for relatively little intuitive gain.

The effects of source 1 in the above list are illustrated by the two thin curves in the plot, which are simulations of the individual sublevels $m_F = +1$ (cyan), and $m_F = +2$ (magenta). Unlike in figure 5.6, these levels *are* spectrally degenerate, but the difference in the inherent coupling strengths between the five sublevels leads to rapid dephasing between them during pulses. We find that the sublevels $m_F = \pm 1$ ($m_F = \pm 2$) exhibit Rabi frequencies which are 6% (25%) lower than that of $m_F = 0$. Given that the observed $|c_2|^2$ is an average value of the five sublevel curves, we can see that source 1 acts to reduce Rabi flopping contrast at short pulse times, and source 2 acts to impede the revival of contrast where the sublevels rephase at later pulse times.

Note that in the simulations performed throughout this thesis, we assume transitions along individual sublevel routes to remain independent throughout the course of the pulse or pulse sequence, and that there is no mixing of population between the sublevels.

As a general comment, the velocity-insensitive Rabi flopping illustrated in figure 5.9 exhibits considerably less dephasing than has been reported for example by Butts *et al* [70], who performed spin-polarization so that only the $m_F = 0$ level was populated before applying their (Gaussian beam) Raman pulses. This may be due to the improved Raman beam homogeneity afforded by the top-hat beams in our experiment.

5.2 Velocity-sensitive Raman pulses

In the velocity-sensitive, *counter-propagating* Raman arrangement, the momentum terms are re-inserted into the model, and we are able to perform useful interferometry by spatially splitting and recombing wavepackets. The ket states are written, for simplicity, as $|1, \mathbf{p}\rangle = |1\rangle$, $|3, \mathbf{p} + \hbar\mathbf{k}_{L1}\rangle = |3\rangle$ and $|2, \mathbf{p} + \hbar(\mathbf{k}_{L1} - \mathbf{k}_{L2})\rangle = |2\rangle$, and as before the associated amplitudes are c_1, c_3 and c_2 respectively.

In the co-propagating arrangement half of the power was 'dumped' at the non-polarising beamsplitter cube before the fibre (see figure 5.1). In the *counter*-propagating arrangement the beams are deliverered to the MOT chamber independently, and (excluding unavoidable losses such as fibre-coupling inefficiencies) all of the power is retained in the Raman beams. We can therefore take advantage of the extra power-broadening in the velocity-sensitive arrangement, but as we demonstrate in section 5.2.2, the spread in atomic velocities and the associated Doppler-broadening of δ leads to significant dephasing.

We begin this section by re-visiting the velocity distribution of the atom cloud. Measurements of the spectral Raman pulse profile in the velocity-sensitive system (equivalent to the velocity-insensitive results of section 5.1.3) are described in the next chapter, where we explore methods for improving fidelity.

5.2.1 Raman velocimetry

Since the Raman transition is sensitive to the atomic velocity v_z, we can use it as a sensitive means of velocimetry, as in the experiments of, for example [12, 58, 60, 67]. The detuning of the velocity-sensitive Raman transition is given in equation 2.57 which, when we include the light shift, becomes

$$\delta - \delta^{AC} = -\delta_L + \frac{\mathbf{p} \cdot (\mathbf{k}_{L1} - \mathbf{k}_{L2})}{M} + \frac{\hbar(\mathbf{k}_{L1} - \mathbf{k}_{L2})^2}{2M}. \tag{5.3}$$

If we set our effective detuning $\delta - \delta^{AC} = 0$ and use counter-propagating Raman beams such that $\mathbf{k}_{L1} \simeq -\mathbf{k}_{L2} = k\hat{\mathbf{z}}$, this becomes

$$\delta_L = 2\frac{p_z k}{M} + 2\frac{\hbar k^2}{M} = 2kv_z + kv_R, \tag{5.4}$$

where v_z is the velocity component in the z-direction and v_R is the two-photon Raman recoil velocity. This tells us that an atom resonant with the Raman beams will have a velocity whose z component is proportional to the detuning δ_L. An atom starting in $|1, \mathbf{p}\rangle$ with the corresponding resonant velocity will be excited by the Raman beams to $|2, \mathbf{p} + \hbar(\mathbf{k}_1 - \mathbf{k}_2)\rangle$. It is therefore possible to build a picture of the atomic velocity distribution simply by measuring the resultant state of the atoms after a Raman pulse at a range of δ_L detunings. Raman velocimetry represents a more robust method for measuring temperature than the previously-performed release-and-recapture method [49, 50, 59], since rather than providing a signal which is integrated over the whole atom cloud, it allows for observation of structure *within* the velocity distribution.

The resolution of the measurement is limited by the intensity of the pulse, since the spectral linewidth of the Raman transition is power-broadened according to the two-photon Rabi frequency Ω_R. In order to achieve high resolution we therefore require a sufficiently low-intensity pulse. Furthermore, the fundamental limit on the resolution of the measurement is determined by the duration t of the Raman pulse, according to the Fourier-limited pulse width (see [42] section 9.8, for example)

$$\frac{\Delta v}{\lambda} \approx \frac{1}{t}, \tag{5.5}$$

which tells us the minimum velocity-width of the transition. Assuming a sufficiently low-intensity pulse, for a resolution equal to v_R with $\lambda \simeq 780\,\text{nm}$, we would set $t = 50\,\mu\text{s}$.

The result of a Raman velocimetry experiment immediately after a $t_M = 6\,\text{ms}$ molasses cooling stage (step 6 in section 3.5) is shown in figure 5.10, where we measure the resultant population $|c_2|^2$ as a function of the laser detuning δ_L for a fixed pulse duration $\tau = 110\,\mu\text{s}$. In figure 5.10 a, the blue circles are experimental data and the red curve is a numerical simulation using the parameters given in the table. As a reminder, the two beams are imbalanced in intensity, assuming equal powers, due to the difference in beam size ($l_1 = 1.7\,\text{mm}$, $l_2 = 1.4\,\text{mm}$). Whilst we would prefer to use low power beams with, say, $P_{1,2} = 1\,\text{mW}$ for increased velocity resolution, this leads to very low signal-to-noise since there are fewer atoms excited by the pulse. To preserve signal-to-noise at a workable level we instead apply beams at $P_{1,2} \approx 12\,\text{mW}$. Because of this, whilst the spectral profile

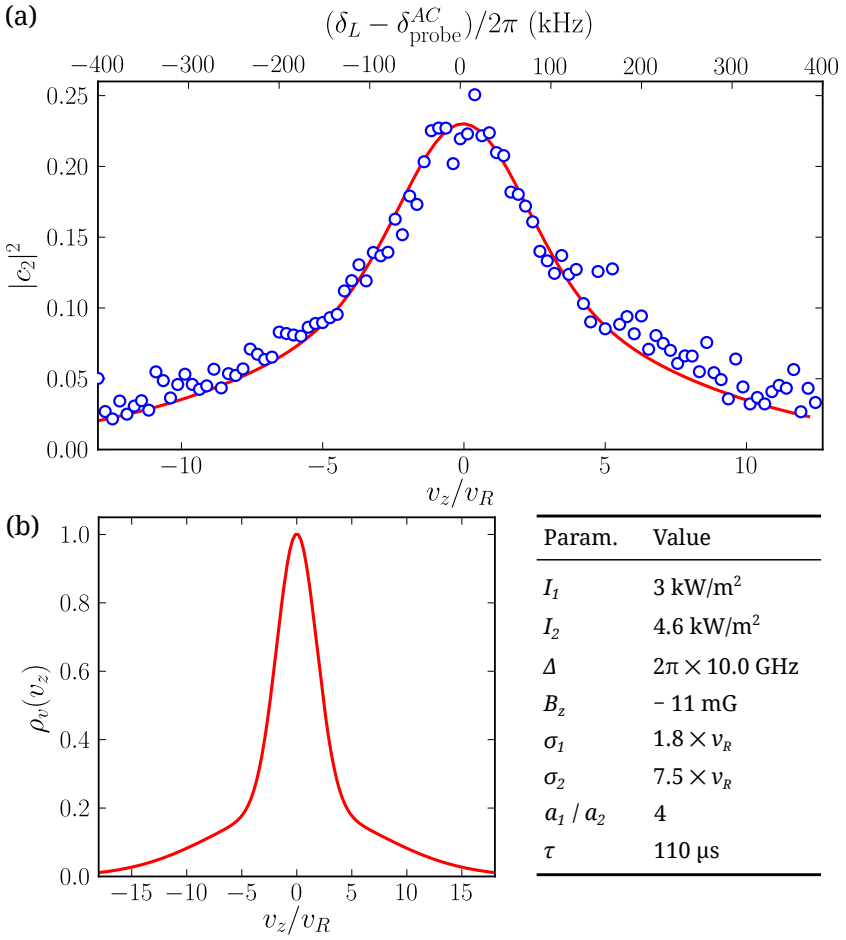

Param.	Value
I_1	3 kW/m^2
I_2	4.6 kW/m^2
Δ	$2\pi \times 10.0$ GHz
B_z	- 11 mG
σ_1	$1.8 \times v_R$
σ_2	$7.5 \times v_R$
a_1 / a_2	4
τ	110 µs

Figure 5.10: Velocity distribution of the atom cloud after a $t_M = 6ms$ molasses phase, measured by Raman velocimetry. (a) Measure of the population in $|2\rangle$ after a velocity-sensitive $\sigma^+ - \sigma^+$ Raman pulse of duration $\tau = 50\mu s$, for a range of detunings δ_L. The blue circles are experimental data and the red curve is a numerical simulation using the parameters given in the table. (b) The reconstructed velocity distribution from the numerical simulation.

of the Raman transition is a good approximation to the velocity distribution of the atom cloud, it is not a *direct* measure. We must instead *reconstruct* an estimate of the velocity distribution from the parameters used in the best-fitting numerical simulation. Sub-Doppler cooling is most effective at the center of the cooling region, as discussed in [71], and it is therefore common for the resultant velocity distribution to exhibit two distinct Gaussians. With this in mind we model the normalised velocity density as

$$\rho_v(v_z) = \frac{1}{a_1 + a_2}\left(a_1 e^{-\frac{1}{2}(v_z/\sigma_1)^2} + a_2 e^{-\frac{1}{2}(v_z/\sigma_2)^2}\right), \tag{5.6}$$

where $a_{1,2}$ are the amplitudes and $\sigma_{1,2}$ the widths of two Gaussians. We find a good fit to the data where $a_1/a_2 = 4$ (the result is independent of the *absolute* amplitudes)

and $\sigma_1 = 1.8 v_R$, $\sigma_1 = 7.5 v_R$. The 1D temperature of a Gaussian velocity distribution of width σ_v is given by

$$T = \frac{M\sigma_v^2}{k_B} = 1.48 \left(\frac{\sigma_v}{v_R}\right)^2 \ \mu\text{K}, \tag{5.7}$$

hence the velocity distribution, as shown in figure 5.10 b, represents a narrow central component with temperature $T = 4.8\,\mu$K and a broader background at $T = 83\,\mu$K. These are realistic parameters, and furthermore the two-component spectral profile we observe is similar to the time-of-flight data published in [71]. For comparison, the recoil limit for sub-Doppler cooling of rubidium-85 is $T_R = 0.37\,\mu$K, and the Doppler cooling limit is $T_D = 145\,\mu$K. Integrating the two estimated distributions, we find that roughly 50% of the cloud is contained within each, hence the *average* temperature of the cloud is $\sim 44\,\mu$K. It is important to note that the velocity distribution is highly sensitive to experimental parameters such as the intensities and detunings of the MOT lasers, the magnetic fields, and the parameters describing the Raman beams themselves. As a consequence, it is highly variable, and we observe variations in temperature from day-to-day. The scan in figure 5.10 was taken after much iterative optimisation.

5.2.2 Rabi Flopping

We now investigate Rabi flopping in the velocity-sensitive Raman arrangement. As mentioned previously, since there is a distribution of atomic velocities within the atom cloud we expect there to be a large inhomogeneity in δ in this arrangement, which will add another source of dephasing to those discussed in section 5.1.4.2.

Velocity-sensitive $\sigma^+ - \sigma^+$ Rabi flopping at $\Omega_{\text{eff}} \approx 2\pi \times 200\,\text{kHz}$ is shown in figure 5.11. The Raman beams were measured to carry powers of $P_1 \approx P_2 = 44\,\text{mW}$, and their single-photon detuning was $\Delta = 2\pi \times 15 \pm 0.5\,\text{GHz}$. To offset the light shift induced sublevel splitting and bring the sublevels into degeneracy, the z-axis shim coil current was set to $I_z = 59\,\text{mA}$, and we empirically located the light-shifted Raman resonance at $\delta_L = \delta^{AC} = 2\pi \times -50\,\text{kHz}$. After running simulations with a range of velocity distribution parameters, we find a suitable approximation to the data where $\sigma_1 = 3 \times v_R$, $\sigma_2 = 10 \times v_R$, and $a_1/a_2 = 3$. This represents a realistic post-molasses velocity distribution, with a central peak at $13\,\mu$K, a background at $148\,\mu$K, and an average temperature of $T \sim 84\,\mu$K. Simulations also approximate the data well where

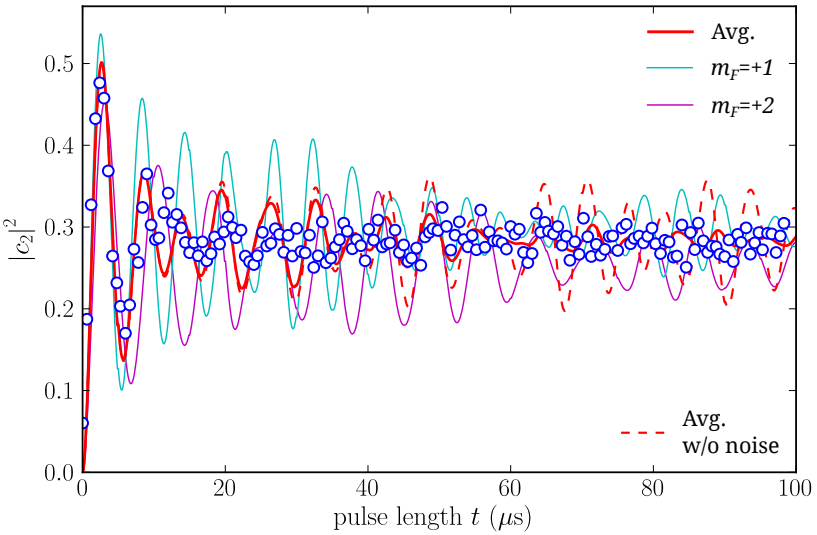

Param.	Value
I_1	12±1 kW/m^2
I_2	17±1 kW/m^2
Δ	$2\pi \times 15.0$ GHz
δ_L	$2\pi \times -50.0$ kHz
B_z	−101 mG
σ_1	$3 \times v_R$
σ_2	$10 \times v_R$
a_1 / a_2	3
S	0.95

Figure 5.11: Zeeman-degenerate Rabi flopping in the counter-propagating $\sigma^+ - \sigma^+$ arrangement. The blue circles are experimental data, and the red curve is a numerical simulation, assuming the parameters given in the table to the right of the plot. The thin curves are numerical simulations of the individual sublevels $m_F = +1, +2$, indicated in the legend.

we set $B_z = -101\,\text{mG}$, suggesting a zero-point current $I_z^{(0)} = 88\,\text{mA}$, which once again agrees with the measured value. Similarly to figure 5.8, we find better agreement with the data where P (Δ) in the simulation is around 20% lower (higher) than the measured value (these are equivalent, but we typically apply a reduction of P, rather than an increase in Δ, in the simulations).

We observe a higher Rabi frequency than that in the velocity-insensitive arrangement, because the beams have greater intensities, and due to the spread in velocity we observe a more rapid dephasing. The initial peak exhibits an upper hyperfine state population of $|c_2|^2 \sim 0.5$, as compared with the ~ 0.85 observed in the velocity-insensitive arrangement. The effects of Doppler-induced dephasing are indicated more clearly in the simulated curves for the individual sublevels, of which we plot $m_F = +1$ (cyan) and $m_F = +2$ (magenta) in the figure. Once again, although the sublevels are spectrally degenerate, they rapidly dephase during pulses due to their different dipole matrix elements, but in the velocity-sensitive arrangement we find that their peak and steady-state $|c_2|^2$ values are greatly reduced. In light of this we conclude that source 4, the broadening of the detuning δ, dominates the dephasing in velocity-sensitive pulses at short pulse times. Furthermore, we expect to observe more dephasing with a wider spread in velocities, given a fixed beam intensity and detuning. We characterise this effective

temperature dependence in the next chapter, where to preempt more specifically, in figure 6.8 we plot the simulated peak fidelity as a function of velocity width.

5.3 Conclusion

In this chapter we have demonstrated that our experimental system is capable of pulsed, velocity-sensitive, two-level manipulation of cold rubidium. We found that the Raman pulses are subject to significant dephasing, due to broadening effects (Doppler, Zeeman, and light shift), beam intensity inhomogeneities, and varying inherent coupling strengths across the Zeeman sublevels. The numerical simulations performed in this chapter, which we find to agree well with the data, have provided extra insight into the behaviour of the Raman pulses, particularly in the cases of Zeeman-degenerate transitions where the behaviour of individual sublevels is not experimentally resolved.

Our investigations into light shifts revealed that in the $\sigma^+ - \sigma^+$ polarisation arrangement, Raman pulses cause a Zeeman-like light-shift-induced splitting of the m_F sublevels, and that such splitting is absent in the $\pi^+ - \pi^-$ (lin-perp-lin) arrangement. From this we learn that the latter is more robust in schemes where varying pulse intensities are applied.

Since coherence (a lack of *decoherence*, where decoherence is distinct from dephasing) is achieved on timescales of over 100 μs, and sufficiently high Rabi frequencies are available (we demonstrate this clearly in section 6.3.2), we conclude that the system is suitable for tests of interferometric cooling.

Chapter 6

Composite Raman pulses

As demonstrated in chapter 5, coherent pulses in the velocity-sensitive Raman system are subject to dephasing of atomic states. Dephasing is brought about by the presence of systematic variations in such system parameters as the intensity and detuning of the control field, and the velocities and angular momenta (Zeeman states) of the atoms (and hence the atom-light coupling strengths). For high-contrast interferometry and cooling we would like our experiment to exhibit robustness against these systematic errors, and, to this end, this chapter details our initial investigations into *composite pulses* for improving pulse efficiency in our system. These investigations represent a basic feasibility study of composite pulses for improving pulse fidelity in atom interferometric sensor applications.

The composite pulse is an established technique, developed by the nuclear magnetic resonance (NMR) community, for suppressing the effects of systematic errors in quantum control. A particularly comprehensive summary of composite pulses and their respective applications in NMR is given by Levitt in [72]. Broadly speaking, a composite pulse is a *sequence* of control field pulses with tailored durations and phases, which acts to replace the 'naive' *single* pulse, and offers increased tolerance to systematic errors.

Whilst composite pulses are a staple tool in NMR, they have not yet been fully exploited in atomic physics labs. They are in principle applicable to any system involving the quantum control of a two state system, and have been applied already outside NMR to the manipulation of superconducting qubits [73] and diamond NV colour-centres [74], and to trapped ions [75–78] for the purposes of quantum information processing (QIP).

In neutral atom based experiments, closer to the work in this thesis, composite pulse techniques have been employed to correct for inhomogeneities in spin squeezing [79] and optical lattice qubits [80–82]. Closer still to this work, composite pulses have been recently demonstrated to improve readout contrast in large area Raman pulse atom interferometry [83]. This latter experiment was performed in a similar system to ours, except that the atom sample was spin-polarised into the magnetic-insensitive Zeeman sublevel $m_F = 0$, and a narrow ($T < 0.5\,\mu$K) velocity class was pre-selected (using a Raman transition) from the initial velocity distribution. Such extra preparation results in a much less inhomogeneous system, but leads to a loss in atom number and hence a lowering of signal-to-noise. Furthermore, we intend to design a system for the cooling of atoms and molecules which have not undergone heavy state preparation and which are not already below the recoil temperature, therefore these initial preparation steps, although essential in precision atom interferometry, are avoided in our investigation.

In the following, we first describe a model for visualisation of systematic errors in two-level quantum systems based on the Bloch sphere picture, which is applicable to the Raman system used in this work. We then go on to report experimental tests of a range of composite pulses, and analyse their behaviour.

6.1 Composite pulse visualisation

In section 2.2, we introduced the Bloch sphere picture as a useful tool for visualisation of coherent pulses in atom interferometry. We defined the unit Bloch vector $\mathbf{R}$, whose Cartesian amplitudes are given by the parameters u, v, & w – the expectation values of the $\boldsymbol{\sigma}_{x,y,z}$ Pauli operators. Control field pulses are manifest as an effective torque on the Bloch vector, and cause it to rotate about an axis defined by the detuning and phase of the field, which we describe by the field vector $\boldsymbol{\Omega}$. In this chapter, we impose a coordinate transformation, and switch to describing the quantum state on the Bloch sphere in terms of the angles ϑ and φ, which are respectively the polar and azimuthal angles of the spherical coordinate system. These angles relate directly to the Cartesian

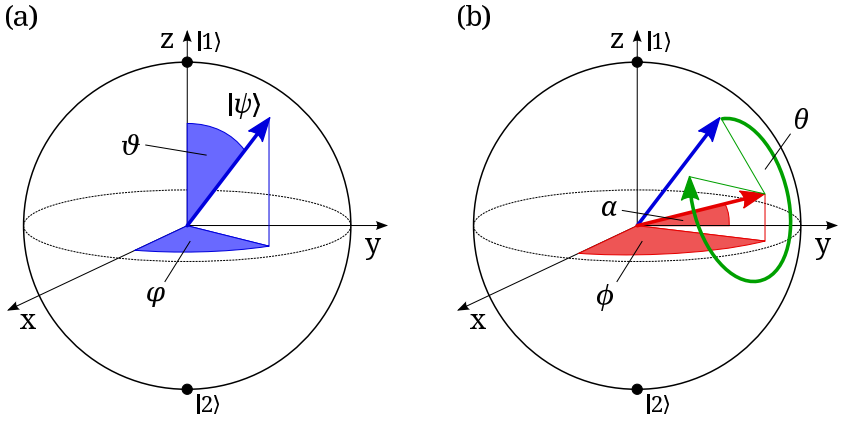

Figure 6.1: (a) A sketch of the quantum state vector $|\psi\rangle$ (blue arrow) on the unit sphere, as defined by the angles ϑ and φ. (b) A sketch of the field vector (red arrow), as defined by the angles α and ϕ. Control field pulses are represented by unitary rotations of the state vector around the field vector by an angle θ, as indicated by the green arrow.

components of $\mathbf{R}$ according to the coordinate transformation

$$u = \sin\vartheta\cos\varphi \tag{6.1a}$$

$$v = \sin\vartheta\sin\varphi \tag{6.1b}$$

$$w = \cos\vartheta, \tag{6.1c}$$

and can be used to define the state $|\psi\rangle$ of the quantum two-level system

$$|\psi\rangle = \cos\left(\frac{\vartheta}{2}\right)|1\rangle + e^{i\varphi}\sin\left(\frac{\vartheta}{2}\right)|2\rangle, \tag{6.2}$$

depicted in figure 6.1 a. As in section 2.2, control field pulses correspond to unitary rotations of $|\psi\rangle$ on the surface of the Bloch sphere. By solving the time-dependent Schrödinger equation, we find that the unitary rotation propagator

$$U(t) = \exp\left(\frac{i}{\hbar}\int_0^t \hat{H}(t')dt'\right) \tag{6.3}$$

which translates $|\psi\rangle$ to some other point $|\psi'\rangle$ on the Bloch sphere according to $|\psi'\rangle = U(t)|\psi\rangle$, takes the form [84]

$$\begin{aligned} U(\theta,\phi,\alpha) = &\cos\left(\frac{\theta}{2}\right)\mathbb{1} - i\sin\left(\frac{\theta}{2}\right)\times \\ &\left[\sigma_{\mathbf{x}}\cos(\phi)\cos(\alpha) + \sigma_{\mathbf{y}}\sin(\phi)\cos(\alpha) + \sigma_{\mathbf{z}}\sin(\alpha)\right], \end{aligned} \tag{6.4}$$

where the desired rotation, azimuth and polar angles are respectively related to the parameters introduced in section 2.2 according to

$$\theta = \tilde{\Omega}_R \times t \tag{6.5a}$$

$$\phi = \phi_L \tag{6.5b}$$

$$\alpha = \arcsin\left(\frac{-(\delta - \delta^{AC})}{\tilde{\Omega}_R}\right). \tag{6.5c}$$

As depicted in figure 6.1 b, and explained in section 2.2, the state vector rotates around the field vector (defined by the angles α and ϕ), by the angle θ. Note that in the above, the variables ϑ and φ are distinct from θ and ϕ. As discussed in section 2.2, interaction with a resonant control field corresponds to rotation about an axis in the equatorial plane ($\alpha = 0$), and results in Rabi oscillations at an angular frequency $\tilde{\Omega}_R = \Omega_R$ in the hyperfine state populations as functions of the interaction time t, while off-resonant fields correspond to inclined rotation axes, as depicted in figure 2.2.

6.1.1 Notation

The composite pulse sequences explored here all use control fields that are intended to be resonant so, for simplicity, we assume α in equation 6.4 to be zero and use the notation $\theta_\phi \equiv U(\theta, \phi, 0)$ to represent a rotation defined by the angles θ and ϕ (written in degrees). A sequence of such rotations is written as $\theta^{(1)}_{\phi_1}\theta^{(2)}_{\phi_2}\ldots$ where the pulses are applied in chronological order from left to right. The two key resonant pulses in the toolkit (section 2.2.4) are therefore denoted 180_0 for the π pulse ($\phi_L = 0$), where we set $\Omega_R\tau = \pi$, and 90_0 for the $\frac{\pi}{2}$ pulse, where $\Omega_R\tau = \pi/2$.

6.1.2 Systematic errors

The θ, ϕ, α formalism lends itself to a simple quantitative treatment of systematic errors and their effects. Systematic errors are manifest in a deviation from the correct rotation propagator, that is, the correct propagator $U(\theta, \phi, \alpha)$ is replaced with an incorrect propagator $V(\theta, \phi, \alpha)$. In the literature on composite pulses for NMR, there are two distinct classes of error, which in the Raman system are linked. These are described below.

6.1.2.1 Pulse-length errors

A pulse length error is represented by a deviation $\Delta\theta = \tilde{\Omega}_R \times \Delta t$ (or equivalently $\Delta\theta = \Delta\tilde{\Omega}_R \times t$) from the desired, or central, rotation angle $\theta = \tilde{\Omega}_R^{(0)} \times t$. For a resonant ($\delta - \delta^{AC} = 0$, $\tilde{\Omega}_R = \Omega_R$) rotation with a small fractional pulse-length error $\epsilon = \Delta\theta/\theta$,

$$\begin{aligned} V(\theta,0,0) &= U\big((1+\epsilon)\theta,0,0\big) + O(\epsilon^2) \\ &\equiv U(\theta,0,0) - \epsilon\frac{\theta}{2}\left[\sin\left(\frac{\theta}{2}\right)\mathbb{1} + i\cos\left(\frac{\theta}{2}\right)\sigma_{\mathbf{x}}\right] + O(\epsilon^2) \end{aligned} \tag{6.6}$$

(plus higher order terms). In our system, these resonant pulse length errors occur due to spatial inhomogeneities across the Raman beams, and to the different dipole coupling strengths associated with the different Zeeman sublevels (sources 1 & 2 in section 5.1.4.2), both of which are manifest in variations in the resonant two-photon Rabi frequency Ω_R.

6.1.2.2 Off-resonance errors

An off-resonance error is represented by an inclination in the axis about which the state vector rotates (the field vector), out of the equatorial plane, due to a non-zero detuning ($\delta - \delta^{AC} \neq 0$). Defining the fractional off-resonance parameter as $f = (\delta - \delta^{AC})/\Omega_R$, we find that for small f,

$$\begin{aligned} V(\theta,\phi,0) &= U\left(\theta,\phi,\sin^{-1}(f)\right) + O(f^2) \\ &\equiv U(\theta,\phi,0) + fi\sin\left(\frac{\theta}{2}\right)\sigma_{\mathbf{z}} + O(f^2). \end{aligned} \tag{6.7}$$

Off-resonance errors occur in our system due to Doppler shifts in the atomic detuning, and to Zeeman and light shift frequency-splitting of the m_F sublevels (sources 3 & 4 in section 5.1.4.2). As illustrated in figure 2.2 of section 2.2, for a fixed Ω_R the field vector $\mathbf{\Omega}$ becomes increasingly *tilted* out of the x-y plane as $\delta - \delta^{AC}$ is increased.

In the Raman system, and indeed any two-level system described by the generalised, off-resonant Rabi frequency $\tilde{\Omega} = \sqrt{\Omega^2 + \delta^2}$ where Ω is the resonant Rabi frequency and δ is the detuning from resonance, an off-resonance error is always accompanied by a pulse length error. This is because a change in δ leads to a change in the rotation rate $\tilde{\Omega}$, and hence a change in the observed rotation angle θ for a given time τ. This somewhat

degrades the relevance of our treatment of these systematic errors as two distinct types; however, since in the following we test composite pulses which are designed for robustness against either pulse length *or* off-resonance errors, we choose to continue with this treatment, and characterise the pulse fidelity as such.

6.1.3 Pulse fidelity

It is common to characterize the effectiveness of a composite pulse by the distance on the Bloch sphere between the final state $V|\psi\rangle$ and the intended target state $U|\psi\rangle$. This leads to the definition of the *pulse fidelity* $\mathcal{F}$, which for a general rotation from an arbitrary starting point is given by

$$\mathcal{F} = \frac{\left|\mathrm{Tr}(U^\dagger V)\right|}{\mathrm{Tr}(U^\dagger U)}, \tag{6.8}$$

and for a specific starting state $|\psi\rangle$ is defined as

$$\mathcal{F}_{|\psi\rangle} = |\langle\psi|V^\dagger U|\psi\rangle|^2. \tag{6.9}$$

In each case, the corresponding *infidelity* $\mathcal{I} = 1 - \mathcal{F}$, and its dependence upon the pulse-length and off-resonance errors ϵ and f, is also used to quantify the pulse's effectiveness. For example the basic 180_0 pulse has infidelity terms $O(\epsilon^2)$ and $O(f^2)$ (plus higher-order terms), due respectively to pulse-length and off-resonance errors (note that $O(\eta^n)$ error terms in $V(\theta, \phi)$ become $O(\eta^{2n})$ in $\mathcal{I}$), where the error terms are determined from the Maclaurin expansion of $\mathcal{I}$. By substituting the 'naive' θ_ϕ pulse with a composite pulse, it is possible to remove or reduce these second (and often higher) order infidelity terms.

There are two distinct types of composite pulse, each characterised by its associated fidelity. The first type is known as the *general rotor*. This is a composite pulse designed to perform the correct rotation from any *arbitrary* starting point on the Bloch sphere. Hence to describe the fidelity $\mathcal{F}$ of a general rotor we typically use equation 6.8. The second type is the *point-to-point pulse*. This is a composite pulse designed to perform a rotation from a *specified* starting point $|\psi_i\rangle$ to a specified end point $|\psi_f\rangle$. Point-to-point pulses are typically shorter than general rotors. The fidelity of a point-to-point pulse is given by equation 6.9.

For components of more complex interferometer schemes, different measures of pulse effectiveness may be relevant, for one may be more interested in, say, the phase uncertainty of a superposition than in the balance of the superposed components. Here, however, we investigate only π, or *inversion* pulses which aim to make the rotation $|1\rangle \rightarrow |2\rangle$ or *vice versa*. For an inversion from the starting state $|\psi\rangle = |1\rangle$ to the target state $U|1\rangle = |2\rangle$, where the erroneous resultant state is $|\psi_{\text{exp}}\rangle = V|1\rangle$, the fidelity takes the form $\mathcal{F}_{|\psi\rangle} = \langle\psi_{\text{exp}}|2\rangle = |c_2|^2$.

For the purposes of this work, the most important characteristic of a composite inversion is its peak fidelity

$$\mathcal{F}_P = |c_2|^2\Big|_{\delta_L - \delta^{AC}=0}, \tag{6.10}$$

which indicates the efficiency of inversion with a resonant pulse. Another key feature is the spectral width of $|c_2|^2$ which, broadly speaking, indicates the robustness of the pulse against off-resonance errors. We characterise both of these in sections 6.3.1 and 6.3.2.

6.2 Rotary spin echoes

In this section, we re-visit velocity-sensitive Rabi flopping, and apply to it what may be considered a basic form of composite rotation – the rotary spin echo.[1] In section 5.2.2 we presented resonant Rabi flopping in the velocity-sensitive Raman arrangement, and discussed the significant sources of dephasing therein. We re-plot those results in figure 6.2 a, where the blue circles are the experimental data and the red curve is the numerical simulation using the parameters given in the table in figure 5.11. In summary, the accrued systematic errors cause the atoms' states to dephase rapidly with respect to each other, until a quasi-steady-state is reached at $|c_2|^2 \approx 0.28$. The system has dephased completely after only one Rabi cycle, and the peak fidelity $\mathcal{F}_P = 0.48$. The two primary sources of dephasing are, as described in sections 5.1.4.2 and 5.2.2, differences in inherent coupling strengths across sublevels, and Doppler-broadening.

A basic method for reducing the dephasing effect in Rabi flopping is the rotary spin echo [82]. Reminiscent of Hahn's original spin echo experiments [85], this is a repeated application of the sequence $\theta_\phi\theta_{\phi+180^\circ}$, which gives greatly enhanced Rabi flopping contrast in

[1] This is not a composite pulse in the traditional sense, but it does give a neat demonstration of how altering the phase of the control field can enhance the contrast of an observable.

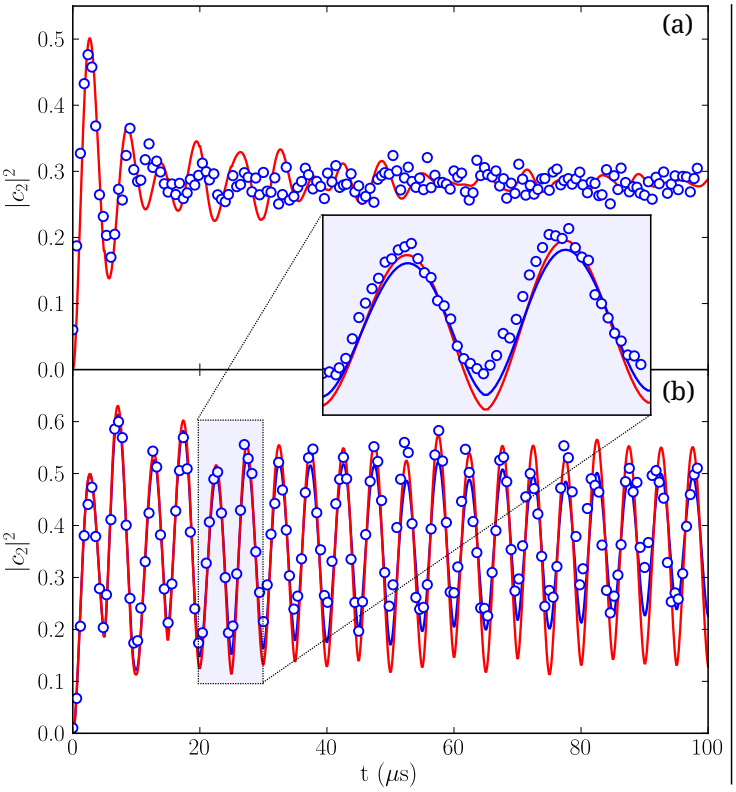

Figure 6.2: Measure of the upper hyperfine state population $|c_2|^2$ as a function of interaction time t with the Raman beams: (a) Rabi flopping with a regular rectangular pulse; (b) Rabi flopping with rotary echoes. The inset is a highly-sampled dataset for the indicated portion of (b). Blue circles are experimental data, and red curves are numerical simulations using the parameters given in figure 5.11. The blue curve is a simulation assuming a $\pi/6$ phase noise; (c) Bloch vector trajectory during the rotary echo 360_0360_{180} in the presence of an off-resonance error: Bloch vector trajectory (dark blue dots) and initial (light blue) and final (dark blue) Bloch vectors, along with the field vectors (red) during the first rotation (i) and the second rotation (ii).

the case where $\theta = 360°$. The 180° phase shift every whole Rabi cycle causes a deflection of spin vector trajectories and a cyclical recombination, or 'echo', of divergent spins. A visual representation of the rotary echo on the Bloch sphere for the case of off-resonance errors, which as previously discussed come with attached pulse-length errors, is shown in figure 6.2 c. During the initial 360_0 rotation (figure 6.2 c i), the Bloch vector (initial – light blue, final – dark blue) rotates about the inclined off-resonant field vector (red), and due to the associated systematic errors, overshoots $|1\rangle$, the target point. When the phase ϕ_L of the beams is shifted by 180°, the field vector $\mathbf{\Omega}$ is rotated 180° about the z-axis (see figure 2.3), hence during the second rotation (figure 6.2 c ii) the Bloch vector follows a *reversed* trajectory which is an approximate mirror image of the initial rotation. Since the duration of both rotations is the same, the initial overshoot is 'undone'

by the second rotation, and the Boch vector arrives at the 'echo' much closer to $|1\rangle$.

The remarkable increase in Rabi flopping contrast with this technique is presented in figure 6.2 b. This scan was taken immediately after that of figure 6.2 a, so that a comparison could be made using a numerical simulation assuming the same parameters (see figure 5.11). Whilst good considering the now-large parameter space, the agreement between experiment and simulation appears divergent with increasing pulse duration, and this behaviour solicits some discussion. The simulation suggests that contrast should be preserved without decay for the duration of the scan after $t \approx 20\,\mu$s. The data, however, exhibit a decaying contrast. It is important to note that since in this scan t was sampled incrementally (from $0\,\mu$s to $100\,\mu$s), as opposed pseudo-randomly, this dataset is subject to drift. Whilst this may contribute to the observed decay in contrast, simulations suggest that the magnitude of drift required to account for *all* of the observed decay is equivalent to a change in Ω_{eff} of -40% from the beginning of the scan to the end. This is unreasonably large, so we must look elsewhere for sources of decay. Rakreungdet *et al* in [82], after observing similar lower-than-expected dephasing times, consider the effects of *phase noise* in rotary echoes, brought about by imperfect performance of frequency-synthesising and phase-shifting apparatus. In light of this, we simulate the rotary echo assuming uniform phase noise, which we model by adding $\eta \times \Delta\phi_L$, where η is a pseudo-randomly generated number $-1 \leq \eta > 1$ (from a uniform distribution) and $\Delta\phi_L$ is the maximum phase excursion, to the phase ϕ_L. We find good qualitative agreement with the data where $\Delta\phi_L = \pi/6$ radians, as represented by the blue curve in figure 6.2 b. The manufacturer of the I&Q modulator (see section 4.3.3) specifies a phase noise of $\pm 7°$ ($\Delta\phi_L = \pi/25$ radians), which is much smaller than the simulation suggests, however we expect that there may be further significant sources of electical phase noise, possibly associated with the electro-optical modulator (see section 4.3.2). Furthermore, it is likely that a large amount of phase noise in the counter-propagating Raman arrangement could accrue due to relative motion of the optics along the two separate beam paths. This effect would be more pronounced on longer timescales, since the mechanical motion of the optics will be relatively slow compared with the Rabi frequencies concerned here.

For completeness, we include here other possible causes for the decay in contrast, namely: (a) accrued effects due to the transient change in intensity upon phase shifts (see figure 4.4); (b) incorrect phase shifts and phase-dependent intensities (see figure 4.5); and (c)

unwanted state evolution during the finite switch-on/off time of the Raman beams (see figure 4.10). None of the above were included in the simulations. Furthermore, we do not rule out the possibility that the velocity distribution and scaling parameters used in the simulation may be incorrect, since we did not take a Raman velocimetry measurement before taking the data.

Aside from the rephasing effects of the rotary echo, figure 6.2 b represents a demonstration that our system exhibits long coherence times. After an interaction with the resonant Raman beams corresponding to $\theta = 40\pi$ radians $= 7200°$ and beyond, time-dependent features in $|c_2|^2$ remain visible over experimental noise. This combined coherent interaction duration is longer than that of any interferometric sequence intended for trial with this experimental setup.

Although it is a neat demonstration of how composite rotations can improve the readout signal of a particular observable, the rotary spin echo is useful only in its enhancement of Rabi flopping, which has little useful application.

6.3 Composite inversion pulses

In this section, we demonstrate composite rotations which counteract dephasing in π, or 'inversion' pulses in our Raman system. There exists a large 'zoo' of composite inversion pulses, all well-documented by the NMR community, but we restrict ourselves to just a select few in this work. Section 6.3.1 details the results of composite inversion pulses in the $\sigma^+ - \sigma^+$ counter-propagating Raman arrangement which, due the light shift behaviour described in section 5.1.2.1, exhibits large off-resonance errors. Following this, section 6.3.2 details the results of composite inversion pulses in the $\pi^+ - \pi^-$ arrangement, in which off-resonance errors are smaller.

In order to characterise the peak fidelity $\mathcal{F}_P$ and the spectral width of each composite inversion pulse, we measure the resultant population $|c_2|^2$ at a range of normalised laser detunings $\delta_L/\Omega_{\text{eff}}$, as shown in figures 6.3 and 6.6. For comparison, the result for a basic 180_0 pulse is shown in each case. To gather these data, measurements for all of the five pulses were interleaved within the same experimental run, at randomised sample detunings δ_L. This ensured that the spectral profile was less vulnerable to drift, and

that all of the pulses could be comfortably modelled by a common set of parameters, as given in the table to the right of the plots. Each data point in figures 6.3 and 6.6 is an average over 16 shots, and each set took around 40 minutes to collect. The effective Rabi frequency was measured (as described in section 5.1.3) in order to estimate the π pulse time t_π. A discussion of each of these curves, along with some which we choose only to simulate, is given in the following. Descriptions of each of the sequences, along with their expected performance in the presence of each type of error, are adapted from discussions with Jonathan Jones of the University of Oxford.

6.3.1 $\boldsymbol{\sigma^+ - \sigma^+}$

In the $\sigma^+ - \sigma^+$ arrangement, the m_F sublevels are separated due to the AC Stark shift, depending on the intensity of the Raman beams (see section 5.1.2.1). As described previously, this intensity-dependent splitting can be counteracted via the Zeeman shift by an offset in the magnetic field along the axis of the beams. The measured beam powers corresponding to figure 6.3 were $P_{1,2} = 60 \pm 2\,\mathrm{mW}$, corresponding to the intensities $I_1 = 20\,\mathrm{kW/m^2}$ and $I_2 = 30\,\mathrm{kW/m^2}$, and the single photon detuning was $\Delta = 2\pi \times 9.0 \pm 0.5\,\mathrm{GHz}$. We find good agreement between the data and simulations where $I_{1,2}$ (Δ) is around 30% lower (higher) than the measured value (see section 5.1.4.1), hence the reduced intensities in the table. With these parameters, and in the absence of a magnetic field along the z-axis, the splitting between adjacent sublevels is approximately 250 kHz. This implies (see section 5.1.1) that a magnetic field of $B_z = -250/(2\times0.47) = -267\,\mathrm{mG}$, corresponding to a shim coil current $I_z \approx 86 - (267/3.43) = 8\,\mathrm{mA}$, would be required to bring the levels into degeneracy. Such an offset would lead to a complete loss of signal (without realignment) due to the shift in the zero-point of the MOT quadrupole field, so we choose not to apply it here, and we instead work at $I_z \approx 80\,\mathrm{mA}$ (equivalent to $B_z = -11\,\mathrm{mG}$ for $I_z^{(0)} = 83\,\mathrm{mA}$). The result is a system with large off-resonance errors, and although this may not be ideal for optimal pulses, it represents a challenging test-bed for composite pulses which are, after all, designed to be robust against such errors.

Figure 6.3 a shows a basic 180_0 rotation, or π pulse at an empirically-measured Rabi frequency of $\Omega_{\mathrm{eff}} \approx 2\pi\times360\,\mathrm{kHz}$. Due in-part to the light shift induced splitting, the peak

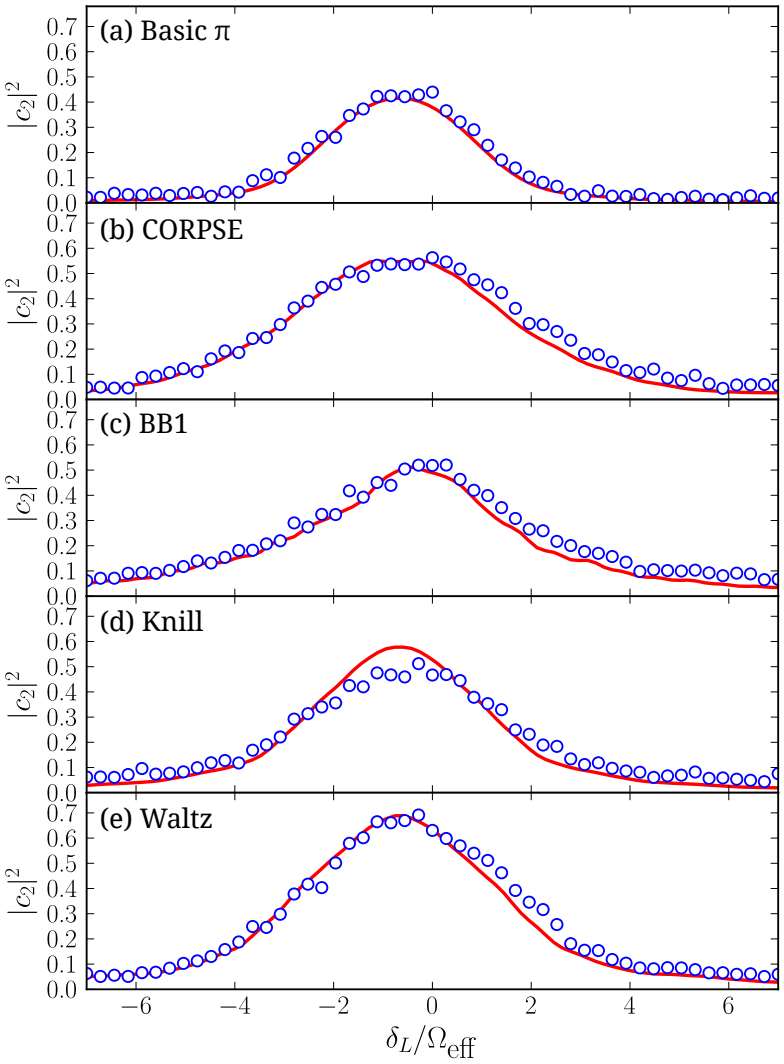

Param.	Value
I_1	14 kW/m^2
I_2	21 kW/m^2
Δ	$2\pi \times 9.0$ GHz
B_z	−11 mG
σ_1	$2.5 \times v_R$
σ_2	$9 \times v_R$
a_1 / a_2	2
S	0.9
t_π	1.4 µs

Figure 6.3: Resultant population $|c_2|^2$ as a function of normalised laser detuning for four different composite inversion pulses, as compared with a basic π 180_0 rotation: (a) Basic π pulse; (b) CORPSE; (c) BB1; (d) Knill; and (d) Waltz. The blue circles are experimental data and the red curves are numerical simulations using the parameters given in the table to the right. These data were taken in the $\sigma^+ - \sigma^+$ counter-propagating Raman arrangement. $\Omega_{\text{eff}} \approx 2\pi \times 360\,\text{kHz}$.

fidelity is limited to $\mathcal{F}_P = 0.42$. Simulations suggest that a system with $B_z = -267\,\text{mG}$, and otherwise identical parameters, would yield $\mathcal{F}_P = 0.66$, and as a pre-emptive remark with the following section in mind, a peak fidelity identical to this is indeed observed in the $\pi^+ - \pi^-$ arrangement, where Zeeman-degeneracy is uncompromised by high beam intensities. We find a good approximation to the data with simulations assuming $\sigma_1 = 2.5 \times v_R$ ($9\,\mu$K), $\sigma_2 = 9 \times v_R$ ($120\,\mu$K), and $a_1/a_2 = 2$, which corresponds to an average temperature of $\sim 80\,\mu$K. To account for the loss of atoms from the interrogation region (see section 5.1.3.1), we set the scaling parameter to $S = 0.9$. As before, to obtain the

Pulse Type	**Rotation Sequence (total angle)**	$\mathcal{F}_P$	$\frac{\mathcal{F}_P}{\mathcal{F}_P(180_0)}$
π-pulse	180_0	0.42	1
CORPSE†	$60_0300_{180}420_0$ (780°)	0.55	1.31
BB1†	$180_{104.5}360_{313.4}180_{104.5}180_0$ (900°)	0.50	1.19
Knill†	$180_{240}180_{210}180_{300}180_{210}180_{240}$ (900°)	0.58	1.38
WALTZ*	$90_0180_{180}270_0$ (540°)	0.69	1.64
90-360-90*	$90_0360_{120}90_0$ (540°)	0.53	1.26
SCROFULOUS†	$180_{60}180_{300}180_{60}$ (540°)	0.40	0.95
Levitt*	$90_{90}180_090_{90}$ (360°)	0.63	1.50
90-240-90†	$90_{240}240_{330}90_{240}$ (420°)	0.57	1.36
90-225-315*	$90_0225_{180}315_0$ (630°)	0.64	1.52

Table 6.1: Summary of composite inversion pulses and their effectiveness in the $\sigma^+ - \sigma^+$ Raman arrangement, where there exists a significant splitting of the m_F sublevels. $\mathcal{F}_P$ values are estimated using the numerical simulation for the set of parameters given in figure 6.3. $\mathcal{F}_P$ can be divided by $S = 0.9$ to give the true estimated peak fidelity. †General rotor; *point-to-point pulse.

'true' values of $|c_2|^2$, one can divide those shown in the figures (and tables) by S.

The CORPSE (Compensation for Off-Resonance with a Pulse SEquence) [86], shown in figure 6.3 b, is a general rotor composite pulse denoted $\alpha_0\beta_{180}\gamma_0$, which in the case of inversion is equal to $60_0300_{180}420_0$. It suppresses off-resonance errors by removing the $O(f^2)$ term [and reducing $O(f^4)$] in the infidelity $\mathcal{I}$, and its sensitivity to pulse-length errors is equal to that of a basic 180_0 pulse; therefore, whilst it should reduce the effect of Doppler-broadening and Zeeman non-degeneracy, we do not expect it to address the errors associated with a range of Raman routes. It exhibits a 31% increase in the peak fidelity $\mathcal{F}_\mathcal{P}$ compared with the basic π pulse, and a relatively broad profile compared with the other pulses in figure 6.3. The large width of the CORPSE profile confirms that it is particularly robust against off-resonance errors.

A popular pulse in NMR, and the second pulse we test, is the general rotor known as BB1 (Broad-Band 1) [87], shown in figure 6.3 c. The BB1 constitutes a standalone correction sequence $180_{104.5}360_{313.4}180_{104.5}$, followed by the regular 180_0 rotation which can be replaced by one 90_0 rotation on either side of the correction sequence to make the pulse time-symmetric. It removes pulse-length infidelity terms $O(\epsilon^2)$ and $O(\epsilon^4)$ at no cost in sensitivity to off-resonance errors. We find in our system that the BB1 is inferior to the CORPSE except out in the wings, where $(\delta - \delta^{AC})/\Omega_{\text{eff}} > 5$, where there is a very small gain. On resonance, we observe an increase in peak fidelity of only

19%. According to the literature the BB1 is the most experimentally effective pulse in the toolkit for combatting pulse-length errors. This leads us to believe that either (a) pulse-length errors are a less significant contributor to dephasing; or (b) the pulse-length errors present in our system are outside the effective range of the BB1. The former would appear more likely.

The third composite pulse we examine is the sequence $180_{240}180_{210}180_{300}180_{210}180_{240}$, shown in figure 6.3 d. This is referred to in literature as the 'Knill' pulse [88], after Emanuel Knill, but its use originates in early work by Tycko and Pines [89]. It is a five-pulse temporally symmetric general rotor which corrects for both pulse-length *and* off-resonance errors such that the $O(\epsilon^2)$ and $O(f^2)$ infidelity terms are removed and the $O(f^4)$ term is reduced. This is the only pulse in the list where we observe significant disagreement between experiment and simulation around $\delta_L - \delta^{AC} = 0$. We expect that this is because our apparatus is less capable of applying the required phase shifts within the Knill pulse than the simple 180° shifts within, say, the CORPSE. This is paid more consideration in section 6.3.3, where we examine the temporal evolution during these composite pulses. With the (simulated) Knill pulse we achieve a 38% increase in $\mathcal{F}_P$, but the increase in $|c_2|^2$ at larger values of detuning is smaller than we observe with the CORPSE. As a general note, we expect temporally symmetric composite pulses such as the Knill to behave differently from asymmetric ones such as the CORPSE in the context of atom interferometry, where unwanted velocity-dependent phase can accrue during pulses. This is explained in a little more detail later on.

The $90_0180_{180}270_0$ sequence, known as 'Waltz' [90] (so-named for its '123' structure), is the fourth and final pulse we test experimentally. This is a point-to-point pulse, shown in figure 6.3 e, which is by far the most effective composite pulse of the four. It is robust against a wide range of off-resonance errors (but does not correct for pulse-length errors), and gives an increase in $\mathcal{F}_P$ of 64% compared with a basic π pulse. The Waltz is also the shortest of the composite pulses tested in this work (540°).

For all of the above composite pulses, with the exception of the Knill pulse, we observe good agreement between experiment and theory. We therefore expect that the model alone can be used to predict the effectiveness of other composite pulses to a good degree of accuracy without the need for experimental verification. With this in mind, we characterise the remainder of the composite pulses using only the numerical simulation.

Like the BB1 pulse, the sequence $90_0360_{120}90_0$ removes $O(\epsilon^2)$ and $O(\epsilon^4)$ terms in $\mathcal{I}$ at no cost to off-resonance sensitivity. However this one is a point-to-point pulse, designed for transfer from pole-to-pole on the Bloch sphere. It is 360° 'shorter' than the BB1 and Knill pulses, thus making it of greater interest in experiments where interrogation time is limited. The $90_0360_{120}90_0$ is predicted to give a $\mathcal{F}_P$ increase of 26%, and to perform relatively well at larger values of detuning.

We find that the $90_{90}180_090_{90}$ point-to-point pulse, which was the very first composite pulse, designed by Levitt [29], performs better than all of the general rotor composite pulses tested experimentally. It affords an increase in peak fidelity of 50%, and only requires twice the interaction duration of a basic π pulse, making it of potential use where interrogation time is strictly limited. We find the $180_{60}180_{300}180_{60}$ SCROFULOUS [91] general rotor, which has infidelity in $O(\epsilon^6)$ but suffers increased sensitivity to off-resonance errors, to be the least effective composite pulse of those tested here, where we are characterising the pulses as a function of the detuning (the off-resonance parameter) only. Another potentially interesting composite pulse, which claims to correct for off-resonance and pulse-length errors simultaneously, is the relatively short sequence $90_{240}240_{330}90_{240}$ [92]. Our simulations suggest that this pulse gives an increase in $\mathcal{F}_P$ of 36%, making it less effective than the Levitt pulse for peak fidelity. Interestingly this pulse behaves as a general rotor for off-resonance errors, and a point-to-point inversion for pulse-length errors.

Of the untested composite pulses, we predict the most effective to be the point-to-point pulse $90_0225_{180}315_0$ [93], which gives an increase in $\mathcal{F}_P$ of 52%. We conclude therefore that the largest improvement in peak fidelity in the $\sigma^+ - \sigma^+$ Raman arrangement (at the particular set of parameters given) is achieved with the Waltz pulse. As a general note, the three most effective composite pulses here are of the point-to-point variety.

The Waltz sequence is presented in the context of atom interferometer augmentation pulses, which act to increase the interferometric area, in [83] with positive results. It is interesting to note that for an equal superposition starting-state $|\psi\rangle = \frac{1}{\sqrt{2}}(|1\rangle + e^{i\phi}|2\rangle)$, a single Waltz inversion pulse performs *worse* than a basic 180_0 pulse in the presence of off-resonance errors (a general rotor would work better in this case), but a sequence of *two* Waltz pulses gives an efficient 2π rotation. Furthermore, when *two* sequences of two Waltz pulses are applied as in the large area interferometer in [83], readout

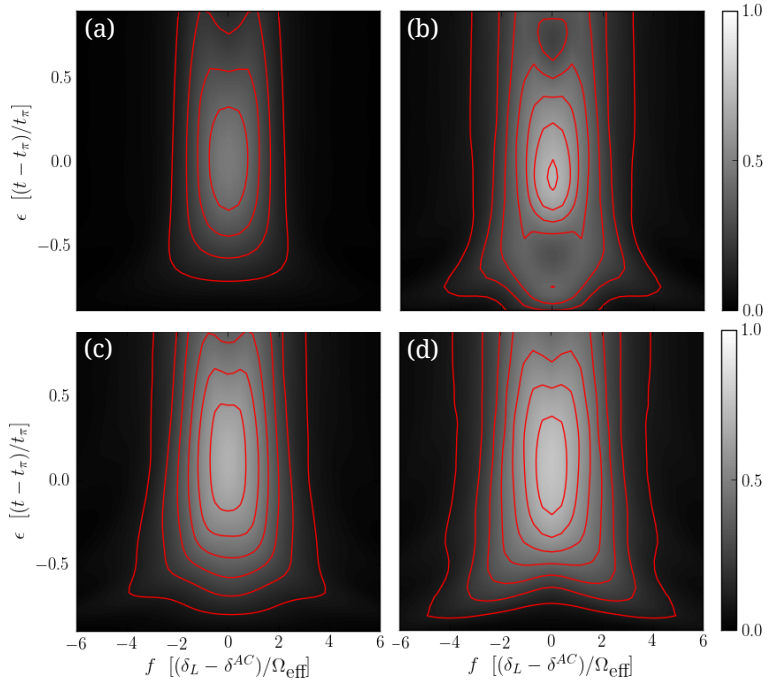

Figure 6.4: Simulated resultant population $|c_2|^2$ as a function of the off-resonance parameter f and the pulse-length parameter ϵ for three different composite inversion pulses, as compared with a basic π 180_0 rotation: (a) Basic π pulse; (b) Knill; (c) Levitt; and (d) Waltz. These simulations were performed in the $\sigma^+ - \sigma^+$ counter-propagating Raman arrangement. $\Omega_{\text{eff}} = 2\pi \times 410$ kHz, $t_\pi = 1.22\,\mu$s. Contours at $0.1, 0.2, 0.3, \ldots$

contrast is increased. In light of this, future work on composite pulses in our system will examine the significance of pulse time-symmetry and the effectiveness of general rotors in contrast with point-to-point pulses, in the more general case where we are not restricted to inversion pulses.

In the above we have characterised the composite pulse performance only as a function of the detuning from resonance at a single, fixed, pulse length, whilst focussing on the peak fidelity as the most important quantity. It is common in the composite pulse literature to see the pulse fidelity plotted as a function of both the off-resonance parameter f *and* the pulse-length parameter ϵ. This allows us to examine and compare the behaviour of composite pulses at a range of different field strengths, and gives us a more complete understanding of the overall pulse performance. Although no data was taken for different pulse lengths, for completeness we show simulations of the composite pulse performance for a select few pulse types in figure 6.4. The simulated curves in figures 6.3 a, d and e correspond to horizontal slices through plots 6.4 a, b and d respectively, at $t = 1.4\,\mu$s ($\epsilon = 0.15$). In general, a composite pulse which exhibits a broader fidelity profile along

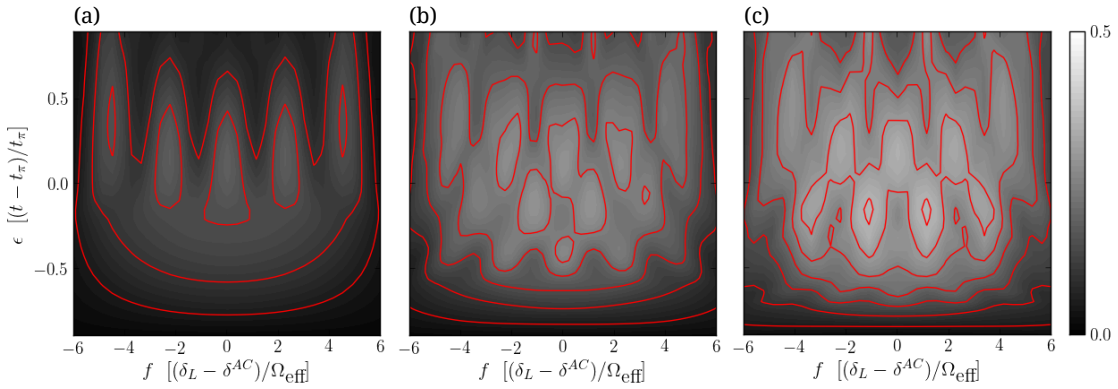

Figure 6.5: Simulated resultant population $|c_2|^2$ as a function of the off-resonance parameter f and the pulse-length parameter ϵ for two different composite inversion pulses, as compared with a basic π 180_0 rotation, where an artificial Zeeman splitting of $m_F \times 700\,\text{kHz}$ has been applied: (a) Basic π pulse; (b) Levitt; and (c) Waltz. These simulations were performed in the $\sigma^+ - \sigma^+$ counter-propagating Raman arrangement. $\Omega_{\text{eff}} = 2\pi \times 410$ kHz, $t_\pi = 1.22\,\mu$s. Contours at $0.05, 0.10, 0.15, \ldots$

the f-axis is more effective at compensating for off-resonance errors, and one which is broader along the ϵ-axis compensates more effectively for pulse-length errors. Figure 6.4, however, illustrates that fidelity is in general non-linear as a function of f and ϵ, and that indeed in some cases [see the Knill pulse (figure 6.4 b), for example], the fidelity is *increased* as one or both of f and ϵ increases. Furthermore, whilst the Levitt pulse (figure 6.4 c) exhibits the lowest peak fidelity of the three composite pulses shown, its 0.1 and 0.2 contours occur at relatively large values of $|f|$ as compared with the Knill pulse. Whilst the peak pulse fidelity $\mathcal{F}_P$ remains the most important measure of the pulse effectiveness in our system, for applications where the experimenter is interested in a greater average fidelity over a large range of errors, a broader fidelity profile is a more desirable characteristic than a large $\mathcal{F}_P$, and the two are not necessarily correlated one-to-one.

To end this section[2], we present simulations of the composite pulse fidelity where we apply an artificial Zeeman splitting to the atomic m_F sublevels. This represents an exagerrated form of the light-shift-induced, Zeeman-like splitting which is present in the $\sigma^+ - \sigma^+$ arrangement at low B_z (but not in $\pi^+ - \pi^-$), and allows us to more easily visualise the effect of Zeeman non-degeneracy on the pulse fidelity. Figure 6.5 shows the pulse fidelity as a function of f and ϵ for (a) a basic π pulse as compared with (b) a Levitt pulse and (c) a Waltz pulse, where in all cases a Zeeman splitting of $m_F \times 700\,\text{kHz}$ has

[2]This was added at the request of the PhD examiner.

been applied. In this case, one can clearly distinguish the five m_F sublevels. In figures 6.3 and 6.4, the sublevels are indeed separated in a qualitatively similar manner (by the light shifts only), but to a quantitatively lesser extent such that it is not clearly visible in the plots. For the basic π pulse, the fidelity $|c_2|^2$ peaks at just below 0.2 for each of the five sublevels, since the population is divided equally between them, and the difference in the Raman Rabi frequencies of the five levels is evident in the different peak positions along the ϵ-axis. Because the Levitt and Waltz composite pulses act to improve the fidelity at where errors are present, we predict an increase in the peak heights due to the effective broadening of each sublevel. These plots also clearly illustrate the *asymmetry* of the composite pulse fidelity as a function of f and ϵ.

6.3.2 $\boldsymbol{\pi^+ - \pi^-}$

We now investigate the $\pi^+ - \pi^-$ arrangement, which we expect to exhibit smaller off-resonance errors due to the nature of the light shifts (see section 5.1.2.2). In this arrangement, the Zeeman levels are degenerate at low B_z, hence off-resonance errors due to sublevel splitting (source 3 in section 5.1.4.2) are absent. As a result, the off-resonance parameter f at $\delta_L - \delta^{AC} = 0$ is broadened only by the Doppler shift. The data are presented in figure 6.6, where the measured parameters are identical to those in figure 6.3, with the exception of the detuning $\Delta = 2\pi \times 8.0 \pm 0.5\,\text{GHz}$. This gave rise to the higher-than-previous empirically-measured Rabi frequency $\Omega_{\text{eff}} \approx 2\pi \times 420\,\text{kHz}$.

As a result of power broadening, the spectral width of the basic π pulse 180_0 (figure 6.6 a) is much larger than the estimated velocity distribution. For a π pulse at $\Omega_{\text{eff}} \approx 2\pi \times 420\,\text{kHz}$, the spectral FWHM is approximately $2\pi \times 780\,\text{kHz}$, which is equivalent to the width of a single-Gaussian velocity distribution with $\sigma_v = 12 v_R$, or temperature $T \approx 210\,\mu\text{K}$. Although the spectral width of the transition is broader than the velocity distribution, this does not represent the regime where $\Omega_{\text{eff}} \gg 2k\sigma_v$, hence $\mathcal{F}_P$ for the basic π pulse is still limited to much less than 0.96. For this pulse, we find good agreement between experiment and theory, and the peak fidelity accounting for the loss of atoms is $\mathcal{F}_P/S = 0.73$.

With the CORPSE pulse (figure 6.6 b) we achieve an increase in $\mathcal{F}_P$ of 8%. The simulation of the CORPSE suggests that periodic structure should be visible within the

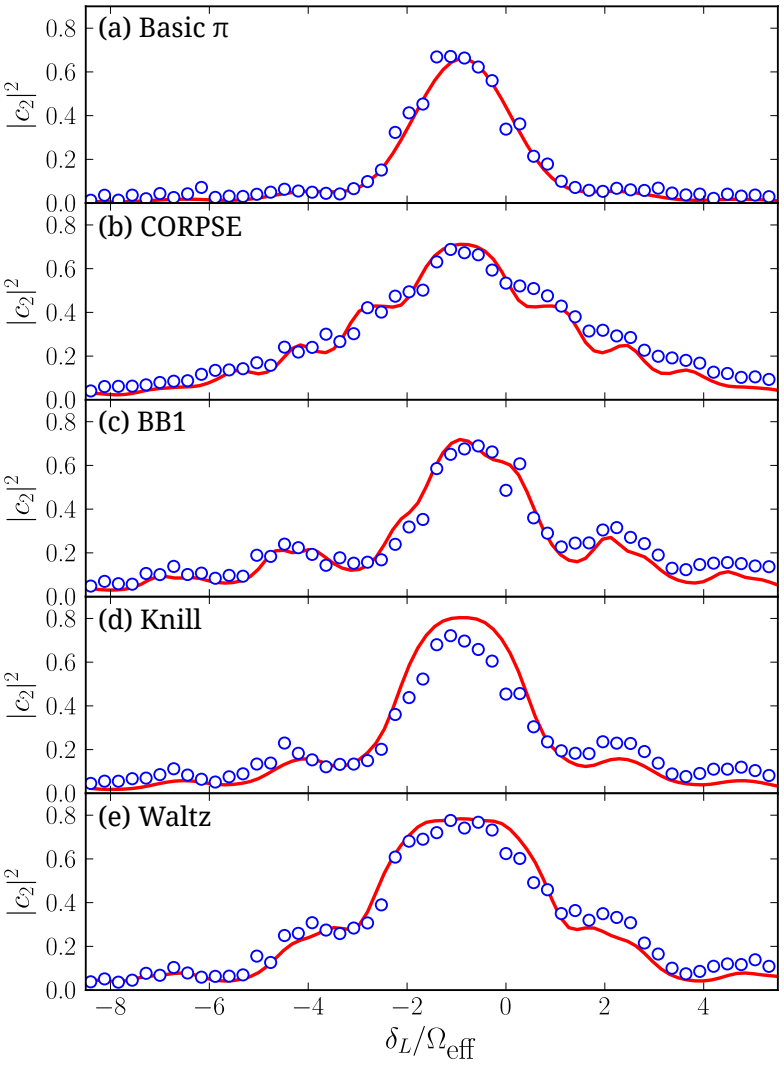

Param.	Value
I_1	14 kW/m^2
I_2	21 kW/m^2
Δ	$2\pi \times 8.0$ GHz
B_z	− 11 mG
σ_1	$2.5 \times \nu_R$
σ_2	$9 \times \nu_R$
a_1 / a_2	2
S	0.9
t_π	1.2 µs

Figure 6.6: Resultant population $|c_2|^2$ as a function of normalised laser detuning for four different composite inversion pulses, as compared with a basic 180_0 rotation: (a) Basic π pulse; (b) CORPSE; (c) BB1; (d) Knill; and (d) Waltz. The blue circles are experimental data and the red curves are numerical simulations using the parameters given in the table to the right. These data were taken in the $\pi^+ - \pi^-$ counter-propagating Raman arrangement. $\Omega_{\text{eff}} \approx 2\pi \times 420\,\text{kHz}$.

spectral profile, although this appears washed out in the experiment. On the other hand, the BB1 (figure 6.6 c) exhibits detuning-dependent structure which is clearly visible in the data. We find that the BB1 performs marginally better than the CORPSE in this case (a 9% improvement), due to the reduced impact of off-resonance errors. In theory, the Knill (figure 6.6 d) pulse is expected to be the most effective of all the $\pi^+ - \pi^-$ composite pulses tested here, owing to the fact that it corrects for both (the already relatively small) pulse-length *and* off-resonance errors. Once again, however, we observe a reduction in experimental fidelity compared with the theory, probably due to

Pulse Type	**Rotation Sequence (total angle)**	$\mathcal{F}_P$	$\frac{\mathcal{F}_P}{\mathcal{F}_P(180_0)}$
π-pulse	180_0	0.66	1
CORPSE†	$60_0300_{180}420_0$ (780°)	0.71	1.08
BB1†	$180_{104.5}360_{313.4}180_{104.5}180_0$ (900°)	0.72	1.09
Knill†	$180_{240}180_{210}180_{300}180_{210}180_{240}$ (900°)	0.80	1.21
WALTZ*	$90_0180_{180}270_0$ (540°)	0.79	1.20
90-360-90*	$90_0360_{120}90_0$ (540°)	0.74	1.12
SCROFULOUS†	$180_{60}180_{300}180_{60}$ (540°)	0.65	0.98
Levitt*	$90_{90}180_090_{90}$ (360°)	0.77	1.17
90-240-90†	$90_{240}240_{330}90_{240}$ (420°)	0.79	1.20
90-225-315*	$90_0225_{180}315_0$ (630°)	0.80	1.21

Table 6.2: Summary of composite inversion pulses and their effectiveness in the $\pi^+ - \pi^-$ Raman arrangement, where the m_F sublevels are degenerate. $\mathcal{F}_P$ values are estimated using the numerical simulation for the set of parameters given in figure 6.6. $\mathcal{F}_P$ can be divided by $S = 0.9$ to give the true estimated peak fidelity. †General rotor; *point-to-point pulse.

the nature of the phase shifts in our particular setup. As in the $\sigma^+ - \sigma^+$ arrangement, we find the most effective experimentally-tested composite pulse for peak fidelity in an inversion to be the Waltz pulse (figure 6.6 e). We observe good agreement between experiment and theory in the spectral profile, and an increase in $\mathcal{F}_P$ compared with the basic π pulse of 20%. The estimated peak fidelity for the Waltz pulse accounting for the loss of atoms is $\mathcal{F}_P/S = 0.88$.

In interferometers where strings of interleaved inversion pulses are applied to increase the interferometric area [94], one requires a high peak fidelity to avoid loss of contrast. After application of 8 resonant basic π pulses (required for the '$N = 2$' interferometer described in [83]) one expects, for the parameters given in the above, a maximum output fidelity of $0.73^8 = 0.08$. By replacing these with Waltz pulses, we expect this fidelity to increase to $0.88^8 = 0.36$, and assuming there is no detrimental impact on the interferometer phase, the output contrast should be much improved.

We refer the reader to table 6.2 for the estimated performances of all the un-tested composite pulses, and state here that of these the greatest improvement in $\mathcal{F}_P$ is afforded by the 90-225-315 pulse, which we predict to be marginally better than the Waltz. Also, the Waltz is matched for $\mathcal{F}_P$ improvement in this arrangement by the 90-240-90 pulse.

6.3.3 Temporal evolution

By terminating the sequence at various times before completion, we are able to measure the evolution of the excited state population $|c_2|^2$ during a resonant composite pulse. This gives us extra insight into the lower-level behaviour of the system, and allows us to pin-point particular effects which may be inhibiting the performance of our composite pulses.

Figure 6.7 shows the temporal evolution of $|c_2|^2$ in the $\sigma^+ - \sigma^+$ Raman arrangement for the same four composite pulses we tested in section 6.3. Each point is an average over 16 shots, and the pulse duration t is sampled pseudo-randomly to avoid the effects of experimental drift. The four scans in this case were not interleaved, due to technical limitations of the *Tabor* 8024 arbitrary waveform generator's sequencing function, however they *were* taken at short intervals to minimise the effects of drift between experimental runs. The solid red curves in the figure are numerical simulations assuming the parameters given in the table, and these parameters are identical to those used in figure 6.3, except for small changes in t_π and the beam intensities. The dashed green curves are numerical simulations (again with the same set of parameters), performed by Rachel Gregory on the *Iridis* supercomputer at the University of Southampton, which take into account the AOM switching time and non-linear behaviour of the I&Q modulator (figures 4.10 & 4.5, respectively). Such simulations require extra computing power because where intensity ramps are involved, many more points must be calculated and stored. These simulations, which would take 3-4 hours on a quad-core desktop computer, take around 2-3 minutes when utilising the many cores available within *Iridis*.

While it is possible to scan parameter space to find more meticulous fits, these often require less physically justifiable parameters, and we are in any case satisfied with our current understanding of the system given the broad experiment-simulation agreement demonstrated in the figures. Furthermore, there are other sources of discrepancy possibly at play in the experiment, including for example Raman beam misalignment and non-circular Raman beam polarisation, both of which would cause the system to behave differently from the ideal $\sigma^+ - \sigma^+$ case considered in the simulations.

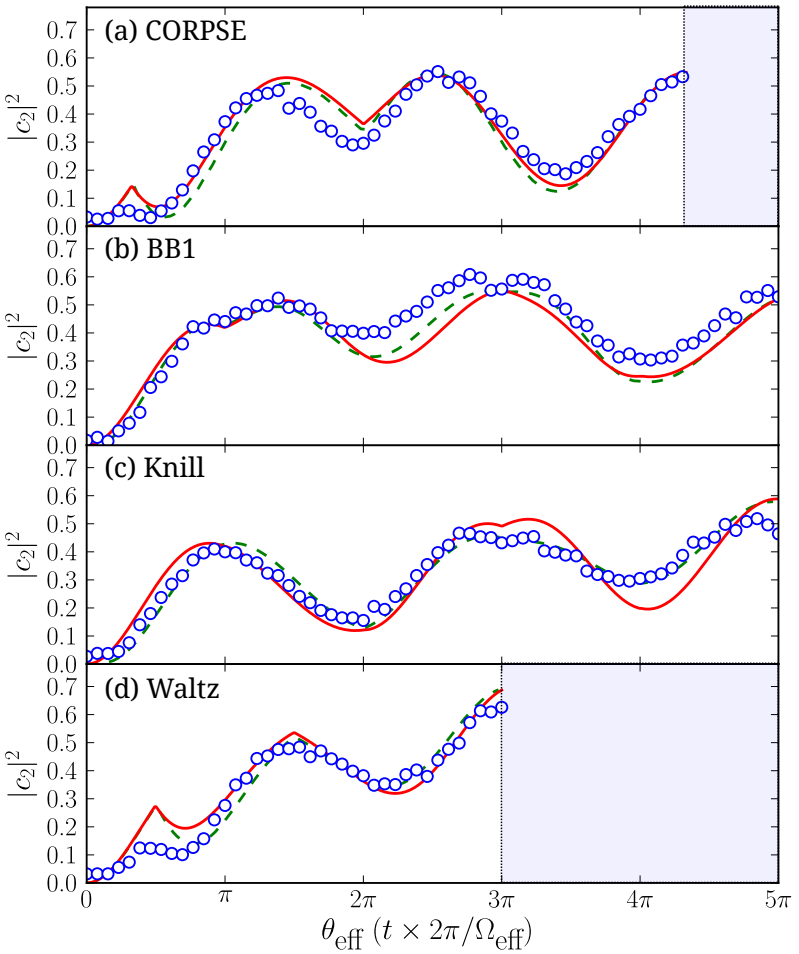

Param.	Value
I_1	14 kW/m^2
I_2	21 kW/m^2
Δ	$2\pi \times 8.5$ GHz
δ_L	$2\pi \times -200$ kHz
B_z	−11 mG
σ_1	$2.5 \times \nu_R$
σ_2	$9 \times \nu_R$
a_1 / a_2	2
S	0.9
t_π	1.3 µs

Figure 6.7: Resultant $|c_2|^2$ population as a function of intra-pulse interaction time t for four different composite pulses: (a) CORPSE; (b) BB1; (c) Knill and; (d) Waltz. The blue circles are experimental data, the solid red curves are numerical simulations based on the parameters given in the table. The dashed green curves are numerical simulations, assuming the same parameters, which incorporate otherwise ignored systematic effects, as described in the text. These data were taken in the $\sigma^+ - \sigma^+$ counter-propagating Raman arrangement, with $\Omega_{\text{eff}} \approx 2\pi \times 380\,\text{kHz}$.

6.3.4 Predicted temperature-dependent performance

A designer of an atom interferometric sensor might ask whether composite pulses allow high-contrast interferometry at higher temperatures, such as those easily attainable in a MOT.[3] This is essentially addressed by the robustness of a composite pulse in the presence of off-resonance errors, since hotter atom clouds have larger ranges of off-resonance error. It is also an interesting line of investigation to consider whether high-fidelity ($\mathcal{F}_P > 0.99$) pulses are possible with Zeeman-degenerate atoms, since spin-polarisation

[3] As a general note, a likely question, put by the skeptic would be ″Do composite pulses *actually work* in atom interferometry?‴. This is a question, already answered in the affirmative in [83], which will be investigated in future work on this experiment.

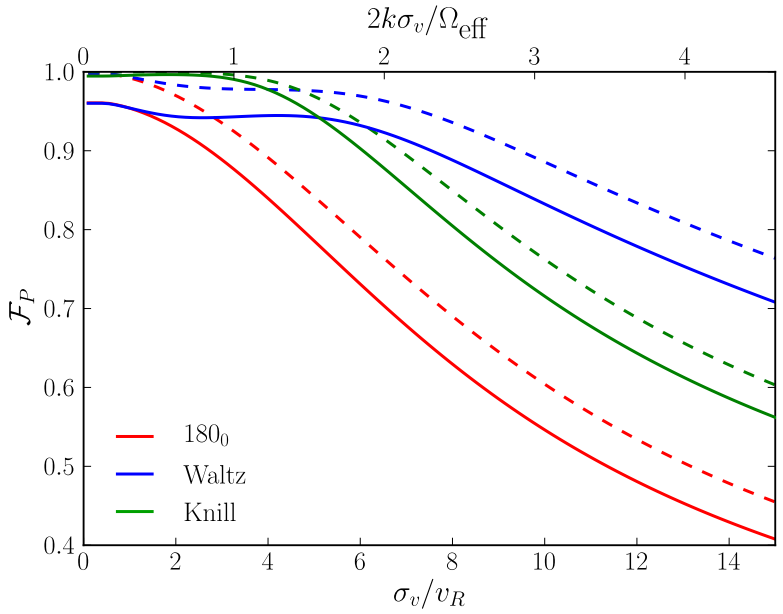

Param.	Value
I_1	14 kW/m^2
I_2	21 kW/m^2
Δ	$2\pi \times 9.0$ GHz
B_z	−261 mG
δ_L (δ^{AC})	$2\pi \times -240$ kHz
S	1
t_π (avg.)	1.58 µs
t_π (m_F=0)	1.43 µs

Figure 6.8: Predicted fidelity achievable using Waltz (blue) and Knill (green) composite pulses, compared with a simple π-pulse (red), for varying Gaussian velocity distribution widths σ_v in units of the Raman recoil velocity v_R (bottom) and normalised to the average two-photon Rabi frequency Ω_{eff}. Dashed lines show predicted behaviour for spin-polarised atoms populating only the $m_F = 0$ state, while solid lines are for an even distribution across all states $m_F = -2 \ldots + 2$.

requires extra experimental complexity and often causes loss of atoms. Broadly speaking, we would like to know how high $\mathcal{F}_P$ can be with thermal, non-spin-polarised atoms, such is the topic of this section.

Figure 6.8 shows the decrease in predicted fidelity with increasing cloud temperature and the presence of multiple Zeeman levels, for two different composite inversion pulses as compared with a basic 180_0. Dashed lines in the plot show predicted behaviour for spin-polarised atoms populating only the $m_F = 0$ state, while solid lines are for an even distribution across all states $m_F = -2 \ldots + 2$. We plot the curves (solid only) as functions of the parameter $2k\sigma_v/\Omega_{\text{eff}}$, which is a normalised measure of the ratio of the velocity width to the effective Rabi frequency. As mentioned previously, the maximum $\mathcal{F}_P$ achievable with a basic 180_0 pulse (red) in Zeeman-degenerate ^{85}Rb is 0.96. Since the Waltz pulse (blue) only corrects for off-resonance errors, it does not improve the maximum achievable fidelity, however it is more effective than the Knill pulse at higher temperatures, and $\mathcal{F}_P$ is predicted to remain above 0.8 up to $\sigma_v = 8 \times v_R$ (95 μK). The Knill pulse (green), because of its tolerance to pulse-length errors, *does* improve fidelity in Zeeman-degenerate pulses. We predict a Zeeman-degenerate fidelity of $\mathcal{F}_P > 0.99$ for

$2k\sigma_v/\Omega_{\text{eff}} < 1$, that is, in our case, where $T < 15\,\mu$K – a temperature readily achievable with optical molasses. Whilst the curves representing spin-polarised atoms (dashed) are merely shifted upwards by around 0.04 as compared with their corresponding Zeeman-degenerate curves for the 180_0 and Waltz pulses, for the Knill pulse we expect a Zeeman-degenerate fidelity at these low temperatures which is no worse than the spin-polarised case. The Waltz pulse becomes more effective than the Knill in both the Zeeman-degenerate and spin-polarised cases at above $\sigma_v \approx 5 \times v_R$ ($37\,\mu$K).

6.4 An alternative to composite pulses

An alternative method for counteracting systematic errors in quantum control systems is adiabatic rapid passage (ARP), a particularly good description of which can be found in James Bateman's PhD thesis [49]. ARP has been implemented in the context of large area atom interferometry [31, 95], with success.

When using ARP pulses, during which the intensity and frequency of the optical fields are swept across resonance, the phase imprinted by the laser on the atoms is difficult to control, thus reducing interferometer contrast. Given that composite pulses are sequences of rotations with known tailored phases, we expect them to behave favourably over ARP pulses in terms of interferometer phase-shifts and readout contrast, because one can apply time-symmetric sequences and easily keep track of the phase during a pulse sequence. Furthermore, ARP requires a higher Rabi-frequency to be most effective, which is currently beyond the capabilities of our apparatus and would in any case directly reduce off-resonance errors via power-broadening.

6.5 Conclusion

In this chapter, we have described a model for visualisation of systematic errors in Raman pulses, demonstrated suppression of Rabi flopping dephasing with rotary spin echoes, and experimentally tested a range of NMR-style composite inversion pulses for improving pulse fidelity in the presence of systematic errors. Our relatively simple numerical model has proved effective in simulating the system, and suggests that the best composite inversion pulse for peak fidelity increase at thermal atom cloud temperatures

is the $90_0180_{180}270_0$ Waltz pulse, whereas the Knill pulse, since it also addresses pulse-length errors, is predicted to achieve a peak fidelity of $\mathcal{F}_P > 0.99$ at temperatures below around $15\,\mu$K. In our particular setup, we find that the Knill pulse performs worse than expected, probably because our apparatus is less capable of imparting the required phase shifts.

Our results suggest that composite pulses can be used to improve the robustness of atom interferometric sensors in the presence of systematic errors. We predict that one may build a high-contrast interferometer which can operate at temperatures achievable in a standard optical molasses, without the need for spin-polarisation. There is of course a trade-off between the improved fidelity afforded by a composite pulse and the increased interrogation time required (the Knill pulse, for example, is five times longer than the basic 180_0), which must be considered in the design process.

Whilst only relatively simple composite (inversion) pulses were examined here, we expect there to be many more interesting types available. For example, when one can alter the direction of the driving fields and apply modulation and chirps to their intensities, frequencies and phases (if the phase imprint during chirps can indeed be controlled), as in adiabatic transfer [30, 31, 95] experiments, we expect a greater degree of control to become available. Future work on this subject will examine the aforementioned techniques for developing more robust composite pulses in inhomogeneous, degenerate atomic systems where large inherent systematic errors are present. A more immediate application of the composite pulses presented here is within large area atom interferometry, as in [83], in the context of which we intend to develop more tailored composite pulses for improving interferometer contrast.

Chapter 7

Interferometric cooling

The concept of interferometric cooling is proposed by Weitz and Hänsch in [28], where the authors describe a system based on Ramsey interferometry with coherent laser pulses for cooling the centre-of-mass motion of atoms and molecules. Their scheme, which we summarise in section 7.6, requires high Rabi frequency pulses with precise control over timings and phases, and to our knowledge it has not yet been tested experimentally. It is of particular interest because of its potential use in the cooling of the translational motion of molecules. Molecules exhibit a complex ro-vibrational energy structure, making them notoriously difficult to laser cool, yet since the principles behind interferometric cooling are the same for atoms and molecules, we can use our cold atomic rubidium system as a test bed for a proof-of-concept of the technique.

We begin this chapter with a description of the proposed scheme for atomic cooling, which is based on the $\frac{\pi}{2} - \frac{\pi}{2}$ Ramsey sequence, where dissipation is induced by spontaneous emission. We then present interference fringes resulting from the Ramsey sequence, and characterise their dependence on the pulse spacing and phase. Thirdly, we characterise the depump pulses required to induce spontaneous emission and reset the atomic populations. We then demonstrate modulation of the atomic velocity distribution, and subsequently a first demonstration of interferometric *cooling* is presented. The chapter ends with a discussion of extensions to the cooling technique, including coherent enhancement and potential application to molecules.

7.1 Proposed cooling scheme

Just as in Doppler-cooling, where we make absorption of photons more probable within a given velocity range via traditional spectroscopy, velocity-sensitive *Ramsey* spectroscopy provides us with a means to a similar velocity-selective force. The resultant state after a $\frac{\pi}{2} - \frac{\pi}{2}$ Ramsey sequence, as described in section 2.3 and illustrated in figure 2.5, is dependent on a combination of the detuning δ, the relative pulse phase $\phi_L^{(\mathrm{rel})} = \phi_L^{(2)} - \phi_L^{(1)}$ (the difference in laser phase between the two pulses), and the time T between the pulses. Building on the introductory remarks made in section 2.3.1, and applying counter-propagating beams ($\mathbf{k}_{L1} \simeq -\mathbf{k}_{L2} = k\hat{\mathbf{z}}$), we find that δ depends on the z component of the velocity (v_z) according to

$$\delta = \delta^{AC} - \delta_L + k(2v_z + v_R), \tag{7.1}$$

where, to recap, δ^{AC} is the combined Raman light shift, δ_L is the laser detuning from the atomic rest-frame resonance, and v_R is the two-photon Raman recoil velocity. Setting $\delta_L = \delta^{AC}$ gives a detuning

$$\delta = k(2v_z + v_R), \tag{7.2}$$

which is dependent only on the velocity of the atom. With a Ramsey sequence, whose output is described by equation 2.55, we can therefore generate a velocity-selective excitation, whereby the resultant population in the upper hyperfine state is determined purely by v_z. Since atoms excited to the upper hyperfine state by the Ramsey sequence recieve a $2\hbar k$ momentum kick, the interferometer imparts a velocity-selective impulse, whose 'comb'-like profile can be engineered by changing the parameters of the Ramsey sequence. As shown in figure 2.5 d, the Ramsey fringes can be shifted along the δ (v_z) axis by changing the relative phase of the two laser pulses, and the width of the fringes can be increased simply by decreasing T, as shown in figure 2.5 c. Note that whilst the velocity distribution of the atoms will be modulated after a Ramsey sequence, the local phase space density will not have changed, because the excited portion of the atom cloud will be in a higher-energy electronic state. This is addressed by causing the excited atoms to relax into the lower hyperfine level (via spontaneous emission) by optical pumping. Note that in a scheme based on single-photon transitions between fine-structure levels,

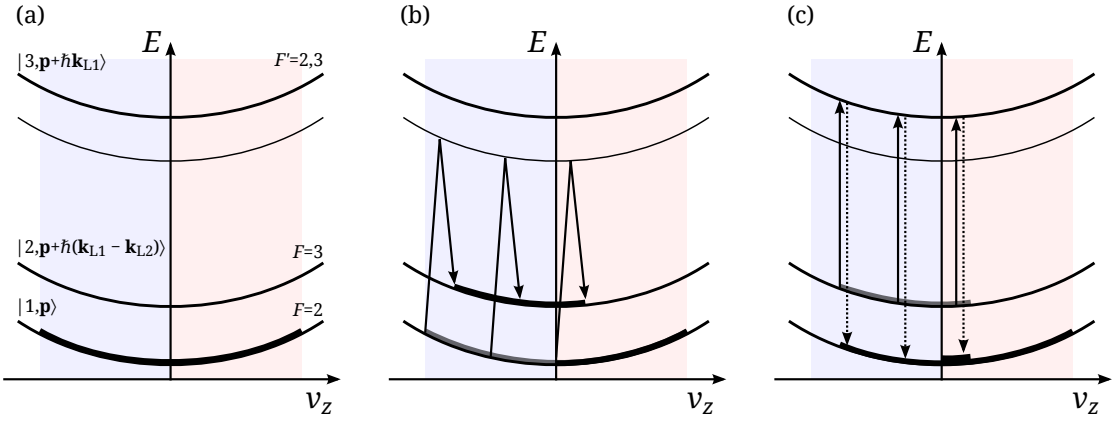

Figure 7.1: Reduction in phase-space density with the Ramsey sequence followed by depumping. The diagrams are sketches of the total energy (electronic + kinetic) as a function of the z-axis velocity. (a) Population (thick black line) is initially distributed across a range of velocities in $F = 2$. (b) A Raman Ramsey sequence excites only the negative-moving atoms, shifting them upwards in velocity by v_R. (c) Pumping from $F = 3 \rightarrow F' = 3$ forces re-population of $F = 2$, and the overall width of the velocity distribution has decreased. The dashed lines indicate spontaneous emission.

spontaneous emission would occur naturally after a short lifetime (typically 10s of ns), thus imposing an upper limit on duration of the Ramsey sequence.

To engineer a *cooling* force, we set $\phi_L^{(\mathrm{rel})}$ such that the excitation profile exhibits a negative slope through zero velocity (and the impulse pushes the atoms towards positive velocity), and T such that the central fringe spans the width of the velocity distribution. For illustration purposes, we represent the idealised excitation profile by the step function

$$|c_2|^2 = \begin{cases} 1 & (v < 0) \\ 0 & (v \geq 0), \end{cases} \tag{7.3}$$

whereby atoms with negative velocity are excited to the upper hyperfine state (and pushed toward positive velocity), and atoms with positive velocity remain in the lower (with their velocities unchanged). In reality the excitation profile is *sloped* through zero velocity, rather than stepped, but the qualitative effects are similar. Atoms not excited by the Ramsey sequence are said to be in a 'dark' velocity class.

The scheme applied to cool the atomic velocity distribution is illustrated in figure 7.1, where we sketch the total energy (electronic + kinetic) as a function of the z-axis velocity at the three stages of the process:

1. **Preparation**

   The atom cloud, which contains a distribution of velocities as indicated by the thick black line in figure 7.1 a (we consider a flat-top velocity distribution for simplicity), is initially prepared into the $F = 2$ level $|1, \mathbf{p}\rangle$.

2. **Ramsey excitation**

   The Ramsey sequence is applied, transferring negative-moving atoms to $|2, \mathbf{p}+\hbar(\mathbf{k}_{L1}-\mathbf{k}_{L2})\rangle$ ($F = 3$) with the associated impulse in the positive z direction, as shown in figure 7.1 b.

3. **Re-population**

   To finish, atoms in $F = 3$ are optically pumped back into $F = 2$ by a laser tuned to the $F = 3 \rightarrow F' = 3$ transition (the depump laser in our setup) via spontaneous emission, as shown in figure 7.1 c. If the depump laser is arranged retro-reflected, then this process has a net ensemble average momentum transfer of zero, but will randomise the velocity distribution to some extent.

As illustrated in the figure, the width of the velocity distribution has reduced without loss of atoms, hence the phase-space density has increased, and the atom cloud is colder. Repeated application of this particular sequence will eventually shunt all atoms into the dark velocity class. One can achieve extra cooling by repeating the above sequence many times with a decreasing dwell time T, such that the dark velocity class becomes increasingly narrow. Furthermore, to induce accumulation of population around $v_z = 0$, rather than causing acceleration of the cloud, one can apply the above sequence with alternating orientations along the z-axis.

In the idealised illustration above, the maximum reduction in velocity width is v_R per-cycle, and the sequence becomes ineffective for cooling where the initial width is less than v_R. Roughly speaking, for a Gaussian distribution of velocities, this puts a theoretical limit equal to the Raman recoil temperature $T_R = Mv_R^2/k_B = 1.48\,\mu$K on this cooling technique. A technique for enhancing the per-cycle increase in phase-space density is discussed in section 7.6.

By applying Ramsey sequences with different excitation profiles one can induce different effects on the velocity distribution. Instead of *cooling* the atoms, for example, it is

possible to *modulate* their velocity distribution by applying a Ramsey sequence whose excitation profile exhibits a periodic oscillatory structure.

Note that the above scheme requires a spontaneous emission event after each Ramsey sequence. One might expect that this, to some extent, precludes its feasibility for molecular cooling. However, since the cooling scheme is based on *short*, *coherent* optical pulses, there are certain enhancements which can be made to relax this dependence, and these are discussed in section 7.6. For the preliminary tests performed in this work, we need not implement them experimentally.

The capture range of the cooling scheme is determined by the width of the central Ramsey fringe, which can be estimated according to $\delta \simeq 2kv_z = \pi/T$, where T is the time between Ramsey pulses (not the temperature), and we can express this in terms of the recoil velocity as

$$\left(\frac{v_z}{v_R}\right) = \frac{\pi}{2Tkv_R}. \tag{7.4}$$

For a cloud of ultracold ^{85}Rb atoms at a temperature of, say, 100 μK ($v_z/v_R = \sqrt{100/1.48} = 8.2$) the required dwell time T for capture of the entire velocity distribution (up to 3σ) is roughly $T = \pi/(12\times 8.2kv_R) \approx 330$ ns, which is just within the possibilities of our experimental setup. For a sample of ^{85}Rb at, for example 1 K ($v_z/v_R = \sqrt{1\times 10^6/1.48} \approx 820$), which is a typical temperature for buffer-gas-cooled particles, the requred dwell time is $T \approx 3$ ns. Furthermore, for room temperature particles, the required dwell time would be $T \approx 200$ fs. Therefore, whilst we are able to use our cold atom system as a test-bed for a proof-of-concept of interferometric cooling, a high power, femtosecond-pulse-based laser system would in fact be required should we wish to extend the scheme to particles which are not already ultracold. Note that the above numbers are specific to rubidium-85 ($M = 85$ amu and $\lambda = 780$ nm), and particles with different masses and transition wavelengths will exhibit different recoil velocities.

7.2 Ramsey fringes

Before testing the cooling scheme, we characterise the behaviour of the Ramsey sequence. By measuring the fringe pattern, or 'velocity comb', at the output of a Ramsey interferometer, we can predict its effect on the atomic velocity distribution. In the

velocity-insensitive Raman arrangement, one can easily observe Ramsey fringes simply by applying the $\frac{\pi}{2}-\frac{\pi}{2}$ sequence and measuring the output as a function of the laser detuning δ_L using the method described in section 3.5.3. In contrast, in the velocity-*sensitive* arrangement, fringe contrast is completely washed out because the power broadened Raman pulse is spectrally much wider than the periodic structure of the Ramsey 'comb'. We *are* able to observe fringes, however, if we apply *two* Ramsey sequences with a relative laser detuning offset δ_{OS}, as illustrated in figure 7.2, and described below. The effect of this scheme is to remove the dependence of the output state on velocity (see section 7.2.1), and instead emulate the range of velocities with a range of laser detunings δ_L. This method, which is an adaptation of the symmetric Ramsey Bordé interferometer [96], has been used to measure the recoil velocity [32, 69] with high precision. For completeness, before presenting the measurements, we digress into a discussion of atom interferometer phase.

7.2.1 Light-pulse atom interferometer phase

A particularly good description of light-pulse atom interferometer phase is given by Bongs *et al* in [97]. The resultant phase after a series of laser pulses is given by

$$\Delta\Phi = \Delta\Phi_{\text{prop}} + \Delta\Phi_{\text{laser}} + \Delta\Phi_{\text{sep}}, \tag{7.5}$$

where $\Delta\Phi_{\text{prop}}$ is the phase shift due to propagation along the two separate paths, $\Delta\Phi_{\text{laser}}$ is the phase 'imprinted' on the atom by the laser, and $\Delta\Phi_{\text{sep}}$ is the phase shift arising due to imperfect overlap of the two wavepackets at the output. We ignore this final term here since it is comparatively small, and refer the reader to [97] for details. The middle term comprises a combination of the laser detuning δ_L and phase ϕ_L: for closed interferometers whose pulses all have the same laser detuning, δ_L-dependence dissapears due to symmetry, but for the Ramsey sequence (as we have already seen) it remains. The first term is given by the difference in the action S, defined by integral of the Lagrangian $L(\mathbf{r}(t), \mathbf{v}(t))$ along the two classical paths $\Gamma_{1,2}$:

$$\Delta\Phi_{\text{prop}} = \frac{S_2 - S_1}{\hbar} = \frac{1}{\hbar}\left(\int_{\Gamma_2} L\left(\mathbf{r}_2(t), \mathbf{v}_2(t)\right) dt - \int_{\Gamma_1} L\left(\mathbf{r}_1(t), \mathbf{v}_1(t)\right) dt\right). \tag{7.6}$$

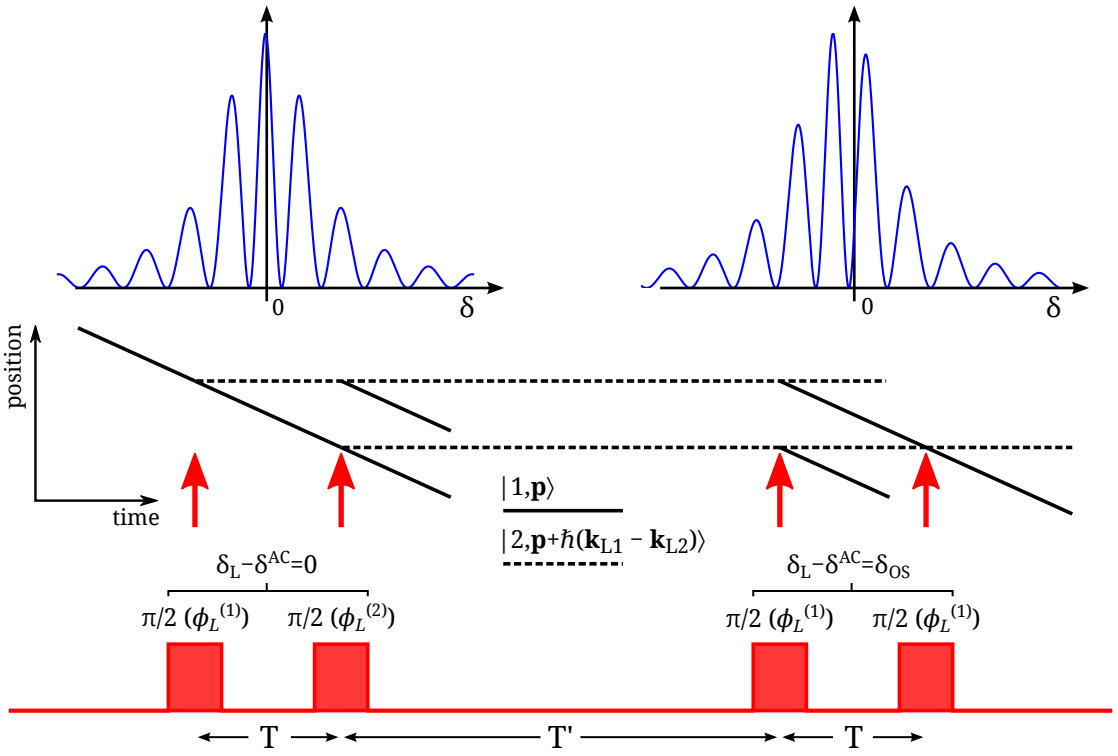

Figure 7.2: The symmetric Ramsey Bordé interferometer used to measure Ramsey fringes. **Bottom:** Two Ramsey sequences (pairs of $\frac{\pi}{2}$ pulses) are applied, with a laser detuning offset $\delta_L - \delta^{AC} = \delta_{OS}$ applied to the second. **Middle:** Trajectories of the atomic wavepackets during the interferometer. The phase accrued along the two 'closed' paths is independent of the initial velocity. Red arrows indicate the direction of the Raman pulse. **Top:** Sketches of the excitation profiles sketches of the two Ramsey sequences. The fringe positions in the second are offset from the first by δ_{OS}. The observed output state of the Ramsey-Bordé interferometer is a convolution of these two patterns.

The Lagrangian contains all classical inertial effects which perturb the phase, including acceleration due to gravity and rotation. Since our interferometer is arranged horizontally, and rotation and all other effects are comparatively small (once again, we refer the reader to [97] for details of the differences in magnitude of these effects), we need only consider the classical kinetic energy $M\mathbf{v}^2/2$ component of the Lagrangian. The propagation phase therefore becomes

$$\Delta\Phi_{\text{prop}} = \frac{M}{2\hbar}\left(\int_{\Gamma_2}\mathbf{v}_2^2(t)dt - \int_{\Gamma_1}\mathbf{v}_1^2(t)dt\right), \tag{7.7}$$

which, where the paths $\Gamma_{1,2}$ share common start and end positions, is equal to zero. This is the reason for the absence of initial velocity dependence in the Ramsey-Bordé interferometer and all other *closed* interferometers. If the paths are not closed, as in the

Ramsey sequence, we calculate the propagation phase, where from the momentum basis defined in section 2.1, $\mathbf{v}_1 = \mathbf{p}/M$ and $\mathbf{v}_2 = (\mathbf{p} + \hbar(\mathbf{k}_{L1} - \mathbf{k}_{L2}))/M$, to be

$$\begin{aligned}\Delta\Phi_{\text{prop}} &= \frac{1}{2}M\left(\mathbf{v}_2^2 - \mathbf{v}_1^2\right)T \\ &= \left(\frac{\mathbf{p}\cdot(\mathbf{k}_{L1} - \mathbf{k}_{L2})}{M} + \frac{\hbar(\mathbf{k}_{L1} - \mathbf{k}_{L2})^2}{2M}\right)T,\end{aligned} \tag{7.8}$$

which is equal to the momentum portion of the δT term in equation 2.55. Adding $\Delta\Phi_{\text{laser}}$ to this, we regain the full form of the phase for the Ramsey interferometer:

$$\Delta\Phi = \left(-\delta_L + \frac{\mathbf{p}\cdot(\mathbf{k}_{L1} - \mathbf{k}_{L2})}{M} + \frac{\hbar(\mathbf{k}_{L1} - \mathbf{k}_{L2})^2}{2M}\right)T - \phi_L^{(\text{rel})} = \delta T - \phi_L^{(\text{rel})}. \tag{7.9}$$

7.2.2 Fringe measurements

For the symmetric Ramsey-Bordé sequence in figure 7.2, there is no phase evolution during the period T' (both paths have the same velocity) and the interferometer is closed (there is no velocity dependence), so the intereferometer phase $\Delta\Phi$ is simply the sum of the phases of the two Ramsey sequences, as imprinted on the atom by the laser:

$$\Delta\Phi = \delta_{OS}\,T - \phi_L^{(\text{rel})}, \tag{7.10}$$

where $\phi_L^{(\text{rel})} = \phi_L^{(2)} - \phi_L^{(1)}$ is the difference in phase between the first two pulses. We can think of this in terms of overlapping fringe patterns: the two spectral profiles shown at the top of figure 7.2 represent the two Ramsey fringe patterns, or 'velocity combs' corresponding to the two Ramsey sequences. When these two combs overlap, that is, where $\delta_{OS} = 0$ and $\phi_L^{(\text{rel})} = 0$, atoms are transferred back to the initial state, and we expect a minimum in $|c_2|^2$. By scanning δ_{OS} for given values of $\phi_L^{(\text{rel})}$ and T, we can hence build up a picture of the initial the Ramsey excitation profile.

The results of the Ramsey-Bordé profile measurement experiment are shown in figure 7.3, where we plot the resultant population $|c_2|^2$ as a function of the offset detuning δ_{OS} for three different inter-pulse dwell-times T, as indicated in the plots. These data were taken in the $\pi^+ - \pi^-$ arrangement. The scans in 7.3 a, b and c use $\phi_L^{(\text{rel})} = 0$ and 7.3 d uses $\phi_L^{(\text{rel})} = \frac{\pi}{2}$. The blue circles are experimental data and the red curves are numerical simulations assuming the parameters given in the table. The measured experimental

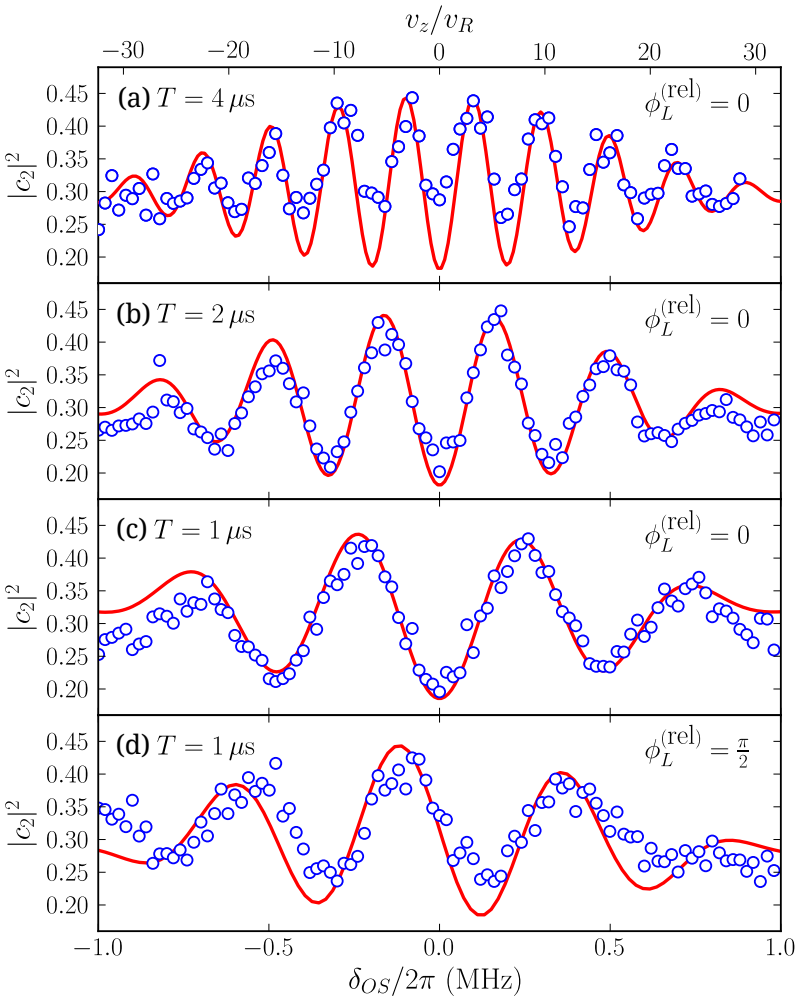

Param.	Value
I_1	14 kW/m^2
I_2	21 kW/m^2
Δ	$2\pi \times 9.0$ GHz
B_z	−11 mG
σ_1	$4 \times v_R$
σ_2	$10 \times v_R$
a_1 / a_2	2
S	0.65
t_π	1.8 µs
δ^{AC}	$2\pi \times$ −100 kHz

Figure 7.3: Resultant upper state population after application of the Ramsey-Bordé sequence in figure 7.2 as a function of the offset detuning δ_{OS}, for three different dwell times T (given in each plot), in the $\pi^+ - \pi^-$ arrangement. In (a), (b) and (c) the relative laser pulse phase $\phi_L^{(\mathrm{rel})} = \phi_L^{(1)} - \phi_L^{(2)} = 0$, in (d) $\phi_L^{(\mathrm{rel})} = \frac{\pi}{2}$. The blue circles are experimental data, and the red curves are numerical simulations assuming the parameters given in the table.

parameters for these data were $\Delta = 2\pi \times 9 \pm 0.5\,\mathrm{GHz}$, $P_{1,2} = 40 \pm 5\,\mathrm{mW}$, $I_z = 79\,\mathrm{mA}$, and $\delta^{AC} = 2\pi \times -100\,\mathrm{kHz}$, and we used a π pulse time of $t_\pi = \pi/\Omega_{\mathrm{eff}} = 1.8\,\mu\mathrm{s}$. We infer the remaining parameters $\sigma_{1,2}$, a_1/a_2 and S by performing manual fitting of the numerical simulations. Furthermore, we allow small adjustments of the experimentally measured parameters for use in the numerical model, to give a better fit to the data. The parameter S in these simulations accounts for two loss mechanisms: the loss of atoms due to ballistic expansion, as in the previous two chapters (see section 5.1.3.1); and the loss of atoms into the 'open' paths in the interferometer which do not contribute to the interference signal, as indicated by the stray lines in figure 7.2.

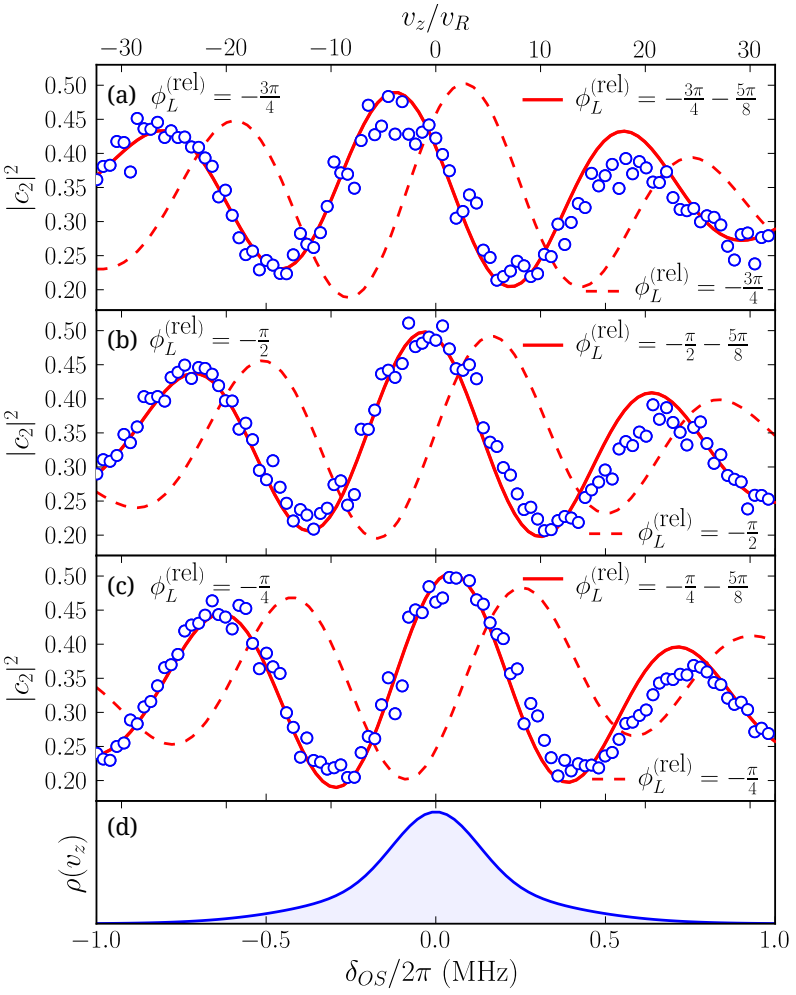

Param.	Value
I_1	15 kW/m^2
I_2	22 kW/m^2
Δ	$2\pi \times 8.0$ GHz
B_z	−11 mG
σ_1	$4 \times v_R$
σ_2	$10 \times v_R$
a_1 / a_2	2
S	0.7
t_π	1.5 µs
δ_L	$2\pi \times$ −200 kHz

Figure 7.4: Resultant upper state population after application of the $\pi^+ - \pi^-$ Ramsey-Bordé sequence as a function of the detuning offset δ_{OS} for a dwell time $T = 500\,\mathrm{ns}$ (blue circles) for (a) $\phi_L^{(\mathrm{rel})} = \frac{3\pi}{4}$, (b) $\phi_L^{(\mathrm{rel})} = \frac{\pi}{2}$, and (c) $\phi_L^{(\mathrm{rel})} = \frac{\pi}{4}$, compared with an estimate of the velocity distribution (d). The blue circles are experimental data, and the red curves are numerical simulations assuming the parameters given in the table, with their respective $\phi_L^{(\mathrm{rel})}$ indicated in the legend.

As expected, we observe an increase in the fringe spacing as T is decreased. We observe a minimum in $|c_2|^2$ at $\delta_{OS} = 0$ for the scans in which $\phi_L^{(\mathrm{rel})} = 0$, and where $\phi_L^{(\mathrm{rel})} = \frac{\pi}{2}$, the data exhibit a negative slope at $\delta_{OS} = 0$. Fringe contrast appears washed out in figure 7.3 a, possibly due to experimental drift (these scans were taken separately), but we observe good contrast, and indeed good agreement between data and simulations, in plots b and c. Plot d exhibits an apparent offset from the expected phase, due probably to the non-linear behaviour of the I&Q modulator (see section 4.3.3), and we observe a slight loss of contrast compared with the simulation, but broadly speaking the data show the expected features. These data demonstate that Ramsey fringes are visible

above experimental noise in our system, and we therefore expect the associated impulse to result in a detectable effect on the atomic velocity distribution when the cooling scheme is applied.

For cooling, we require a central fringe which spans the majority of the Doppler width. Figure 7.4 shows the resultant upper state population after application of the Ramsey-Bordé sequence, for a pulse spacing $T = 500\,\text{ns}$ and three relative phases: (a) $\phi_L^{(\text{rel})} = -\frac{3\pi}{4}$, (b) $\phi_L^{(\text{rel})} = -\frac{\pi}{2}$, and (c) $\phi_L^{(\text{rel})} = -\frac{\pi}{4}$. We plot the estimated velocity distribution (plot d), which we find, as anticipated, to be comparable in width to the central Ramsey fringe in all three plots. The predicted excitation profiles are represented in the plots by the dashed red curves. Interestingly, we find that the fringe positions are not consistent with what is expected at this small pulse spacing, and that the data for all three cases are more closely matched when we add a phase shift of $-\frac{5\pi}{8}$ to the experimentally-applied $\phi_L^{(\text{rel})}$ in the simulations (solid red curves). This apparent offset may arise for small T because of the non-rectangular temporal pulse shape (the two Ramsey pulses are expected to merge, to some extent, at small T – see figure 4.10), or to relative systematic offsets in the timings of the phase shifts and pulses. It is important to note that it may be a peculiar characteristic of the Ramsey-Bordé sequence (as applied in this experiment, not in all Ramsey-Bordé interferometers), and may not be present when applying a single Ramsey sequence within a cooling scheme.

7.3 Depump pulses

The re-population stage in the proposed cooling scheme (see figure 7.1 c) is achieved by optical pumping into $F = 2$ with the depump laser (see section 3.2). Here we characterise the pumping efficiency and required duration of the depump pulse. We initialised the atom cloud in $F = 3$, distributed (assumed approximately evenly) accross all 7 m_F states, and measured the fraction of atoms remaining in $F = 3$ as a function of the depump pulse duration t_D for three different input polarisation configurations. The depump beam (diameter 7 mm, power 3 mW) is retro-reflected to avoid a net *pushing* effect, and propagates perpendicular to the quantisation field $B_z\hat{\mathbf{z}}$. The quarter waveplate (see figure 3.3) is at an angle such that for linear input polarisation, the retro-reflected

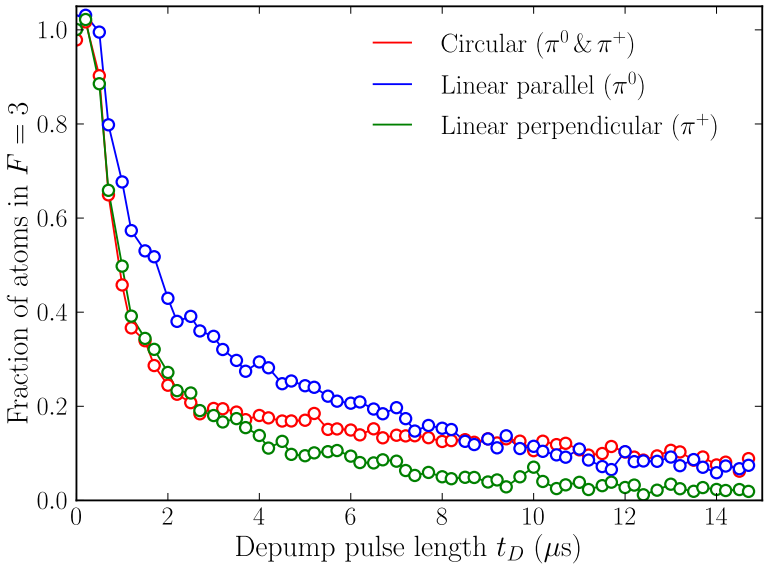

Figure 7.5: Optical pumping from $F = 3$ into $F = 2$ as a function of the depump laser interaction time t_D, for three different beam polarisations, indicated in the legend. The quantisation magnetic field lies perpendicular to the **k** vector of the depump beam.

beam is linearly polarised in the same plane as the input. For circular input polarisation, the retro-reflected beam is circularly polarised, with opposite handedness to the input, for any quarter waveplate rotation angle we choose. Figure 7.5 shows the data for circular input polarisation (red) and linear input polarisation aligned parallel (blue) and perpendicular (green) to the quantisation axis. We find the most efficient pumping into $F = 2$ with perpendicular linear polarisation, which exhibits a remaining $F = 3$ fraction of ~ 0.02 after a $t_D = 12\,\mu$s pulse. In the experiments, we apply the depump laser pulses as such.

With parallel linear polarisation, we observe slower optical pumping due to the presence of the dark state $m_F = 0$, yet since the resultant fraction in $F = 3$ goes below $1/(2F + 1) = 0.14$, either the input polarisation (or the quarter waveplate) is imperfectly aligned, or there is significant coupling occurring to the upper state $F' = 2$. We would expect slightly faster optical pumping into $F = 2$ with the depump laser tuned to the $|5S_{1/2}, F = 3\rangle \rightarrow |5P_{3/2}, F' = 2\rangle$ because (a) from $F' = 2$, relaxation to $F = 2$ is marginally favourable over $F = 3$ on average across all m_F sublevels, and (b) population in this case (unlike the current) is not pumped into the outer $m'_F = \pm 3$ sublevels of $F' = 3$, from which relaxation to $F = 3$ is around 25% more favourable than to $F = 2$. With the current apparatus this is more difficult to implement experimentally.

7.4 Modulation of the velocity distribution

In this section we test the scheme described in section 7.1, and characterise its effect on the atomic velocity distribution for a $(\sigma^+ - \sigma^+)$ Ramsey sequence with $T = 500\,\text{ns}$ at range of $\phi_L^{(\text{rel})}$. Given high-contrast Ramsey fringes and efficient depump pulses, we expect to observe cooling or heating of the atom cloud dependent on the phase of the Ramsey fringes. Note that the resolution of our velocimetry does not allow for detection of small structure on the velocity distribution. We therefore restrict ourselves to the exploration of small T schemes which are expected to primarily cool or heat the entire distribution.

A sample experimental procedure is illustrated in figure 7.6, and described as follows. The atoms are collected in the MOT, cooled in the molasses for $t_M = 6\,\text{ms}$, and prepared into $|5S_{1/2}, F = 2\rangle$ as normal. We then apply a resonant ($\delta_L = \delta^{AC}$, measured empirically) Ramsey sequence with a dwell time T and a relative phase $\phi_L^{(\text{rel})}$, followed by a $t_D = 12\,\mu\text{s}$ depump pulse, and repeat this process N times. After this we apply a weak Raman pulse of duration t_{probe} at the detuning $\delta_L = \delta^{AC} + \omega_{\text{probe}}$ to probe the number of atoms in the corresponding velocity class. We then repeat this entire sequence for a range of ω_{probe} detunings in order to build a picture of the velocity distribution (see section 5.2.1). In these experiments we shift the detuning during the probe pulse by applying the sinusoidal signals $I = \cos(\omega_{\text{probe}} t)$ and $Q = \sin(\omega_{\text{probe}} t)$ to the respective channels of the I&Q modulator (see section 4.3.3). Note that δ^{AC} here corresponds to the central light shift for the (higher intensity) Raman pulses constituting the Ramsey sequence. As a general note, in this experiment, and all experiments throughout this thesis, care was taken to characterise and compensate for experimental delays between the various components of the setup. As one specific example, without a software-programmed delay, a phase shift induced by the I&Q modulator would occur before the respective Raman pulse impinged on the cold atoms, because the AOM driver exhibits a longer signal delay than the I&Q modulator.

The un-modulated (blue) and modulated (red) velocimetry profiles for a modulation experiment with $T = 500\,\text{ns}$ at a range of $\phi_L^{(\text{rel})}$ are shown in figure 7.7. Each point is an average over 16 shots, and the entire scan took around 25 minutes to complete. Measurements of the modulated and un-modulated distributions were interleaved to give

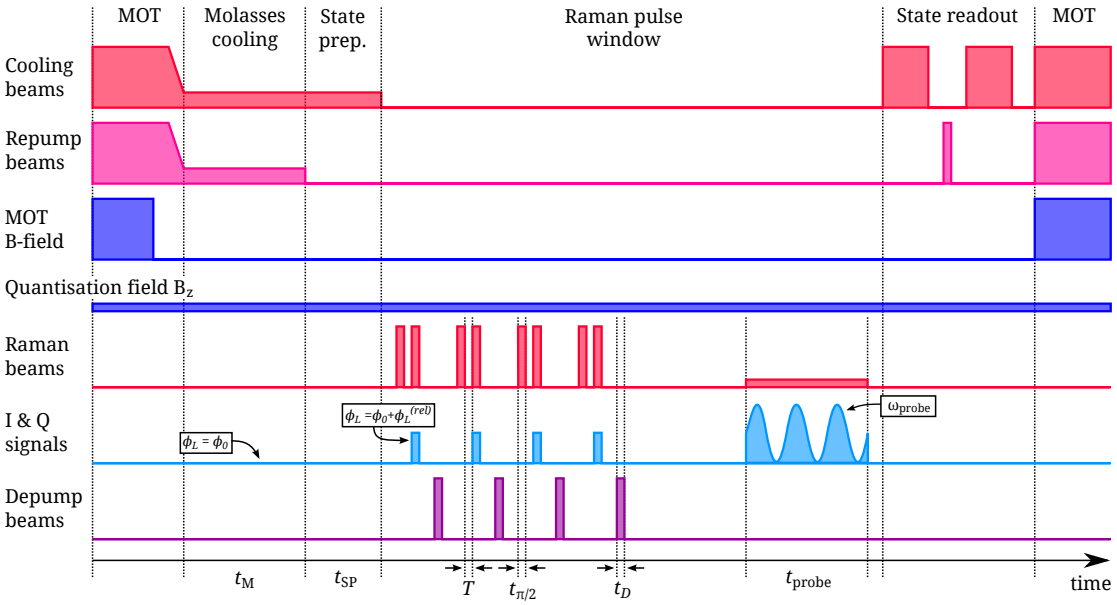

Figure 7.6: Timing diagram of an interferometric velocity modulation experiment with $N = 4$. Described in the text.

a reliable comparison between the two, and the points were sampled pseudo-randomly to minimise the effects of drift during the experiment. The solid curves are 8-point moving averages of the respective data points. These data were taken in the $\sigma^+ - \sigma^+$ polarisation arrangement, and the z axis magnetic field was adjusted in order to counteract the splitting of the Zeeman sublevels (see section 5.1.2.1) *during the probe pulse*. This means that there are significant light shift splittings during the Ramsey pulses, but the resultant effect of this is simply a reduction in fringe contrast (the fringe *positions* are unchanged from the $\pi^+ - \pi^-$ case). The measured Rabi frequency was $\Omega_{\text{eff}} \approx 2\pi \times 250\text{kHz}$, hence the duration of the Ramsey $\pi/2$ pulses was $t_{\pi/2} = 1\,\mu\text{s}$. We applied a probe pulse of duration $t_P = 100\,\mu\text{s}$, and measured the probe light shift to be $\delta^{AC}_{\text{probe}} \approx -30\,\text{kHz}$.

In all cases population is pushed towards positive velocities as expected, yet in no case do we observe a *cooling* effect. Note that the signature of cooling for these data is a reduction in the width of the velocity distribution, and the corresponding reduction in the width of the Raman velocimetry scan. Heating, on the other hand, results in an increase in width. To aid the analysis of these curves we plot predicted modulated velocity distributions (red) for a range of $\phi_L^{(\text{rel})}$ in figure 7.8. To generate these plots we use a simple numerical simulation in *Python*, which moves population along the v_z/v_R axis according to the excitation profile (dashed lines) of the $T = 500\,\text{ns}$ Ramsey interferometer, where we assume Ramsey fringes with peak-to-peak amplitudes of 0.4

(slightly larger than those presented in section 7.2.2). In the simulation we do not include the directionally random recoils upon spontaneous emission, but their effect is expected to be a general broadening (heating) of the modulated distributions, as discussed in section 7.4.2. In each case the initial velocity distribution (blue) is Gaussian, with a width of $\sigma_v = 4 \times v_R$.

7.4.1 Analysis of the data

It is important to re-iterate at this stage that the Raman velocimetry profiles in figure 7.7 do not map one-to-one to their corresponding velocity distributions, due to power-broadening during the probe pulse. Nevertheless, the two are qualitatively similar, and we can compare and match the curves in figures 7.7 and 7.8 legitimately. There is one caveat to this: structure observed on the modulated data is not *necessarily* an artefact of a change in the velocity distribution, but could instead be due to a detuning-dependent distribution of population between the hyperfine levels. This could occur, for example, due to incomplete optical pumping from $F = 3$ into $F = 2$ during the depump pulses, which would lead to an 'imprint', whose prominence would be greater for a less efficient depump pulse, of the Ramsey excitation profile on the resultant velocimetry profile. One easily noticable signature of such an effect, since accurate Raman velocimetry relies on *all* population being in the lower state, would be an increase in the area under the modulated curve as compared with the un-modulated one. By integrating the 8 point-moving averages of the data, we find that the area under the modulated velocimetry curves is on average only $3.0 \pm 0.8\,\%$ larger than under the un-modulated curves (the quoted error is the standard deviation), and that the largest increase is 4.5% (observed for $\phi_L^{(\mathrm{rel})} = \frac{\pi}{4}$). This indicates that some imprint is indeed present, but since the numbers are small we can be confident that the broad effects observed here occur due to a genuine change in the velocity distribution. The effect of incomplete optical pumping is highlighted in [61], where the authors subtract a significant signal from Raman velocimetry data which is found to exhibit a non-zero (albeit flat, in their case) background after a series of Raman-pulse-depump cycles.

Figure 7.7 a shows the effect on the velocity distribution of a modulation sequence with $\phi_L^{(\mathrm{rel})} = 0$, and this can be compared to the predicted effect shown in figure 7.8 a. Whilst

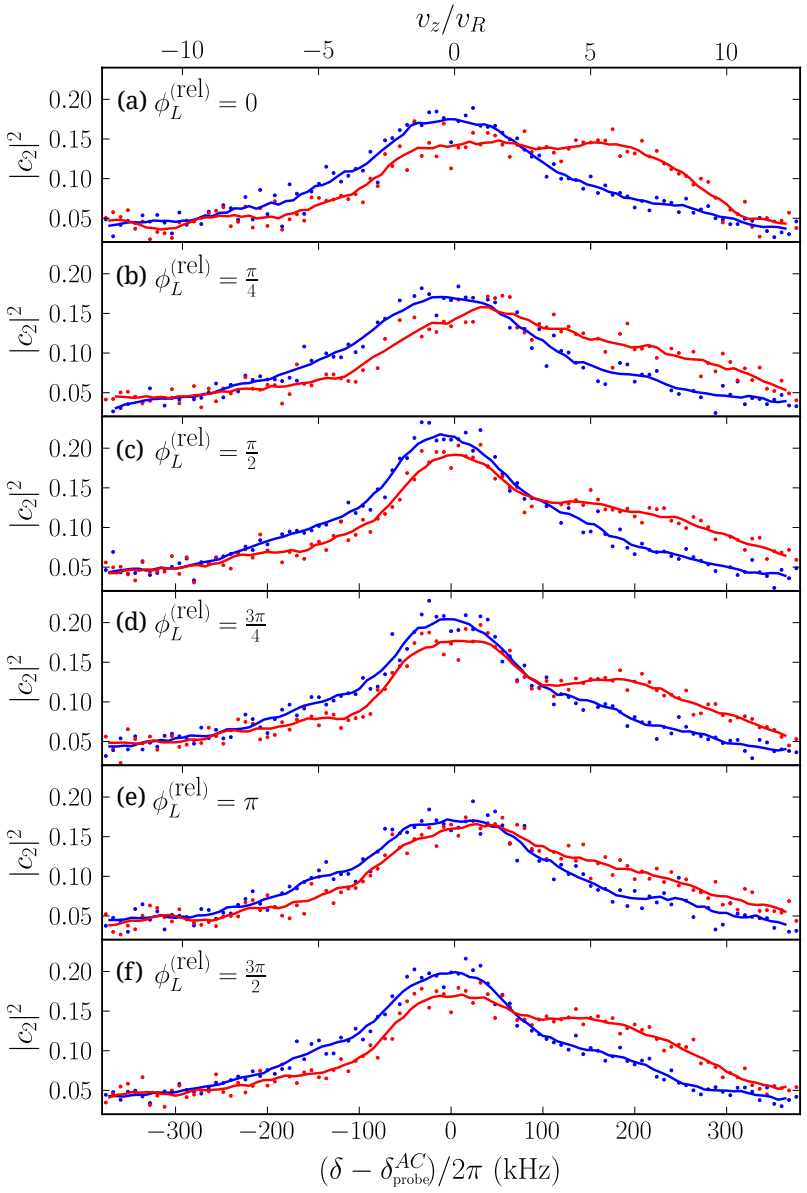

Figure 7.7: Results showing interferometric modulation of the velocity distribution with $T = 500\,\mathrm{ns}$ and $N = 4$ at a range of $\phi_L^{(\mathrm{rel})}$ in the $\sigma^+ - \sigma^+$ polarisation arrangement. Each plot shows the Raman velocimetry profile (a measure of the atomic velocity distribution) without (blue) and with (red) application of the modulation sequence. The dots are experimental data, and the solid curves are their 8-point moving averages.

we expect to observe a small cooling effect, the resultant experimental distribution is actually wider than the initial, indicating that unwanted heating is occurring. The possible sources of this heating are discussed in section 7.4.2. The profiles of figure 7.7 b, to be compared with figure 7.8 b, show a similar general push to the right, and whilst we do expect heating in this case, the resultant profile is not quite as expected, in that it does not exhibit a pronounced peak at $v_z/v_R = 5$. Profiles 7.7 c and d (7.8 c and d) appear to match the expected profiles well, but only in the left and right thirds of the

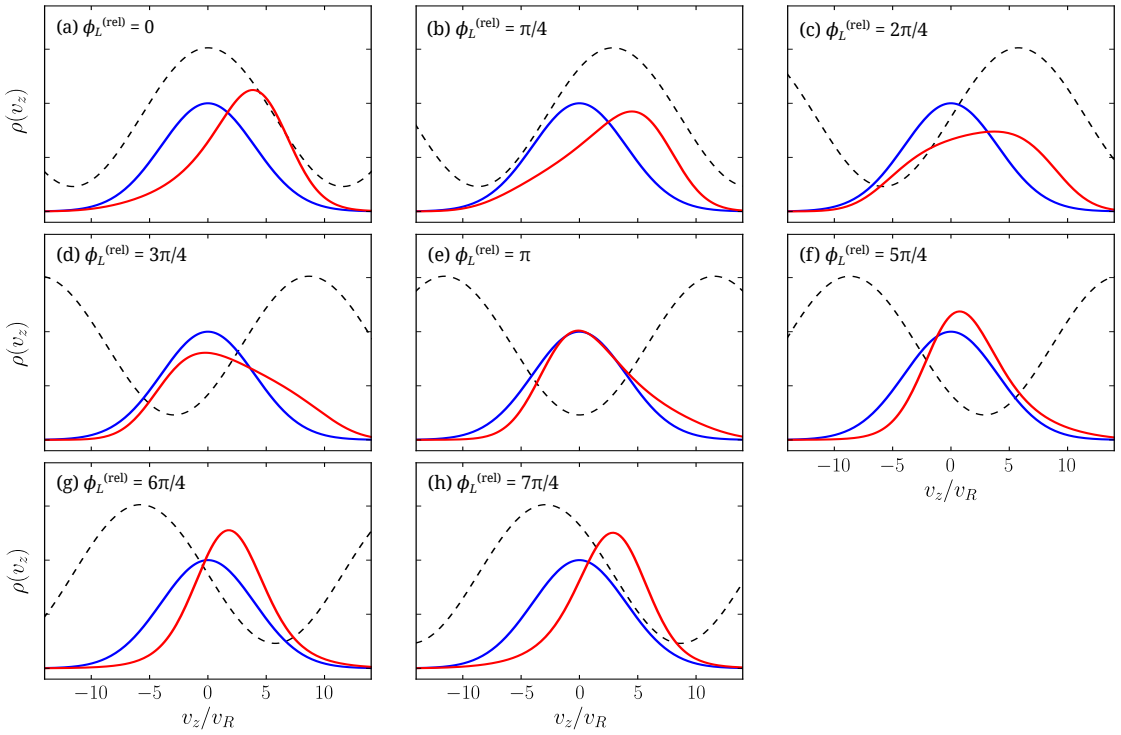

Figure 7.8: Predicted velocity distributions for several Ramsey fringe phases. In each plot, the initial Gaussian velocity distribution (blue) is modulated by $N = 4$ applications of a Ramsey sequence with $T = 500\,\text{ns}$, whose excitation profile is indicated by the dashed line. We plot the resultant velocity distribution (red) for 8 different relative phases (given in each plot).

scans. Indeed, it appears as though population in the middle third is 'left behind'. One scan which does appear to behave as expected is that with $\phi_L^{(\text{rel})} = \pi$ (figures 7.7 e and 7.8 e), where since the excitation profile has a minimum at zero velocity, the central peak position remains largely unchanged, and there is a slight shift of the distribution towards positive velocity. The sequence which is expected to give the most efficient cooling effect is that with $\phi_L^{(\text{rel})} = 3\pi/2 = -\pi/2$ (figures 7.7 f and 7.8 g), since the excitation profile exhibits a maximal slope (where $\frac{d}{dt}|c_2|^2 < 0$ and $\frac{d^2}{dt^2}|c_2|^2 = 0$) at zero velocity. Once again, we do not observe a cooling effect, but instead a significant heating effect is present.

It is possible that these curves do not match their respective predictions due to an offset in the Ramsey fringe phase where a non-zero relative phase is applied, such as that illustrated in figure 7.4. However, since we have tested a fairly comprehensive range of phases, and a simple offset would not lead to cooling-inducing profiles becoming inaccessible (we would expect to observe cooling in *at least one* of the plots in figure

7.7), we instead focus on sources of unwanted heating as the reasons for the absence of cooling.

7.4.2 Sources of unwanted heating

The most likely source of heating is the randomising effect brought about by the depump pulses. Averaging over the ensemble, spontaneous emission will exhibit a *net* momentum impulse of zero, just as it does in Doppler cooling. With only one spontaneous emission event per cooling cycle (of which there are N) the effect on the velocity distribution will be a simple addition of noise and a slight reduction in the cooling effect. However, the optical pumping of population from $F = 3$ into $F = 2$ on average requires *more than one* spontaneous emission event, since once excited to the upper level $F' = 3$ by the depump laser, relaxation into each of the two lower levels is approximately equally favourable. Assuming a 50/50 branching ratio, it would take on average four spontaneous emission cycles to pump over 90% of the $F = 3$ population back to $F = 2$, and indeed 50% of the population which is shifted by the Ramsey sequence will undergo two or more spontaneous emission cycles per Ramsey sequence. This is expected to contribute a considerable amount to the washing out of any cooling effect which might be induced by the Ramsey sequence.

Similar depumping pulses have been applied in other laser cooling experiments with success, but there are subtle differences. In [61], the authors report a Raman cooling scheme for sodium (Na has a similar structure to ^{85}Rb, except the nuclear spin quantum number is $I = 3/2$) in which the depump (referred to as the 'optical-pumping beam') couples the equivalent levels to ours, and a similar scheme for cesium ($I = 7/2$) is reported in [60] and [98]. Raman cooling is based on the creation of a dark velocity class around $v_z = 0$, into which population can spontaneously decay, via sequences of Raman pulses with tailored durations and detunings (and directions), which all act to push population towards $v_z = 0$. Once population decays into the dark velocity class, the probability that it will be excited out of it is ~ 0. We can draw parallels here with interferometric cooling in that the minima of the Ramsey fringes represent dark velocity states, but these are not *completely* dark in our experiments because the minima of the Ramsey fringes do not correspond to a transfer fraction of $|c_2|^2 = 0$, due

to dephasing. Indeed, in the $\sigma^+ - \sigma^+$ arrangement where we do not cancel the light shift induced splitting (as in figure 7.7), the additional dephasing further increases this minimum $|c_2|^2$. This implies that even at the minima of the Ramsey excitation profile, population will still be excited with some non-negligible probability, and the associated velocity-randomisation by spontaneous emission will occur after every application of the Ramsey-depump sequence, across the entire velocity distribution. In light of this, in section 7.5 we switch to the $\pi^+ - \pi^-$ arrangement, where we observe evidence of cooling.

As mentioned previously, in an attempt to reduce heating resulting from spontaneous emission, we may in future experiments switch the depumping transition to $|5S_{1/2}, F = 3\rangle \rightarrow |5P_{3/2}, F' = 2\rangle$, whereby relaxation to $F = 2$ is marginally favourable once in the excited state (see section 7.3), and hence the depumping process requires fewer spontaneous emission cycles on average.

Another possible cause of heating is misalignment of the depump beams. A deviation from perfect overlap on the incoming and retro-reflected beam paths would cause a slight heating along the z-axis of those atoms which are excited by the Ramsey sequence, since the atomic recoil upon absorption would exhibit a component parallel to the z-axis. Once again, the above effects will be amplified where more spontaneous emission cycles take place. Experimentally, the incoming and retro-reflected beams are measured to overlap to within 20 mrad, hence this effect is expected to be much smaller than the $2\hbar k$ imparted by the Ramsey pulses. Further to this, if the depump intensity is imbalanced between the incoming and retro-reflected paths (which it unavoidably *is*, due to losses at the chamber window, quarter waveplate and mirror), there will be a net *pushing* effect induced by the depump beams. This effect is again expected to be small compared with the Ramsey impulse, and furthermore the detectable effect can be minimised by ensuring that the depump beams are aligned perfectly perpendicular to the Raman beams.

7.5 Preliminary demonstration of cooling

In light of the above findings, we switch in this section to the $\pi^+ - \pi^-$ (lin-perp-lin) Raman arrangement. Here we expect higher contrast Ramsey fringes because the m_F sublevels are not separated by the light shift (see section 5.1.2.2), thus reducing off-resonance pulse errors and the associated dephasing.

The results of a modulation sequence with $\phi_L^{(\mathrm{rel})} = -\pi/2$ and $N = 4$ in the $\pi^+ - \pi^-$ arrangement are shown in figure 7.9 a. To gather these data, we applied the same experimental procedure as that described in section 7.4. The effective Rabi frequency in this case was measured to be $\Omega_{\mathrm{eff}} \approx 2\pi \times 400\mathrm{kHz}$ (the Ramsey pulse intensities were higher in this experiment), thus giving rise to broader Raman pulses and, respectively, higher contrast Ramsey fringes. In the plot, the points are experimental data, which are again averages over 16 shots, and the dashed curves are 10 point moving averages of the data. We measured the probe light shift to be $\delta^{AC}_{\mathrm{probe}} \approx -2\pi \times 25\,\mathrm{kHz}$. The solid curves are numerically simulated Raman velocimetry profiles (manually fitted to the data), whose corresponding predicted velocity distributions are plotted in figure 7.9 b along with their double-Gaussian (see equation 5.6) parameters.

We find that the initial (blue) velocimetry profile corresponds roughly to a double-Gaussian velocity distribution with $\sigma_1 = 4.5 \times v_R$ ($30\,\mu\mathrm{K}$), $\sigma_2 = 11 \times v_R$ ($179\,\mu\mathrm{K}$), and $a_1/a_2 = 2$. The resultant (red) velocimetry profile is well-approximated assuming the parameters $\sigma_1 = 3.5 \times v_R$ ($18\,\mu\mathrm{K}$), $\sigma_2 = 11 \times v_R$ ($179\,\mu\mathrm{K}$), and $a_1/a_2 = 2.5$, where the colder peak is centered at $v_z/v_R = 3.5$. This represents a reduction in temperature of the central portion of the velocity distribution by a factor of 1.7, where the broad background is left unchanged. Figure 7.9 b is expected to approximately represent figure 7.8 g, and we find that this is broadly correct, although it appears that figure 7.8 h ($\phi_L^{(\mathrm{rel})} = -\pi/4$) more closely matches the observed effect. This may be due to an experimental offset in the Ramsey fringe phase, such as that observed in figure 7.4.

Once again, we observe an increase in the area under the Raman velocimetry curve due to incomplete optical pumping. This is more difficult to quantify in this case since the entire velocity distribution is not visible, but considering the range of data in the plot, the area under the cooled profile is 7% larger than that under the un-cooled profile. This accounts for the fact that the simulated profile (solid red line) has a smaller amplitude than the observed profile (dashed red line), and further to this, we expect a larger discrepancy (due to the 'imprint', see section 7.4.1) at negative velocity, where the Ramsey excitation profile exhibits a maximum, as is indeed observed.

The above represents the first succesful demonstration of interferometric cooling. These

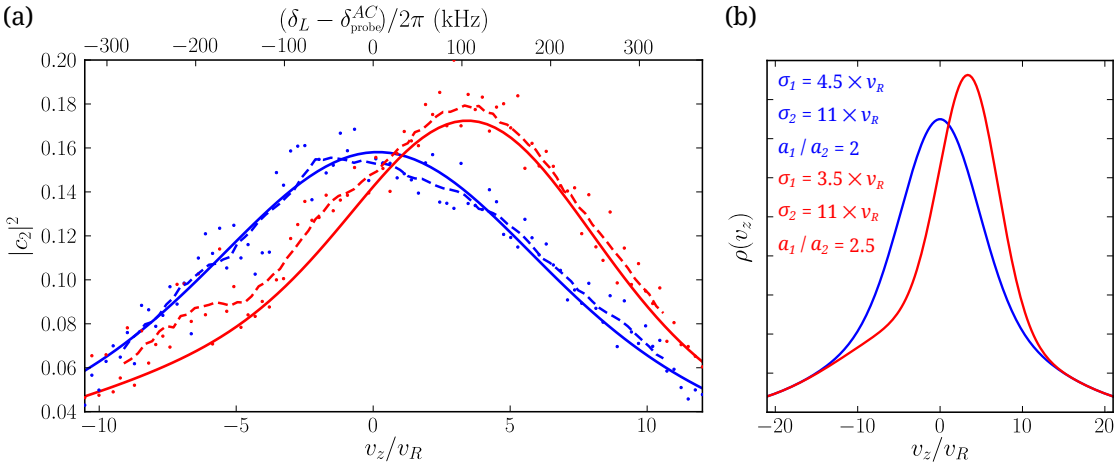

Figure 7.9: Preliminary demonstration of interferometric cooling. (a) Raman velocimetry profiles: blue – initial (un-cooled); red – resultant (cooled); dots – data, dashed curves – 10-point moving averages of the data; solid curves – numerical simulations. (b) Empirically fitted velocity distributions corresponding to the curves in (a), with the associated double-Gaussian parameters inset.

data were taken late on in the PhD project, and a full characterisation (and exploitation) of cooling in the $\pi^+ - \pi^-$ arrangement is yet to be performed. There are some experimental improvements to be made which we expect will enhance the cooling effect, as described below.

7.5.1 Immediate future improvements

The scheme presented above employs Raman pulses which impart momentum to the atom cloud in only the positive direction. As observed, this leads to an *acceleration* of the atom cloud along with the reduction in the velocity width. To counteract this effect, one must simply follow the Ramsey-depump sequence with a corresponding one in the opposite direction. In our experimental setup this can be achieved by swapping the direction of the Raman pulses with the Pockels cell (see section 4.11). It can also be achieved by preparing the atoms into the $|5S_{1/2}, F = 3\rangle$ state before the pulses are applied, instead of $|5S_{1/2}, F = 2\rangle$ (making no changes to the Raman beams), although in this case some atoms would be pumped into the outer $m_F = \pm 3$ sublevels of $F = 3$, which do not interact with the Raman beams.

The effect of cooling, whereby population accumulates in the minima of the excitation profile, can be enhanced by appling a series of cooling sequences (with alternating directions) with gradually increasing T. This will gradually reduce the width of the Ramsey

fringes, and therefore of the dark velocity class as population accumulates there, resulting in a colder sample.

One general improvement to the experiment would be an increase in the available laser power. With extra power-broadening, we would achieve higher contrast Ramsey fringes, and therefore more efficient cooling. Further to this, a reduction in the rise/fall time of the Raman pulses (see figure 4.10) is desirable, since currently at $T = 500\,\text{ns}$ the Ramsey pulses overlap in time. This would allow more control over the timings of phase shifts at small dwell times T, and is expected to improve fringe contrast. It would also allow for smaller experimental dwell times and the associated increase in the velocity capture range of the cooling scheme.

7.6 Coherent enhancements in interferometric cooling

In the introduction, and at the beginning of this chapter, we suggested that interferometric cooling is in principle applicable to a large range of species, including molecules. In this section, we describe extensions to the interferometric cooling scheme, which act to (a) make cooling within molecular structure possible, and (b) reduce the dependence of cooling upon spontaneous emission events, thus making molecular interferometric cooling a possibility.

Molecules exhibit complex ro-vibrational structure. Along with the familiar hyperfine splittings, electronic energy levels are split into vibrational ($\sim$ THz splitting) and rotational ($\sim$ GHz splitting) sublevels respectively by the molecule's vibrational and rotational degrees of freedom. The ease at which population can decay into the myriad ro-vibrational states within this structure makes traditional laser cooling of molecules extremely difficult. Despite this, laser cooling of diatomic alkaline earth halides has been succesfully demonstrated [17–19] by application of multiple repumping frequencies which address the dark ro-vibrational (and hyperfine) states. Although such techniques represent a large step forward in molecular cooling, they are only applicable to molecules with the simplest of structures.

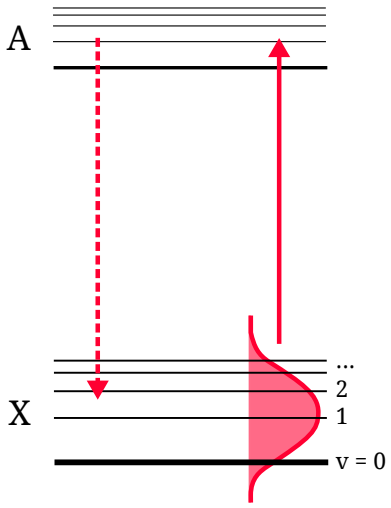

Figure 7.10: Sketch illustrating transitions between the ground and first electronic excited state of a simple molecule, where the first five vibrational levels v in each electronic state are indicated. Broad pulses lead to simultaneous excitation of all vibrational levels to the upper state.

By applying short ($< 1\,\mathrm{ns}$) pulses, in conjunction with composite pulses or adiabatic chirps, one can excite multiple molecular ro-vibronic transitions *simultaneously*, as illustrated in figure 7.10. If population decays from the upper state back to one of the lower states addressed by the broad pulses, further transitions can take place, and the transition is closed. A significant drawback of this broad pulse approach would be the large proportion of laser power wasted on frequencies that do not drive transitions, however one could envisage a scheme based on mutually phase-locked beams whose power is focussed around the required frequencies as an alternative. Such a scheme could potentially be realised in simple alkali halide molecules. Indeed, femtosecond pulse techniques in molecules have already been developed to great extent in the field of molecular *coherent control* [99–101]. Simple interferometric cooling would be ineffective in the arrangement depicted in figure 7.10, however, since there are multiple transitions present (with vastly different detunings), and for off-resonant pulses there is a contribution to the Ramsey phase from the laser detuning (that is, where $\delta_L \neq \delta^{AC}$ in equation 7.1). This is addressed in the following.

7.6.1 Frequency-independent interferometric cooling

The scheme proposed in [28], which we illustrate in figure 7.11, is based on a coherent spin echo effect (described in chapter 6 as a type of composite pulse), whereby the

dependence of the Ramsey phase on the laser detuning is removed. A more detailed description of the scheme, and a discussion of its potential for molecular cooling, can be found in the reference, and we merely summarise it here. The scheme is the same as the Ramsey $\frac{\pi}{2} - \frac{\pi}{2}$ sequence reported earlier on in this chapter, except for the addition of the two inner, counter-propagating π pulses. These pulses are timed such that a particle spends an equal amount of time in each electronic state ($|1\rangle$ and $|2\rangle$) within the interferometer. The second pulse is applied at a time T' after the first, the third $2T$ after the second, and the fourth $2T - T'$ after the third, where $0 < T' < 2T$. The result of this is that the laser detuning terms δ_L drop out of the expression for the resultant phase, and we are left with a purely velocity-dependent excitation, that is, $c_2 \propto \frac{1}{2}\left(1 + e^{-i\Delta\Phi}\right)$ where for single-photon transitions

$$\Phi = (v_z k + \omega_R)8T - \phi_1 + 2\phi_2 - 2\phi_3 + \phi_4, \tag{7.11}$$

in which ω_R is the single-photon recoil frequency and ϕ_n is the phase of the n^{th} pulse. The sequence must satisfy the condition $4T < \tau$, where τ is the lifetime of the excited state. It is important to note that for molecular structures (see figure 7.10 for a simplistic example), the first pulse will induce a superposition between one vibrational state in the ground electronic state X and all vibrational states in the excited electronic state A, and the second pulse will then populate multiple vibrational states in X. With the addition of such superpositions, pulses must be precisely timed to coincide with wavefunction revivals and the scheme becomes more involved. Nevertheless, numerical simulations performed by the authors of [28] suggest that interferometric contrast is achievable, and indeed that experimental studies appear worthwhile.

7.6.2 Coherent amplification of a velocity-selective impulse

In more complex molecular structures, population will inevitably decay into dark states not addressed even with broad laser pulses. One potential workaround for this is to reduce the dependence of the cooling scheme on spontaneous emission events. This could be achieved with the technique known as 'amplified cooling', which is analysed by Freegarde, Daniell and Segal in [102], and earlier, proposed in a similar form, by Bakos *et al* in [103]. In amplified cooling, which we illustrate in figure 7.12, an initial

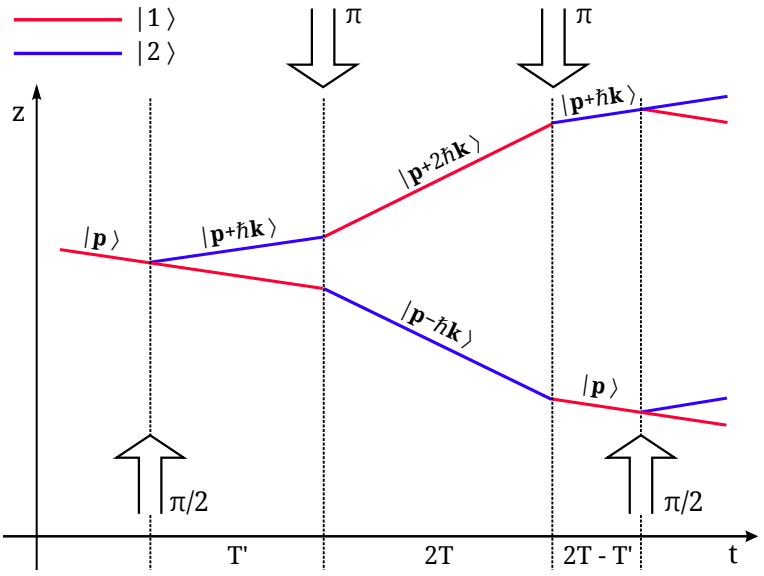

Figure 7.11: Scheme proposed in [28] for frequency-independent interferometric laser cooling.

velocity-selective excitation (a Ramsey sequence, for example), is reinforced by several interleaved π pulses before spontaneous emission occurs. The initial excitation acts to excite negative-moving atoms to the upper state (and shift them towards positive velocity), and leave positive-moving atoms in the ground state. The first π pulse is applied counter-propagating to the initial excitation, such that as the populations are inverted, the impulse acts to overlap their velocity distributions further, and the initial impulse is reinforced. The second π pulse couter-propagates relative to the first, the third counter-propagates relative to the second, and so on. When spontaneous emission occurs, and population relaxes into the ground state, the resultant velocity distribution is narrower.

Where the interferometric cooling schemes presented previously can impart only an $\hbar k$ (or $2\hbar k$ for Raman transitions) impulse to the particle per spontaneous emission event, with amplified cooling we are limited by the number of π pulses we can apply before spontaneous emission occurs.

7.7 Conclusion

In this chapter we have discussed the laser cooling of atoms and molecules with sequences of coherent laser pulses. We described the proposed scheme for cooling in our cold

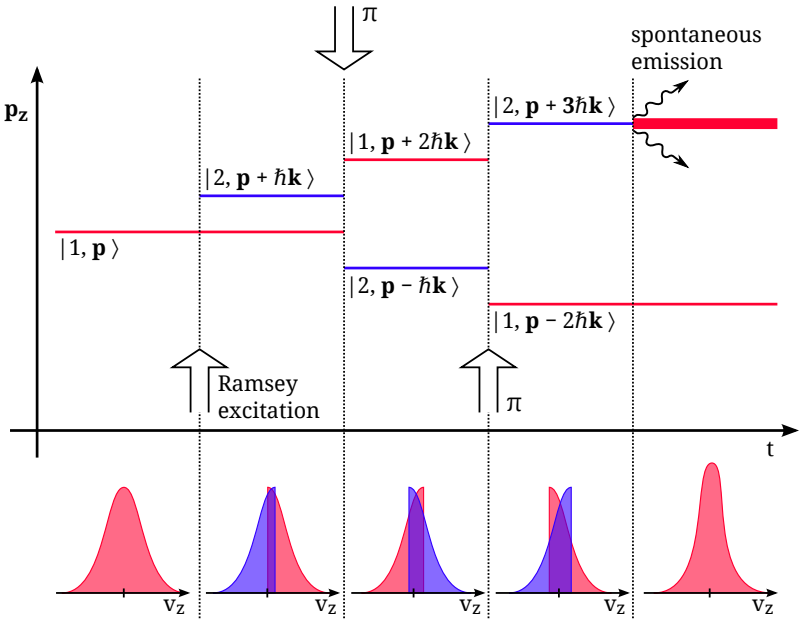

Figure 7.12: Scheme proposed in [102] for coherent amplification of a velocity-selective impulse.

rubidium system, whereby a Ramsey interferometer provides a velocity-selective impulse in a manner analogous to conventional Doppler cooling, and dissipation is induced by spontaneous emission. After characterising the vital components of the experimental sequence, we demonstrated modulation of the atomic velocity distribution at a range of system parameters, where the Raman pulses were applied in the $\sigma^+ - \sigma^+$ polarisation arrangement. In this case we did not observe cooling, probably because of a light-shift-induced washing-out of fringe contrast. In the $\pi^+ - \pi^-$ arrangement, where fringe contrast is higher, cooling was observed, and numerical simulations manually fitted to the data indicated a reduction in the temperature of the central velocity peak by a factor of 1.7, after a series of $N = 4$ cooling cycles.

The experiments performed here using already-ultracold atoms represent a first experimental step towards the interferometric cooling of molecules. With an improved laser system, and the addition of the enhancement schemes described here, namely frequency-independent interferometric cooling, and 'amplified cooling', one can envisage future schemes based on coherent laser pulses for molecular cooling.

Chapter 8

Conclusions

Laser cooling has revolutionised experimental atomic physics since its first demonstrations almost thirty years ago. It has opened up new and exciting branches of study such as trapped-ion quantum computing, lattice-based quantum simulation and condensate wavefunction dynamics, and pushed the boundaries of precision measurement and timing with cold atom clocks and interferometric sensors.

In the same way that ultracold atoms inspired groundbreaking research, ultracold *molecules* offer the potential for exciting new discoveries, through, for example, ultracold chemistry and tests for variations in the fundamental constants. Whilst there exist other techniques for ultracold molecule production, of which photo-association is perhaps the most prominent, techniques for the laser cooling of molecules are still in their infancy. Indeed, the current state-of-the-art is highly species-selective, in that only molecules (and *atoms*, for that matter) with the simplest of structure can be laser cooled.

The primary line of investigation of this thesis was the development of atomic and molecular cooling techniques based on sequences of laser pulses, which can be applied to a broad range of species. As a test-bed for our pulse schemes, we used ultracold rubidium-85 atoms in free-fall after release from a magneto-optical trap. We realised a two-level quantum system in the atoms by inducing stimulated Raman transitions between ground hyperfine states, whereby the coherent pulses impart momentum to the atoms. The detailed characterisation of the Raman pulses (chapter 5) gave us a good

understanding of the system's behaviour. In particular, studies of the polarisation-dependent light shift (section 5.1.2) and magnetic fields (section 5.1.1) provided insight into the dephasing of atomic states during pulses, and how it could be reduced.

Coherent operations intended for precise quantum control of ultracold atoms, such as quantum gates in QIP, beamsplitters and mirros in atom inteferometry, and our Raman pulses, unavoidably suffer from systematic errors in such system parameters as the control field intensity and frequency, and these lead to a reduction in the fidelity of the operations. The second major line of investigation in this thesis was the improvement of fidelity of coherent operations in our notably inhomogeneous system, by way of composite pulses (chapter 6). Composite pulses, whereby 'naive' single pulses are replaced by sequences of rotations with tailored durations and phases, were found to considerably improve fidelity in our experimental system. Whilst they have not yet been fully exploited by the cold atom community, the benefits of their application are of growing interest. Indeed, closer to home, it is expected that such error-resistant techniques as composite pulses and adiabatic chirps will be necessary in future realisations of interferometric cooling. We found that where significant 'off-resonance' errors were present, the WALTZ-type composite pulse afforded a 64% increase in the fidelity of a π pulse. Furthermore, with the 'Knill' composite pulse, one could potentially induce population inversion with $> 99\%$ efficiency in a Zeeman-degenerate atom cloud (where multiple coupling strengths are present) at temperatures readily achievable in a magneto-optical trap.

With the Raman system in place, we began preliminary tests of interferometric cooling (chapter 7), whereby velocity-selective Ramsey interferometry is used to provide a velocity-selective impulse in a similar fashion to traditional Doppler cooling. In fact, the demonstration of cooling with this technique is perhaps the most significant result presented in this thesis. In preliminary tests, we observe a factor of 1.7 reduction in temperature of the central component of the velocity distribution after $N = 4$ repeated applications of the cooling scheme. Coherent pulse-based cooling schemes, by their nature, are open to fidelity-enhancing techniques, such as composite pulses, adiabatic chirps and spin echoes. Indeed, the latter provides us with a means for removing the dependence of the interferometer output on the laser frequency (leaving a purely *velocity*-selective excitation), and in turn allows for the interferometric cooling of species

with ro-vibrational structure. Furthermore, one can exploit such techniques as 'amplified cooling' in pulse-based schemes to reduce the dependence of cooling upon spontaneous emission. With this, we conclude that such laser-pulse-based schemes for molecular cooling are a promising prospect for the future.

Some suggested experimental improvements

We end with a suggested select few technical changes which can be made to the present experimental setup to improve its performance. The item at the top of most experimental atomic physicist's wishlists is a bigger, more powerful laser system, and this is no exception. Higher power, which could be gained from a frequency-doubled fibre laser system such as that described in [104] ($\sim 43\,\mathrm{W}$ at $780\,\mathrm{nm}$), would allow for higher Rabi frequencies, which would in turn lead to less dephasing, higher interferometric contrast, and broader capture ranges for cooling. As described in section 3.3.2.2, switching off the MOT coils induces significant eddy currents in the surrounding conductors, leading to slow field decay. Second on the wishlist for the next experimenter might be a glass vacuum cell, which by its nature would not conduct eddy currents. More minor improvements might include: calibration of the I&Q modulator channels to remove the present non-linearities (see section 4.3); stabilisation of the frequency and power of the Raman laser to prevent drifts in the detuning from single-photon resonance and pulse intensity, respectively; and focussing of the Raman beams through the pulse AOM to reduce the rise/fall time of the Raman pulses, thus allowing for greater control via composite pulses and broader capture ranges in interferometric cooling.

Part IV

Appendices

Appendix A

Theory Supplements

A.1 Two-level atom-laser interaction

A useful tool for describing coherent atomic manipulation is the 'toy' two-level atom model, in which an atom is approximated simply as two stable energy levels, $|g\rangle$ and $|e\rangle$, which can be coupled by some driving field. Often in atomic physics this driving field takes the form of a coherent oscillating electric field, or laser beam, which couples the two states via the dipole interaction. If starting in the lower state, $|g\rangle$, the atom can absorb a photon from the beam, causing a transition to the upper state $|e\rangle$. When starting in $|e\rangle$ the atom can be forced to emit a photon into the laser beam, causing a transition down to $|g\rangle$. These two processes are known as *absorption* and *stimulated emission* respectively, and in the absence of any *incoherent* processes, such as *spontaneous* emission, they allow us to drive *coherent* transitions between $|g\rangle$ and $|e\rangle$. The following gives a detailed introduction to coherent two-level atom-light interactions. Many of the principles introduced below emerge in the three-level treatment given in chapter 2, such as the rotating wave approximation, the dressed state picture, and the light shift.

A.1.1 The two-level Hamiltonian

The two energy levels $|g\rangle$ and $|e\rangle$ in the two-level atom have energy eigenvalues given by their atomic frequencies: $E_g = \hbar\omega_g$ and $E_e = \hbar\omega_e$. The atom can exist in a superposition of the two states, determined by the amplitudes $c_g(t)$ and $c_e(t)$, of the quantum state

vector

$$|\psi(t)\rangle = c_g(t)|g\rangle + c_e(t)|e\rangle = \begin{pmatrix} c_g(t) \\ c_e(t) \end{pmatrix}. \tag{A.1}$$

Our laser, an oscillating electromagnetic field $\mathbf{E} = \mathbf{E_0}\cos(\omega t + \phi)$, where ω and ϕ are the frequency and phase of the field respectively, interacts with the atom as described by the Hamiltonian

$$\hat{H} = \hbar\omega_g|g\rangle\langle g| + \hbar\omega_e|e\rangle\langle e| - \mathbf{d}\cdot\mathbf{E}. \tag{A.2}$$

The first two terms represent the internal, 'bare' Hamiltonian, and $V = -\mathbf{d}\cdot\mathbf{E} = -e\mathbf{r}\cdot\mathbf{E}$ represents the atom-field dipole interaction, where $\mathbf{r}$ is the vector defining the position of the electron relative to the atomic nucleus. We can re-write the Hamiltonian in matrix form:

$$\hat{H} = \begin{pmatrix} \hbar\omega_g & V_{eg} \\ V_{ge} & \hbar\omega_e \end{pmatrix}, \tag{A.3}$$

where we define the element-wise coupling terms[1] as

$$V_{ge} = V_{eg}^* = \langle e|V|g\rangle = \hbar\Omega_{ge}\cos(\omega t + \phi) = \hbar\Omega_{ge}\left(\frac{e^{i(\omega t+\phi)} + e^{-i(\omega t+\phi)}}{2}\right). \tag{A.4}$$

Ω_{ge} in this equation determines the strength of the coupling between the levels, and is known as the *Rabi frequency*:

$$\Omega_{ge} = \Omega_{eg}^* = -\frac{\langle e|\mathbf{d}\cdot\mathbf{E_0}|g\rangle}{\hbar}. \tag{A.5}$$

The atom will evolve according to the time-dependent Schrödinger equation (TDSE)

$$i\hbar\frac{\partial}{\partial t}|\psi(t)\rangle = \hat{H}|\psi(t)\rangle, \tag{A.6}$$

which in terms of the time-varying state amplitudes can be written as two coupled differential equations:

$$i\hbar\frac{\partial}{\partial t}c_g(t) = \hbar\omega_g c_g(t) + V_{eg}c_e(t) \tag{A.7}$$

$$i\hbar\frac{\partial}{\partial t}c_e(t) = \hbar\omega_e c_e(t) + V_{ge}c_g(t). \tag{A.8}$$

[1] The dipole interaction does not couple a level to itself, therefore in equation A.3, $V_{gg} = V_{ee} = 0$.

These equations exhibit fast oscillations of $c_g(t)$ and $c_e(t)$ at their respective atomic frequencies ω_g and ω_e, alongside relatively slow oscillations, assuming $\Omega_{ge} \ll \omega_{g,e}$, due to interaction with the laser. We can factor out the fast oscillations by making the substitutions

$$c_g(t) = \tilde{c_g}(t)e^{-i\omega_g t} \tag{A.9}$$

$$c_e(t) = \tilde{c_e}(t)e^{-i\omega_e t} \tag{A.10}$$

which, when applied in equations A.7 and A.8, give

$$i\hbar\frac{\partial}{\partial t}\tilde{c_g}(t) = V_{eg}\tilde{c_e}(t)e^{-(\omega_{eg})t} \tag{A.11}$$

$$i\hbar\frac{\partial}{\partial t}\tilde{c_e}(t) = V_{ge}\tilde{c_g}(t)e^{-(\omega_{ge})t} \tag{A.12}$$

where $\omega_{eg} = \omega_e - \omega_g$. At this point we introduce the *rotating wave approximation*, which simplifies the TDSE, as follows. Writing out equation A.12 explicitly via equation A.4 and integrating over an interaction period from $t_0 \to t$ gives

$$i\hbar\tilde{c_e}(t) = i\hbar\tilde{c_e}(t_0) + \hbar\Omega_{ge}\int_{t_0}^{t}\tilde{c_e}(t')\left(\frac{e^{i((\omega-\omega_{eg})t'+\phi)} + e^{-i((\omega+\omega_{eg})t'+\phi))}}{2}\right)dt'. \tag{A.13}$$

Whilst we do not solve the TDSE from this form, by inspection we can see that upon integration the $e^{i((\omega-\omega_{eg})}t$, 'resonant' term will be much larger than the $e^{i((\omega+\omega_{eg})}t$, 'off-resonant' term in the case where ω and ω_{eg} are similar. The rotating wave approximation acts to drop the off-resonant term from the TDSE. We now define the detuning of the laser with respect to the atomic resonance as $\delta \equiv \omega - \omega_{eg}$, and re-write equations A.11 and A.12 with the rotating wave approximation:

$$i\hbar\frac{\partial}{\partial t}\tilde{c_g}(t) = \frac{\hbar}{2}\Omega_{eg}\tilde{c_e}(t)e^{i(\delta t+\phi)} \tag{A.14}$$

$$i\hbar\frac{\partial}{\partial t}\tilde{c_e}(t) = \frac{\hbar}{2}\Omega_{ge}\tilde{c_g}(t)e^{-i(\delta t+\phi)}, \tag{A.15}$$

and the Hamiltonian is therefore

$$\hat{H} = \frac{\hbar}{2}\begin{pmatrix} 0 & \Omega_{eg}e^{i(\delta t+\phi)} \\ \Omega_{eg}^{*}e^{-i(\delta t+\phi)} & 0 \end{pmatrix}. \tag{A.16}$$

This is a time-dependent Hamiltonian, which includes a rotation around the z-axis at a rate δ. At $\delta = 0$, the Hamiltonian becomes time-independent and the atom oscillates between $|g\rangle$ and $|e\rangle$ at the resonant Rabi frequency Ω_{eg}. We would, however, like to work with a time-indepentent Hamiltonian in the more general case where $\delta \neq 0$, and this is possible by transforming to a rotating frame, as follows. We have the freedom to make the substitution $|\psi\rangle = \hat{O}|\psi'\rangle$, where $\hat{O}$ is some operator and $|\psi'\rangle$ is a transformed state vector. With such a substitution, the TDSE becomes

$$i\hbar\frac{\partial}{\partial t}(\hat{O}|\psi'\rangle) = \hat{H}(\hat{O}|\psi'\rangle), \tag{A.17}$$

and if we apply the product rule to the left hand side, operate with $\hat{O}^\dagger$ from the left, and re-arrange, we find

$$i\hbar\hat{O}^\dagger\hat{O}\frac{\partial}{\partial t}|\psi'\rangle = \left(\hat{O}^\dagger\hat{H}\hat{O} - i\hbar\hat{O}^\dagger\frac{\partial}{\partial t}\hat{O}\right)|\psi'\rangle. \tag{A.18}$$

In order to transform to the rotating frame, we choose

$$\hat{O} = \hat{R}(t) = e^{i\sigma_z\delta t/2}\begin{pmatrix} e^{i\delta t/2} & 0 \\ 0 & e^{-i\delta t/2} \end{pmatrix}, \tag{A.19}$$

where σ_z is the Pauli spin matrix which represents a rotation about the z-axis. Inserting $\hat{R}(t)$ into equation A.18 gives the TDSE with a time-independent Hamiltonian:

$$i\hbar\frac{\partial}{\partial t}|\psi'\rangle = \hat{H_R}|\psi'\rangle, \text{ where } \hat{H_R} = \frac{\hbar}{2}\begin{pmatrix} \delta & \Omega_{eg}e^{i\phi} \\ \Omega_{eg}^* e^{-i\phi} & -\delta \end{pmatrix}. \tag{A.20}$$

In this arrangement, we observe evolution which is purely due to the interaction between the atom and the laser.

A.1.2 The dressed-state eigenfunctions

The eigenvalues λ of this matrix, which we calculate by setting the determinant of $\lambda\mathbb{I} - \hat{H_R}$ (where $\mathbb{I}$ is the identity matrix) to zero and solving, are $\lambda_\pm = \pm\frac{\hbar}{2}\Omega$, where we

define the *generalised*, off-resonant Rabi frequency as

$$\Omega = \sqrt{|\Omega_{eg}|^2 + \delta^2}\,. \tag{A.21}$$

Taking the approach offered in complement B_{IV} of *Quantum Mechanics* by Cohen-Tannoudji *et al*, in which the angles Θ and Φ are defined by

$$\tan\Theta = \frac{2|\hat{H}_{12}|}{\hat{H}_{11} - \hat{H}_{22}} = \frac{\Omega_{eg}}{\delta} \tag{A.22}$$

$$e^{i\Phi} = \frac{\hat{H}_{12}}{|\hat{H}_{12}|} = e^{i\phi}, \tag{A.23}$$

and therefore $\sin\Theta = \Omega_{eg}/\Omega$ and $\cos\Theta = \delta/\Omega$ with $0 \leq \Theta \leq \pi$, we can write the *dressed-state* eigenvectors of the Hamiltonian $\hat{H_R}$, as

$$|\lambda_+\rangle = \cos\frac{\Theta}{2}|g\rangle_R\, e^{i\Phi/2} + \sin\frac{\Theta}{2}|e\rangle_R\, e^{-i\Phi/2} \tag{A.24}$$

$$|\lambda_-\rangle = \sin\frac{\Theta}{2}|g\rangle_R\, e^{i\Phi/2} - \cos\frac{\Theta}{2}|e\rangle_R\, e^{-i\Phi/2}. \tag{A.25}$$

This is found by writing out the Schrödinger equation $\hat{H_R}|\lambda_+\rangle = \lambda_+|\lambda_+\rangle$ in terms of the eigenvector components a and b:

$$\frac{\hbar}{2}\begin{pmatrix} \delta & \Omega_{eg}e^{i\phi} \\ \Omega^*_{eg}e^{-i\phi} & -\delta \end{pmatrix}\begin{pmatrix} a \\ b \end{pmatrix} = \frac{\hbar}{2}\Omega\begin{pmatrix} a \\ b \end{pmatrix} \tag{A.26}$$

which, if we divide both sides by $\delta e^{i\phi}$, can be re-written (for a real and positive Ω_{eg}) in terms of the angles Θ and Φ:

$$\frac{\hbar}{2}\begin{pmatrix} e^{-i\Phi} & \tan\Theta \\ e^{-2i\Phi}\tan\Theta & -e^{-i\Phi} \end{pmatrix}\begin{pmatrix} a \\ b \end{pmatrix} = \frac{\hbar}{2}e^{-i\Phi}\cos\Theta\begin{pmatrix} a \\ b \end{pmatrix}. \tag{A.27}$$

The above equation yields

$$a\left(1 - \frac{1}{\cos\Theta}\right)e^{-i\Phi} + b\tan\Theta = 0, \tag{A.28}$$

which if we multiply both sides by $\cos\Theta$ and apply double-angle formulae to the remaining trigonometric terms, becomes

$$-ae^{-i\Phi/2}\cos\frac{\Theta}{2}+be^{i\Phi/2}\sin\frac{\Theta}{2}=0, \tag{A.29}$$

and from this we get the normalised eigenvector $|\lambda_+\rangle$ as in equation A.24. We apply the same procedure to find $|\lambda_-\rangle$.

A.1.3 Light shifts

In the case where $|\delta|\gg\Omega_{ge}$, we can calculate the shift in the energy of the eigenvalues caused by the laser beam, known as the AC Stark shift or *light shift*, by taking the Maclaurin expansion of $\lambda_\pm$ in powers of Ω_{eg}/δ:

$$\lambda_\pm=\pm\frac{\hbar}{2}\delta\sqrt{\left|\frac{\Omega_{eg}}{\delta}\right|^2+1}\approx\pm\left(\frac{\hbar}{2}\delta+\frac{\hbar\Omega_{eg}^2}{4\delta}+\dots\right). \tag{A.30}$$

In the case of positive detuning ($\delta>0$), $\cos\Theta\simeq 1$ and therefore $\Theta\simeq 0$, so equations A.24 and A.25 become $|\lambda_+\rangle\simeq|g\rangle_R e^{i\Phi/2}$ and $|\lambda_-\rangle\simeq|e\rangle_R e^{-i(\Phi/2-\pi)}$ respectively. Consequently, the lower state $|g\rangle_R$ is shifted *up* in energy by $\Delta E_g\simeq+\hbar\Omega_{ge}^2/4\delta$, and the upper state $|e\rangle_R$ is shifted *down* by $\Delta E_e\simeq-\hbar\Omega_{ge}^2/4\delta$. Conversely, with negative detuning ($\delta<0$): $\Theta\simeq\pi$, and equations A.24 and A.25 become $|\lambda_+\rangle\simeq|e\rangle_R e^{-i\Phi/2}$ and $|\lambda_-\rangle\simeq|g\rangle_R e^{i\Phi/2}$ respectively. In this case $|g\rangle_R$ is shifted *down* in energy, and $|e\rangle_R$ is shifted *up*.

A.1.4 Solutions to the TDSE

Now that we have a time-independent Hamiltonian, for which we have defined energy eigenvalues and eigenvectors, we are able to derive the solutions to the time-dependent Schrödinger equation in the interaction picture, as follows. We begin at time t_0 with our atom in the state $|\psi(t_0)\rangle=\tilde{c_g}(t_0)|g\rangle+\tilde{c_e}(t_0)|e\rangle$. We can transform $|\psi(t_0)\rangle$ to the rotating frame, in which we have defined the eigenvectors $|\lambda_\pm\rangle$, by acting on it with the operator $\hat{R}^{-1}(t_0)=\hat{R}^\dagger(t_0)$ from equation A.19:

$$|\psi(t_0)\rangle_R=\tilde{c_g}(t_0)e^{i\delta t_0/2}|g\rangle+\tilde{c_e}(t_0)e^{-i\delta t_0/2}|e\rangle=\tilde{c_g}(t_0)|g\rangle_R+\tilde{c_e}(t_0)|e\rangle_R. \tag{A.31}$$

During an interaction with the laser of duration t, the atom will evolve according to the TDSE given in equation A.20, which can be solved in terms of the time-evolution operator $U(t_0, t)$:

$$|\psi(t_0 + t)\rangle_R = U(t_0, t)|\psi(t_0)\rangle_R, \text{ where } U(t_0, t) = e^{-i\hat{H}_R(t-t_0)/\hbar}. \tag{A.32}$$

Given that we have a set of eigenvalues $\lambda_\pm$ and eigenvectors $|\lambda_\pm\rangle$, which are represented in the eigenvalue equations $\hat{H}_R|\lambda_\pm\rangle = \lambda_\pm|\lambda_\pm\rangle$, a function $f(\hat{H}_R)$ of the Hamiltonian (an operator) will obey the equation

$$f(\hat{H}_R)|\lambda_\pm\rangle = f(\lambda_\pm)|\lambda_\pm\rangle. \tag{A.33}$$

This can be applied to the exponential function $U(t_0, t)$ in equation A.32 along with the identity relation in our two-eigenvector basis ($|\lambda_+\rangle\langle\lambda_+| + |\lambda_-\rangle\langle\lambda_-| = 1$) to give

$$\begin{aligned} U(t_0, t) &= e^{-i\hat{H}_R(t-t_0)/\hbar}\left(|\lambda_+\rangle\langle\lambda_+| + |\lambda_-\rangle\langle\lambda_-|\right) && \text{(A.34)} \\ &= e^{i\lambda_+(t-t_0)/\hbar}|\lambda_+\rangle\langle\lambda_+| + e^{i\lambda_-(t-t_0)/\hbar}|\lambda_-\rangle\langle\lambda_-|. && \text{(A.35)} \end{aligned}$$

We can then use $\hat{R}(t_0 + t)$ to convert back to the basis $|g\rangle$, $|e\rangle$:

$$|\psi(t_0 + t)\rangle = \hat{R}(t_0 + t)|\psi(t_0 + t)\rangle_R \tag{A.36}$$

From this, we obtain the amplitudes $\tilde{c}_g(t_0 + t)$ and $\tilde{c}_e(t_0 + t)$ after an interaction of time t with the laser field:

$$\begin{aligned} \tilde{c}_g(t_0 + t) = e^{i\delta t/2}\Bigg(&\tilde{c}_e(t_0)e^{i(\delta t_0+\phi_0)}\left[-i\sin\Theta\sin\left(\frac{\Omega t}{2}\right)\right] \\ &+ \tilde{c}_g(t_0)\left[\cos\left(\frac{\Omega t}{2}\right) + i\cos\Theta\sin\left(\frac{\Omega t}{2}\right)\right]\Bigg) \end{aligned} \tag{A.37}$$

$$\begin{aligned} \tilde{c}_e(t_0 + t) = e^{-i\delta t/2}\Bigg(&\tilde{c}_e(t_0)\left[\cos\left(\frac{\Omega t}{2}\right) - i\cos\Theta\sin\left(\frac{\Omega t}{2}\right)\right] \\ &+ \tilde{c}_g(t_0)e^{-i(\delta t_0+\phi_0)}\left[-i\sin\Theta\sin\left(\frac{\Omega t}{2}\right)\right]\Bigg). \end{aligned} \tag{A.38}$$

A.2 Full Raman Hamiltonian

For simplicity, in the Hamiltonian of expression 2.10, and in the subsequent derivations in chapter 2 we omitted the couplings indicated by the dashed lines in figure 2.1, namely the terms Ω_{an} where $a \neq n$. In the following we write out the complete mathematical expressions. When we consider the coupling of both lower levels by both Raman lasers, the three-level Hamiltonian is written

$$\hat{H} = \begin{pmatrix} \frac{\mathbf{p}^2}{2M} + \hbar\omega_1 & 0 & \frac{\hbar\Omega_{11}}{2}e^{i(\omega_{L1}t-\phi_{L1})} + \frac{\hbar\Omega_{12}}{2}e^{i(\omega_{L2}t-\phi_{L2})} \\ 0 & \frac{(\mathbf{p}+\hbar(\mathbf{k}_{L1}-\mathbf{k}_{L2}))^2}{2M} + \hbar\omega_2 & \frac{\hbar\Omega_{22}}{2}e^{i(\omega_{L2}t+\phi_{L2})} + \frac{\hbar\Omega_{21}}{2}e^{i(\omega_{L1}t+\phi_{L1})} \\ \frac{\hbar\Omega_{11}^*}{2}e^{-i(\omega_{L1}t-\phi_{L1})} + \frac{\hbar\Omega_{12}^*}{2}e^{-i(\omega_{L2}t-\phi_{L2})} & \frac{\hbar\Omega_{22}^*}{2}e^{-i(\omega_{L2}t+\phi_{L2})} + \frac{\hbar\Omega_{21}^*}{2}e^{-i(\omega_{L1}t+\phi_{L1})} & \frac{(\mathbf{p}+\hbar\mathbf{k}_{L1})^2}{2M} + \hbar\omega_3 \end{pmatrix}, \tag{A.39}$$

which is different from equation 2.10 in that there are two terms in each of the non-zero off-diagonals, instead of one. If we apply the same mathematical treatment to this as given in sections 2.1.3 and 2.1.4, we arrive at the effective two-level Hamiltonian of the form

$$\hat{H} = \begin{pmatrix} H_{11} & H_{12} \\ H_{21} & H_{22} \end{pmatrix}, \tag{A.40}$$

where the respective components are

$$H_{11} = -\frac{\hbar|\Omega_{11}|^2}{4\Delta} - \frac{\hbar\Omega_{11}\Omega_{12}^*}{4\Delta_{12}}e^{i[(\omega_{HFS}+\delta)t-\phi_L]} - \frac{\hbar\Omega_{12}\Omega_{11}^*}{4\Delta}e^{i[-(\omega_{HFS}+\delta)t+\phi_L]} - \frac{\hbar|\Omega_{12}|^2}{4\Delta_{12}} \tag{A.41a}$$

$$H_{12} = -\frac{\hbar\Omega_{11}\Omega_{22}^*}{4\Delta}e^{i(\delta t-\phi_L)} - \frac{\hbar\Omega_{11}\Omega_{21}^*}{4\Delta_{21}}e^{-i\omega_{HFS}t} - \frac{\hbar\Omega_{12}\Omega_{22}^*}{4\Delta}e^{-i\omega_{HFS}t} - \frac{\hbar\Omega_{12}\Omega_{21}^*}{4\Delta_{21}}e^{i[-(2\omega_{HFS}+\delta)t+\phi_L]} \tag{A.41b}$$

$$H_{21} = -\frac{\hbar\Omega_{22}\Omega_{11}^*}{4\Delta}e^{-i(\delta t-\phi_L)} - \frac{\hbar\Omega_{22}\Omega_{12}^*}{4\Delta_{12}}e^{i\omega_{HFS}t} - \frac{\hbar\Omega_{21}\Omega_{11}^*}{4\Delta}e^{i\omega_{HFS}t} - \frac{\hbar\Omega_{21}\Omega_{12}^*}{4\Delta_{12}}e^{i[(2\omega_{HFS}+\delta)t-\phi_L]} \tag{A.41c}$$

$$H_{22} = -\frac{\hbar|\Omega_{22}|^2}{4\Delta} - \frac{\hbar\Omega_{22}\Omega_{21}^*}{4\Delta_{21}}e^{i[-(\omega_{HFS}+\delta)t+\phi_L]} - \frac{\hbar\Omega_{21}\Omega_{22}^*}{4\Delta}e^{i[(\omega_{HFS}+\delta)t-\phi_L]} - \frac{\hbar|\Omega_{21}|^2}{4\Delta_{21}}. \tag{A.41d}$$

Note that this is equivalent to the two-level Hamiltonian of expression 2.22 if we only consider the 1st term in each of the above Hamiltonian elements. We can see that all terms which are not underlined oscillate and quickly average to zero [32, 105], leaving only the underlined terms. Therefore the only *additional* terms that emerge in the full two-level Hamiltonian are the 4th terms in each of H_{11} and H_{22}, and we arrive at the form given in equation 2.22, where the off-diagonal light shift terms are defined as in equation 2.23.

Appendix B

Numerical model

B.1 Summary of model parameters

The numerical simulations accompanying the data in chapters 5 through 7 are performed in *Python*, by application of equations 2.36. Each plot has an associated table of model parameters, which we describe in the following.

1. I_1, I_2: The intensities of the two Raman beams. I_1 is the intensity of the higher-frequency AOM-shifted 'pump' beam, and I_2 is that of the lower-frequency, EOM-shifted 'Stokes' beam. $P_{1,2}$ are measured experimentally using an optical power meter, and inserted into $I_{1,2} = P_{1,2}/l_{1,2}^2$, where $l_1 = 1.7\,\text{mm}$ and $l_2 = 1.4\,\text{mm}$ are the side-lengths of the top-hat Raman beams. We calculate the electric field amplitudes using $E_{1,2} = \sqrt{2I_{1,2}/c\epsilon_0}$, and insert these into equations 2.36 for the numerical simulations. There is often (but not always) a discrepancy between the expected (based on the measured beam powers) and observed Rabi frequencies (see section 5.1.4.1), possibly due to a systematic offset in the power measurements or the measurements of Δ. In light of this, we choose arbitrarily in the simulations to alter $I_{1,2}$ (rather than Δ, although this would be equivalent) such that a better fit to the data is achieved.

2. Δ: The single-photon detuning, as defined in equation 2.17. This is measured experimentally with the *Advantest* wavemeter, and inserted directly into the numerical simulations. The resolution of the wavemeter, and experimental drift (the Tiger laser is not frequency-locked) imposes an uncertainty of $2\pi \times 0.5\,\text{GHz}$ on the measurement.

As mentioned above, there may be a systematic offset in the measurements of Δ because *both* Raman beams ($\sim 3\,\text{GHz}$ apart, relative amplitudes unknown at this point) are channelled into the wavemeter.

3. δ_L: The two-photon laser detuning from the hyperfine splitting: $\delta_L = (\omega_1 - \omega_2) - (\omega_{L1} - \omega_{L2})$. The experimentally-applied δ_L, which we can control with 1 Hz resolution, is inserted directly into the numerical simulation.

4. δ_{AC}: The empirically-measured combined AC stark shift. This is taken as the central resonance point in a scan of the laser detuning δ_L.

5. B_z: The z-axis magnetic field. This is inferred from the current I_z passed through the z-axis shim coil pair, according to a gradient of $3.43\,\text{mG/mA}$, as calculated in section 5.1.1. We estimate the zero-point of B_z to occur at $I_z = 86 \pm 5\,\text{mA}$ (see section 5.1.2.1). The large error on this value is a result of drifts and realignments of the MOT optics, and changing lab magnetic fields (some chamber components, such as the bolts, can become magnetised).

6. τ: The experimentally-applied pulse-length. t_π is the measured duration of a π pulse.

7. σ_1, σ_2: The inferred standard deviations of the two estimated overlapping Gaussian velocity distributions (see section 5.2.1), often given in units of the Raman recoil velocity v_R. The velocity distribution parameters are inferred by manually fitting the numerical simulation to the data.

8. a_1/a_2: The inferred ratio of the amplitudes of the two Gaussian estimated velocity distributions. The form of the velocity density distribution is given in equation 5.6 in section 5.2.1

9. S: The scaling parameter, which reflects the maximum achievable experimental fidelity. The physical source of this is the loss of atoms from the interrogation region (see section 5.1.3.1). For single-pulse experiments, the upper bound on S is 1, and the lower bound we find to be 0.65 (see figure 5.7). In the figures, the red curves are the 'output' simulated populations, multiplied by this scaling factor: $|c_2|^2 \times S$.

B.2 Sample code

SampleCode.py **Page 1**

```
#-------------------------------------------------------------------------------#
# Python code for simulating the spectral profile of a Raman CORPSE pulse       #
# A. Dunning, Jan 2014                                                          #
#                                                                               #
# Note: c_{1,2} notation is replaced by c_{g,e} in this code and                #
# the equations of motion (eqns 2.36 in the text) are replaced in this code     #
# with (the equivalent) eqns 51 and 52 from Young et al, ref 35                 #
#-------------------------------------------------------------------------------#

from numpy import *
from pylab import *

#define some standard quantities
m = 85*1.66e-27; h = 6.63e-34; hbar = h/(2*pi); i=1j; e0 = 8.85e-12; c = 2.99e8

#set THETA to 0 for sigma+ transitions, pi for sigma- or pi/2 for lin-perp-lin
THETA = 0*pi/2.

#hyperfine frequencies and Raman wavenumber
omega_2 = 2*pi*(384.230406373e12 - 1.264888e9)
omega_1 = 2*pi*(384.230406373e12 + 1.770843e9)
omega_eg = omega_1 - omega_2; k_eff = (omega_1+omega_2)/(3e8)

Nz=5 #number of Zeeman states to consider (5 is all of them)
RME = 3.58e-29 #reduced dipole matrix element (see Steck)

#simga+ transition dipole matrix elements (see Steck)
# (DMeValsAB indicates transition FROM F=A TO F'=B)
DMeVals33 = array([sqrt(25./216),sqrt(5./36),sqrt(5./36),sqrt(25./216),sqrt(5./72)])
DMeVals23 = array([sqrt(2./135),sqrt(2./45),sqrt(4./45),sqrt(4./27),sqrt(2./9)])
DMeVals32 = array([sqrt(10./189),sqrt(2./63),sqrt(1./63),sqrt(1./189),0.])
DMeVals22 = array([sqrt(7./54),sqrt(7./36),sqrt(7./36),sqrt(7./54),0.])
DMeVals21 = array([sqrt(3./10),sqrt(3./20),sqrt(1./20),0.,0.])
DMeVals34 = array([sqrt(3./56),sqrt(3./28),sqrt(5./28),sqrt(15./56),sqrt(3./8)])
DMeValsPlus = RME*array(((DMeVals33),(DMeVals23),(DMeVals32),(DMeVals22),(DMeVals34)
,(DMeVals21)))

#sigma- transition dipole matrix elements (see Steck)
DMeVals33 = array([-sqrt(5./72),-sqrt(25./216),-sqrt(5./36),-sqrt(5./36),-sqrt(25./2
16)])
DMeVals23 = array([sqrt(2./9),sqrt(4./27),sqrt(4./45),sqrt(2./45),sqrt(2./135)])
DMeVals32 = array([0.,sqrt(1./189),sqrt(1./63),sqrt(2./63),sqrt(10./189)])
DMeVals22 = array([0.,-sqrt(7./54),-sqrt(7./36),-sqrt(7./36),-sqrt(7./54)])
DMeVals21 = array([0.,0.,sqrt(1./20),sqrt(3./20),sqrt(3./10)])
DMeVals34 = array([sqrt(3./8),sqrt(15./56),sqrt(5./28),sqrt(3./28),sqrt(3./56)])
DMeValsMinus = RME*array(((DMeVals33),(DMeVals23),(DMeVals32),(DMeVals22),(DMeVals34
),(DMeVals21)))

def E(I): return sqrt(2*I/(c*e0)) #electric field for a given intensity

#--------------------PULSE TIMING PARAMETERS---------------------------------
ntimes=50 #number of timesteps per pi time
pi_time = 1.2e-6 #duration of a pi pulse
tvals=linspace(0,pi_time*13./3,int(ntimes*13./3)) #array of times
tstep=pi_time/ntimes #interval between sampled times
#indices corresponding to the separate sections of the composite pulse
ind1=0; ind2=int(ntimes*1./3); ind3=int(ntimes*2.); ind4=int(ntimes*13./3)

#--------------------EXPERIMENTAL PARAMETERS---------------------------------
#zshift is the Zeeman shift in 2\pi\times Hz, relating to the B-field
I_1 = 14e3; I_2 = 21e3; Delta = 2*pi*8.0e9; zshift = -10*2*pi*1e3
ndeltas=100 #number of sampled laser detunings
deltas=linspace(-3.0,3.0,ndeltas)*2*pi*1e6 #array of laser detunings \delta_L

#----------------MOMENTUM DISTRIBUTION PARAMETERS-----------------------------
Nps = 50 #number of momenta to sample
sigma_1 = 2.5*hbar*k_eff; sigma_2 = 9.0*hbar*k_eff #widths of the two Gaussians
a_1 = 2; a_2 = 1 #amplitudes of the two Gaussians
p_max = 35*hbar*k_eff; p_min = -35*hbar*k_eff
p_vals = linspace(p_min,p_max,Nps) #momentum values array

#momentum distribution
p_dist = a_1*e**(-0.5*(p_vals/sigma_1)**2) + a_2*e**(-0.5*(p_vals/sigma_2)**2)
```

SampleCode.py **Page 2**

```
p_dist /= max(p_dist) #normalise (this makes no difference to the result)

#empty arrays for amplitudes
c_e1=zeros((ndeltas,Nz,Nps)),dtype=complex64)
c_g1=zeros((ndeltas,Nz,Nps)),dtype=complex64)
c_e2=zeros((ndeltas,Nz,Nps)),dtype=complex64)
c_g2=zeros((ndeltas,Nz,Nps)),dtype=complex64)
c_e3=zeros((ndeltas,Nz,Nps)),dtype=complex64)
c_g3=zeros((ndeltas,Nz,Nps)),dtype=complex64)
pop_e=zeros((ndeltas,Nz,Nps))
pop_g=zeros((ndeltas,Nz,Nps))
state_e=zeros((ndeltas,Nz))
state_g=zeros((ndeltas,Nz))
tot_e=zeros((ndeltas))

#----------------------------NUMBER CRUNCHING-------------------------------------
#calculate amplitudes for each laser detuning \delta_L, at all momenta, in all
#Zeeman sublevels

for d in range(ndeltas): #d index of the laser detuning

        for n in range(Nps): #n index of the momentum class

                for z in range(Nz): #z index of the Zeeman sublevel

                        #sigma- dipole matrix elements for Zeeman sublevel n

                        DMe1M=DMeValsMinus[0,z]
                        DMe2M=DMeValsMinus[1,z]
                        DMe3M=DMeValsMinus[2,z]
                        DMe4M=DMeValsMinus[3,z]
                        DMe5M=DMeValsMinus[4,z]
                        DMe6M=DMeValsMinus[5,z]

                        #sigma+ dipole matrix elements for Zeeman sublevel n
                        DMe1P=DMeValsPlus[0,z]
                        DMe2P=DMeValsPlus[1,z]
                        DMe3P=DMeValsPlus[2,z]
                        DMe4P=DMeValsPlus[3,z]
                        DMe5P=DMeValsPlus[4,z]
                        DMe6P=DMeValsPlus[5,z]

#------------------------SINGLE PHOTON RABI FREQUENCIES-----------------------------
                        #M/P indicates sigma-/+ and 1/2 indicates beam 1/2)
                        Omega_eM2 = -(sqrt(DMe1M**2+DMe3M**2+DMe5M**2)/hbar)*E(I_2)
                        Omega_gM1 = -(sqrt(DMe2M**2+DMe4M**2+DMe6M**2)/hbar)*E(I_1)
                        Omega_eM1 = -(sqrt(DMe1M**2+DMe3M**2+DMe5M**2)/hbar)*E(I_1)
                        Omega_gM2 = -(sqrt(DMe2M**2+DMe4M**2+DMe6M**2)/hbar)*E(I_2)
                        Omega_eP2 = -(sqrt(DMe1P**2+DMe3P**2+DMe5P**2)/hbar)*E(I_2)
                        Omega_gP1 = -(sqrt(DMe2P**2+DMe4P**2+DMe6P**2)/hbar)*E(I_1)
                        Omega_eP1 = -(sqrt(DMe1P**2+DMe3P**2+DMe5P**2)/hbar)*E(I_1)
                        Omega_gP2 = -(sqrt(DMe2P**2+DMe4P**2+DMe6P**2)/hbar)*E(I_2)

#--------------------RESONANT RAMAN RABI FREQUENCY (Omega_R)-----------------------
                        Omega_R = (-(abs((DMe1M*DMe2M)+(DMe3M*DMe4M))/hbar)*E(I_1))*
(-1./hbar)*E(I_2)/(2*Delta)*cos(THETA)**2 + (-(abs((DMe1P*DMe2P)+(DMe3P*DMe4P))/hbar
)*E(I_1))*(-1./hbar)*E(I_2)/(2*Delta)*sin(THETA)**2

#---------------------------------LIGHT SHIFTS-----------------------------------
                        #light shifts due to sigma- components (of both beams)
                        Omega_e_ACM = Omega_eM2**2/(4*Delta) + Omega_eM1**2/(4*(Delt
a-omega_eg))
                        Omega_g_ACM = Omega_gM1**2/(4*Delta) + Omega_gM2**2/(4*(Delt
a+omega_eg))

                        #light shifts due to sigma+ components (of both beams)
                        Omega_e_ACP = Omega_eP2**2/(4*Delta) + Omega_eP1**2/(4*(Delt
a-omega_eg))
                        Omega_g_ACP = Omega_gP1**2/(4*Delta) + Omega_gP2**2/(4*(Delt
a+omega_eg))

                        #total light shifts of each hyperfine level
                        Omega_e_AC = Omega_e_ACP*sin(THETA)**2 + Omega_e_ACM*cos(THE
```

SampleCode.py **Page 3**

```
TA)**2
                        Omega_g_AC = Omega_g_ACP*sin(THETA)**2 + Omega_g_ACM*cos(THE
TA)**2

                        #Relative light shift \delta^{AC}
                        delta_AC = Omega_g_AC - Omega_e_AC

                        #Raman detuning \delta
                        delta_12 = deltas[d] - (p_vals[n]*k_eff/m + hbar*k_eff**2/(2
*m)) + (z-2.0)*zshift

                        #generalised Rabi frequency (\tilde{\Omega}_R in text)
                        Omega_r = sqrt(Omega_R**2 + (delta_12 - delta_AC)**2)

                        #angles from equations 2.31
                        stheta = Omega_eff/Omega_r
                        ctheta = -(delta_12 - delta_AC)/Omega_r

#----------------------CALCULATING THE STATE AMPLITUDES---------------------------

#applying equations 2.36 to obtain the state amplitudes at the end of each part of
#the pulse (initial phase is 0.5*pi)

                        c_e1[d,z,n] = exp(-i*(Omega_e_AC + Omega_g_AC)*ind2*tstep*0.
5)*exp(-i*delta_12*ind2*tstep*0.5)*(0*(cos(Omega_r*ind2*tstep*0.5) - i*ctheta*sin(Om
ega_r*ind2*tstep*0.5)) + 1.*exp(-i*(0.5*pi))*(-i*stheta*sin(Omega_r*ind2*tstep*0.5))
)

                        c_g1[d,z,n] = exp(-i*(Omega_e_AC + Omega_g_AC)*ind2*tstep*0.
5)*exp(i*delta_12*ind2*tstep*0.5)*(1.*(cos(Omega_r*ind2*tstep*0.5) + i*ctheta*sin(Om
ega_r*ind2*tstep*0.5)) + 0*exp(i*0.5*pi)*(-i*stheta*sin(Omega_r*ind2*tstep*0.5)))

#notice the addition of pi to the phase here during the second part of the corpse

                        c_e2[d,z,n] = exp(-i*(Omega_e_AC + Omega_g_AC)*(ind3-ind2)*t
step*0.5)*exp(-i*delta_12*(ind3-ind2)*tstep*0.5)*(c_e1[d,z,n]*(cos(Omega_r*(ind3-ind
2)*tstep*0.5) - i*ctheta*sin(Omega_r*(ind3-ind2)*tstep*0.5)) + c_g1[d,z,n]*exp(-i*(1
.5*pi+delta_12*ind2*tstep))*(-i*stheta*sin(Omega_r*(ind3-ind2)*tstep*0.5)))

                        c_g2[d,z,n] = exp(-i*(Omega_e_AC + Omega_g_AC)*(ind3-ind2)*t
step*0.5)*exp(i*delta_12*(ind3-ind2)*tstep*0.5)*(c_g1[d,z,n]*(cos(Omega_r*(ind3-ind2
)*tstep*0.5) + i*ctheta*sin(Omega_r*(ind3-ind2)*tstep*0.5)) + c_e1[d,z,n]*exp(i*(1.5
*pi+delta_12*ind2*tstep))*(-i*stheta*sin(Omega_r*(ind3-ind2)*tstep*0.5)))

#and back to 0.5*pi
                        c_e3[d,z,n] = exp(-i*(Omega_e_AC + Omega_g_AC)*(ind4-ind3)*t
step*0.5)*exp(-i*delta_12*(ind4-ind3)*tstep*0.5)*(c_e2[d,z,n]*(cos(Omega_r*(ind4-ind
3)*tstep*0.5) - i*ctheta*sin(Omega_r*(ind4-ind3)*tstep*0.5)) + c_g2[d,z,n]*exp(-i*(0
.5*pi+delta_12*ind3*tstep))*(-i*stheta*sin(Omega_r*(ind4-ind3)*tstep*0.5)))

                        c_g3[d,z,n] = exp(-i*(Omega_e_AC + Omega_g_AC)*(ind4-ind3)*t
step*0.5)*exp(i*delta_12*(ind4-ind3)*tstep*0.5)*(c_g2[d,z,n]*(cos(Omega_r*(ind4-ind3
)*tstep*0.5) + i*ctheta*sin(Omega_r*(ind4-ind3)*tstep*0.5)) + c_e2[d,z,n]*exp(i*(0.5
*pi+delta_12*ind3*tstep))*(-i*stheta*sin(Omega_r*(ind4-ind3)*tstep*0.5)))

                        #calculate the populations
                        pop_e[d,z,n] = abs(c_e3[d,z,n])**2*p_dist[n]
                        pop_g[d,z,n] = abs(c_g3[d,z,n])**2*p_dist[n]

#------------------------AVERAGING AND NORMALISATION-----------------------------
#average and normalise across the momentum values
for z in range(Nz):
        for d in range(ndeltas):
                        state_e[d,z]=sum(pop_e[d,z,:])/(sum(pop_e[d,z,:])+sum(pop_g[
d,z,:]))
                        state_g[d,z]=sum(pop_g[d,z,:])/(sum(pop_e[d,z,:])+sum(pop_g[
d,z,:]))

#average and normalise across the Zeeman sublevels
for d in range(ndeltas):
        tot_e[d] = sum(state_e[d,:])/(sum(state_e[d,:])+sum(state_g[d,:]))

#we can then plot tot_e*S on the y axis and delta on the x.
```

Appendix C

An introduction to atom interferometry

As proposed by de Broglie in 1924 and confirmed soon after by Thomson, particles of matter exhibit wave-like behaviour, with a characteristic *de Broglie* wavelength

$$\lambda_{\mathrm{db}} = \frac{h}{p}, \tag{C.1}$$

where p is the particle's momentum. We can utilise this 'wave-particle duality' to build a matter-wave interferometer, in which a particle's centre-of-mass wavepacket is physically split and recombined, analogous to splitting and recombining a laser beam in an optical interferometer. Upon recombination, the wavepackets interfere to give an interference pattern which is dependent upon the phase-difference accrued between the interferometer paths. Unlike light-waves in an optical interferometer, matter-waves interact strongly with external (electric, magnetic, gravitational etc.) potentials. These interactions are manifested in phase-shifts of the de Broglie waves, which are mapped onto the interference pattern at the output of the interferometer. Matter-wave interferometry therefore enables precise measurements of such physical potentials, along with measurements of fundamental properties of the matter itself.

The main obstacle to overcome towards useful matter-wave interferometry is the design of suitable *optics* for splitting (beamsplitters), redirecting (mirrors), and recombining

(again, beamsplitters) the matter-wave, since the structure of such optics must be of similar order to the de Broglie wavelength. Early matter-wave interferometry experiments utilised magnet-guided *electron* beams ([106], 1954), where beamsplitting and recombining was achieved by diffraction from thin crystals (for an electron at 1 eV, $\lambda_{\mathrm{dB}} = 1.2\,\mathrm{nm}$). Some years later, the *neutron* interferometer was demonstrated ([107], 1962), in which a neutron beam (for a typical 'cold' neutron at 0.02 eV, $\lambda_{\mathrm{dB}} = 200\,\mathrm{pm}$) was split by single-slit diffraction and recombined with a biprism, and in 1974 a more robust kind of neutron interferometer was developed by Rauch [108], in which the optics were formed by diffraction from silicon crystals whose lattice structure was matched to the neutron de Broglie wavelength. This allowed for larger wavepacket separations within the interferometer (around 2 cm, as compared with 100 μm in [107]), and therefore greater phase-sensitivity to external potentials.

Atom interferometry was largely held back by the capabilities of technology until the early 1990s. An atomic beam of sodium, for example, with a speed of $1000\,\mathrm{m\,s^{-1}}$ has a de Broglie wavelength $\lambda_{\mathrm{dB}} = 17\,\mathrm{pm}$, which is far smaller than those of previous electron and neutron experiments, and since atoms do not penetrate crystal structure in the same way as electrons and neutrons, an alternative kind of grating was required. To this end, phase-coherent *nanofabricated* thin grid-like structures with periodicity $100 - 200\,\mathrm{nm}$ were developed in the early 90s, and put to use in three-grating atom (and molecule) interferometer geometries [109, 110]. Use of similar grating structures continues in more recent experiments, such as large molecule interferometry [111]. Material grating atom optics have their drawbacks, however. For phase coherence they require precision nanofabrication and subsequent delicate handling. Also, by their nature they only transmit a fraction of the impinging particles (many simply hit the 'bars' of the structure), thus putting constraints on signal-to-noise. Most modern precision atom interferometers bypass these problems, and instead utilise light waves for their atom optical elements, as discussed in the following.

Unlike electrons and neutrons, atoms offer a rich internal structure, which can be exploited for the purposes of interferometry. We can induce coherent transitions between internal states of an atom (see section 2.1) by absorption and emission of photons, and since photons carry momentum, such transitions cause coupling of the internal (electronic) and external (momentum) states. With this we can build an atom interferometer

with light-wave-based atom optics. Laser-based beamsplitters and mirrors can take the form of, for example:

1. **Single-photon transitions:** A *continuous-wave* near-resonant laser beam induces transitions between some ground internal state and an excited state, with some probability ρ based on the interaction time, intensity and frequency, by absorption or emission of a photon. See, for example [112]. In this case, a momentum $\hbar k$ is transferred to the atom;

2. **Bragg diffraction:** A *standing-wave*, off-resonant laser beam induces *Bragg diffraction*, whereby the atom remains in the ground state but is diffracted into one of several momentum states separated by $2\hbar\mathbf{k}$, where $\mathbf{k}$ is the wavevector of the laser beam. For example [113], and more recently [114];

3. **Raman transitions:** Two counter-propagating laser beams, separated by some (typically microwave) frequency interval, induce *Raman transitions* between two internal hyperfine states and impart $\hbar(\mathbf{k_1} - \mathbf{k_2})$ to the atom. See, as a milestone example [12].

One particular advantage of the Raman technique over Bragg diffraction, whereby atoms can be lost to multiple diffraction orders, is that in principle, beamsplitters which induce coherent equal superpositions between *only* two states, and mirrors which induce *complete* inversion, are achievable, *i.e.* *all* of the atoms in an atomic beam can contribute to the interferometer signal. Raman transitions are preferred over single-photon transitions firstly because single-photon optical excitation often involves an unstable, radiative upper state (although species such as Strontium [115] is a promising candidate for alleviating this problem), and secondly because the Raman transition offers twice the momentum transfer.

Since the invention and development of laser cooling and trapping (section **??**) it has been possible to perform atom interferometry on a sub-millikelvin (and in some cases sub-microkelvin) sample of atoms confined to a small region of space. In this regime, atom interferometry is performed in the *temporal* domain on a cold, ballistically expanding cloud of atoms. In this case the beamsplitters and mirrors are timed *pulses* of light, as opposed to the always-on arrays of laser beams through which an atomic beam passes in the *spatial* domain. Experiments such as that in [12] use timed, vertically-aligned Raman

pulses in an atomic fountain configuration, where the atoms are projected upwards and allowed to fall under gravity. This arrangement allows for increased interferometer *area*, and therefore increased phase-sensitivity to the gravitational potential, since the time between pulses can be large.

Appendix D

Publications, talks and posters

D.1 Publications

At the time of submission of this thesis, I have not (as a lead-author) published its findings. Publications are, however, in the pipeline:

- I have a paper which presents the composite pulse results of chapter 6, namely [116] in the final stages of preparation.
- Further experiments on interferometric cooling will be performed immediately after submission of this thesis, towards a publication on the results.
- The results given in section 5.1.2 regarding the light shifts of the individual Zeeman sublevels in the Raman system may also constitute a publication, since such a characterisation is absent in the literature.

I have co-authored two publications (both of which were lead-authored by Nathan Cooper) regarding the experimental techniques for Raman beam generation:

- In [63] we describe polarisation-filtering methods for removing the carrier from a phase-modulated spectrum (see section 4.4).
- In [66] we describe the stabilised Mach–Zehnder arrangement for filtering the carrier from a phase-modulated spectrum (see section 4.5, where we employ this setup for *sideband* removal).

D.2 Talks

Just one on this list:

- "Broadband atom interferometry with composite pulses: Towards interferometric cooling "– 19th August 2013, AMO seminar, UCLA Physics and Astronomy, Los Angeles, CA

D.3 posters

I have presented posters regarding this work at the following conferences and schools:

- International Conference on Quantum, Atomic, Molecular and Plasma Physics (QuAMP), September 2013, Swansea University, Swansea, UK (See opposite).
- International School of Physics 'Enrico Fermi', Summer Course on Atom Interferometry, July 2013, Varenna, Italy.
- International Conference on Laser Spectroscopy (ICOLS), June 2013, University of California, Berkeley, Berkeley, CA.
- International Conference on Quantum Optics, Feb 2012, Obergurgl, Austria.
- L'Ecole de Physique, des Houches, Summer course on Cold gases with Long Range Interactions, September 2011, Les Houches, France.
- Young Atom Opticians Conference (YAO), February 2011, Hannover, Germany.

Cooling of atomic motion with broadband composite light-pulse atom interferometry

Alex Dunning, Rachel Gregory, James Bateman, Matt Himsworth & Tim Freegarde

UNIVERSITY OF Southampton

QuAMP 2013 - Swansea - alexander.dunning@gmail.com

Introduction

We are investigating the use of light-pulse interferometry techniques for cooling atomic motion. Interferometer sequences where the output phase is dependent on the initial atomic velocity can be tailored to give cooling forces, and have potential for use in molecular cooling.

As a test bed, we work on a Doppler-broadened, Zeeman-degenerate sample of Rubidium-85 atoms after release from a MOT, where stimulated Raman pulses form the interferometer beamsplitters and mirrors. These pulses are subject to large amounts of dephasing, which we counteract by adapting NMR-type spin echo and composite pulse techniques.

Composite Raman Pulses

Stimulated Raman pulses in 10^7 Zeeman-degenerate Rubidium-85 atoms

Counter-propagating beams impart momentum

Doppler-shifted detuning δ

off-resonance errors

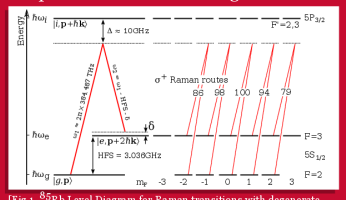

[Fig 1. ^{85}Rb Level Diagram for Raman transitions with degenerate Zeeman sub-levels]

Many degenerate Raman routes

Different coupling strengths

pulse-length errors

Significant pulse dephasing

Spin Echoes

We counteract dephasing in Rabi flopping by applying **rotary** spin echoes [1]

- Reverse the state vector rotation axis by shifting the Raman beam phase by π every Rabi cycle
- This reconverges divergent spin vectors to give a spin echo every cycle

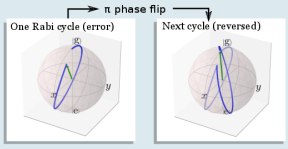

- Greatly **increased dephasing time** in Rabi flopping

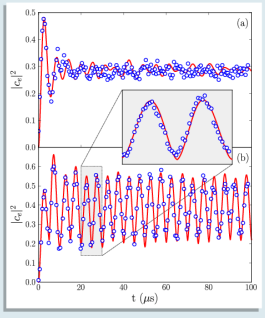

[Fig 2. Measured $|e\rangle$ state population as a function of interaction time t with the Raman beams. (a) Rabi flopping - notice the rapid dephasing; (b) Rabi flopping with rotary spin echo rephasing. Blue circles: data; red line: simulation.]

Composite Pulses

We adapt NMR-style composite rotation techniques to improve pulse **fidelity** [2,3]

- Basic square pulses are replaced with multiple tailored θ, φ rotations
- $\alpha_{\varphi_3}\beta_{\varphi_2}\gamma_{\varphi_3}\ldots$
- Example: 'CORPSE'
- $60_0320_{180}420_0$

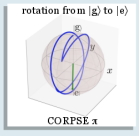

- Replacing beamsplitter and mirror pulses in interferometers [5] with composite pulses can improve contrast [4]. Many composite pulses exist [2, 3, 6, 7]; choice is determined by need to balance error tolerance with length of correction sequence

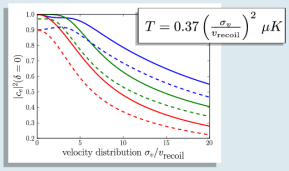

[Fig 4. Predicted peak pulse fidelity achievable using a WALTZ $90_x180_{y}270_x$, Knill $180_{5\pi/6}180_{3\pi/6}180_{\pi/6}180_{5\pi/6}180_{3\pi/6}180_{\pi/6}$ and basic π 180_0. Solid lines: atoms all in mF=0; dashed: atoms evenly distributed across mF=-2,...,+2]

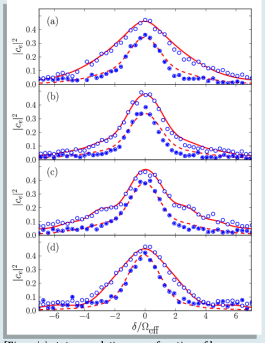

[Fig 3. $|e\rangle$ state populations as a function of laser detuning for four different composite π pulses: basic pulse (filled circles) and composite pulse (open circles). **An improvement in peak fidelity** and width is clear in all cases. Red lines: simulation. (a) CORPSE $60_0320_{\pi}420_0$; (b) Knill $180_{5\pi/6}180_{3\pi/6}180_{\pi/6}180_{5\pi/6}180_{3\pi/6}180_{\pi/6}$; (c) BB1 $180_{\pi/3}360_{3\pi}180_{\pi/3}180_0$; (d) $90_x360_{x}90_x$]

Experimental Setup

Our Raman beams are derived from a single diode laser, where the 3.036 GHz splitting is provided by acousto- and electro-optical modulators. The beams are amplified and shaped to give a high intensity, homogeneous profile.

[Fig 5. Experimental setup for generation of Raman pulses]

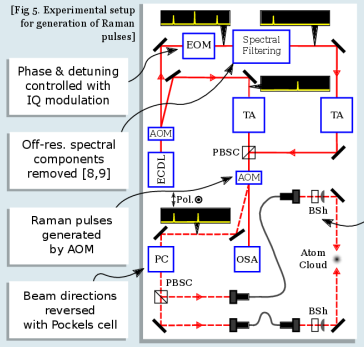

Fields & levels

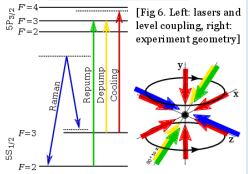

[Fig 6. Left: lasers and level coupling, right: experiment geometry]

- Raman pulses are applied to ~10^7 atoms after release from MOT at 20μK.
- Magnetic fields are nulled with 3 orthogonal sets of shims.
- Atoms are pumped into F=2 before Raman pulses (no m_F spin-polarisation).

Beam shaping

- Raman beams focussed to ~1mm top hat [15] by refractive beam shaper (right).
- Rabi frequency up to 500kHz.

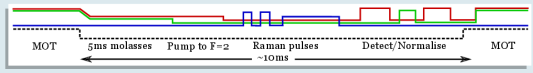

[Fig 7. Experiment timing sketch (NTS). Colours as Fig.6 (dashed line: MOT B fields)]

Interferometric Cooling

Ramsey interferometry to manipulate & cool an atomic velocity distribution

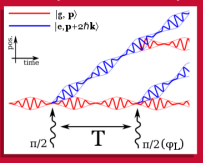

The output state is dependent on the initial atomic velocity. This is a v-dependent force, which can be engineered to give a damping force

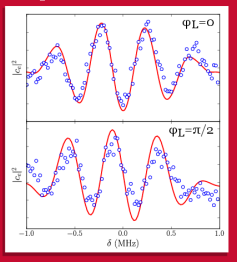

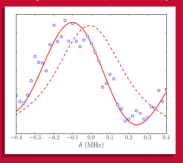

[Figs 8. Left: Ramsey interferometer sequence; Middle: Output state of Ramsey interferometer (T = 1μs) as a function of laser detuning δ with laser phase φ_L; Right: Output state (T = 500ns) overlapped with the velocity distribution (dashed line)]

Output state: $|c_e|^2 \propto |1 - e^{i\Phi}|^2$ → Output phase: $\Phi = \delta T + (\mathbf{k}\bullet\mathbf{v} + \omega_{recoil})T + \varphi_L$

First demonstration

We have demonstrated atomic cooling with the Ramsey interferometer sequence

- We follow the Ramsey interferometer with a 'depump' pulse to force spontaneous emission. This 'resets' atoms to $|g\rangle$ and allows for a reduction in phase-space density
- The Ramsey - depump sequence is repeated N times
- With N=4 we observe a **factor of 2 reduction in the central temperature** of the atom cloud. The mean velocity is shifted up
- Alternating the sequence direction will give cooling

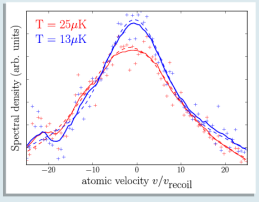

[Fig 9. Demonstration of interferometric cooling. Red - Initial velocity distribution of the atom cloud; Blue - Velocity distribution of the atom cloud after 4 applications of the T=500ns Ramsey interferometer followed by re-thermalisation by spontaneous emission]

Removing δ dependence [10]

Incorporating a spin echo into the Ramsey sequence makes **Φ purely dependent on v**

- Adding two timed π pulses makes the atom spend equal times in g and e, causing a spin echo
- Output phase is only dependent on the velocity

Output phase: $\Phi = (\mathbf{k}\bullet\mathbf{v} + \omega_{recoil})8T + \varphi_L$

- This has applications in translational cooling of **molecules**, [10] if broad (fs) interferometer pulses can be achieved
- This can be combined with coherent force amplification schemes [11,16] to reduce the dependence on spontaneous emission events

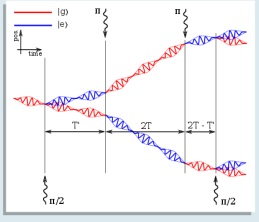

[Fig 10. Ramsey interferometer augmented with two π pulses, which remove the output state dependence on the laser detuning δ, allowing for a purely velocity-dependent force]

Literature

- [1] Rakreungdet *et al*, Phys. Rev. A, **79** 022316 (2009)
- [2] Alway, Jones, J Mag. Res., **189** pp. 114-120 (2007)
- [3] Levitt, Composite Pulses, eMagRes (1996)
- [4] Butts *et al*, JOSA. B **30** pp. 922-927 (2013)
- [5] Young *et al*, Atom Interferometry, Academic Press (1997)
- [6] Ryan *et al*, , Phys. Rev. Lett. **105**, 200402 (2010)
- [7] S. Wimperis, J. Magn. Reson. Ser. A 109, 221 (1994)
- [8] Cooper *et al*, JOSA. B. **29** pp. 646-649 (2012).
- [9] Cooper *et al*, 'Mach-Zehnder' etc. submitted (2013).
- [10] Weitz & Hänsch, Europhys. Lett. **49** pp. 302-308 (2000)
- [11] Freegarde *et al*, Phys. Rev. A **73**, 033409 (2006)
- [12] Freegarde & Segal, Phys. Rev. Lett. **91**, 037904 (2003)
- [13] Chiow *et al*, Phys. Rev. Lett., 130403 **107** (2011)
- [14] McGuirk *et al*, Phys. Rev. Lett., pp. **85** 4498-4501 (2000)
- [15] Boutu *et al*, Phys. Rev. A, **84** 063406 (2011)
- [16] Bakos *et al*, Phys. Rev. A, **53** 2885 (1996)

EPSRC

References

[1] C. E. Wieman, D. E. Pritchard, and D. J. Wineland, "Atom Cooling, Trapping, and Quantum Manipulation," in *More Things in Heaven and Earth*, edited by B. Bederson (Springer New York, 1999) pp. 426–441.

[2] A. Ashkin, "Atomic-Beam Deflection by Resonance-Radiation Pressure," Physical Review Letters **25**, 1321 (1970).

[3] T. W. Hänsch and A. L. Schawlow, "Cooling of gases by laser radiation," Optics Communications **13**, 68 (1975).

[4] D. Wineland and W. Itano, "Laser cooling of atoms," Physical Review A **20**, 1521 (1979).

[5] E. L. Raab, M. Prentiss, A. Cable, S. Chu, and D. E. Pritchard, "Trapping of Neutral Sodium Atoms with Radiation Pressure," Physical Review Letters **59**, 2631 (1987).

[6] M. H. Anderson, J. R. Ensher, M. R. Matthews, C. E. Wieman, and E. A. Cornell, "Observation of Bose-Einstein Condensation in a Dilute Atomic Vapor," Science **269**, 198 (1995).

[7] K. Davis, M. Mewes, M. Andrews, N. van Druten, D. Durfee, D. Kurn, and W. Ketterle, "Bose-Einstein Condensation in a Gas of Sodium Atoms," Physical Review Letters **75**, 3969 (1995).

[8] I. Bloch, J. Dalibard, and S. Nascimbene, "Quantum simulations with ultracold quantum gases," Nature Physics **8**, 267 (2012).

[9] D. Greif, T. Uehlinger, G. Jotzu, L. Tarruell, and T. Esslinger, "Short-Range Quantum Magnetism of Ultracold Fermions in an Optical Lattice," Science **340**, 1307 (2013), arXiv:1212.2634 .

[10] J. Cirac and P. Zoller, "Quantum Computations with Cold Trapped Ions," Physical Review Letters **74**, 4091 (1995).

[11] S. Bize, P. Laurent, M. Abgrall, H. Marion, I. Maksimovic, L. Cacciapuoti, J. Grünert, C. Vian, P. dos Santos, P. Rosenbusch, P. Lemonde, G. Santarelli, P. Wolf, A. Clairon, A. Luiten, M. Tobar, and C. Salomon, "Cold atom clocks and applications," Journal of Physics B: Atomic, Molecular and Optical Physics **38**, S449+ (2005).

[12] M. Kasevich and S. Chu, "Atomic interferometry using stimulated Raman transitions," Physical Review Letters **67**, 181 (1991).

[13] L. D. Carr, D. DeMille, R. V. Krems, and J. Ye, "Cold and ultracold molecules: science, technology and applications," New Journal of Physics **11**, 055049+ (2009).

[14] J. M. Hutson, "Ultracold Chemistry," Science **327**, 788 (2010).

[15] E. Hudson, H. Lewandowski, B. Sawyer, and J. Ye, "Cold Molecule Spectroscopy for Constraining the Evolution of the Fine Structure Constant," Physical Review Letters **96**, 143004+ (2006).

[16] C. Chin, V. V. Flambaum, and M. G. Kozlov, "Ultracold molecules: new probes on the variation of fundamental constants," New Journal of Physics **11**, 055048+ (2009).

[17] E. S. Shuman, J. F. Barry, and D. DeMille, "Laser cooling of a diatomic molecule," Nature **467**, 820 (2010).

[18] M. T. Hummon, M. Yeo, B. K. Stuhl, A. L. Collopy, Y. Xia, and J. Ye, "2D Magneto-Optical Trapping of Diatomic Molecules," Physical Review Letters **110**, 143001+ (2013).

[19] V. Zhelyazkova, A. Cournol, T. E. Wall, A. Matsushima, J. J. Hudson, E. A. Hinds, M. R. Tarbutt, and B. E. Sauer, "Laser cooling and slowing of CaF molecules," (2013), http://arxiv.org/abs/1308.0421, arXiv:1308.0421 .

[20] H. Thorsheim, J. Weiner, and P. Julienne, "Laser-induced photoassociation of ultracold sodium atoms," Physical Review Letters **58**, 2420 (1987).

[21] K. K. Ni, S. Ospelkaus, M. H. G. de Miranda, A. Pe'er, B. Neyenhuis, J. J. Zirbel, S. Kotochigova, P. S. Julienne, D. S. Jin, and J. Ye, "A High Phase-Space-Density Gas of Polar Molecules," Science **322**, 231 (2008).

[22] J. G. Danzl, M. J. Mark, E. Haller, M. Gustavsson, R. Hart, J. Aldegunde, J. M. Hutson, and H.-C. Nagerl, "An ultracold high-density sample of rovibronic ground-state molecules in an optical lattice," Nature Physics **6**, 265 (2010).

[23] D. Egorov, W. C. Campbell, B. Friedrich, S. E. Maxwell, E. Tsikata, L. D. Buuren, and J. M. Doyle, "Buffer-gas cooling of NH via the beam loaded buffer-gas method," *The European Physical Journal D - Atomic, Molecular, Optical and Plasma Physics*, **31**, 307 (2004).

[24] B. K. Stuhl, M. T. Hummon, M. Yeo, G. Quemener, J. L. Bohn, and J. Ye, "Evaporative cooling of the dipolar hydroxyl radical," Nature **492**, 396 (2012).

[25] W. G. Rellergert, S. T. Sullivan, S. J. Schowalter, S. Kotochigova, K. Chen, and E. R. Hudson, "Evidence for sympathetic vibrational cooling of translationally cold molecules," Nature **495**, 490 (2013).

[26] J. R. Bochinski, E. R. Hudson, H. J. Lewandowski, G. Meijer, and J. Ye, "Phase Space Manipulation of Cold Free Radical OH Molecules," Physical Review Letters **91**, 243001+ (2003), arXiv:physics/0306062 .

[27] B. Sawyer, B. Lev, E. Hudson, B. Stuhl, M. Lara, J. Bohn, and J. Ye, "Magneto-electrostatic Trapping of Ground State OH Molecules," Physical Review Letters **98** (2007), 10.1103/physrevlett.98.253002.

[28] M. Weitz and T. W. Hänsch, "Frequency-independent laser cooling based on interferometry," Europhysics Letters **49**, 302 (2000).

[29] M. H. Levitt and R. Freeman, "Compensation for pulse imperfections in NMR spin-echo experiments," Journal of Magnetic Resonance (1969) **43**, 65 (1981).

[30] J. Bateman and T. Freegarde, "Fractional adiabatic passage in two-level systems: Mirrors and beam splitters for atomic interferometry," Physical Review A **76**, 013416 (2007).

[31] L. S. Goldner, C. Gerz, R. J. C. Spreeuw, S. L. Rolston, C. I. Westbrook, W. D. Phillips, P. Marte, and P. Zoller, "Momentum transfer in laser-cooled cesium by adiabatic passage in a light field," Physical Review Letters **72**, 997 (1994).

[32] D. S. Weiss, B. C. Young, and S. Chu, "Precision measurement of the photon recoil of an atom using atomic interferometry," Physical Review Letters **70**, 2706 (1993).

[33] K. Moler, D. S. Weiss, M. Kasevich, and S. Chu, "Theoretical analysis of velocity-selective Raman transitions." Physical review. A **45**, 342 (1992).

[34] U. Gaubatz, P. Rudecki, S. Schiemann, and K. Bergmann, "Population transfer between molecular vibrational levels by stimulated Raman scattering with partially overlapping laser fields. A new concept and experimental results," The Journal of Chemical Physics **92**, 5363 (1990).

[35] B. Young, M. Kasevich, and S. Chu, "Precision atom interferometry with light pulses," in *Atom interferometry*, edited by P. Berman (1997) Chap. 9, pp. 363–406.

[36] N. F. Ramsey, "A Molecular Beam Resonance Method with Separated Oscillating Fields," Physical Review Online Archive (Prola) **78**, 695 (1950).

[37] R. P. Feynman, F. L. Vernon, and R. W. Hellwarth, "Geometrical Representation of the Schrodinger Equation for Solving Maser Problems," Journal of Applied Physics **28**, 49+ (1957).

[38] I. Rabi, N. Ramsey, and J. Schwinger, "Use of Rotating Coordinates in Magnetic Resonance Problems," Reviews of Modern Physics **26**, 167 (1954).

[39] F. Bloch, "Nuclear Induction," Physical Review **70**, 460 (1946).

[40] B. W. Shore, *Manipulating Quantum Structures Using Laser Pulses*, 1st ed. (Cambridge University Press, 2011).

[41] U. Fano, "Description of States in Quantum Mechanics by Density Matrix and Operator Techniques," Reviews of Modern Physics **29**, 74 (1957).

[42] C. J. Foot, *Atomic Physics* (Oxford University Press, 2005).

[43] P. Atkins and R. Friedman, *Molecular Quantum Mechanincs*, 4th ed. (Oxford University Press, 2005).

[44] D. A. Steck, "Rubidium 85 D Line Data," Http://steck.us/alkalidata/.

[45] D. Budker, D. F. Kimball, and D. P. DeMille, *Atomic physics: An exploration through problems and solutions*, 2nd ed. (Oxford University Press, 2008).

[46] H. Jahn and J. Hope, "Symmetry Properties of the Wigner 9j Symbol," Physical Review **93**, 318 (1954).

[47] W. R. Inc., "Mathematica," (2010).

[48] J. Bateman, A. Xuereb, and T. Freegarde, "Stimulated Raman transitions via multiple atomic levels," Physical Review A **81**, 043808+ (2010).

[49] J. Bateman, *Novel schemes for the optical manipulation of atoms and molecules*, Ph.D. thesis, School of Physics and Astronomy, University of Southampton (2009), (online copy at http://phyweb.phys.soton.ac.uk/quantum/articles.php).

[50] M. Himsworth, *Coherent manipulation of ultracold rubidium*, Ph.D. thesis, School of Physics and Astronomy, University of Southampton (2009), (online copy at http://phyweb.phys.soton.ac.uk/quantum/articles.php).

[51] H. J. Metcalf and P. Van der Straten, *Laser Cooling and Trapping* (Springer, 1999).

[52] J. Weiner and P. T. Ho, *Light-Matter Interaction*, Vol. 1 (Wiley, 2003).

[53] R. Murray, *Coherent two-photon excitation within an extended cloud of Rubidium 85 for the purposes of atomic interferometry and cooling*, Ph.D. thesis, School of Physics and Astronomy, University of Southampton (2011), (online copy at http://phyweb.phys.soton.ac.uk/quantum/articles.php).

[54] S. Patel, *A chirped, pulsed laser system and magneto-optical trap for rubidium*, Ph.D. thesis, School of Physics and Astronomy, University of Southampton (2009), (online copy at http://phyweb.phys.soton.ac.uk/quantum/articles.php).

[55] J. Appel, A. MacRae, and A. I. Lvovsky, "A versatile digital GHz phase lock for external cavity diode lasers," Measurement Science and Technology **20**, 055302+ (2009).

[56] C. J. Dedman, K. G. H. Baldwin, and M. Colla, "Fast switching of magnetic fields in a magneto-optic trap," Review of Scientific Instruments **72**, 4055 (2001).

[57] A. Vorozcovs, M. Weel, S. Beattie, S. Cauchi, and A. Kumarakrishnan, "Measurements of temperature scaling laws in an optically dense magneto-optical trap," J. Opt. Soc. Am. B **22**, 943 (2005).

[58] J. Chabé, H. Lignier, P. Szriftgiser, and J. C. Garreau, "Improving Raman velocimetry of laser-cooled cesium atoms by spin-polarization," Optics Communications **274**, 254 (2007).

[59] W. D. Phillips, "Nobel Lecture: Laser cooling and trapping of neutral atoms," Reviews of Modern Physics **70**, 721 (1998).

[60] J. Reichel, O. Morice, G. M. Tino, and C. Salomon, "Subrecoil Raman Cooling of Cesium Atoms," Europhysics Letters **28**, 477 (1994).

[61] M. Kasevich and S. Chu, "Laser cooling below a photon recoil with three-level atoms," Physical Review Letters **69**, 1741 (1992).

[62] G. C. Tarr, "Single-sideband frequency modulation," Electronics and Power **11**, 286+ (1965).

[63] N. Cooper, J. Bateman, A. Dunning, and T. Freegarde, "Actively stabilized wavelength-insensitive carrier elimination from an electro-optically modulated laser beam," J. Opt. Soc. Am. B **29**, 646 (2012).

[64] T. W. Hansch and B. Couillaud, "Laser frequency stabilization by polarization spectroscopy of a reflecting reference cavity," Optics Communications **35**, 441 (1980).

[65] J. E. Bateman, R. L. D. Murray, M. Himsworth, H. Ohadi, A. Xuereb, and T. Freegarde, "Hänsch-Couillaud locking of Mach-Zehnder interferometer for carrier removal from a phase-modulated optical spectrum," J. Opt. Soc. Am. B **27**, 1530 (2010).

[66] N. Cooper, J. Woods, J. Bateman, A. Dunning, and T. Freegarde, "Stabilized fiber-optic MachZehnder interferometer for carrier-frequency rejection," Appl. Opt. **52**, 5713 (2013).

[67] F. K. Fatemi, M. L. Terraciano, M. Bashkansky, and Z. Dutton, "Cold atom Raman spectrography using velocity-selective resonances," Opt. Express **17**, 12971 (2009).

[68] B. Mathur, H. Tang, and W. Happer, "Light Shifts in the Alkali Atoms," Physical Review **171**, 11 (1968).

[69] D. S. Weiss, B. C. Young, and S. Chu, "Precision measurement of $\hbar/m_{Cs}$ based on photon recoil using laser-cooled atoms and atomic interferometry," Applied Physics B: Lasers and Optics **59**, 217 (1994).

[70] D. L. Butts, J. M. Kinast, B. P. Timmons, and R. E. Stoner, "Light pulse atom interferometry at short interrogation times," J. Opt. Soc. Am. B **28**, 416 (2011).

[71] C. G. Townsend, N. H. Edwards, C. J. Cooper, K. P. Zetie, C. J. Foot, A. M. Steane, P. Szriftgiser, H. Perrin, and J. Dalibard, "Phase-space density in the magneto-optical trap," Physical Review A **52**, 1423 (1995).

[72] M. H. Levitt, "Composite pulses," Encyclopedia of Nuclear Magnetic Resonance **2**, 1396 (1996).

[73] E. Collin, G. Ithier, A. Aassime, P. Joyez, D. Vion, and D. Esteve, "NMR-like Control of a Quantum Bit Superconducting Circuit," Physical Review Letters **93**, 157005+ (2004).

[74] C. D. Aiello, M. Hirose, and P. Cappellaro, "Composite-pulse magnetometry with a solid-state quantum sensor," Nat Commun **4**, 1419+ (2013).

[75] F. Schmidt-Kaler, H. Haffner, M. Riebe, S. Gulde, G. P. T. Lancaster, T. Deuschle, C. Becher, C. F. Roos, J. Eschner, and R. Blatt, "Realization of the CiracZoller controlled-NOT quantum gate," Nature **422**, 408 (2003).

[76] S. Gulde, M. Riebe, G. P. T. Lancaster, C. Becher, J. Eschner, H. Haffner, F. Schmidt-Kaler, I. L. Chuang, and R. Blatt, "Implementation of the

DeutschJozsa algorithm on an ion-trap quantum computer," Nature **421**, 48 (2003).

[77] M. Riebe, M. Chwalla, J. Benhelm, H. Häffner, W. Hänsel, C. F. Roos, and R. Blatt, "Quantum teleportation with atoms: quantum process tomography," New Journal of Physics **9**, 211+ (2007).

[78] N. Timoney, V. Elman, S. Glaser, C. Weiss, M. Johanning, W. Neuhauser, and C. Wunderlich, "Error-resistant single-qubit gates with trapped ions," Physical Review A **77** (2008), 10.1103/physreva.77.052334.

[79] M. H. Schleier-Smith, I. D. Leroux, and V. Vuletić, "States of an Ensemble of Two-Level Atoms with Reduced Quantum Uncertainty," Physical Review Letters **104**, 073604+ (2010).

[80] N. Lundblad, J. M. Obrecht, I. B. Spielman, and J. V. Porto, "Field-sensitive addressing and control of field-insensitive neutral-atom qubits," Nature Physics **5**, 575 (2009).

[81] M. G. Bason, M. Viteau, N. Malossi, P. Huillery, E. Arimondo, D. Ciampini, R. Fazio, V. Giovannetti, R. Mannella, and O. Morsch, "High-fidelity quantum driving," Nat Phys **8**, 147 (2012).

[82] W. Rakreungdet, J. H. Lee, K. F. Lee, B. E. Mischuck, E. Montano, and P. S. Jessen, "Accurate microwave control and real-time diagnostics of neutral-atom qubits," Physical Review A **79**, 022316 (2009).

[83] D. L. Butts, K. Kotru, J. M. Kinast, A. M. Radojevic, B. P. Timmons, and R. E. Stoner, "Efficient broadband Raman pulses for large-area atom interferometry," J. Opt. Soc. Am. B **30**, 922 (2013).

[84] J. Rooney, "A survey of representations of spatial rotation about a fixed point," Environment and Planning B **4**, 185 (1977).

[85] E. L. Hahn, "Spin Echoes," Physical Review Online Archive (Prola) **80**, 580 (1950).

[86] H. K. Cummins and J. A. Jones, "Use of composite rotations to correct systematic errors in NMR quantum computation," New Journal of Physics **2**, 6 (2000).

[87] S. Wimperis, "Broadband, Narrowband, and Passband Composite Pulses for Use in Advanced NMR Experiments," Journal of Magnetic Resonance, Series A **109**, 221 (1994).

[88] C. A. Ryan, J. S. Hodges, and D. G. Cory, "Robust Decoupling Techniques to Extend Quantum Coherence in Diamond," Physical Review Letters **105**, 200402 (2010).

[89] R. Tycko and A. Pines, "Iterative schemes for broad-band and narrow-band population inversion in NMR," Chemical Physics Letters **111**, 462 (1984).

[90] A. J. Shaka, J. Keeler, T. Frenkiel, and R. Freeman, "An improved sequence for broadband decoupling: WALTZ-16," Journal of Magnetic Resonance (1969) **52**, 335 (1983).

[91] H. K. Cummins, G. Llewellyn, and J. A. Jones, "Tackling systematic errors in quantum logic gates with composite rotations," Physical Review A **67**, 042308 (2003), arXiv:quant-ph/0208092 .

[92] R. Freeman, S. P. Kempsell, and M. H. Levitt, "Radiofrequency pulse sequences which compensate their own imperfections," Journal of Magnetic Resonance (1969) **38**, 453 (1980).

[93] Z. Starčuk and V. Sklenář, "Composite pulse sequences with variable performance," Journal of Magnetic Resonance (1969) **62**, 113 (1985).

[94] J. M. McGuirk, M. J. Snadden, and M. A. Kasevich, "Large Area Light-Pulse Atom Interferometry," Physical Review Letters **85**, 4498 (2000).

[95] T. Kovachy, S. W. Chiow, and M. A. Kasevich, "Adiabatic-rapid-passage multiphoton Bragg atom optics," Physical Review A **86**, 011606 (2012).

[96] C. Bordé, "Atomic interferometry with internal state labelling," Physics Letters A **140**, 10 (1989).

[97] K. Bongs, R. Launay, and M. A. Kasevich, "High-order inertial phase shifts for time-domain atom interferometers," *Applied Physics B*, **84**, 599 (2006).

[98] J. Reichel, F. Bardou, M. B. Dahan, E. Peik, S. Rand, C. Salomon, and C. C. Tannoudji, "Raman Cooling of Cesium below 3 nK: New Approach Inspired by Lévy Flight Statistics," Physical Review Letters **75**, 4575 (1995).

[99] T. Baumert, J. Helbing, and G. Gerber, "Coherent Control With Femtosecond Laser Pulses," *Advances in Chemical Physics*, , 47 (2007).

[100] J. Vala and R. Kosloff, "Coherent mechanism of robust population inversion." Optics express **8**, 238 (2001).

[101] R. Hildner, D. Brinks, and N. F. van Hulst, "Femtosecond coherence and quantum control of single molecules at room temperature," Nat Phys **7**, 172 (2011).

[102] T. Freegarde, G. Daniell, and D. Segal, "Coherent amplification in laser cooling and trapping," Physical Review A **73**, 033409+ (2006).

[103] J. Bakos, G. Djotyan, G. Demeter, and Z. Sörlei, "Transient laser cooling of two-level quantum systems with narrow natural linewidths," Physical Review A **53**, 2885 (1996).

[104] S.-w. Chiow, T. Kovachy, J. M. Hogan, and M. A. Kasevich, "Generation of 43W of quasi-continuous 780nm laser light via high-efficiency, single-pass frequency doubling in periodically poled lithium niobate crystals," Opt. Lett. **37**, 3861 (2012).

[105] M. Zhu and L. S. Cutler, "Theoretical and Experimental Study of Light Shift in a CPT-Based RB Vapor Cell Frequency Standard," in *32nd Annual Precise Time and Time Interval (PTTI) Meeting* (2000).

[106] L. Marton, Simpson, and J. A. Suddeth, "An Electron Interferometer," Review of Scientific Instruments **25**, 1099 (1954).

[107] H. Maier-Leibnitz and T. Springer, "Ein Interferometer für langsame Neutronen," *Zeitschrift für Physik*, **167**, 386 (1962).

[108] H. Rauch, W. Treimer, and U. Bonse, "Test of a single crystal neutron interferometer," Physics Letters A **47**, 369 (1974).

[109] D. Keith, C. Ekstrom, Q. Turchette, and D. Pritchard, "An interferometer for atoms," Physical Review Letters **66**, 2693 (1991).

[110] M. S. Chapman, C. R. Ekstrom, T. D. Hammond, R. A. Rubenstein, J. Schmiedmayer, S. Wehinger, and D. E. Pritchard, "Optics and Interferometry with Molecules," Physical Review Letters **74**, 4783 (1995).

[111] B. Brezger, L. Hackermüller, S. Uttenthaler, J. Petschinka, M. Arndt, and A. Zeilinger, "Matter-Wave Interferometer for Large Molecules," Physical Review Letters **88**, 100404+ (2002).

[112] K. Sengstock, U. Sterr, G. Hennig, D. Bettermann, J. H. Müller, and W. Ertmer, "Optical Ramsey interferences on laser cooled and trapped atoms, detected by electron shelving," Optics Communications **103**, 73 (1993).

[113] D. Giltner, R. McGowan, and S. Lee, "Atom Interferometer Based on Bragg Scattering from Standing Light Waves," Physical Review Letters **75**, 2638 (1995).

[114] H. Müller, S.-w. Chiow, Q. Long, S. Herrmann, and S. Chu, "Atom Interferometry with up to 24-Photon-Momentum-Transfer Beam Splitters," Physical Review Letters **100** (2008), 10.1103/physrevlett.100.180405.

[115] P. W. Graham, J. M. Hogan, M. A. Kasevich, and S. Rajendran, "New Method for Gravitational Wave Detection with Atomic Sensors," Physical Review Letters **110** (2013), 10.1103/physrevlett.110.171102.

[116] A. Dunning, R. Gregory, J. Bateman, N. Cooper, M. Himsworth, and T. Freegarde, "Composite pulses for interferometry in a cold atom cloud," (2014), article in preparation.